

AN ABSTRACT OF THE THESIS OF

Nikola Milivoj Catipovic for the degree of Doctor of Philosophy
in Chemical Engineering presented on March 7, 1979

Title: HEAT TRANSFER TO HORIZONTAL TUBES IN FLUIDIZED
BEDS: EXPERIMENT AND THEORY

Abstract approved: Redacted for privacy
Thomas J. Fitzgerald

Heat transfer to horizontal tubes is of particular significance for fluid-bed combustion of coal and other materials. Very little information exists for beds operating with particles larger than 0.4 mm. A detailed study was undertaken with the goal of filling this gap and producing data and correlations of value for design.

An instrumented cylinder was developed making possible simultaneous measurements of instantaneous, as well as time-averaged, local heat transfer coefficients, voidage, and surface pressure variations at several positions around its circumference. The instrument enabled the collection of a large body of data which give detailed information about fluid dynamic and heat transfer behavior in the vicinity of the instrumented tube and suggest answers to some crucial heat transfer problems.

Experimental work was performed at room temperature and atmospheric pressure, in a bed of a 0.48 m x 0.13 m cross section, with air as the fluidizing gas. Runs were made with a single immersed tube, as well as with a closely spaced tube array. Heat transfer and voidage results, covering a wide range of particle sizes (0.37-6.6 mm) and superficial gas velocities (0.1-5.6 m/s), are reported and discussed from a design standpoint. Among several

findings, two are most notable: a) voidage at the surface of the tube varies much less with gas velocity than the overall bed voidage, and b) the gas convective component of heat transfer is not affected by the superficial velocity.

Data for conditions near minimum fluidization are compared with the recently developed Adams analytical model of heat transfer for large particles. The model gives accurate predictions of local instantaneous and time-averaged coefficients, with and without the presence of bubbles. All of its aspects, except the radiative heat exchange, are fully verified.

A theoretical model, applicable over a wide range of fluidizing conditions in bubbling and slugging beds, is proposed. The theory assumes that heat exchange between a cold fluidized bed and a horizontal tube takes place by three parallel paths--heat is transferred by packets of particles, by gas percolating between the particles and the tube surface, and by gas bubbles or slugs. Correlations are presented for the corresponding particle convective, gas convective, and bubble heat transfer coefficients, as well as for the voidage around the tube. An analysis shows that, from a heat transfer standpoint, particles may be classified as fine ($d_p < 0.4$ mm), intermediate ($0.4 \text{ mm} < d_p < 1 \text{ mm}$), and large ($d_p > 1 \text{ mm}$). For each of these cases, equations for the time-averaged heat transfer coefficient to the tube as a whole are given.

Predictions based on the proposed theory are compared with the experimental results of this study, as well as with literature data for intermediate and large particles. The model is shown to be very reliable for a variety of operating conditions. It is therefore introduced as a general model for the conductive and convective modes of heat transfer.

Heat Transfer to Horizontal Tubes in Fluidized
Beds: Experiment and Theory

by

Nikola Milivoj Catipovic

A THESIS

submitted to

Oregon State University

in partial fulfillment of
the requirements for the
degree of

Doctor of Philosophy

Completed March 1979

Commencement June 1979

APPROVED:

Redacted for privacy _____

Professor of Chemical Engineering

in charge of major

Redacted for privacy

Head of Department of Chemical Engineering

Redacted for privacy

Dean of Graduate School

Date thesis is presented March 7, 1979

Typed by Clover Redfern for Nikola M. Catipovic

ACKNOWLEDGMENTS

My appreciation goes to Dr. Tom Fitzgerald for his advice and help in the course of this research. He was once described as a "fountain of ideas, both good and bad". I consider that description quite unfair. He is more like the Old Faithful Geyser--excellent ideas erupt with regularity! It has been an honor, as well as a pleasure, to collaborate with him.

I am also very grateful to Dr. Octave Levenspiel for his wise suggestions and assistance whenever necessary. Working with these two gentlemen has been a stimulating and unforgettable experience.

I shall cherish my stay at the Chemical Engineering Department in Corvallis as a most memorable period due in no small part to the attention, friendliness and warmth of Dr. Charles Wicks, Chairman, and other members of the faculty.

I wish to express gratitude to my old friend Goran Jovanovic, with whom I have cooperated successfully for so many years, and to my new friend Manuk "The T" Colakyan, who was unselfishly available whenever the word "computer" was mentioned. My thanks also go to RTC for his assistance with electronics, to Alan George for his contribution to Chapter V, to Ron Hill for the immense drafting job, and to Ksenija for the invaluable help in the last few months of thesis work.

I am thankful to the Electric Power Research Institute and Babcock and Wilcox Company for their financial support and to the Institute for Chemistry, Technology and Metallurgy in Belgrade for granting me a leave of absence to work on this doctorate.

Finally, and most importantly, I come to my family. My apologies to precious little Maja for not being a devoted father in the first few months of her life. I intend to make up for it in the very near future. My greatest appreciation and gratefulness to my beloved wife Mira for her patience, support, encouragement and assistance.

TABLE OF CONTENTS

<u>Chapter</u>	<u>Page</u>
I. INTRODUCTION	1
II. PREVIOUS WORK	4
A. Instrumentation	4
Instantaneous Measurements	4
Time-Averaged Local Measurements	5
Summary	6
B. Data and Correlations	7
III. EXPERIMENTAL EQUIPMENT	10
A. Instrumented Cylinder for Heat Transfer Studies	10
Heat Transfer Measuring Elements	12
Calculation of Heat Transfer Coefficients	17
Capacitance Elements for Voidage Measurement	20
Local Pressure Measurement	23
Typical Signals from the Measuring Elements	24
B. Fluidized Bed Facility	27
C. Bed Expansion Measurement	31
D. Data Acquisition System	31
IV. EXPERIMENTAL RESULTS	35
A. Fluidizing Conditions	35
B. Heat Transfer Results	39
Graphical Presentation	39
General Comments	44
Instantaneous Coefficients	58
Time-Averaged Local Coefficients	60
Time-Averaged Overall Coefficients	63
C. Results from Capacitance Measurements	66
Graphical Presentation	66
General Comments	77
Local Behavior	78
Overall Behavior	81
D. Bed Expansion Results	82
V. HEAT TRANSFER NEAR MINIMUM FLUIDIZATION FOR LARGE PARTICLES: COMPARISON OF EXPERIMENTAL RESULTS WITH THE ADAMS ANALYTICAL MODEL	86
A. Regimes of Large-Particle Fluidization	86
B. The Adams Analytical Model	88

<u>Chapter</u>	<u>Page</u>
C. Comparison of Time-Averaged Local Coefficients	93
D. Comparison of Instantaneous Local Coefficients in the Presence of Bubbles	102
E. Conclusions about the Adams Model	109
VI. HEAT TRANSFER OVER A WIDE RANGE OF FLUIDIZING CONDITIONS: DEVELOPMENT OF A THEORETICAL MODEL	110
A. Physical Model	110
Particle Convective Component	113
Gas Convective Component	115
Bubble Component	117
B. Clues from Experiment	118
Particle Convective Component	119
Gas Convective Component	127
Bubble Component	131
Information on the Emulsion Contact Fraction	133
C. Special Cases	136
Fine Particles	136
Intermediate Particles	137
Large Particles	138
D. Significance of the Model	139
VII. COMPARISON BETWEEN MODEL PREDICTIONS AND EXPERIMENTAL RESULTS	140
A. Our Results	140
Intermediate Particles	140
Large Particles	142
General Comments about Time-Averaged Overall Coefficients	145
Comments about Local Coefficients	148
B. Results of Other Investigators	149
Results of Xavier and Davidson	149
Results of Canada, McLaughlin and Staub	150
C. Comparisons of Existing Heat Transfer Correlations with Experimental Results	154
D. Conclusions about the Proposed Model	158
VIII. SUMMARY AND CONCLUSIONS	162
BIBLIOGRAPHY	165

<u>Chapter</u>	<u>Page</u>
APPENDICES	175
Appendix A: Temperature Control Circuit for the Heat Transfer Measuring Elements	175
Appendix B: Mathematical Model for the Heat Transfer Measuring Elements	179
Appendix C: Calibrating Procedure for Determining the Temperatures of the Platinum Heating Elements	184
Appendix D: Comparison of Measured and Predicted Heat Transfer Coefficients in Air Flow	186
Appendix E: Error Analysis of Heat Transfer Measurement	189
Appendix F: Capacitance Element Circuitry	192
Appendix G: Particle Thermal Time Constant as a Function of Particle Size	194

LIST OF FIGURES

<u>Figure</u>	<u>Page</u>
3. 1. Sketch of the instrumented cylinder for heat transfer studies.	11
3. 2. Photo of the instrumented cylinder and the cartridge heater.	13
3. 3. Sketch of the platinum film heater element.	14
3. 4. Detail of the heating element and the surrounding capacitance probes.	19
3. 5. Simplified schematic drawing of the capacitance probe.	21
3. 6. Simultaneous voltage records of: (a) capacitance and heat transfer elements, and (b) capacitance probe pair; at the side of the copper cylinder, $\theta = 90^\circ$ ($d_p = 4.0$ mm).	25
3. 7. Simultaneous voltage records of: (a) pressure and capacitance elements, and (b) pressure and heat transfer elements; at $\theta = 45^\circ$ ($d_p = 4.0$ mm).	26
3. 8. Diagram of the fluidized bed facility.	28
3. 9. (a) Photo of the fluidization vessel with the instrumented cylinder in position; (b) Photo of the fluidized bed with a horizontal tube (cylinder) array.	30
3. 10. Experimental setup of pressure probes for bed expansion measurement.	32
3. 11. Block diagram of the Chemical Engineering Department minicomputer facility.	33
4. 1. Bed geometry (slumped bed heights are indicated by broken lines, distances from the distributor are in meters).	38
4. 2. Bed pressure drop as a function of superficial gas velocity for $d_p = 1.3$ mm (thinner lines indicate bounds of pressure fluctuations).	40

- 4.3. Time-averaged local heat transfer coefficients as functions of superficial gas velocity, for $d_p = 0.37$ mm (lines indicate maximum and minimum instantaneous values, $h_{\theta i, \max}$ and $h_{\theta i, \min}$). 42
- 4.4. Time-averaged overall heat transfer coefficient as a function of superficial gas velocity, for $d_p = 0.37$ mm. 43
- 4.5. Time-averaged local heat transfer coefficients as functions of superficial gas velocity, for $d_p = 0.8$ mm (lines indicate maximum and minimum instantaneous values, $h_{\theta i, \max}$ and $h_{\theta i, \min}$). 45
- 4.6. Time-averaged overall heat transfer coefficient as a function of superficial gas velocity, for $d_p = 0.8$ mm. 46
- 4.7. Time-averaged local heat transfer coefficients as functions of superficial gas velocity, for $d_p = 1.3$ mm (lines indicate maximum and minimum instantaneous values, $h_{\theta i, \max}$ and $h_{\theta i, \min}$). 47
- 4.8. Time-averaged overall heat transfer coefficient as a function of superficial gas velocity, for $d_p = 1.3$ mm. 48
- 4.9. Time-averaged local heat transfer coefficients as functions of superficial gas velocity, for $d_p = 2.0$ mm (lines indicate maximum and minimum instantaneous values, $h_{\theta i, \max}$ and $h_{\theta i, \min}$). 49
- 4.10. Time-averaged overall heat transfer coefficient as a function of superficial gas velocity, for $d_p = 2.0$ mm. 50
- 4.11. Time-averaged local heat transfer coefficients as functions of superficial gas velocity, for $d_p = 2.85$ mm (lines indicate maximum and minimum instantaneous values, $h_{\theta i, \max}$ and $h_{\theta i, \min}$). 51
- 4.12. Time-averaged overall heat transfer coefficient as a function of superficial gas velocity, for $d_p = 2.85$ mm. 52

<u>Figure</u>	<u>Page</u>
4.13. Time-averaged local heat transfer coefficients as functions of superficial gas velocity, for $d_p = 4.0$ mm (lines indicate maximum and minimum instantaneous values, $h_{\theta i, \max}$ and $h_{\theta i, \min}$).	53
4.14. Time-averaged overall heat transfer coefficient as a function of superficial gas velocity, for $d_p = 4.0$ mm.	54
4.15. Time-averaged local heat transfer coefficients as functions of superficial gas velocity, for $d_p = 6.6$ mm (lines indicate maximum and minimum instantaneous values, $h_{\theta i, \max}$ and $h_{\theta i, \min}$).	55
4.16. Time-averaged overall heat transfer coefficient as a function of superficial gas velocity, for $d_p = 6.6$ mm.	56
4.17. Maximum and minimum instantaneous local heat transfer coefficients for $d_p = 0.37$ and 4.0 mm, at $U - U_{mf} = 0.6$ m/s.	59
4.18. Time-averaged local heat transfer coefficients for $d_p = 0.37$ and 4.0 mm, at several values of U/U_{mf} .	61
4.19. Time-averaged overall heat transfer coefficients for all particle sizes used, as functions of superficial gas velocity.	64
4.20. Time-averaged overall heat transfer coefficients for all particle sizes used, as functions of U/U_{mf} --single tube case.	65
4.21. Time-averaged overall heat transfer coefficients for all particle sizes used, as functions of U/U_{mf} --tube array case.	67
4.22. Maximum time-averaged overall heat transfer coefficient as a function of particle size.	68
4.23. Typical signals from capacitance probes, with local emulsion and bubble residence times indicated.	69

<u>Figure</u>	<u>Page</u>
4.24. Average local emulsion residence times and local emulsion contact fractions as functions of U/U_{mf} , for $d_p = 0.37$ mm.	72
4.25. Average local emulsion residence times and local emulsion contact fractions as functions of U/U_{mf} , for $d_p = 1.3$ mm.	73
4.26. Average local emulsion residence times and local emulsion contact fractions as functions of U/U_{mf} , for $d_p = 4.0$ mm.	74
4.27. Overall average emulsion residence times for $d_p = 0.37, 1.3$ and 4.0 mm, as functions of U/U_{mf} .	75
4.28. Overall emulsion contact fractions (fractions of time which tube spends in contact with emulsion) for $d_p = 0.37, 1.3$, and 4.0 mm, as functions of U/U_{mf} .	76
4.29. Average local emulsion residence times for $d_p = 0.37$ and 4.0 mm, at several values of U/U_{mf} .	79
4.30. Local emulsion contact fractions for $d_p = 0.37$ and 4.0 mm, at several values of U/U_{mf} .	80
4.31. Calculation of bed expansion, H/H_0 , from pressure probe measurements.	83
4.32. Average bed volume fraction for the emulsion phase, $1 - \delta$, as a function of U/U_{mf} .	84
5.1. Regimes of fluidization for large particles.	87
5.2. Transient cooling of a dolomite particle--theoretical curves [1, 2] are compared with our experimental data (residence times decrease further with increasing gas velocity).	89
5.3. Interstitial channel.	90
5.4. Boundaries of the slow bubble region--range of applicability of the Adams model--for dolomite particles, with $H_0 = 0.46$ m.	92

<u>Figure</u>	<u>Page</u>
5.5. Voidage distribution at cylinder wall, used in the heat transfer modeling.	95
5.6. Comparison between predicted and experimental values of pressure drop at cylinder surface, for (a) $d_p = 2.85$ mm, and (b) $d_p = 4.0$ mm (Δp given in cm and inches of water column).	97
5.7. Comparison between theoretical and measured values of local heat transfer coefficients for $d_p = 4.0$ mm.	98
5.8. Comparison between theoretical and measured values of local Nusselt numbers, $Nu_{p\theta}$, for particles used in our study (see Table 5.1).	99
5.9. Comparison between theoretical and measured values of the overall Nusselt number, Nu_p , for particles used in our study and in reference [23].	101
5.10. Comparison between theoretical and measured values of instantaneous local Nusselt numbers based on tube diameter, $Nu_{D\theta i}$, for bubble configuration shown ($d_p = 4.0$ mm, narrow bed).	105
5.11. Comparison between theoretical and measured values of instantaneous local heat transfer coefficients, $h_{\theta i}$, for bubble configuration shown ($d_p = 4.0$ mm, narrow bed).	106
5.12. Comparison between theoretical and measured values of instantaneous local heat transfer coefficients, $h_{\theta i}$, for bubble configuration shown ($d_p = 2.85$ mm, narrow bed).	107
5.13. Comparison between theoretical and measured values of instantaneous local heat transfer coefficients, $h_{\theta i}$, for bubble configuration shown ($d_p = 4.0$ mm, wider bed).	108
6.1. Model of heat transfer from an immersed tube to a fluidized bed.	111

<u>Figure</u>	<u>Page</u>
6.2. Fraction of total particle convective thermal resistance, $R_c + R_e$, due to the contact resistance, $R_c = d_p/6.0k_g$, as a function of particle size, for our fluidizing conditions.	124
6.3. Particle thermal time constant as a function of particle size, and a comparison with emulsion (particle) residence times.	126
6.4. Gas convective Nusselt number as a function of Archimedes number in air-fluidized beds.	129
6.5. Bubble Nusselt number as a function of Reynolds number at $3U_{mf}$, based on tube diameter.	132
6.6. Overall emulsion contact fraction (fraction of time which tube spends in contact with emulsion) as a function of the excess gas velocity.	135
7.1. Comparison of model predictions with our experimental results for intermediate particles.	141
7.2. Comparison of model predictions with our experimental results for large particles.	143
7.3. Comparison between model predictions and experimental results for each of the three contributions to the maximum time-averaged overall coefficient.	146
7.4. Comparison between experimental results reported by Canada and McLaughlin [23] and predictions of our model, for 2.6 mm glass particles at air pressures of 5 and 10 atm.	152
7.5. Comparison between experimental results, showing the dependence of heat transfer coefficient on pressure, and corresponding model predictions ($d_p = 2.6$ mm, $U = 1.2 U_{mf}$).	153
7.6. Agreement between experimental results reported by Canada et al. [24] and predictions of our model, for 2.6 mm glass particles and Freon-12 at 1.2 and 2.3 atm.	155

<u>Figure</u>	<u>Page</u>
7.7. Comparison between our experimental results and predictions based on four existing correlations for horizontal tubes ($d_p = 1.3 \text{ mm}$).	159
7.8. Comparison between our experimental results and predictions based on four existing correlations for horizontal tubes ($d_p = 4.0 \text{ mm}$).	160

Appendix

A.1. Block diagram of a heating element temperature control circuit.	176
A.2. Detailed schematic drawing of the electronic circuitry on a temperature controller printed circuit card.	178
B.1. (a) Sketch of variables involved; (b) sketch of deviation variables involved; (c) block diagram representation of the system.	180
D.1. Comparison between predicted and experimental heat transfer coefficients in air flow: (a) natural convection; $Gr_D Pr = 557,000$; (b) forced convection, $Re_D = 7200$.	187
F.1. (a) Voidage detector amplifier card circuitry; (b) connection of multiple capacitance elements.	193

LIST OF TABLES

<u>Table</u>	<u>Page</u>
2. 1. A summary of previous experimental studies dealing with heat transfer to horizontal tubes.	8
4. 1. Properties of solids and ranges of velocities and temperatures used in the experiments. Air is the fluidizing gas.	36
5. 1. Gas velocity at which the average voidage around the tube is 0.57 ($1 - f_o \approx 0.73$).	94
6. 1. Information about the average thickness of the gas layer between the tube surface and particles (ST = single tube, TA = tube array).	121
6. 2. Information related to the gas convective component of heat transfer from (to) horizontal tubes.	128
7. 1. Value of U/U_{mf} corresponding to the maximum time-averaged overall coefficient.	145
7. 2. Summary of existing correlations for heat transfer to horizontal tubes in fluidized beds.	156

NOTATION

<u>Symbol</u>	<u>Description</u>	<u>Units</u>
A	heat transfer area	m ² , cm ²
A _p	half-surface area of particle	m ² , cm ²
Ar = $\left[\frac{g d_p^3 \rho_g (\rho_s - \rho_g)}{\mu} \right]$	Archimedes number	
C _{cond}	conduction constant for heat flowing between platinum sensor and copper cylinder	W/°C
C(s)	integration constant--see Appendix B	
c _p	heat capacity	J/kg°C
c _{pg}	heat capacity of gas	J/kg°C
c _{ps}	heat capacity of solid	J/kg°C
c _{pl}	heat capacity of glass	J/kg°C
D	diameter of immersed tube (cylinder)	m, mm (in)
d _p	particle diameter or surface mean particle diameter	m, mm
d _{pi}	diameter of particles in size interval i (used only when a mixture is considered)	m, mm
e, e(t)	instantaneous voltage	V
e _C	instantaneous voltage across the capacitance element	V
e _{HT}	instantaneous voltage drop across the heat transfer measuring element	V
e _p	instantaneous output voltage of the pressure transducer	V

<u>Symbol</u>	<u>Description</u>	<u>Units</u>
e_0, e_1	instantaneous voltages in the heat transfer element temperature control circuit	V
f_o	fraction of time which tube, as a whole, spends in contact with bubble phase (overall bubble contact fraction)	
$1 - f_o$	fraction of time which tube, as a whole, spends in contact with emulsion phase (overall emulsion contact fraction)	
$f_{o\theta}$	local bubble contact fraction at angular position θ	
$(1 - f_o)_{\theta}$	local emulsion contact fraction at angular position θ	
g	acceleration due to gravity	m/s^2
$Gr_D (= \frac{g \beta \rho_g^2 D^3 \Delta T}{\mu_g})$	Grashof number based on tube (cylinder) diameter	
H	bed height (measured from distributor plate)	m (in)
H_o	slumped bed height	m (in)
H_p	position of pressure probe above distributor plate	m (in)
h	time-averaged heat transfer coefficient for the whole tube (time-averaged overall coefficient)	$W/m^2 \cdot ^\circ C$ (BTU/hr ft ² · °F)
h_b	time-averaged overall coefficient between the tube and a bubble (or slug)	$W/m^2 \cdot ^\circ C$ (BTU/hr ft ² · °F)
h_{gc}	time-averaged overall gas convective coefficient	$W/m^2 \cdot ^\circ C$ (BTU/hr ft ² · °F)

<u>Symbol</u>	<u>Description</u>	<u>Units</u>
h_{gci}	instantaneous overall gas convective coefficient	$W/m^2 \cdot ^\circ C$ (BTU/hr ft ² · °F)
h_i	instantaneous average coefficient for the whole tube (average of $h_{\theta i}$)	$W/m^2 \cdot ^\circ C$ (BTU/hr ft ² · °F)
h_{mf}	time-averaged overall coefficient at minimum fluidization (overall quiescent bed coefficient)	$W/m^2 \cdot ^\circ C$ (BTU/hr ft ² · °F)
h_{pc}	time-averaged overall particle convective coefficient	$W/m^2 \cdot ^\circ C$ (BTU/hr ft ² · °F)
h'_{pc}	time-averaged overall particle convective coefficient as defined by Xavier and Davidson [91]	$W/m^2 \cdot ^\circ C$ (BTU/hr ft ² · °F)
h_{pci}	instantaneous overall particle convective coefficient	$W/m^2 \cdot ^\circ C$ (BTU/hr ft ² · °F)
h_r	time-averaged overall radiative coefficient	$W/m^2 \cdot ^\circ C$ (BTU/hr ft ² · °F)
$h(t), h_t$	instantaneous heat transfer coefficient measured by a platinum sensor	$W/m^2 \cdot ^\circ C$ (BTU/hr ft ² · °F)
\bar{h}_t	Laplace transform of h_t	
h_θ	time-averaged local heat transfer coefficient at angular position θ	$W/m^2 \cdot ^\circ C$ (BTU/hr ft ² · °F)
$h_{\theta b}$	time-averaged local coefficient between surface and bubble (slug) at angular position θ	$W/m^2 \cdot ^\circ C$ (BTU/hr ft ² · °F)
$h_{\theta gc}$	time-averaged local gas convective coefficient at angular position θ	$W/m^2 \cdot ^\circ C$ (BTU/hr ft ² · °F)
$h_{\theta i}$	instantaneous local heat transfer coefficient at angular position θ	$W/m^2 \cdot ^\circ C$ (BTU/hr ft ² · °F)

<u>Symbol</u>	<u>Description</u>	<u>Units</u>
$h_{\theta mf}$	time-averaged local coefficient at minimum fluidization (local quiescent coefficient) at angular position θ	$W/m^2 \cdot ^\circ C$ (BTU/hr ft ² °F)
$h_{\theta pc}$	time-averaged local particle convective coefficient at angular position θ	$W/m^2 \cdot ^\circ C$ (BTU/hr ft ² °F)
$i, i(t)$	instantaneous current	amp
K	effective gain of the linearized heat transfer element temperature control system	$W/m^2 \cdot ^\circ C$ (BTU/hr ft ² °F)
k	thermal conductivity	$W/m \cdot ^\circ C$ (BTU/hr ft°F)
k_e	effective thermal conductivity of the emulsion packet	$W/m \cdot ^\circ C$
k_e^o	effective stagnant packed bed thermal conductivity (no fluid motion)	$W/m \cdot ^\circ C$
k_g	thermal conductivity of gas	$W/m \cdot ^\circ C$
k_s	thermal conductivity of solid	$W/m \cdot ^\circ C$
k_l	thermal conductivity of glass	$W/m \cdot ^\circ C$
L_c	average spacing between particles at tube surface	m
N	number of times that an emulsion packet (or bubble) contacts a probe during the data-collecting period	
$Nu_D (= \frac{hD}{k_g})$	time-averaged overall Nusselt number based on tube diameter	
$Nu_{D, b} (= \frac{h_b D}{k_g})$	time-averaged overall bubble Nusselt number based on tube diameter	

<u>Symbol</u>	<u>Description</u>	<u>Units</u>
$Nu_{D\theta i} (= \frac{h_{\theta i} D}{k_g})$	instantaneous local Nusselt number at angular position θ , based on tube diameter	
$Nu_p (= \frac{h d_p}{k_g})$	time-averaged overall Nusselt number based on particle diameter	
$Nu_{p,b} (= \frac{h_b d_p}{k_g})$	time-averaged overall bubble Nusselt number based on particle diameter	
$Nu_{p,mf} (= \frac{h_{mf} d_p}{k_g})$	time-averaged overall Nusselt number at minimum fluidization, based on particle diameter	
$Nu_{p\theta} (= \frac{h_{\theta} d_p}{k_g})$	time-averaged local Nusselt number at angular position θ , based on particle diameter	
$Nu_{p\theta i} (= \frac{h_{\theta i} d_p}{k_g})$	instantaneous local Nusselt number at angular position θ , based on particle diameter	
n	bubble frequency (frequency of replacement)	s^{-1}
n_{θ}	local bubble frequency at angular position θ	s^{-1}
P_o	zero level power dissipated by the platinum sensor, i. e. power dissipated by conduction to the copper cylinder	W
$P(t), P_t$	instantaneous power dissipated by the platinum sensor due to heat transfer to the fluidized bed	W
$P_{t, total}$	total instantaneous power dissipated by the platinum sensor	W
\bar{P}_t	Laplace transform of P_t	

<u>Symbol</u>	<u>Description</u>	<u>Units</u>
$Pr (= \frac{\mu_g^c}{k_g} pg)$	Prandtl number	
p	pressure	cm H ₂ O, atm (in H ₂ O)
$q_b [= h_b(T_{tube} - T_b)]$	heat flux between tube surface and bubble	W/m ²
$q_{gc} [= h_{gc}(T_{tube} - T_b)]$	gas convective heat flux at tube surface	W/m ²
$g_{pc} [= h_{pc}(T_{tube} - T_b)]$	particle convective heat flux at tube surface	W/m ²
R_c	thermal contact resistance presented by gas film between heat transfer surface and particle	m ² °C/W
R_e	effective thermal resistance presented by the emulsion packet phase	m ² °C/W
R_{ei}	instantaneous thermal resistance of the emulsion phase	m ² °C/W
R_o	0.5 Ω resistor in the heat transfer element temperature controller	Ω
RE_h	relative error in heat transfer coefficient measurement	
$Re_D (= \frac{U \rho_g D}{\mu_g})$	Reynolds number based on tube diameter	
$Re_p (= \frac{U \rho_g d_p}{\mu_g})$	Reynolds number based on particle diameter	
$Re_{p, mf} (= \frac{U_{mf} \rho_g d_p}{\mu_g})$	Reynolds number at minimum fluidization, based on particle diameter	

<u>Symbol</u>	<u>Description</u>	<u>Units</u>
r_p	radius of particle	m
s	Laplace transform variable	
T	temperature	$^{\circ}\text{C}$
$T^* (= T - T_{\text{set}})$	temperature deviation variable	$^{\circ}\text{C}$
\bar{T}^*	Laplace transform of T^*	
T_{air}	air temperature	$^{\circ}\text{C}$
T_b	temperature of fluidized bed	$^{\circ}\text{C}$
T_{Cu}	temperature of copper cylinder	$^{\circ}\text{C}$
$\bar{T}_0^* [= \bar{T}^*(s, 0)]$	value of \bar{T}^* at $z = 0$	
T_{Pt}	temperature of platinum sensor	$^{\circ}\text{C}$
T_{set}	set point temperature	$^{\circ}\text{C}$
T_{surface}	temperature of particle surface	$^{\circ}\text{C}$
T_{tube}	temperature of tube surface	$^{\circ}\text{C}$
t	time	s
t_r	response time	s, ms
U	superficial gas velocity	m/s (ft/s)
U_{mf}	minimum fluidizing velocity	m/s (ft/s)
$U_{\text{mf(exp)}}$	experimental minimum fluidizing velocity	m/s (ft/s)
$U_{\text{mf(th)}}$	theoretical minimum fluidizing velocity	m/s (ft/s)

<u>Symbol</u>	<u>Description</u>	<u>Units</u>
$U_{mf(2-D)}$	minimum fluidizing velocity in two-dimensional bed	m/s (ft/s)
U_t	terminal velocity of particle	m/s
u'	interstitial turbulence intensity	
V_p	volume of particle	m^3
x_i	weight fraction of particles in size interval i	
$y (= \frac{d_p}{\delta^*})$	number indicating ratio between particle diameter and gas film thickness in the overall heat transfer coefficient analysis (1/y = fraction of particle diameter equivalent to thickness of gas film)	
$y_\theta (= \frac{d_p}{\delta_\theta^*})$	same as y, except it applies for local heat transfer	
z	distance	m

Greek Symbols

α_1	thermal diffusivity of glass	m^2/s
β_g	coefficient of thermal expansion of gas	$^{\circ}C^{-1}$
$\Delta h, \Delta e, \Delta R_o, \Delta A, \Delta T$	errors in measurement (see Appendix E)	
Δp	pressure drop	cm H_2O , atm (in H_2O)
Δp_{A-B}	pressure drop between points A and B	cm H_2O , atm (in H_2O)
ΔT	temperature difference	$^{\circ}C$
δ	average volume fraction of bubbles in the bed	

<u>Symbol</u>	<u>Description</u>	<u>Units</u>
$1-\delta$	average bed volume fraction for the emulsion phase	
δ^*	average thickness of gas film for the tube as a whole	m, mm
δ_θ^*	average thickness of gas film at angular position θ	m, mm
ϵ	bed voidage	
ϵ_{mf}	bed voidage at minimum fluidization	
ϵ_θ	local voidage at angular position θ	
θ	angle on the tube surface measured from the lower stagnation point	degrees, radians
μ	viscosity	kg/m s
μ_g	viscosity of gas	kg/m s
ρ	density	kg/m ³
ρ_e	effective density of the emulsion packet	kg/m ³
ρ_g	density of gas	kg/m ³
ρ_s	density of solid	kg/m ³
ρ_l	density of glass	kg/m ³
τ	time or time constant	s, ms
$\bar{\tau}_b$	average bubble residence time for the whole tube (overall average bubble residence time)	s
$\tau_{b\theta}$	local bubble residence time at angular position θ	s
$\bar{\tau}_{b\theta}$	average local bubble residence time at angular position θ	s

<u>Symbol</u>	<u>Description</u>	<u>Units</u>
τ_e	overall emulsion residence time	s
$\bar{\tau}_e$	overall average emulsion residence time	s
$\tau_{e\theta}$	local emulsion residence time at angular position θ	s
$\bar{\tau}_{e\theta}$	average local emulsion residence time at angular position θ	s
τ_p	thermal time constant of particle	s
τ_s	time constant of the heat transfer element control system	s, ms
ϕ_s	sphericity of a particle	

Other Subscripts

air	denotes air
Fr	denotes Freon-12
max	denotes maximum
min	denotes minimum

HEAT TRANSFER TO HORIZONTAL TUBES IN FLUIDIZED BEDS: EXPERIMENT AND THEORY

I. INTRODUCTION

Gas-fluidized beds are noted for their excellent heat transfer characteristics. High rates of heat exchange can be achieved between the bed and immersed surfaces or vessel walls. As a result, fluidized bed heat transfer has received considerable attention in chemical engineering literature; a comprehensive review is given by Botterill [19]. Most of the reported studies have concentrated on fine-particle systems which initially established fluidization as a significant unit operation in the chemical and petrochemical industries. Such systems consist of particles generally smaller than 0.4 mm in diameter and use relatively low superficial gas velocities. From these studies came the widely-used "packet" theory of heat transfer, according to which heat is transported to or from surfaces by an unsteady state process involving groups or packets of particles.

Fluidized beds of intermediate ($0.4 \text{ mm} < d_p < 1 \text{ mm}$) and large particles ($d_p > 1 \text{ mm}$) have only recently become a topic of investigation, primarily as a result of the increasing importance of several new processes. The most significant of these is the fluidized bed combustion of coal, which has attracted major research and development efforts in the U.S. and abroad [73, 74], and toward which our study is primarily directed. Large-particle fluidization is also finding use in waste incineration [5, 6, 52], hydrocarbon processing [28], calcination and combustion of liquid and solid radioactive material in nuclear technology [72, 96], and dry cooling towers [3, 4], to mention several applications in which heat exchange between the bed and immersed surfaces could be of significance. Only a few

studies dealing with heat transfer in such systems have appeared.

Fluidized bed coal combustors typically use dolomite or limestone particles greater than 0.5 mm in diameter to scavenge the sulfur dioxide produced by burning sulfur-containing coal at temperatures of 750-850°C. The coal makes up only 1-2% of the bed material. The heat produced in the bed is transferred to an array of immersed tubes which are usually horizontal [73, 74]. These heat exchange tubes are used for steam generation in electric utility applications and for liquid or gas heating in the process industries. There is a lack of reliable bed-to-surface heat transfer data and correlations for these coarse-particle beds--which have to operate at high gas velocities to be fluidized at all. The situation is especially unfavorable for horizontal tubes.

The data needed for a good understanding of the heat transfer process and for design purposes include information on temporal and spatial variations of local heat transfer coefficients, as well as the time-averaged and space-averaged values. Information on hydrodynamic characteristics of the bed in the vicinity of tubes is also required. Differences in instantaneous and local values of the heat transfer coefficient, caused by the passage of bubbles or the formation of a stack of particles on top of a horizontal tube, may give rise to thermal cycling, stresses, fatigue and even corrosion of the tube material [51, 79]. The knowledge of these heat transfer variations over a wide range of particle sizes and gas velocities would be of particular interest for the designer in charge of materials selection. Reliable data and correlations for the time-averaged overall heat transfer coefficient to tubes have great commercial importance since the tubes constitute a significant portion of the total cost of a fluid-bed combustor. An increase in the heat transfer coefficient could cause a nearly proportional reduction in the cost of the combustor.

In quest of this type of data, we developed an instrument which makes possible simultaneous measurements of instantaneous, as well as time-averaged, local heat transfer coefficients, voidage, and surface pressure variations at several positions around the circumference of a tube. We used it to conduct a detailed heat transfer study in beds of intermediate and large sand and dolomite particles under a variety of operating conditions. The experimental work was conducted at room temperature and is therefore directed toward the conductive and convective components of heat transfer which, according to some recent studies [1, 2, 12, 15], constitute at least 70% of the total heat transferred even at actual combustion temperatures where radiation enters the picture.

The large body of data obtained in our study should give answers to some crucial heat transfer problems. We present a theory applicable over a wide range of fluidizing conditions and compare it with our data, as well as with the limited number of data available in literature.

II. PREVIOUS WORK

Related work in fluid-bed heat transfer will be reviewed from two aspects. Since a detailed fundamental analysis of the heat transfer process in the vicinity of immersed surfaces requires the use of rather delicate instruments, we shall first present a review of the instrumentation used in previous studies. We shall then give a summary of the available data and correlations dealing with the time-averaged overall heat transfer coefficient to horizontal tubes.

A. Instrumentation

Instantaneous Measurements

The measurement of instantaneous heat transfer coefficients requires fast-responding measuring elements or probes. Mickley et al. [66] were the first to obtain such data in fluidized beds by using a thin platinum foil on a vertical tube and following its temperature changes. Being the authors of the original version of the packet theory, they obtained data on packet residence times to verify their postulates [65] but limited their work to very fine particles. Other fast-responding heat transfer elements--mostly low thermal capacity heaters in the form of small and thin metal foils and films--followed: Tuot and Clift [85] (vessel wall-to-bed heat transfer; maximum $d_p = 0.25$ mm), Baskakov et al. [12, 14] (vertical and horizontal tubes and plates; maximum $d_p = 0.5$ mm), and Bernis et al. [17, 18] (vertical cylinder; $d_p = 0.15$ mm). One instrument was not sufficiently rapid in its response (Selzer and Thompson [77]), while another required a complicated procedure for getting the local coefficients (Zakkay et al. [67, 97]).

Most results obtained in these studies could be subject to errors for two reasons: a) the probe surface temperature and heat flux varied during any test (the measurements of Bernis et al. being the notable exception since a tiny isothermal element was used), and b) the measuring element temperature differed significantly from the temperature of the object on which it was placed (this point will be discussed in detail in Section III. A).

Along with their heat transfer measurements, Baskakov et al. [14] obtained simultaneous data on bubble passage by using photo transducers located on each side of their platinum element. These data were used to calculate bubble frequencies and packet residence times. Chen and Ozkaynak [27, 70] used capacitance sensors to get similar information for vertical tubes, while Kilkis et al. [55] employed a cylinder equipped with pressure transducers to study bubble behavior around a horizontal tube.

All these measuring elements can be described as single-position probes; i. e., when used on an immersed tube, the tube had to be rotated for measurements at different locations. Common to all of the studies listed is the fact that the instrumentation was used in fine-particle beds under very specific fluidizing conditions, with the sole purpose of testing various postulates of the packet theory.

Time-Averaged Local Measurements

The measurement of time-averaged local heat transfer coefficients does not require rapid-response probes and is therefore easier to perform. Noack [68] obtained local heat transfer data around a horizontal tube by measuring the power dissipation from an isothermal metal strip. He conducted a systematic study of heat transfer, as well as of time-averaged pressure at the tube surface, but

limited his experiments to a single particle size ($d_p = 0.6$ mm). Similar heat transfer elements were used by Gelperin et al. [42, 45] (horizontal and sloping tubes; maximum $d_p = 0.35$ mm), Samson [75] (horizontal cylinder and sphere; $d_p = 0.14$ mm), and Berg and Baskakov [16] (horizontal tubes; maximum $d_p = 0.32$ mm) to map the distribution of local coefficients. A study of local heat transfer to horizontal tubes of unusually large diameters in beds of somewhat coarser particles, using a Noack-type probe of rather low accuracy, is currently underway at Exxon Research and Engineering Company [28].

All of these studies have utilized single-position probes, and, with the exception of Noack [68] and Berg and Baskakov [16], could have introduced considerable experimental error by having the heat transfer elements at a temperature quite different from that of the surrounding surface (see Section III. A). The experimental work has usually been limited to a narrow velocity range, and, with the exception of Cherrington et al. [28], has hardly been conducted outside the fine-particle region.

Summary

To our knowledge, there has not yet been a comprehensive investigation which would unite the various aspects described above to obtain detailed information about the local thermal and fluid dynamic characteristics which govern the process of heat transfer to horizontal tubes in beds of intermediate and large particles. Such information could serve as a basis for testing heat transfer models that would be applicable over a wide range of fluidizing conditions.



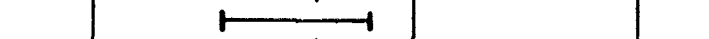

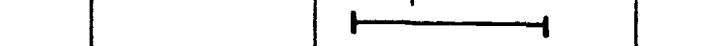

B. Data and Correlations

The time-averaged heat transfer coefficient to an immersed tube as a whole is the single most important piece of heat transfer information for the combustor designer. Although it can be calculated from the local coefficients of the type described above, this quantity is usually obtained by measuring the power dissipation of a tube-sized cylindrical heater. Vertical tubes have been more popular in literature, and several studies in large-particle beds have recently appeared (Baskakov and Suprun [13], Botterill and Denloye [21, 33], and Zakkay et al. [67, 97]). As far as horizontal tubes are concerned, a short summary of the limited number of studies that have dealt with at least two different particle sizes is presented in Table 2.1 (all involve air-fluidized beds at low and moderate temperatures, with negligible radiation).


Table 2.1 shows that most of the experimental work has been done in the fine-particle region, with some studies overlapping slightly into the intermediate-particle zone. With the exception of the ongoing work at General Electric Corporate and Research and Development Center (Canada et al. [23, 78]), no experimental data exist for more than 85% of the particle size range used in actual fluid-bed combustors. Canada et al. are concentrating on the high-velocity region known as the turbulent regime [94] and have thus far used only two particle sizes (0.65 and 2.6 mm). It should be pointed out that other authors also used only a few different particle sizes.

The correlations described in Table 2.1 are practically applicable only for the range of fluidizing conditions under which they were obtained. It will be shown in Chapter VII that, when extrapolated to larger particles and higher velocities, they give predictions which deviate significantly from the experimental data and are

Table 2.1. A summary of previous experimental studies dealing with heat transfer to horizontal tubes.

Investigator	Range of Particle Sizes	Material	Other details	Correlations
Vreedenberg [86]		cracking catalyst, sand, iron ore	single tube, different tube diameters (D = 17-51 mm)	widely-used Vreedenberg correlations for very fine and less fine particles
Gelperin et al. [42, 43, 46]		quartz sand	single tube and staggered tube array (D = 20-80 mm), different tube spacings	correlations for h and h_{max} (the latter as a function of tube spacing)
Petrie et al. [72]		sand, metal oxide	staggered tube array (D = 12.7 mm), one tube spacing	Vreedenberg correlation; authors' own correlation for their specific data
Andeen and Glicksman [4]		sand	one row of tubes (D = 19 mm), single tube spacing	Vreedenberg correlation modified for intermediate particles
Canada et al. [23, 78]		glass	staggered tube array (D = 32 mm), one tube spacing, air at different pressures, high velocities (turbulent regime reached)	None
Xavier and Davidson [91]		sand	staggered tube array (D = 28 mm), one tube spacing	correlation based on a modified packet theory

NOMINAL FBC OPERATING RANGE
(Strom et al [80])



fine inter- large

 mediate

Particle Diameter, d_p (mm)

0.05 0.1 0.5 1.0 5.0 10.0

therefore inadequate. The best example of this discrepancy is the Vreedenberg correlation [86], which is frequently used in the analysis of heat transfer to horizontal tubes [4, 19, 59, 72].

Canada et al. are the only investigators who give a detailed description of the fluid dynamic regimes in which their heat transfer data were obtained. Since fluid dynamics and heat transfer are very closely related, this is a point of particular importance for beds of coarse particles where several distinct regimes are possible (Canada et al. [25], Catipovic et al. [26]).

In summary, this review lends itself to the conclusion that a significant amount of work remains to be done for beds of intermediate and large particles.

III. EXPERIMENTAL EQUIPMENT

One of the main tasks of our study is the collection of a large data base in beds of intermediate and large particles, which would enable a thorough analysis of the heat transfer process. A description of the instrument developed to fulfill this task will take up most of this chapter. The fluidized bed facility, the pressure probes (used in bed expansion studies), and the data acquisition system will also be described.

A. Instrumented Cylinder for Heat Transfer Studies

The instrument was designed having in mind the need for simultaneous information on the instantaneous and time-averaged heat transfer and fluid dynamic characteristics at several locations along the circumference of an immersed tube. It consists of five independent heat transfer measuring elements, ten independent capacitance elements for voidage measurement, and four pressure ports, all located in a copper rod which can be inserted as a section of an immersed 50.8 mm (2 in) diameter heat transfer tube. This diameter was selected because 2-in tubes are either being used or have been scheduled for future use in most electric utility oriented fluidized bed combustors [74, 80]. Measurements are made at five radial positions around the heated cylinder (see Figure 3.1). The heat transfer measuring elements are platinum resistance heaters which are maintained at a constant temperature by an electronic control circuit. The instantaneous heat transfer coefficients are obtained by measuring the power required to hold the temperature constant. The heating elements are inlaid in the copper rod which is maintained at a temperature very close to that of the elements by a cartridge heater and a

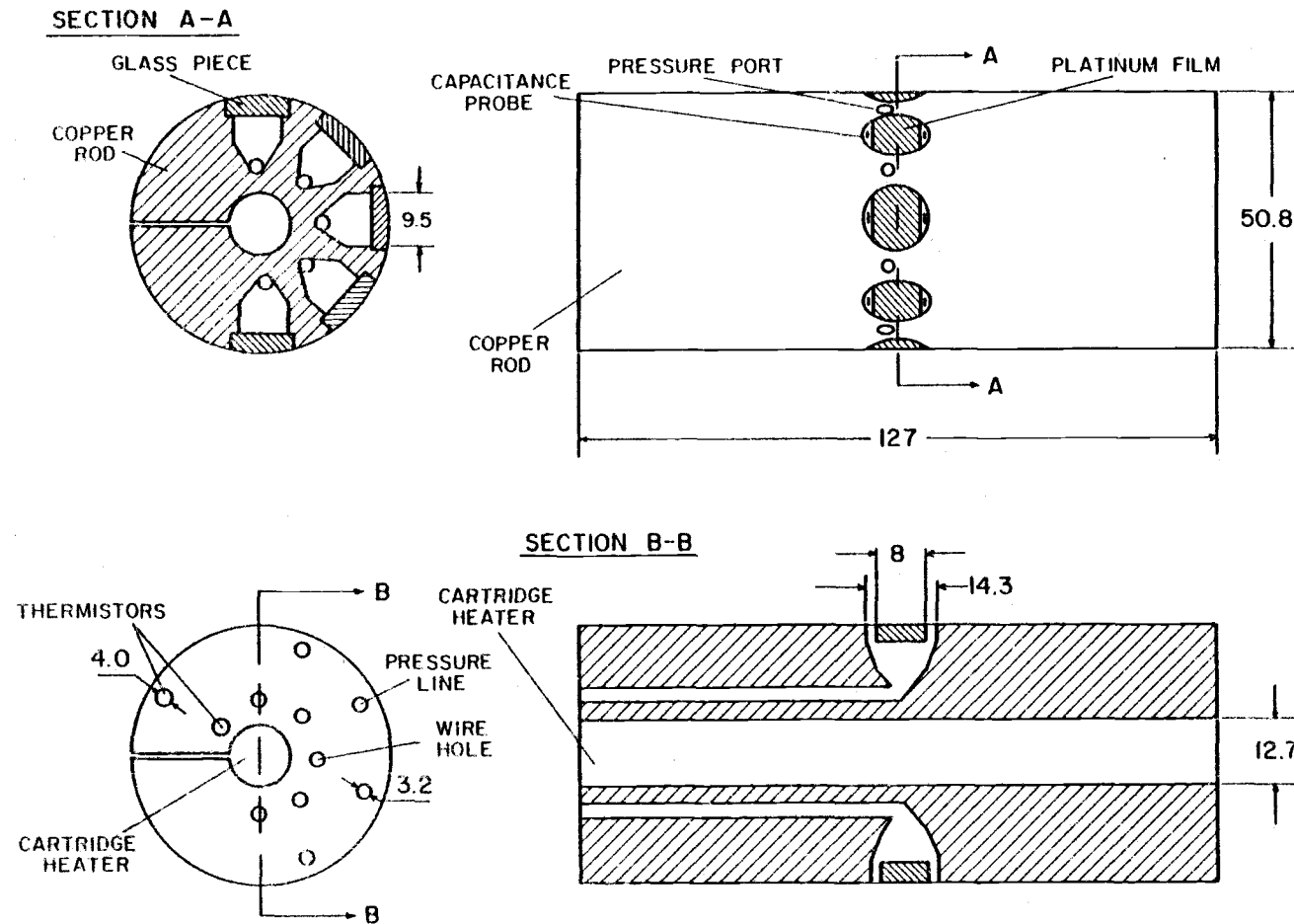


Figure 3.1. Sketch of the instrumented cylinder for heat transfer studies.

separate control circuit. On either side of each heat transfer element is a small capacitance probe used to measure the instantaneous voidage in its vicinity. Located between the five heat transfer elements are four pressure sensing ports which provide instantaneous static pressure measurements necessary for calculating the gas flow pattern around the tube. A photograph of the instrument is shown in Figure 3.2.

Heat Transfer Measuring Elements

The supports of the heating elements are made of borosilicate glass. They are shaped to conform exactly to the surface of the cylinder (see Figure 3.3) and were manufactured on special order by J. L. Wood Optical Systems, Santa Ana, California. The curved top surface is plated with platinum. The plating is accomplished by applying a platinum paint (Engelhard Industries Liquid Bright Platinum 05-X) with a very fine silk screen, then baking off the volatile organic material, and finally heating the film to just below the softening point of the glass (675°C). Sensors of this type have been used previously by Foltz and Mesler [36] (boiling heat transfer) and Tuot and Clift [85] (fluid-bed heat transfer). In our application, extra care must be taken to ensure the uniform thickness ($1500\text{-}2000\text{ \AA}$) of the platinum film since that is a necessary condition for a fast-responding sensor. The uniformity is considered satisfactory only after satisfying two criteria: a) uniform steady-state temperature distribution as measured by liquid crystal indicators, and b) rapid power response to a change in the heat transfer coefficient.

Lead wires are connected by painting the parallel flat sides of the glass piece with a silver-filled epoxy cement (Engelhard Industries Conductive Epoxy Ag A-2781). The epoxy is allowed to overlap

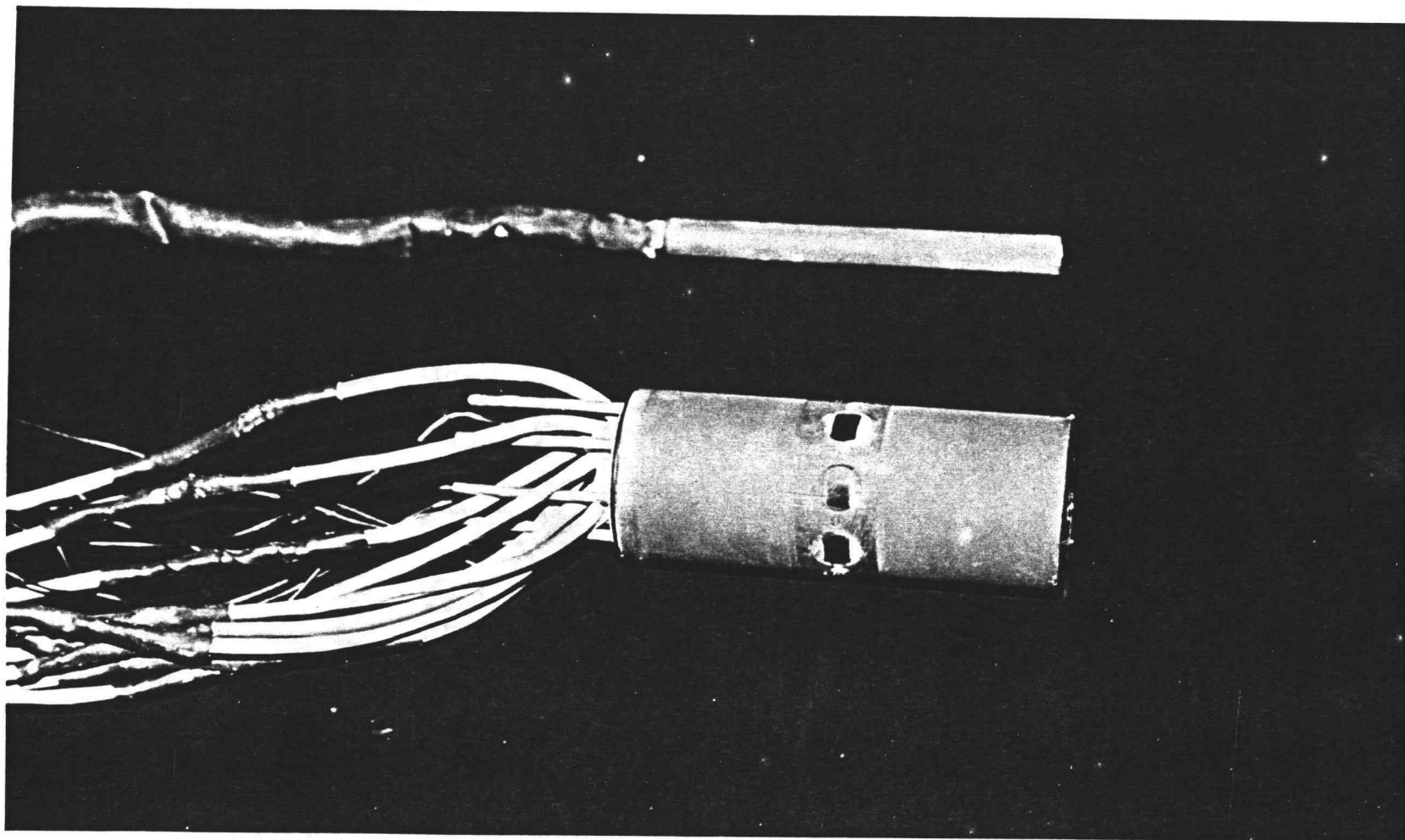


Figure 3.2. Photo of the instrumented cylinder and the cartridge heater.

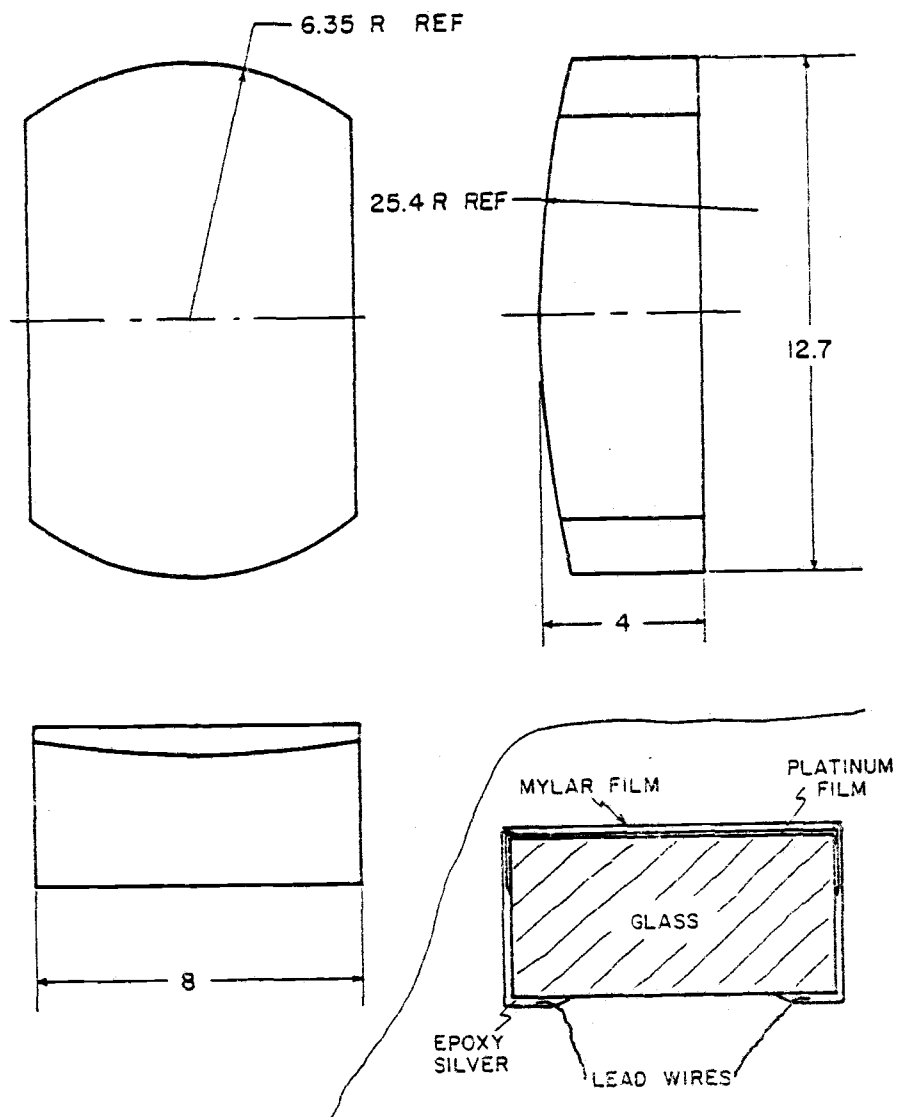


Figure 3.3. Sketch of the platinum film heater element.

the top surface by about 0.3 mm to insure good contact. Electrical contacts are made with teflon insulated copper wire leads which are embedded in the epoxy cement. The epoxy cement is cured by baking at 150°C.

The resistivity of platinum changes with temperature, and the film temperature can therefore be obtained from its measured resistance. This is accomplished electronically by measuring the voltage drop and current through the heater and dividing the voltage drop by the current. If the temperature is lower than the desired set point, the measured resistance will likewise be below a set point resistance. To bring the resistance back to the set point, the voltage across the heater is increased. This increase in power raises the temperature of the heating element and brings it back to its set point. The rapid heat transfer measurement response of the probe is due to the fact that its temperature changes very little. If a very high gain amplifier is used, the temperature of the probe need change only a fraction of a degree while the heat transfer coefficient changes by an order of magnitude. The effect of thermal inertia is thereby minimized, enabling us to measure changes in the heat transfer coefficient with a time constant as short as a millisecond.

The temperature of the platinum film is held constant by a special feedback control circuit, which is described in Appendix A. The circuit calculates the resistance (temperature) of the film, compares it to a desired set point and either increases or decreases the power to the heater in order to maintain it at the set point resistance (temperature). From the measurement of current and voltage, the instantaneous power dissipation--and from it the instantaneous heat transfer coefficient--can be obtained. The resistances of the fabricated platinum films are in the range of 2.5-3.0 ohms.

The temperature distribution throughout the borosilicate element can be modeled mathematically, and the response time can be theoretically estimated--see Appendix B. In practice, the rapid response time to a step change in the heat transfer coefficient is lengthened because a mylar film 0.013 mm (0.0005 in) thick (supplied by the 3M Company) covers the heat transfer element to protect it from abrasion in the fluidized bed. The mylar remains intact for tens of hours of operation in the bed, even at temperatures of the instrumented cylinder as high as 110°C. Without the mylar film, the platinum heater resistance starts changing in a matter of seconds under the scraping action of the relatively coarse particles used. The response time of the circuit with the mylar film covering the element is about 20 ms, as measured on an oscilloscope; i.e., the power response to a step change in the heat transfer coefficient requires 20 ms to come to 98% of its final value. This is considered thoroughly satisfactory for the type of changes taking place in fluidized beds.

The solid copper cylinder, in which the heat transfer elements are mounted, is maintained at nearly the same temperature as the platinum heating elements themselves. This thermal guard insures that the measured heat transfer coefficients will correspond to the coefficients which would be obtained around a uniform-temperature tube. This is approximately the situation experienced by the elements of a tube in a real fluid-bed heat exchanger. Much of the heat transfer data reported in literature has been taken from sensors which were heated to a temperature substantially above that of the surrounding surface (see Section II. A). In such a case, particles and gas moving along the surface are abruptly heated when passing over the heated sensor. In our case, the particles and gas can be preheated, resulting in a smaller heat flux from the sensor surface. Thus, keeping the tube (cylinder) and the heat transfer measuring elements at

the same temperature is necessary in order to prevent erroneously high heat transfer coefficients from being obtained.

A separate proportional controller (Yellow Springs Instrument Company, Model 72) is used to regulate the temperature of the copper cylinder. The temperature is measured by two thermistors (YSI type 403)--see Figure 3.1. The thermistor temperature can be read directly from an electronic thermometer (YSI Telethermometer, Model 42SF). The temperature feedback to the controller is given by the thermistor located near the cartridge heater (ITT Vulcan, Type TB507B, 500W, 220V). The thermal conductivity of copper (3.90 W/m°C or 225 BTU/hr ft°F for the copper used in the cylinder) is great enough to keep the temperature drop through the copper cylinder (between the heater and the cylinder surface) to less than 1.6°C when the external heat exchange coefficient is 340 W/m²°C or 60 BTU/hr ft²°F. At steady state, the temperature at the cylinder surface is only a couple of tenths of a degree lower than the temperature indicated by the outer thermistor.

Calculation of Heat Transfer Coefficients. The instantaneous heat transfer coefficient is calculated from the instantaneous power dissipation of the platinum measuring element by the formula

$$h(t) = \frac{P(t)}{A(T_{Pt} - T_b)} \quad (3.1)$$

The temperature of the platinum element is held constant throughout the experiment. It is calculated by a calibrating procedure described in Appendix C. The fluidized bed temperature is measured by several thermistors at various locations in the bed. It is logged on the computer and is usually constant during an experimental run. The operating temperature of the measuring elements is selected through the consideration of two criteria. The first is that the

platinum film temperature should not exceed 100°C , to avoid possible damage to the mylar film and the epoxy adhesive used to hold the glass piece in place (Tra-Con, Inc. Epoxy Resin, Type 2112)--see Figure 3.4. The second consideration is to provide a maximum temperature difference $T_{\text{Pt}} - T_{\text{b}}$ to minimize errors in the computation of the heat transfer coefficients. This difference is at least 50°C in all our experiments.

The power dissipation is obtained from the instantaneous voltage and current readings, which are measured by the control circuit (Appendix A) and relayed directly to the computer. The exact power dissipated to the fluidized bed is calculated from a formula described in Appendix C.

The area through which heat transfer takes place, A , is estimated at 1.20 cm^2 . This value was verified by experiments conducted in environments for which the heat transfer coefficient is known. In a large number of test runs under different conditions (gas flow only; fluidized beds of different particles), the cylinder was rotated to confirm that all five platinum elements gave identical readings when placed in the same location relative to a chosen axis. As expected, in all cases the results showed symmetry about the vertical axis. Measured values of heat transfer coefficients in air flow were checked against theoretical and empirical values for natural and forced convection past a horizontal cylinder (McAdams [61], Welty et al. [88], Knudsen and Katz [56]). The agreement was very good and several examples are given in Appendix D. The relative error in measured values is estimated at approximately 6%, with the error analysis given in Appendix E.

Obviously, the direction of heat transfer in our experiments is from the measuring elements to the fluidized bed (as was the case with all investigators listed in Chapter II). However, throughout the

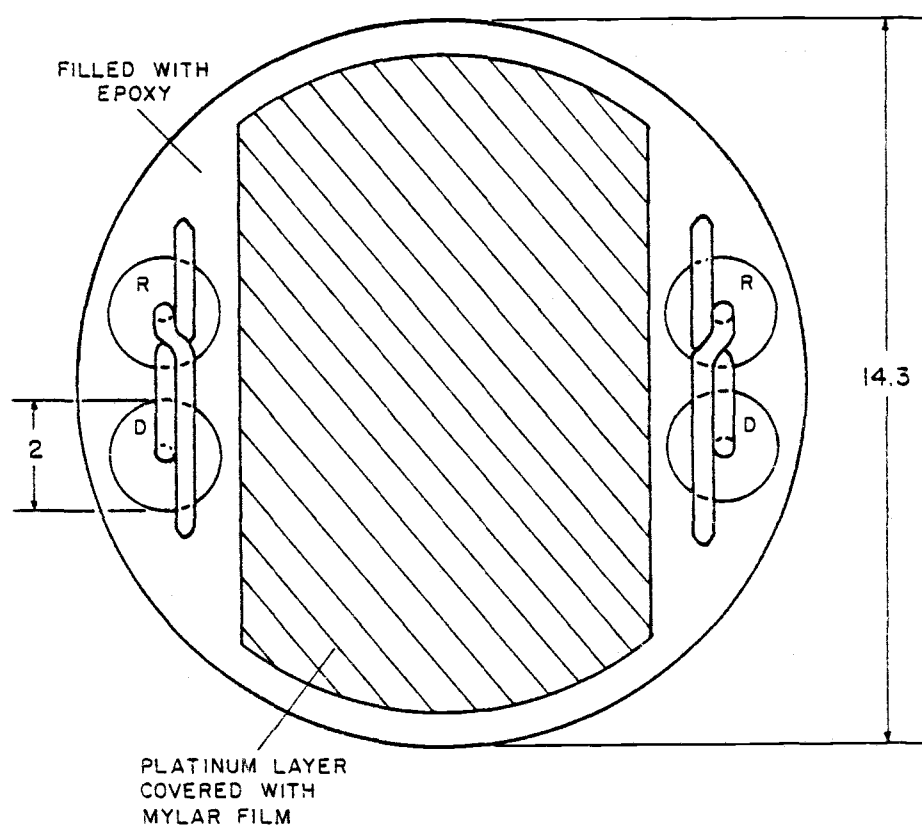


Figure 3. 4. Detail of the heating element and the surrounding capacitance probes.

text we refer to heat transfer to horizontal tubes because in the process being studied the coefficients in opposite directions are identical. In most industrial applications it is the transfer to tubes that is of interest.

Capacitance Elements for Voidage Measurement

Capacitance-type elements are used in conjunction with heat transfer measurements to detect bubbles and obtain local voidage data. Figure 3.5 shows a simplified circuit diagram for the capacitance probe. A 200 KHz signal is produced by a signal generator. The amplitude of the signal is about ± 10 volts. At the end of the lead wire, there is a small diode which allows current to flow only in one direction. The piece of wire which connects the diode (type 1N931) and the resistor ($10\text{ M}\Omega$, $1/8\text{ W}$) behaves as a very small capacitor to ground. The assymetric current from the diode charges the capacitor when there is a flow through the diode; when the flow is cut off, the capacitor discharges at a rate which is inversely proportional to its capacitance. Thus, the average emf across the capacitor is a measure of probe capacitance: the larger the capacitance, the larger the emf. The emf signal from the capacitor is then amplified and the high frequency (200 KHz) is filtered out. As a capacitor probe changes its capacitance, the output voltage of the amplifier changes accordingly. The speed of response depends on the distributed capacitance of the wire from the capacitor to the amplifier. The two-conductor shielded wire used in the capacitance probes has a distributed capacitance of about 35 pf per foot; therefore for a 16-ft total length, the capacitance is $5.6 \times 10^{-10}\text{ f}$. The probe resistance is $10^7\ \Omega$ and the time constant of the probe is therefore $(10^7)(5.6 \times 10^{-10}) = 0.0056\text{ s}$.

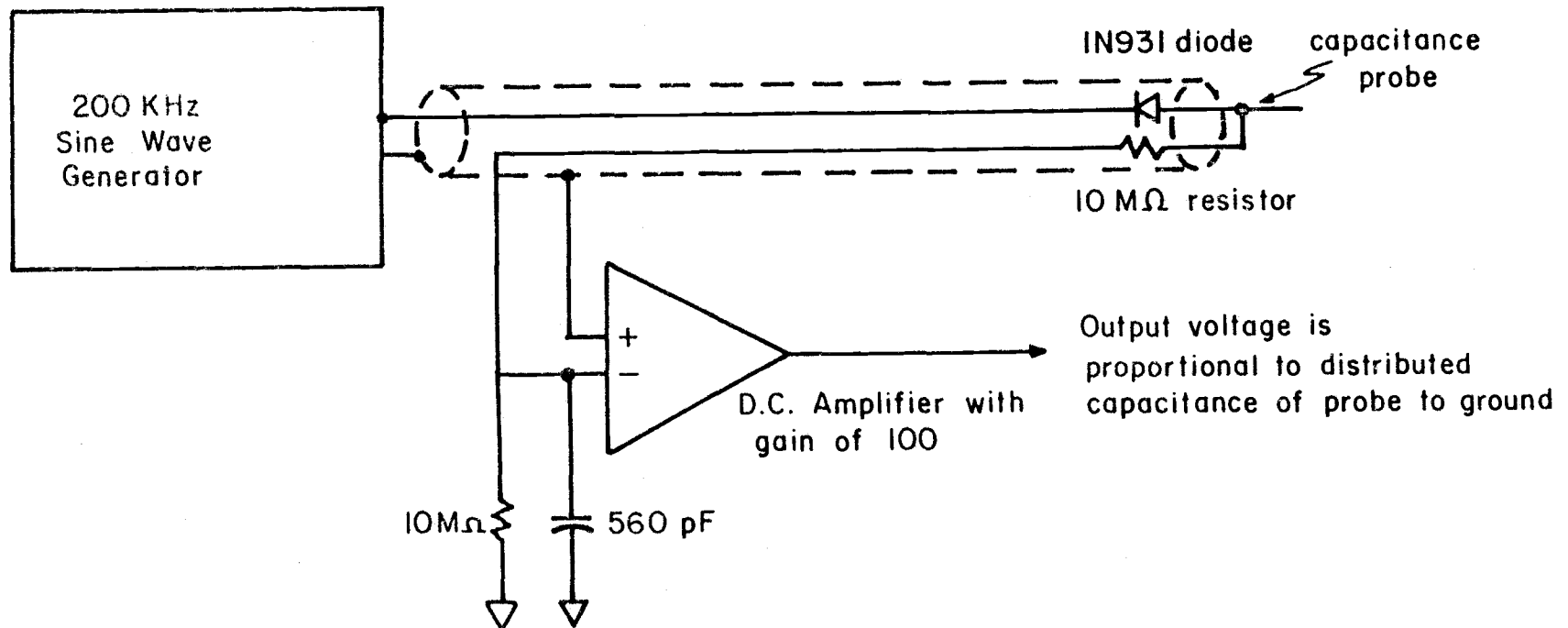


Figure 3.5. Simplified schematic drawing of the capacitance probe.

The capacitance measuring elements are located on either side of each of the platinum film heating elements, and they, too, conform to the surface of the copper cylinder (see Figure 3.4). As noted above, the active site of the capacitance probe consists of the short connecting wires where the diode and the resistor are soldered together. The distributed capacitance between this connection and the ground is measured. Since the copper rod itself is at ground potential, the distance to ground is approximately 2 mm. When the probe is immersed in sand or dolomite, the capacitance increases since the dielectric constant of the solid is greater than the dielectric constant of air. The change in capacitance is approximately 5×10^{-14} f.

There are ten capacitance probes in the instrumented cylinder. Each probe measures the voidage in its immediate vicinity--in a volume of $0.3-0.4 \text{ cm}^3$. When both capacitance elements associated with a heat transfer element register a void in the fluidized bed, it is assumed that the surface is temporarily covered by a bubble; when both probes register no voidage, the surface is in the emulsion phase. Thus it is possible to distinguish between heat transfer to the bubble and to the emulsion phase. The two lead wires for each of the capacitance probes and the two wires which supply power to the heating element all pass through a common 3.2 mm (0.125 in) diameter hole in the copper rod (see Figures 3.1 and 3.2). No shielding surrounds the wires within the cylinder since the copper cylinder itself is grounded and serves as a shield. Just outside the cylinder, however, the capacitance leads are shielded to protect them from 60 Hz pickup. To avoid possible ground loops, the shields on the lead wires are connected to common at the main console and do not touch the heated copper rod. The capacitance probes are insulated by mylar and held in place with epoxy resin (see Figure 3.4). Further

details on the capacitance probe circuitry are given in Appendix F.

Local Pressure Measurement

The copper heat transfer test section also contains four pressure ports, 3.2 mm (0.125 in) in diameter, which are flush with the surface (see Figure 3.1). Pressures are monitored instantaneously at each of these ports and are recorded simultaneously with the heat transfer and capacitance data. The pressure lines connect through 6.4 mm (0.25 in) tubing to differential pressure transducers. The pressure sampling holes are plugged with steel wool to prevent bed material from entering them. The steel wool is sufficiently coarse so that there is a negligible pressure drop across it. A constant small flow of purge air for each of the pressure probes is delivered through mini flow meters equipped with a needle valve (Fischer and Porter Company, Series 10A3135, Model No. 53RB2110). The purge air tends to keep particles and dust from moving into the pressure measuring lines, and this prevents the slow response which occurs when solids partially plug the lines.

The pressure transducers are manufactured by National Semiconductor (Model LX1601D) and are true integrated circuit type transducers. The output voltage is linearly related to the differential pressure across the transducer which can be operated with either a positive or negative difference (with a maximum range of ± 5 psi). The response of this instrument is extremely rapid. The output signal from each of the transducers is scaled using operational amplifiers located inside a pressure measuring module.

Typical Signals from the Measuring Elements

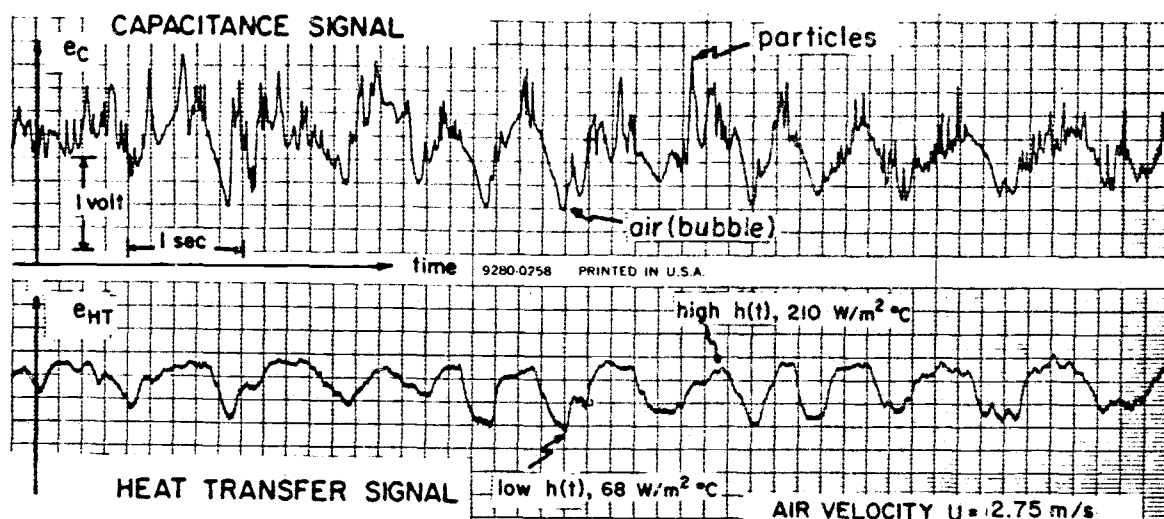
The instrumented cylinder can be inserted as a section of a horizontal or vertical tube and can, in principle, be used in several different applications: natural fluid convection, forced fluid convection (see Appendix D), gas-fluidized beds, and liquid-fluidized beds (both fine and large particle systems). However, in this study we are concerned with heat transfer to horizontal tubes in gas-fluidized beds of particles having diameters larger than 0.4 mm; several characteristic signals from the measuring elements will be presented.

They were obtained in a bed of 4 mm dolomite particles

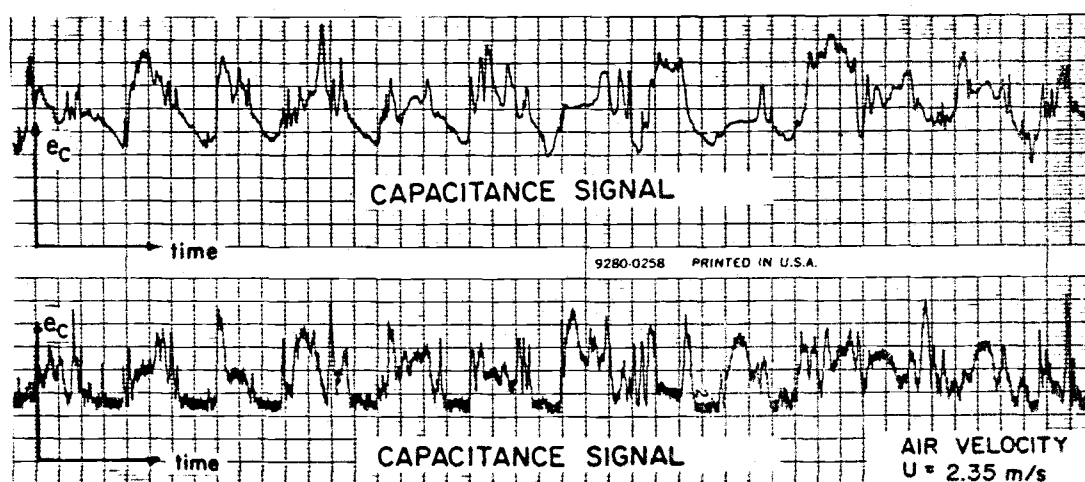
($U_{mf} = 1.83 \text{ m/s}$).

Figure 3.6(a) shows simultaneous records of bubble passage detection and heat transfer coefficient variation at the side of the instrumented copper rod ($\theta = 90^\circ$), for a gas velocity well above U_{mf} . A drop in voltage in the capacitance signal indicates the presence of voids or bubbles, while a rise in voltage detects the presence of particles. The heat transfer signal is a record of the voltage drop across the platinum heater and is an indication of the change in the local heat transfer coefficient (the actual values are calculated using measured voltage and current signals). It can be seen that the capacitance signal correlates well with the corresponding heat transfer signal. When the emulsion contacts the capacitance element, the heat transfer coefficient goes up. The peaks in the heat transfer coefficient occur with a frequency of about one per second, which appears to be the bubble frequency as indicated by the capacitance signal. Figure 3.6(b) shows records of the capacitance probe pair.

Figures 3.7(a) and (b) give records of the pressure drop variations with simultaneous capacitance and heat transfer variations, respectively (at $\theta = 45^\circ$). The pressure difference signal is lowest



(a)



(b)

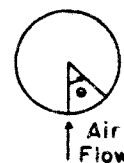
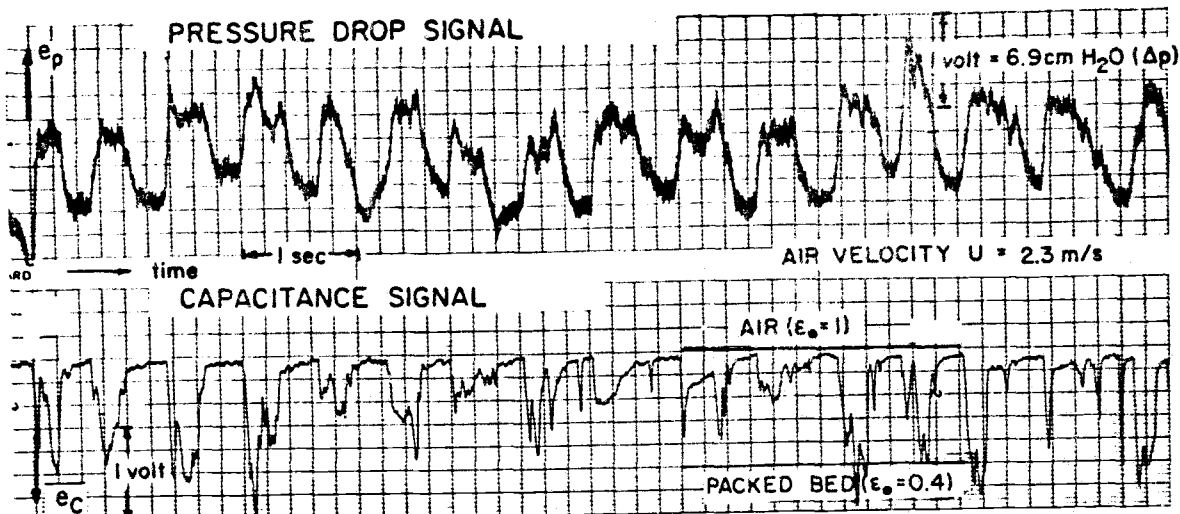
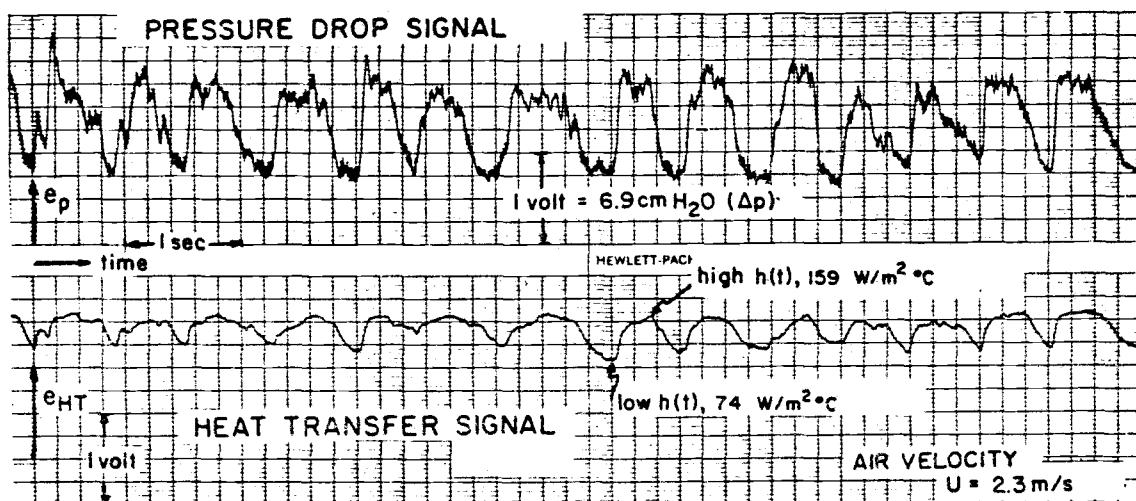


Figure 3.6. Simultaneous voltage records of: (a) capacitance and heat transfer elements, and (b) capacitance probe pair; at the side of the copper cylinder, $\theta = 90^\circ$ ($d_p = 4.0$ mm).



(a)



(b)

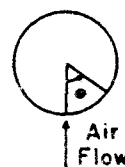


Figure 3.7. Simultaneous voltage records of: (a) pressure and capacitance elements, and (b) pressure and heat transfer elements; at $\theta = 45^\circ$ ($d_p = 4.0$ mm).

(practically zero) when a bubble engulfs two ports and highest when the emulsion is between them.

The platinum elements give instantaneous values of the heat transfer coefficient at a particular position on the tube. The time-averaged local values, as well as the average value of h for the whole tube are calculated from the logged instantaneous data.

The capacitance elements detect bubble passage and indicate the bubble frequency. Information on emulsion and bubble residence times is available from the capacitance records. Upon calibration, values of the time-averaged local voidage can be obtained by interpolating between the packed bed and air limits.

Pressure drop values can be used to determine gas flow patterns in the immediate vicinity of the tube and to check whether the assumed flow regimes for gas in and around bubbles are reasonable. Pressure values can also give information on bubble frequency and residence times, with the added advantage that this type of local pressure measuring system may be used at very high temperatures (while the heat transfer and capacitance probes are limited to low and moderate temperatures).

The fluctuations in capacitance and pressure signals give an indication of the fluid dynamic regime in which the bed is operating. The cross-correlation between any two pressure or capacitance signals at different locations will give information on the bubble velocity around the immersed tube.

B. Fluidized Bed Facility

A diagram of the experimental setup used in our investigation is shown in Figure 3.8. The vessel in which the particles are fluidized is made of metal and plexiglass and has dimensions of

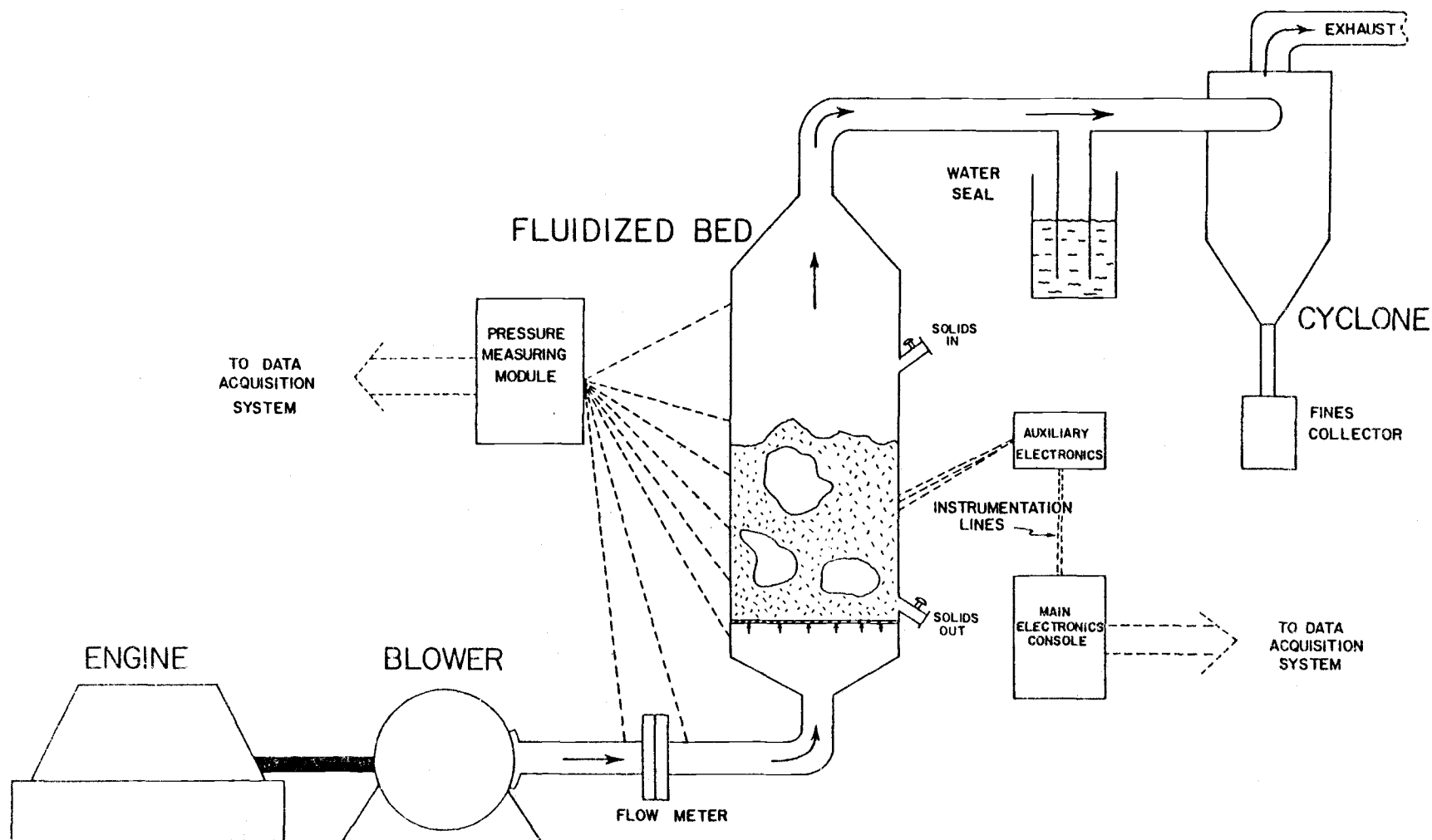
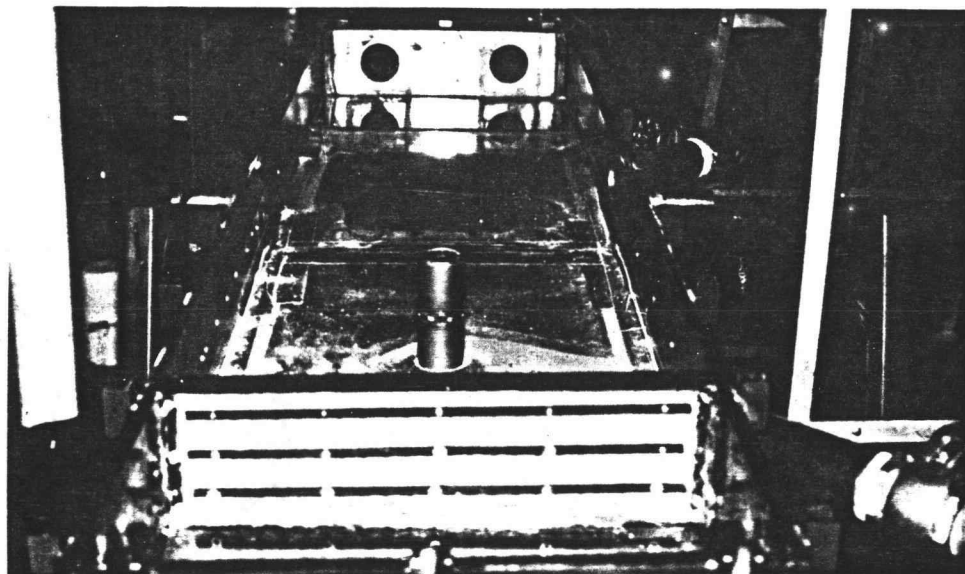


Figure 3.8. Diagram of the fluidized bed facility.

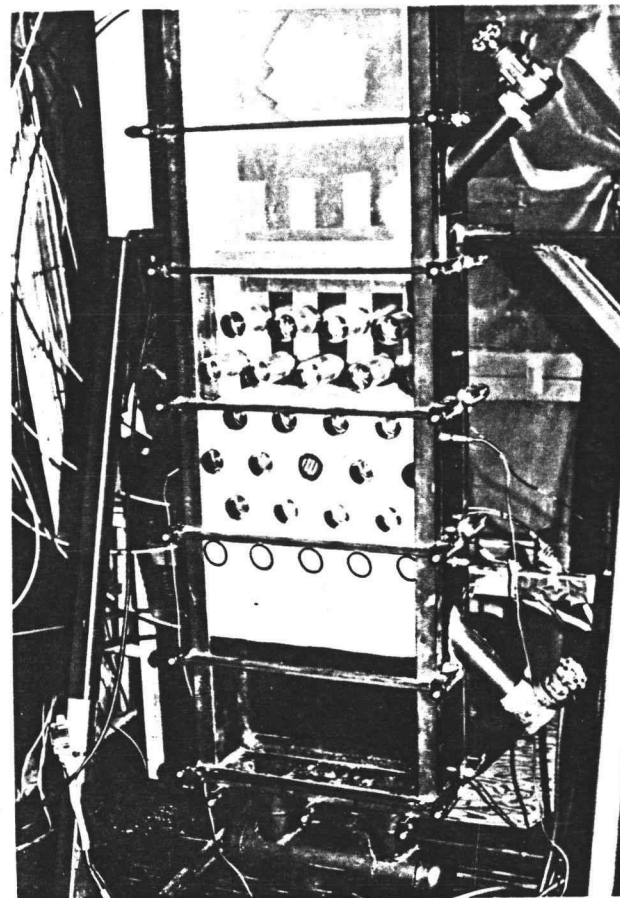
0.480 x 0.127 x 2.000 m (18.8 x 5.0 x 79.9 in). Two slumped bed heights were used: 0.46 and 0.71 m (18 and 28 in). The instrumented copper cylinder is placed into position by fitting a hole drilled in the center of one of the vessel's plexiglass walls, as shown in Figure 3.9(a). Its horizontal axis is located 0.35 m (13.8 in) above the distributor plate. The other plexiglass wall is easily removable to facilitate the insertion or withdrawal of the instrument, or to accommodate different combinations of immersed tubes. Figure 3.9(b) is a photograph of the fluidized bed with the cylinder in position in the midst of a staggered tube array. The instrumented rod and the plexiglass cylinders (dummy heat exchange tubes) are locked into position by tightening the removable vessel wall. The gas distributors used are perforated plates with wire screens covering their openings. The percentage of open area and the screen size depend on the diameter of particles, the goal being the attainment of a sufficient pressure drop across the distributor plate. The bed is equipped with numerous pressure taps connected to the pressure measuring module.

The bed is thin enough (0.127 m) to facilitate visual observation and filming from the outside, but is also thick enough that it cannot be considered a two-dimensional bed in the usual sense of that term. The experimental minimum fluidizing velocity of each of the particle sizes used agrees very closely with theoretical values of U_{mf} , whereas a very thin bed would prevent the system from fluidizing until higher velocities were reached. The rectangular shape of the bed was chosen because it is characteristic of fluid-bed combustors.

The diesel engine (Caterpillar, Model 3406T, 325 HP) and the blower (Rader Pneumatics Roots Blower, Model 1228) can produce superficial gas velocities in the bed well above 6 m/s; however, due to particle carryover considerations, the maximum used in our study is 6 m/s (and only with the coarser material). All our work is



(a)



(b)

Figure 3.9. (a) Photo of the fluidization vessel with the instrumented cylinder in position;
(b) Photo of the fluidized bed with a horizontal tube (cylinder) array.

carried out in the batch mode--the elutriated material is not recycled.

C. Bed Expansion Measurement

Heat transfer coefficients cannot usually be correlated without knowing the bed expansion and, from it, the average voidage. Bed expansion is obtained from pressure measurements as shown in Figure 3.10. Four levels are used to determine the average location of the bed top under different fluidizing conditions. In this application, the pressure probe consists of a 6.4 mm (0.25 in) OD thin-walled steel tube with a fine wire screen at one end. At its other end the probe connects to a pressure transducer and a purge system as previously described. At each level the probe can be moved transversally. Bed voidage is calculated as described in Section IV. D.

D. Data Acquisition System

Five heat transfer measuring elements, ten capacitance elements, the pressure measuring module (which serves for local pressure measurements on the tube, bed expansion determination, and pressure drop measurements between various parts of the apparatus), and several thermistors are all connected via the main electronics console (containing all the control and amplifier circuits) to a 128-channel analog to digital converter which forms the real-time interface with the Data General Nova 840 Minicomputer, located in the Chemical Engineering Department. Figure 3.11 shows the block diagram of the computer facility.

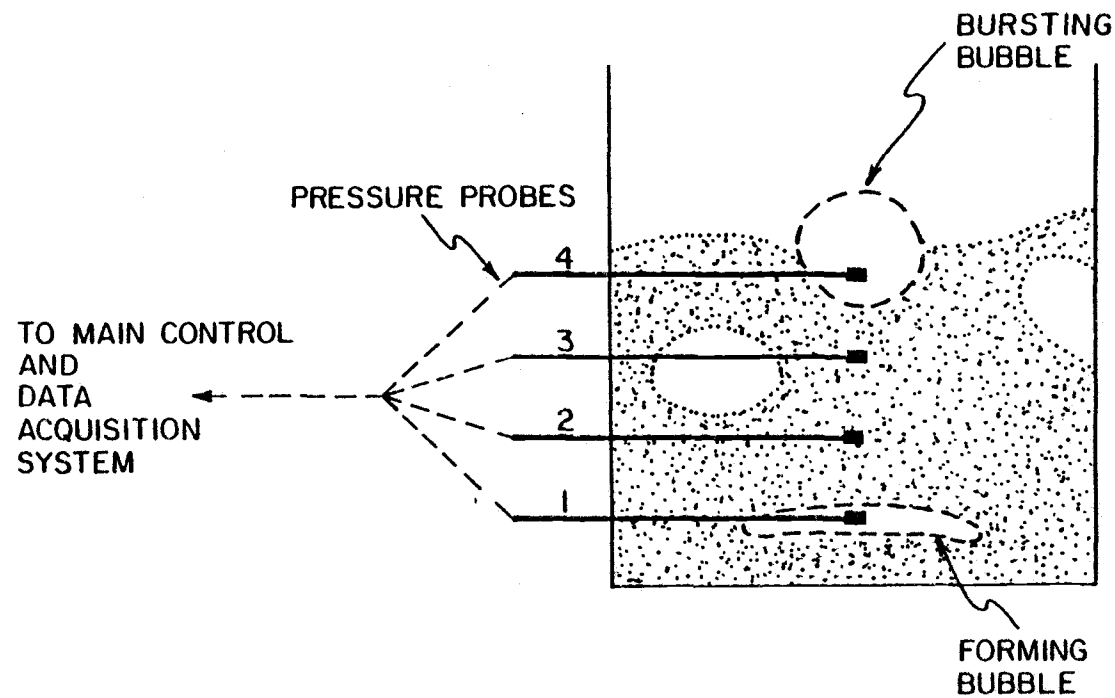


Figure 3.10. Experimental setup of pressure probes for bed expansion measurement.

Oregon State University
Chemical Engineering Department
Real-Time Computer Laboratory

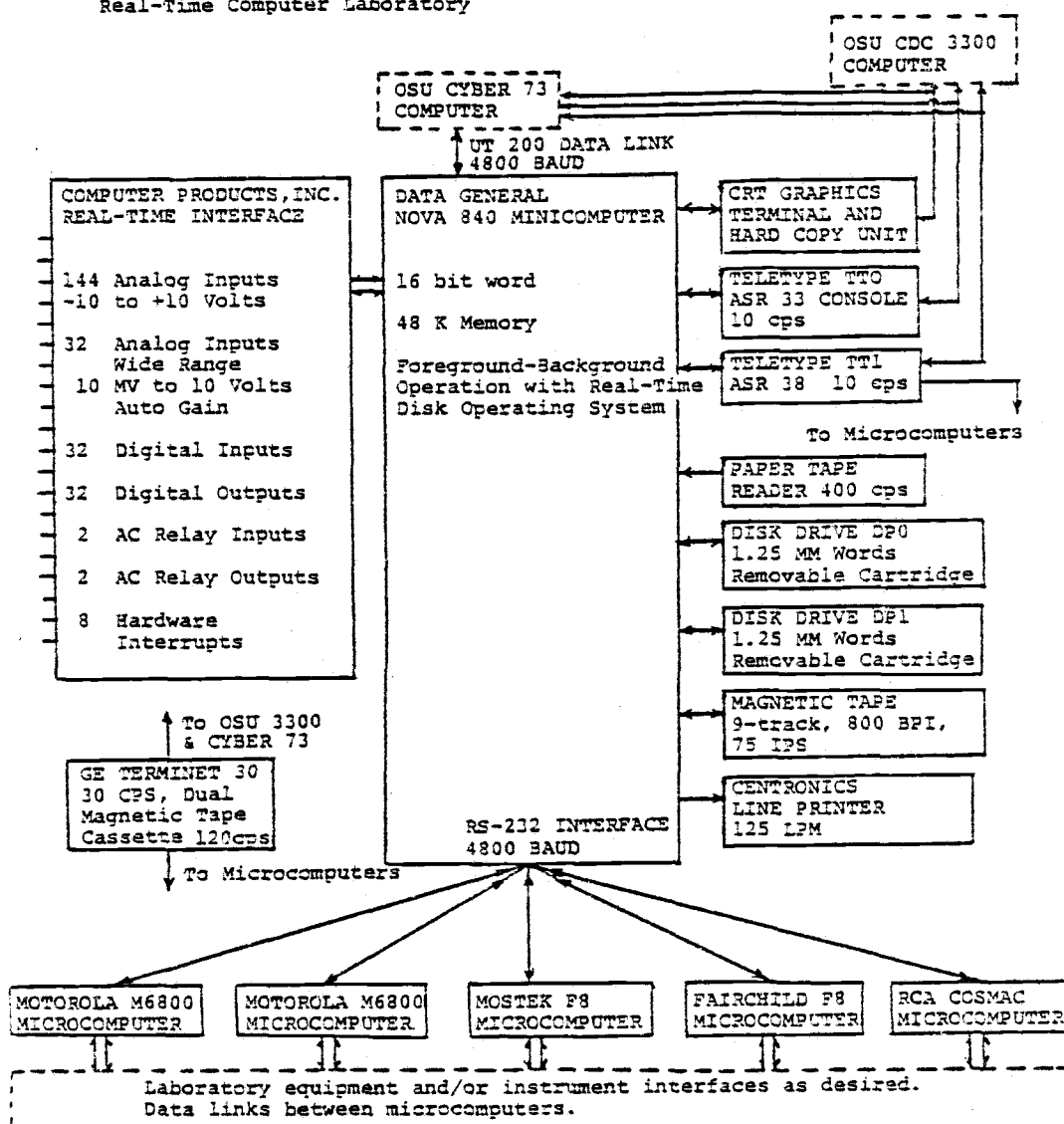


Figure 3.11. Block diagram of the Chemical Engineering Department minicomputer facility.

The Nova 840 system was used for all data collection and for most of the data reduction and processing. The CDC 3300 Computer was used for the development of the more complicated software and for the lengthier calculations.

IV. EXPERIMENTAL RESULTS

A. Fluidizing Conditions

Properties of the solids fluidized, ranges of the superficial velocities used, and values of the bed temperatures attained in our experiments are summarized in Table 4.1. Quartz sand and dolomite were selected because they resemble very closely the solids fluidized in actual coal combustors. Their densities were measured experimentally, while thermal conductivities and heat capacities were obtained by consulting several standard reference books [32, 71, 83, 87]. Whenever particles in a particular range spanned several screen sizes, their mean diameter was calculated according to the formula for the surface mean [57]:

$$d_p = \frac{1}{\sum_{(i)} \frac{x_i}{d_{pi}}} \quad (4.1)$$

Voidage at minimum fluidization was obtained from experiment (volumetric as well as pressure drop measurements), while sphericity was estimated from a generalized graph given by Wen and Yu [89]. The experimental minimum fluidizing velocity resulted from standard pressure drop measurements at different gas velocities [57]; it is compared to the theoretical value from the Wen and Yu correlation [89]. Superficial gas velocities spanned several different regimes: from packed beds to high-velocity beds slightly below the turbulent regime. Excessive particle carryover prevented the use of still higher velocities. Bed temperature did not change by more than 1°C during an experimental run at a given velocity; however, higher gas velocities produced higher temperatures. Measurements were made

Table 4.1. Properties of solids and ranges of velocities and temperatures used in the experiments. Air is the fluidizing gas.

Material	Density ρ_s (kg/m ³)	Thermal conduc- tivity k_s (W/m°C)	Heat capacity c_{ps} (J/kg°C)	Mean particle diameter d_p (mm)	Size range (mm)	Minimum fluidiza- tion voidage ϵ_{mf}	Sphericity ϕ_s	Minimum fluidizing velocity		Gas super- ficial velocity range U (m/s)	U_{max}/U_{mf}	Bed temperature T_b (°C)
								experimental $U_{mf(exp)}$ (m/s)	theoretical $U_{mf(th)}$ (m/s)			
Quartz sand	2700	40.0	791	0.37	0.21- 0.595	0.49	0.75	0.15	0.13	0.10- 1.00	6.65	27-36
				0.80	0.595- 1.00	0.46	0.78	0.46	0.43	0.10- 1.90	4.15	26-37
				1.30	1.00- 1.68	0.45	0.82	0.70	0.75	0.15- 2.60	3.75	25-38
Dolomite	2750	1.3	879	2.00	1.68- 2.38	0.43	0.85	1.14	1.13	0.25- 3.40	3.00	29-38
				2.85	2.38- 3.36	0.41	0.95	1.44	1.45	0.35- 4.25	2.95	26-39
				4.00	3.36- 4.76	0.40	0.97	1.83	1.81	0.45- 5.25	2.85	29-42
				6.60	4.76- 8.00	0.41	0.95	2.44	2.38	1.35- 5.60	2.30	29-42

(Note: 1 kg/m³ = 0.062 lb/ft³; 1 W/m°C = 57.84 BTU/hr ft°F; 1 J/kg °C = 2.39 x 10⁻⁴ BTU/lb °F; 25.4 mm = 1 in; 1 m/s = 3.28 ft/s)

5784

by thermistors (described in Section III. A) placed at several locations in the bed. Telethermometer readings indicated very little temperature difference (less than 1°C), regardless of whether thermistors were placed on the downstream or upstream side of the instrumented cylinder, or far from or near the vessel wall. All experiments were conducted at atmospheric pressure, with air as the fluidizing gas.

Two types of experimental runs were made: a) with a single immersed tube, and b) with a staggered tube array. Figure 4.1 illustrates the bed geometry. The instrumented cylinder remained in the same position for both types of experiments. Plexiglass cylinders acted as dummy heat exchange tubes in the array. Two slumped bed heights were used: the lower height was approximately at the boundary between shallow (bed height \leq bed width) and deep beds, while the higher bed was deep enough to cover the entire 6-row array.

The single tube case represents a reference point for studying the effect of tube spacing on heat transfer. The particular equilateral triangular tube array was selected for the following reasons: a) a staggered (triangular pitch) tube assembly seems to give better fluidization characteristics, and hence better heat transfer, than an in-line (square pitch) array [44, 80]; b) the bottom of the tube bundle should clear the gas jet zone of irregular fluidization (and lower heat transfer) near the distributor, a minimum height of 0.15 m (6 in) being suggested [64, 80, 90]; and c) based on several previous studies [9, 42, 43, 59, 64], the minimum spacing between tubes should not fall much below a pitch/diameter ratio of 2, to prevent a severe restriction of particle motion and a sharp decrease in heat transfer. The instrumented cylinder was placed in a position which ought to be characteristic for most tubes in an actual, large-bed array. Some studies [9, 23, 64] suggest that the heat transfer coefficient to individual tubes

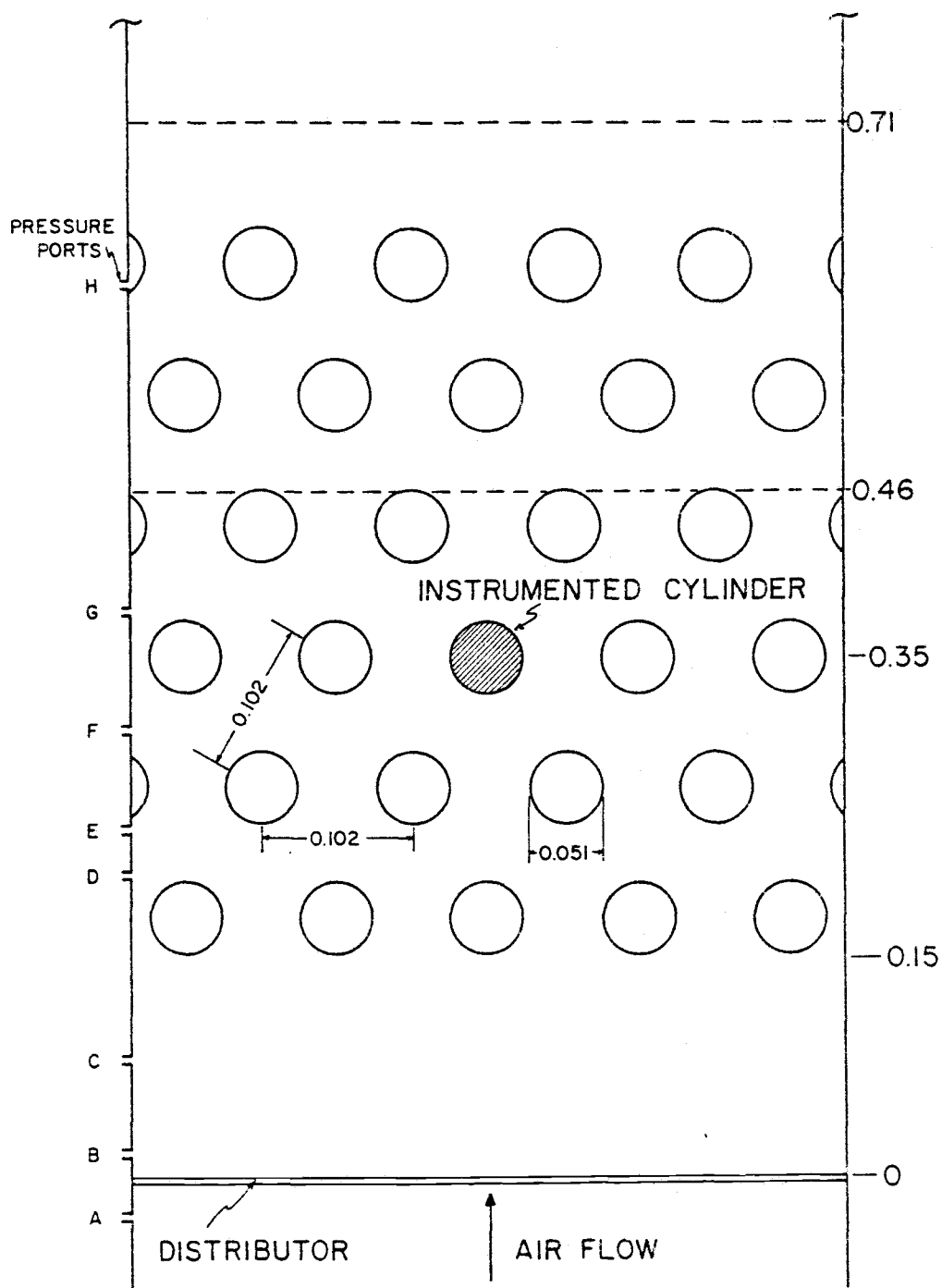


Figure 4. 1. Bed geometry (slumped bed heights are indicated by broken lines, distances from the distributor are in meters).

does not vary significantly with their position inside the bundle (the only exception could be tubes in close proximity to the vessel wall).

The locations of ports for pressure measurement are marked on Figure 4.1. Possible channeling and irregular fluidization were prevented by insuring a sufficient pressure drop across the distributor plate (Δp_{A-B}). In all experiments, this pressure difference amounted to at least 30% of the pressure drop across the bed ($\Delta p_{B-\infty}$). A typical bed pressure drop vs. gas velocity diagram is shown in Figure 4.2 (for $d_p = 1.3$ mm). Minimum fluidization velocities were approximately the same for both the single tube and the array (although local fluidization on the sides of a tube starts at lower velocities when the tube is part of an array). Pressure fluctuations decrease significantly when the array is placed in the bed. Large exploding bubbles and slugs characteristic for the single tube case change to smaller, uniformly distributed bubbles in the presence of the bundle. The constantly increasing pressure fluctuations at higher velocities indicate that the turbulent regime was not attained in our study.

The heat transfer, capacitance, and pressure data presented in Sections B, C, and D were collected at a rate of 18 per second for a period of 150 seconds (a total of 2700 samples per channel). All the results will be used in the theoretical analyses given in Chapters V, VI, and VII.

B. Heat Transfer Results

Graphical Presentation

The basic information on heat transfer is the instantaneous heat transfer coefficient at a particular angular position on the tube, $h_{\theta i}$.

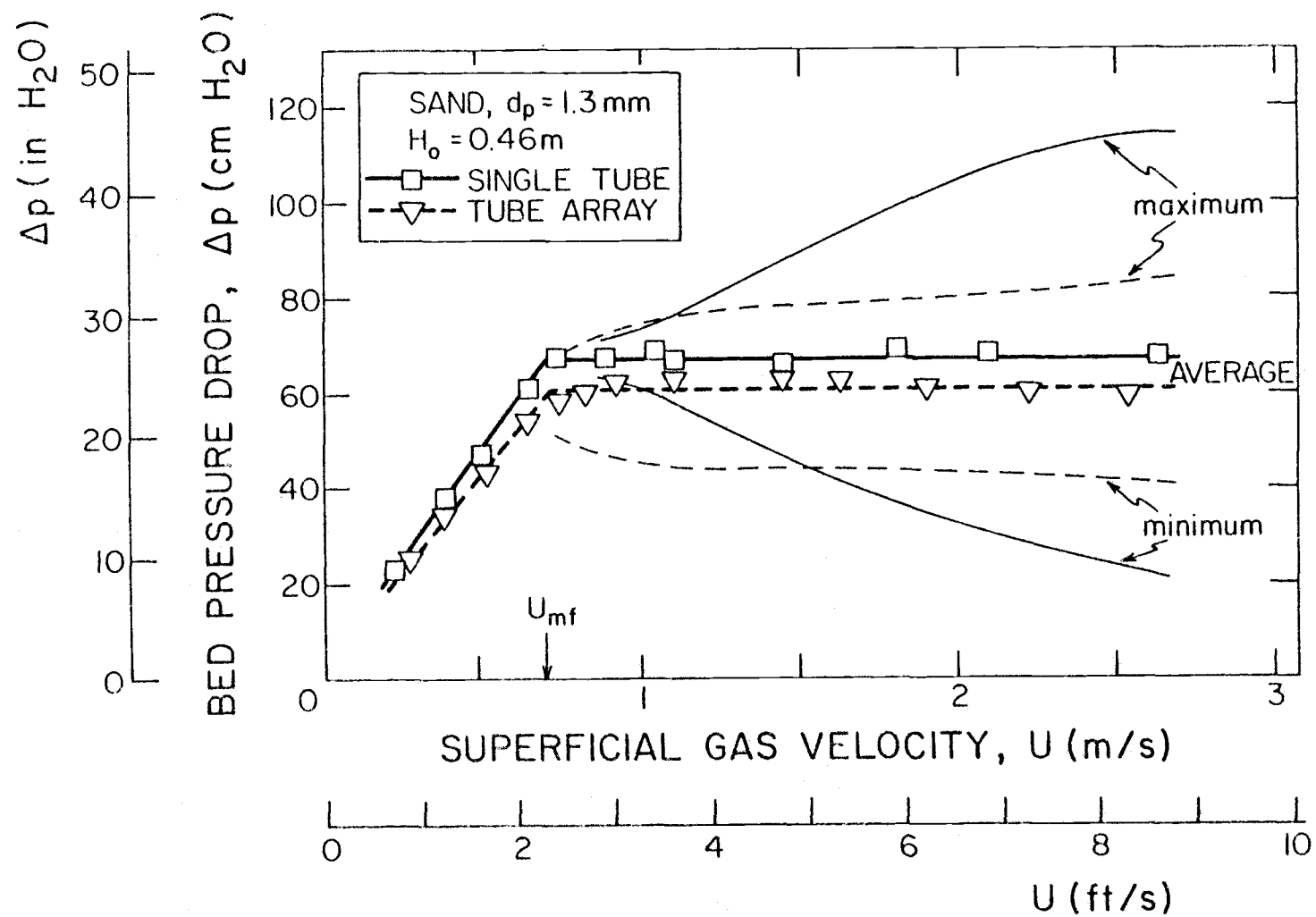


Figure 4.2. Bed pressure drop as a function of superficial gas velocity for $d_p = 1.3$ mm (thinner lines indicate bounds of pressure fluctuations).

From it, we obtain the time-averaged local coefficient at that position, h_{θ} :

$$h_{\theta} = \frac{1}{2700} \sum_{n=1}^{2700} h_{\theta i, n} \quad (4.2)$$

Figure 4.3 presents time-averaged coefficients, as well as the maximum and minimum instantaneous values ($h_{\theta i, \max}$ and $h_{\theta i, \min}$), for all five locations on a tube, as functions of the superficial gas velocity (for $d_p = 0.37$ mm). Both the single tube data and the array data are shown. The maximum instantaneous local values are recorded at times when the sensor makes initial contact with the emulsion (particles), while the minimum coefficients occur when the platinum heating element is immersed in a bubble (see Figure 3.6(a)).

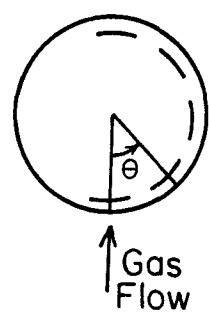
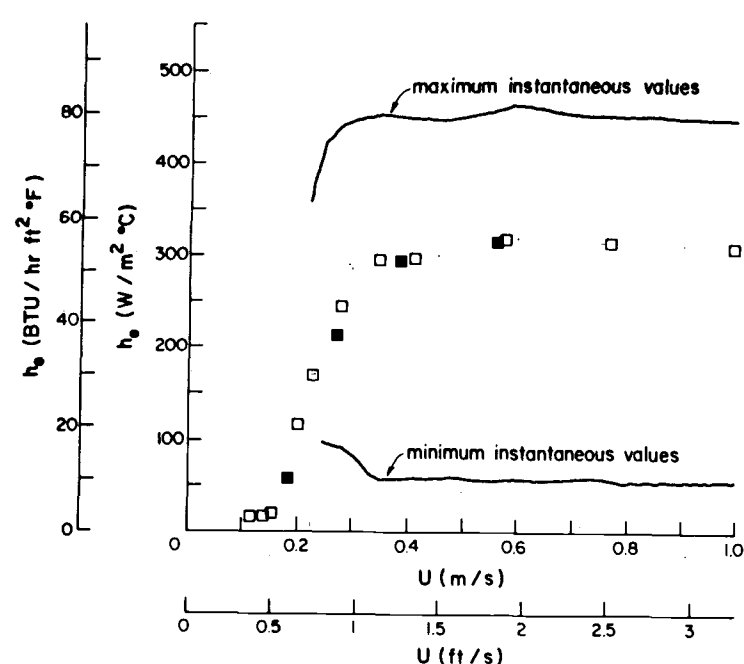
The time-averaged coefficient for the whole circumference of the tube (i.e., the time-averaged overall coefficient) is obtained from the formula:

$$h = \frac{h_{180^\circ} + 2h_{135^\circ} + 2h_{90^\circ} + 2h_{45^\circ} + h_{0^\circ}}{8} \quad (4.3)$$

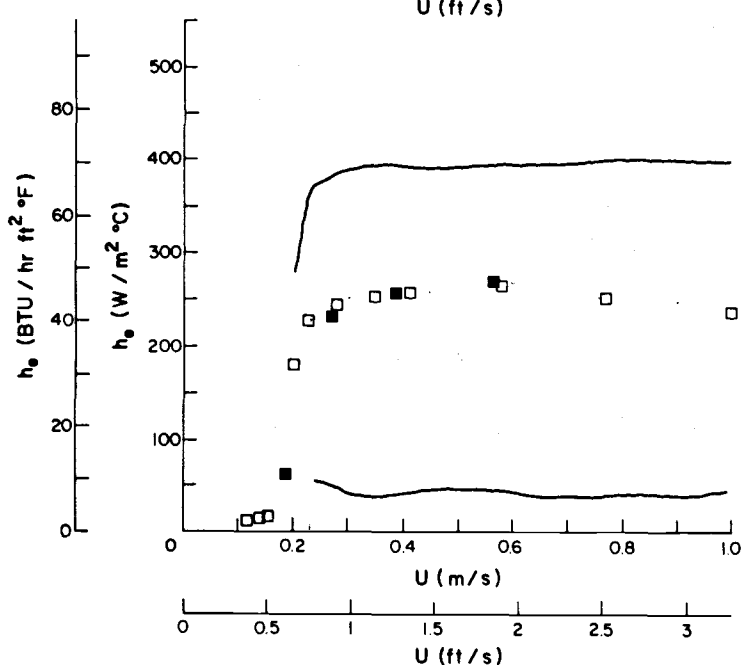
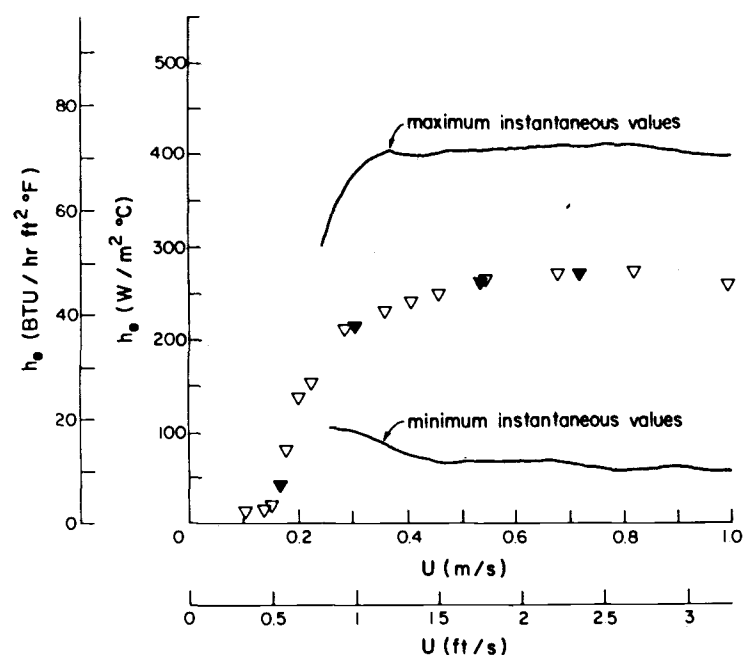
The average overall coefficient for $d_p = 0.37$ mm, obtained from the data in Figure 4.3, is shown in Figure 4.4. Data for the single tube are represented by the thick solid line while the tube array results are indicated by the thick broken line. The latter line starts a sharp rise at a lower velocity than the former; this is due to somewhat livelier fluidization near U_{mf} in the array. The thinner lines represent the averages of the maximum and minimum instantaneous local coefficients, and are obtained from:

SINGLE TUBE

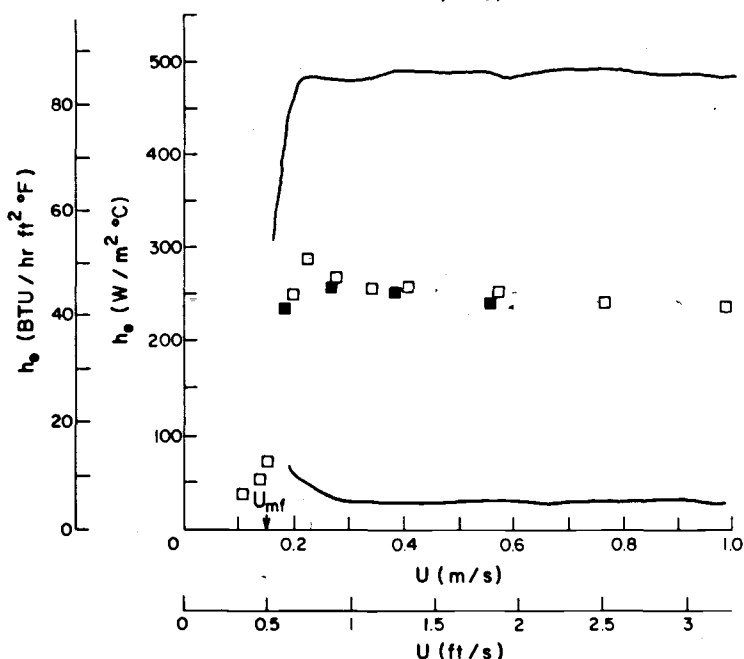
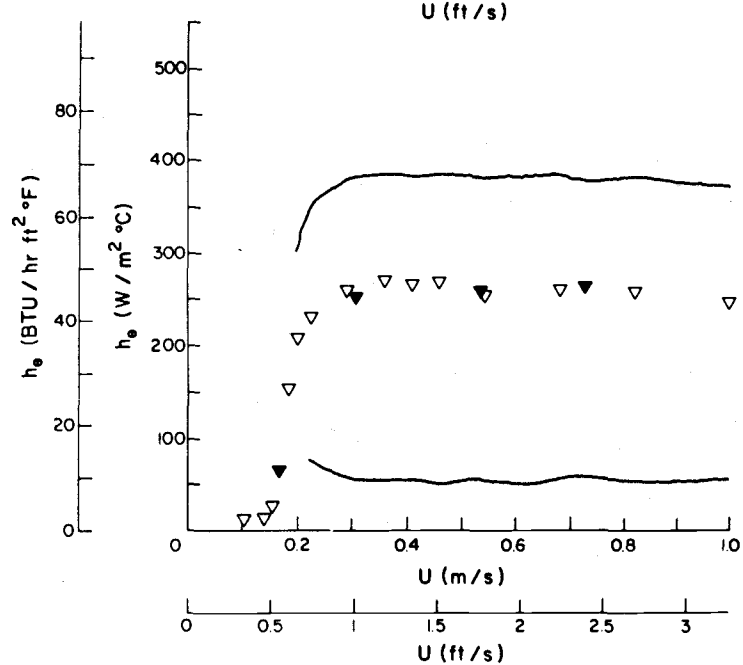
TUBE ARRAY



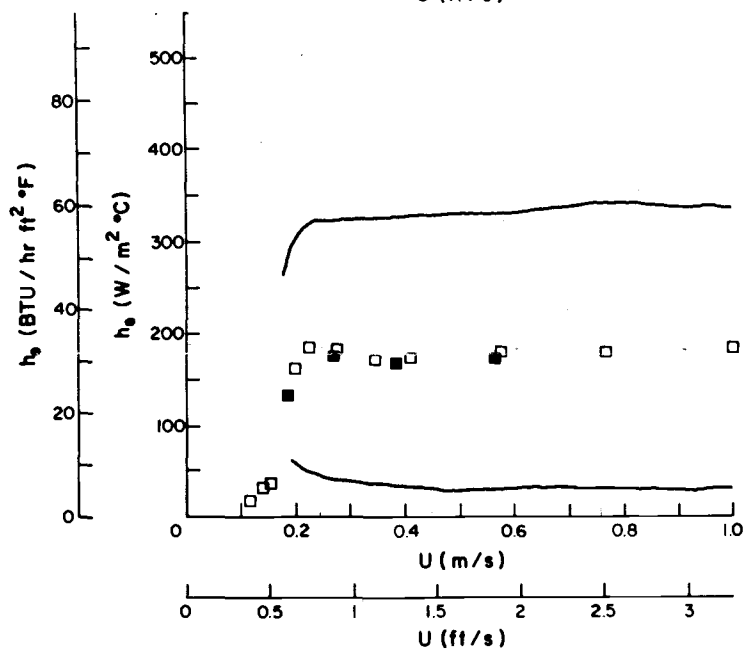
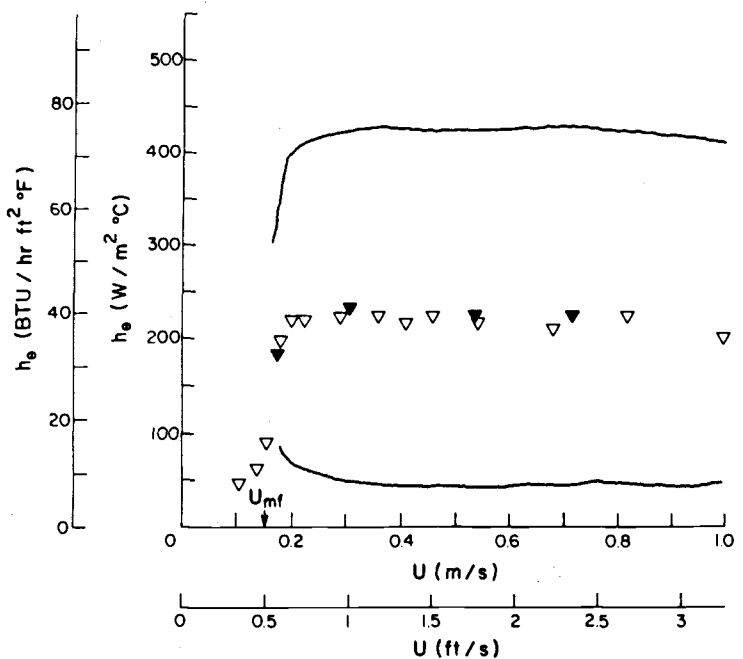
$\theta = 180^\circ$



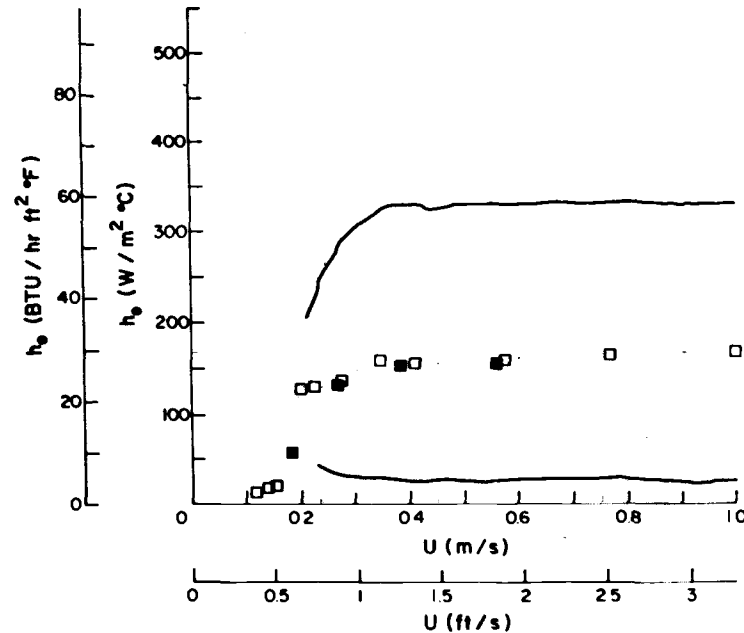
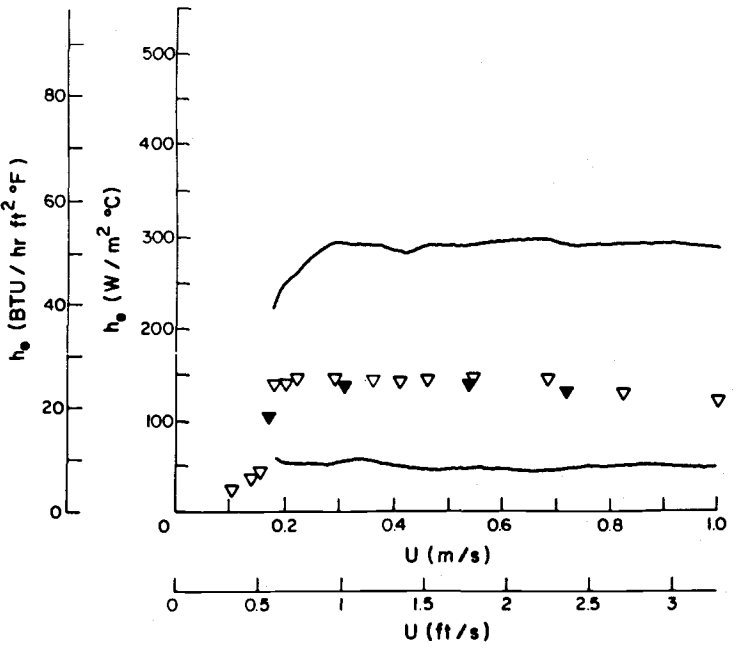
135°



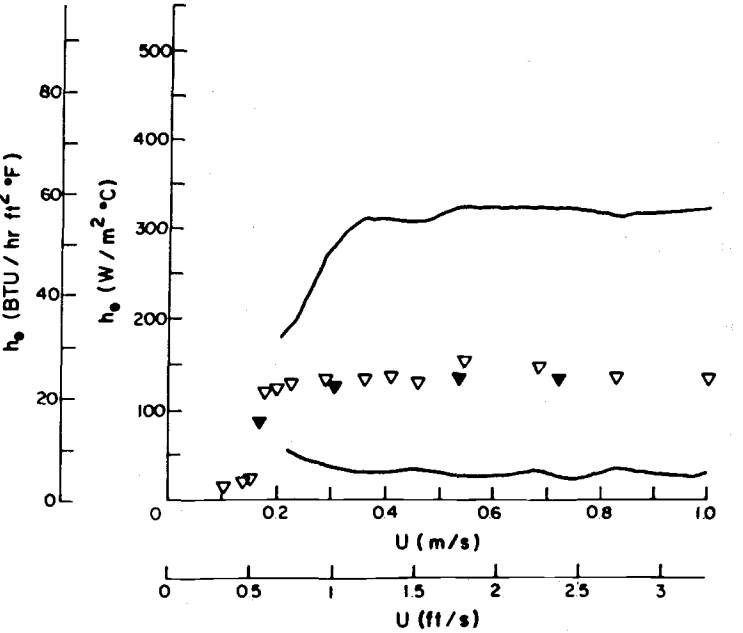
90°



45°



0°



SAND
 $d_p = 0.37 \text{ mm}$

SINGLE TUBE TUBE ARRAY

□ $H_o = 0.46 \text{ m}$ ▽
■ $H_o = 0.71 \text{ m}$ ▼

Figure 4.3. Time-averaged local heat transfer coefficients as functions of superficial gas velocity, for $d_p = 0.37 \text{ mm}$ (lines indicate maximum and minimum instantaneous values, $h_{\theta i, \max}$ and $h_{\theta i, \min}$).

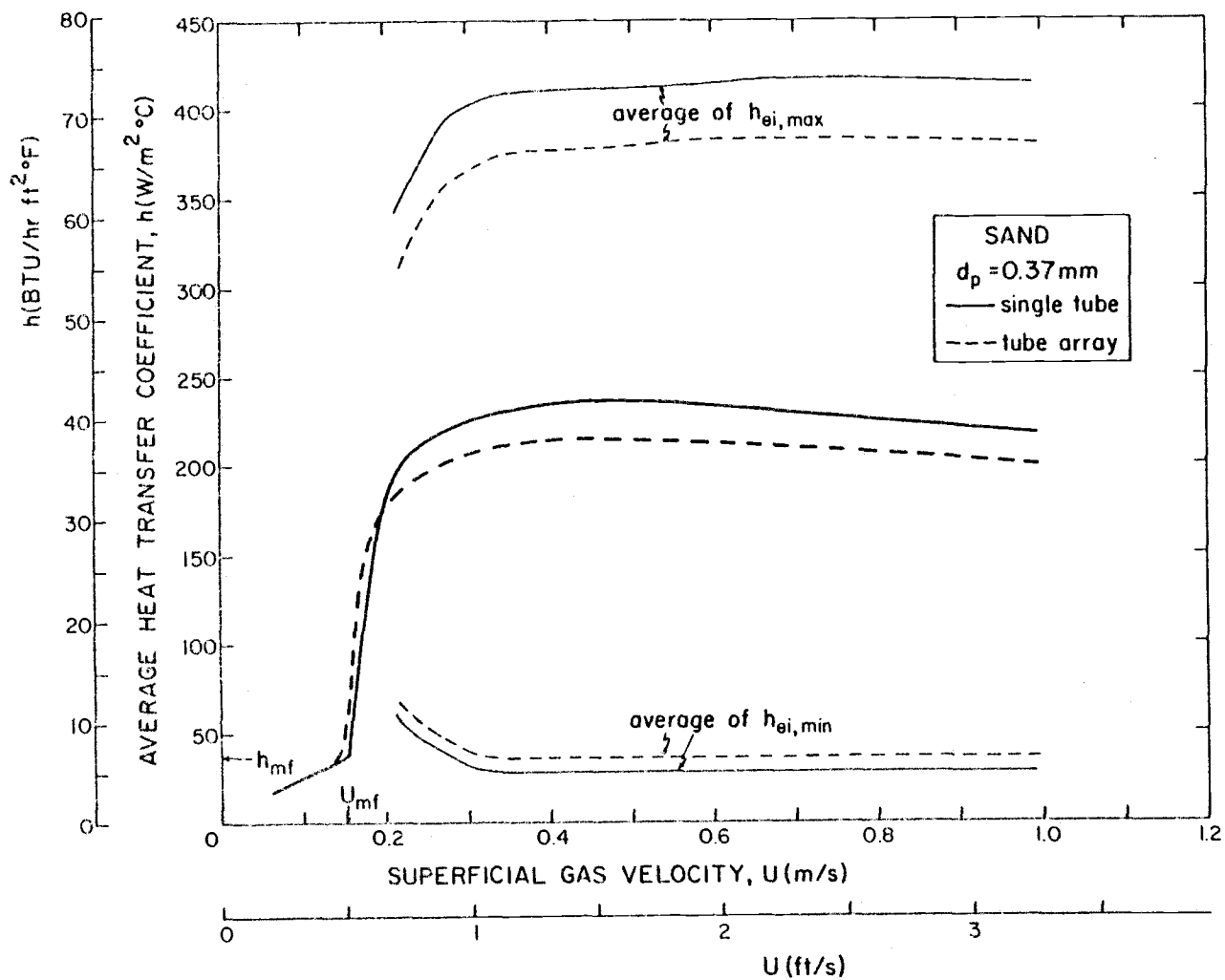


Figure 4.4. Time-averaged overall heat transfer coefficient as a function of superficial gas velocity, for $d_p = 0.37 \text{ mm}$.

$$h_{i,\max} = \frac{h_{180^\circ i, \max} + 2h_{135^\circ i, \max} + 2h_{90^\circ i, \max} + 2h_{45^\circ i, \max} + h_{0^\circ i, \max}}{8} \quad (4.4)$$

$$h_{i, \min} = \frac{h_{180^\circ i, \min} + 2h_{135^\circ i, \min} + 2h_{90^\circ i, \min} + 2h_{45^\circ i, \min} + h_{0^\circ i, \min}}{8} \quad (4.5)$$

These thinner lines give values which would be obtained if all probes were simultaneously covered by either the emulsion (maximum) or bubble(s) (minimum).

The type of data presented in Figures 4.3 and 4.4 provide very useful information for the designer concerned with thermal cycling arising from differences in instantaneous values, and thermal stresses and fatigue resulting from variations in local coefficients. Figures 4.5 and 4.6 ($d_p = 0.8$ mm), 4.7 and 4.8 ($d_p = 1.3$ mm), 4.9 and 4.10 ($d_p = 2.0$ mm), 4.11 and 4.12 ($d_p = 2.85$ mm), 4.13 and 4.14 ($d_p = 4.0$ mm), and 4.15 and 4.16 ($d_p = 6.6$ mm) show the corresponding data for other particle sizes used in our study. Although the true significance of the graphs presented here will come to light in later theoretical development, their extensiveness warrants certain comments and comparisons without delay.

General Comments

A large number of data points were collected in the packed bed region. These points required a somewhat different procedure than data representing the fluid-bed heat transfer, as sufficient time had to be allowed for the establishment of a steady-state bed temperature profile. By contrast, the fluid-bed data could be obtained as soon as the desired gas flow rate was set. The packed bed data will not be used in later analyses; however, they could be of value for

SINGLE TUBE

TUBE ARRAY

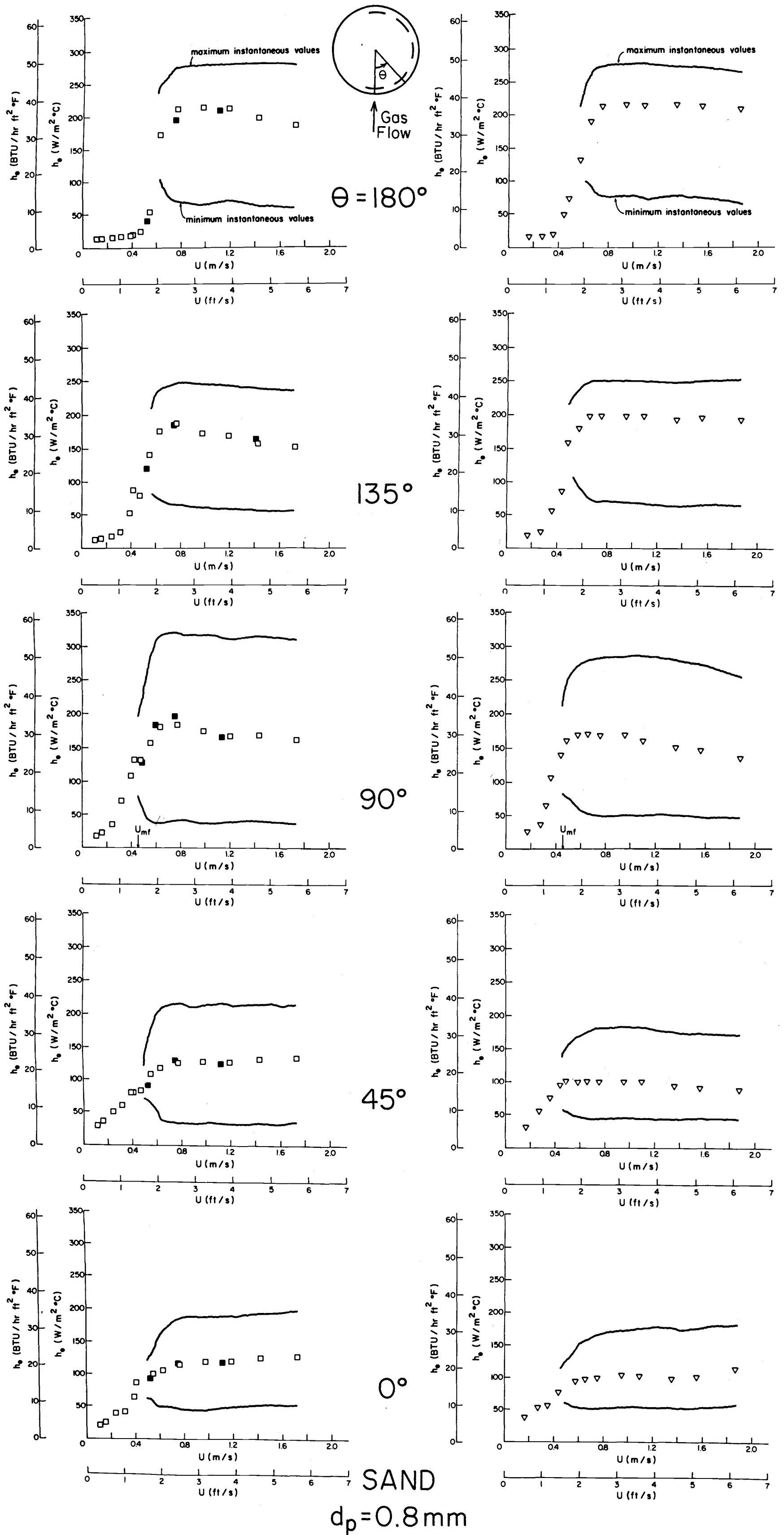


Figure 4.5. Time-averaged local heat transfer coefficients as functions of superficial gas velocity, for $d_p = 0.8 \text{ mm}$ (lines indicate maximum and minimum instantaneous values, $h_{\theta i, \max}$ and $h_{\theta i, \min}$).

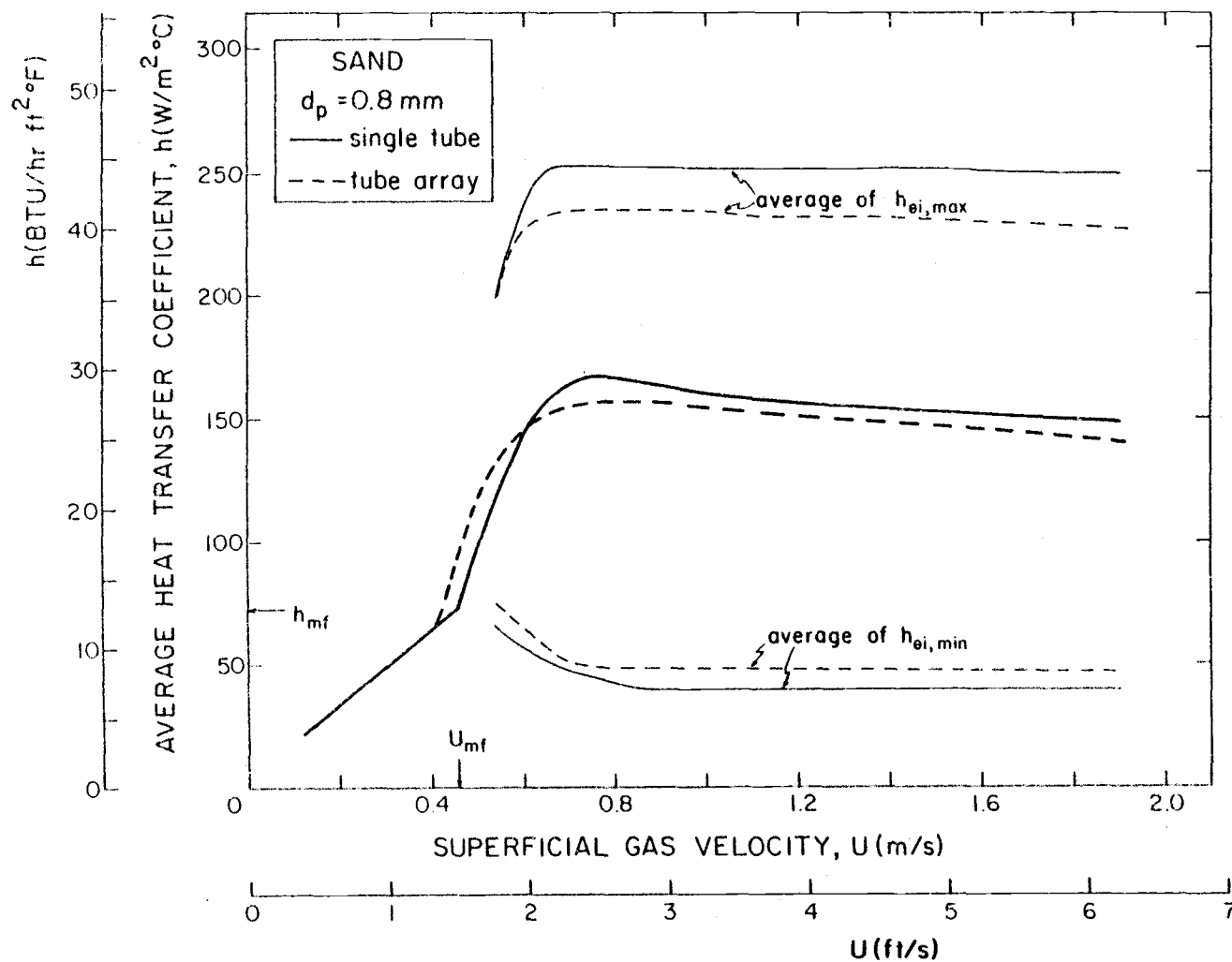
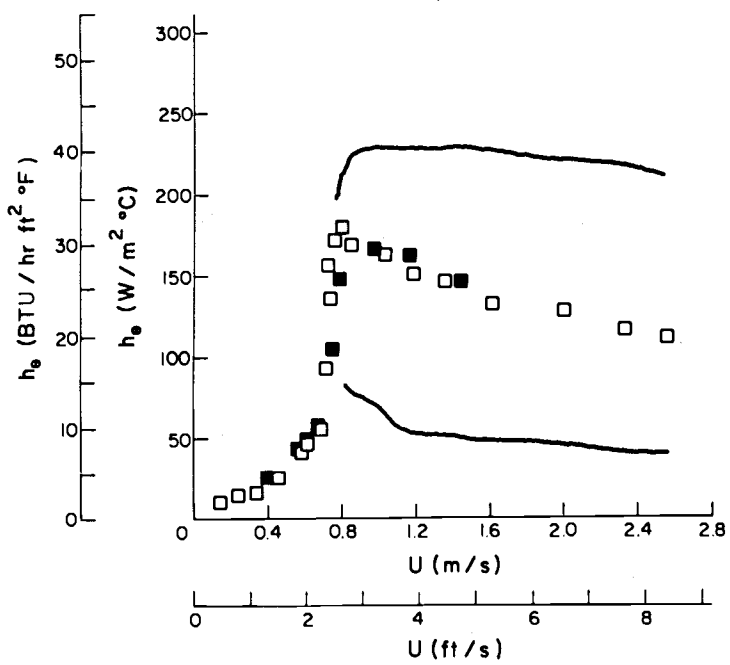
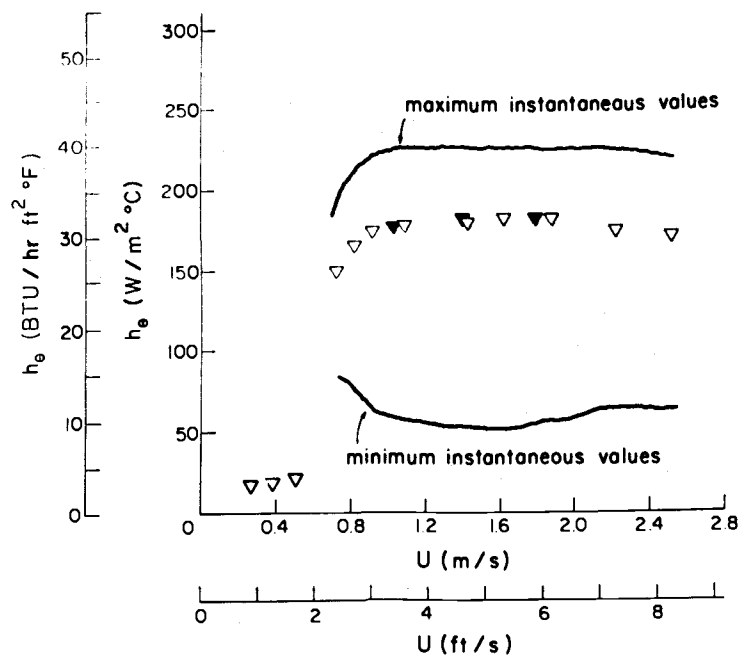
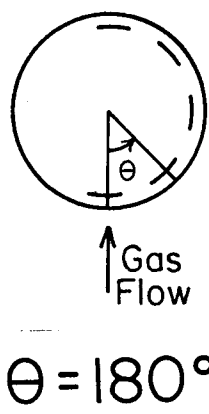
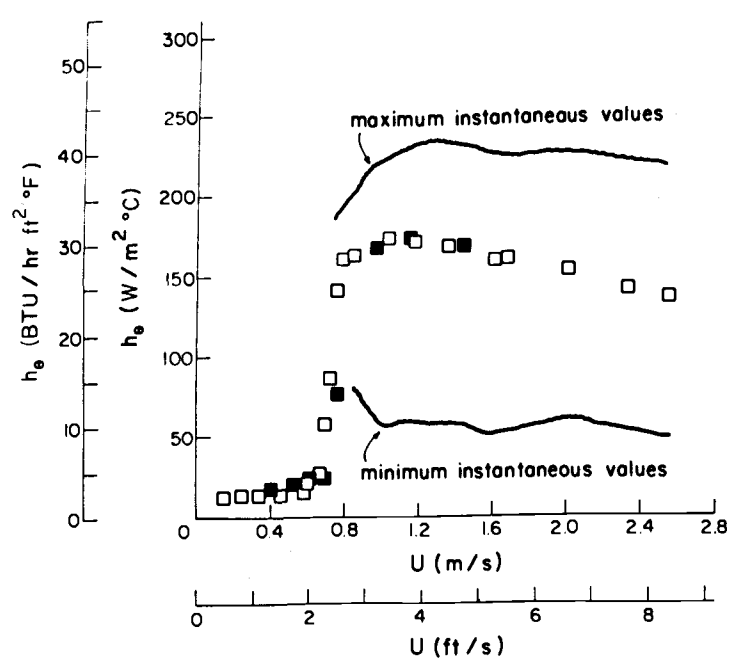


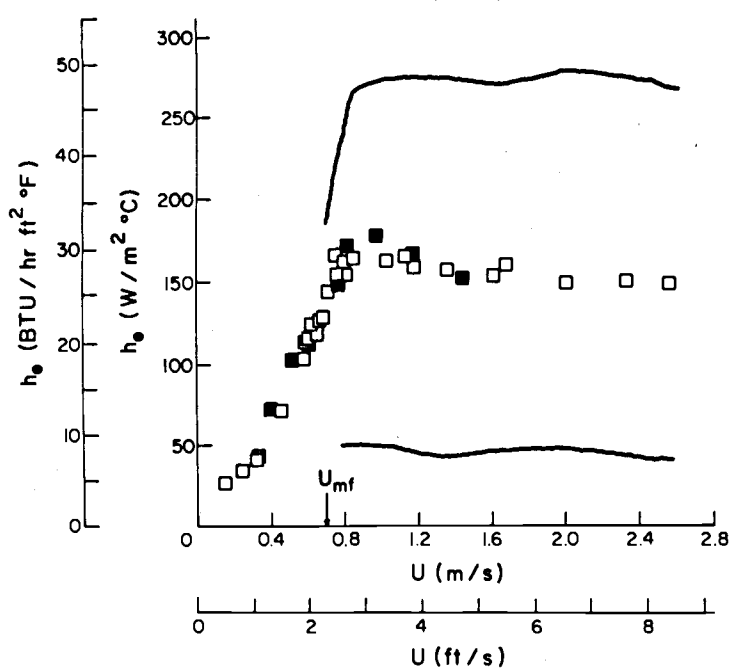
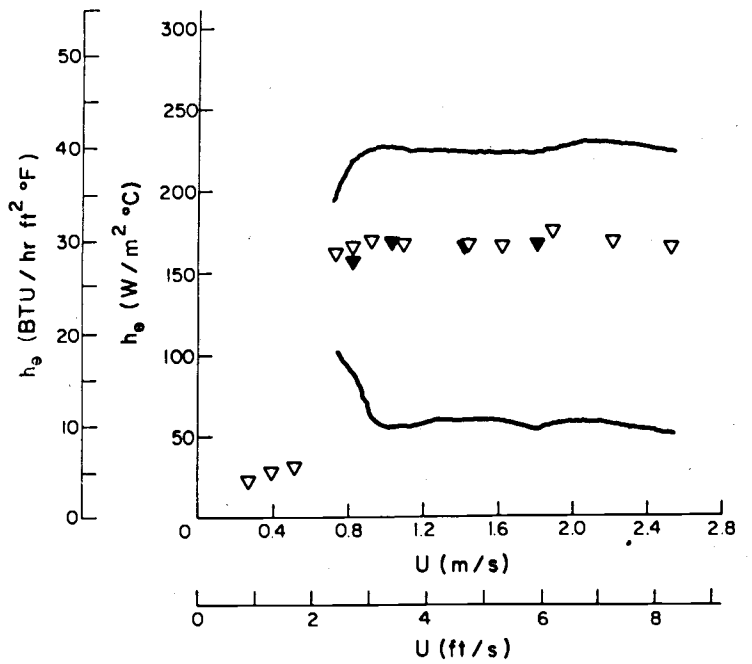
Figure 4.6. Time-averaged overall heat transfer coefficient as a function of superficial gas velocity, for $d_p = 0.8 \text{ mm}$.

SINGLE TUBE

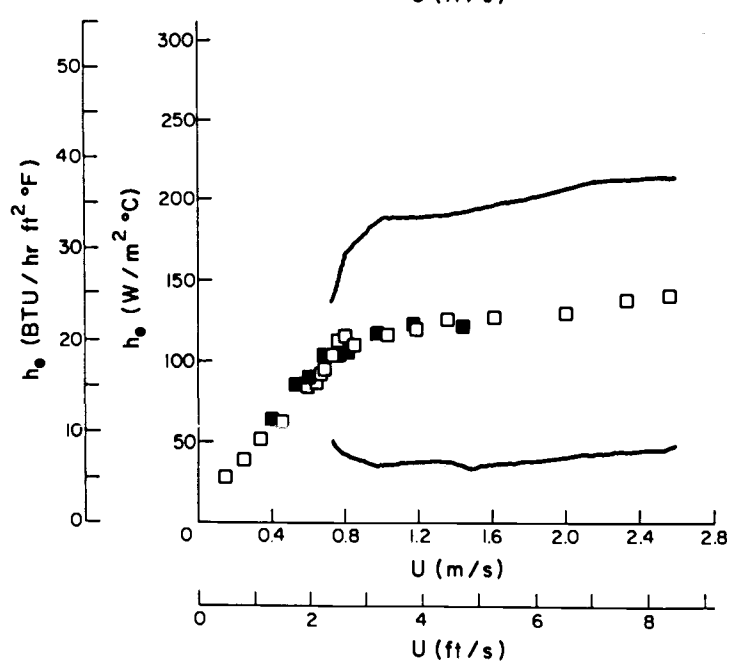
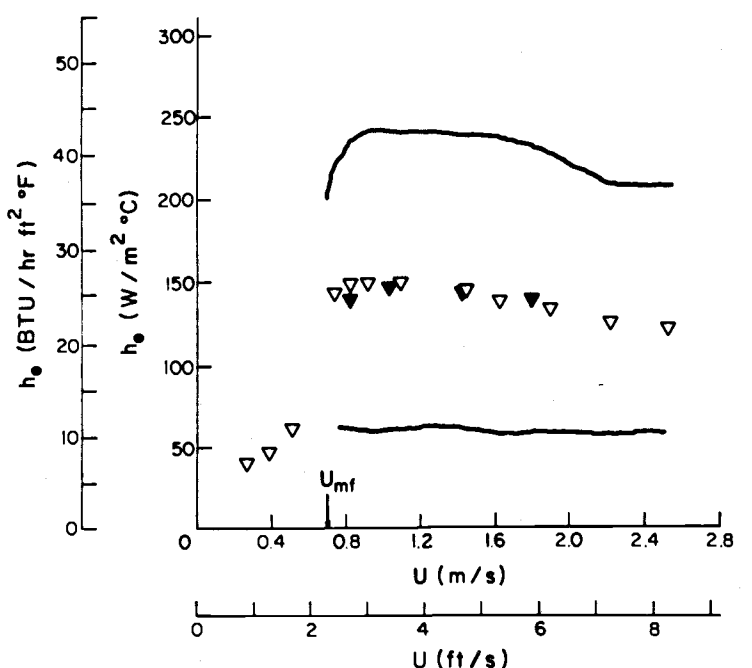
TUBE ARRAY



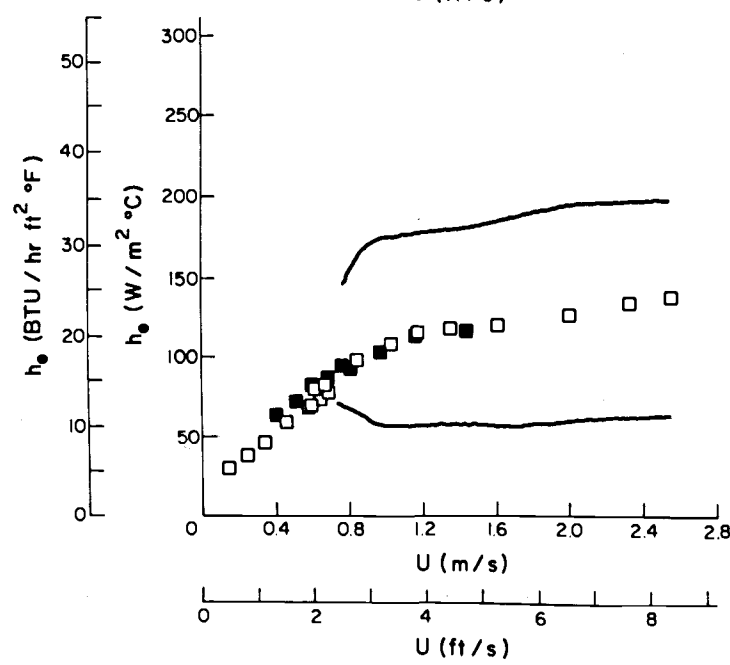
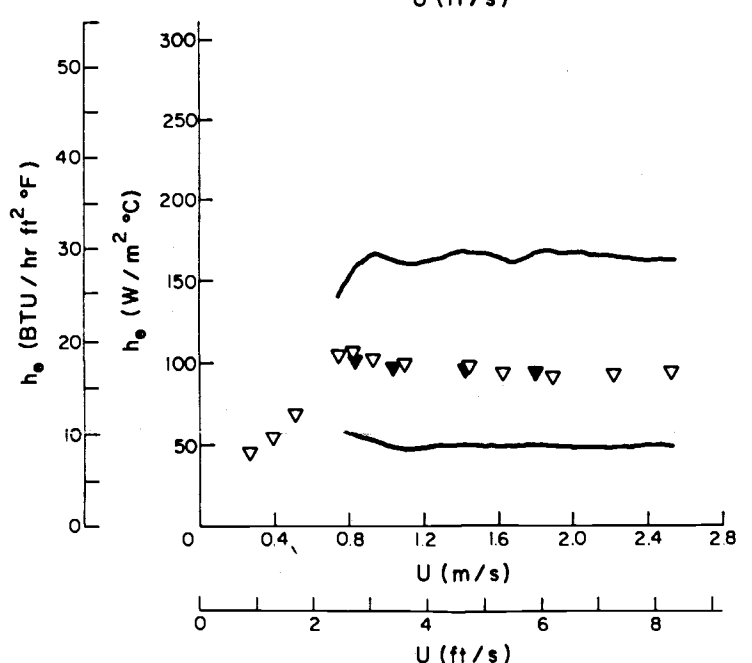
135°



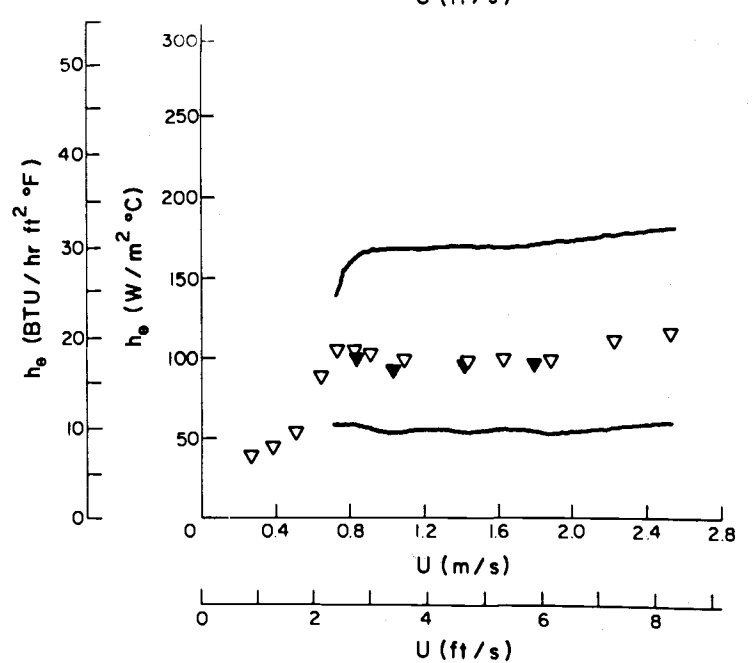
90°



45°



0°



SAND
 $d_p = 1.3 \text{ mm}$

SINGLE TUBE TUBE ARRAY

□ $H_0 = 0.46 \text{ m}$ ▽
■ $H_0 = 0.71 \text{ m}$ ▼

Figure 4.7. Time-averaged local heat transfer coefficients as functions of superficial gas velocity, for $d_p = 1.3 \text{ mm}$ (lines indicate maximum and minimum instantaneous values, $h_{0i, \max}$ and $h_{0i, \min}$).

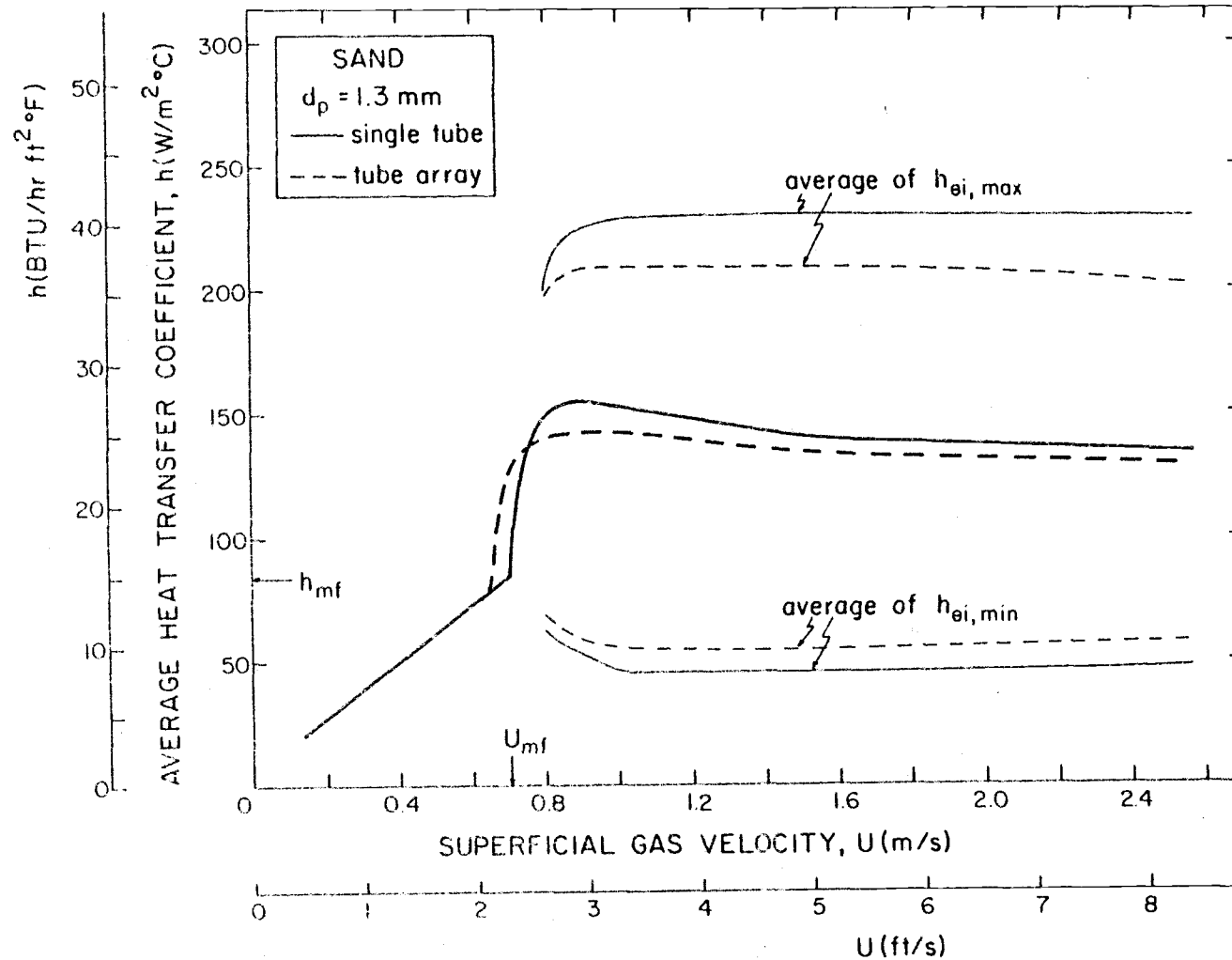
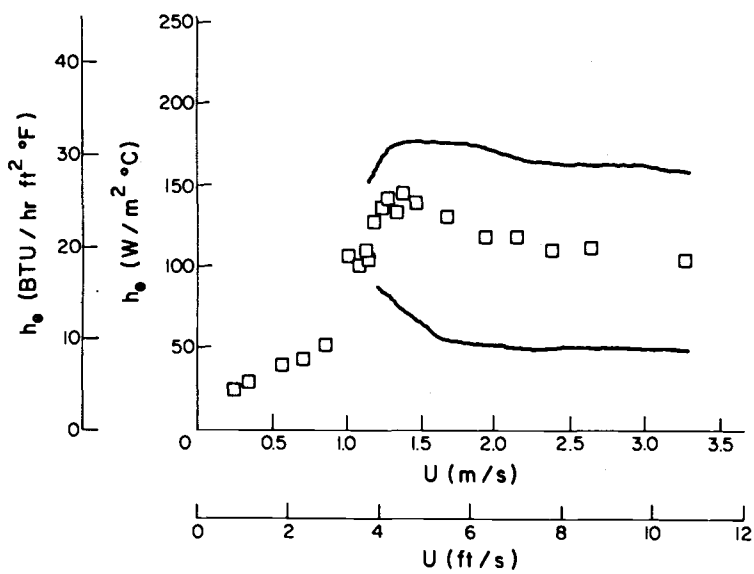
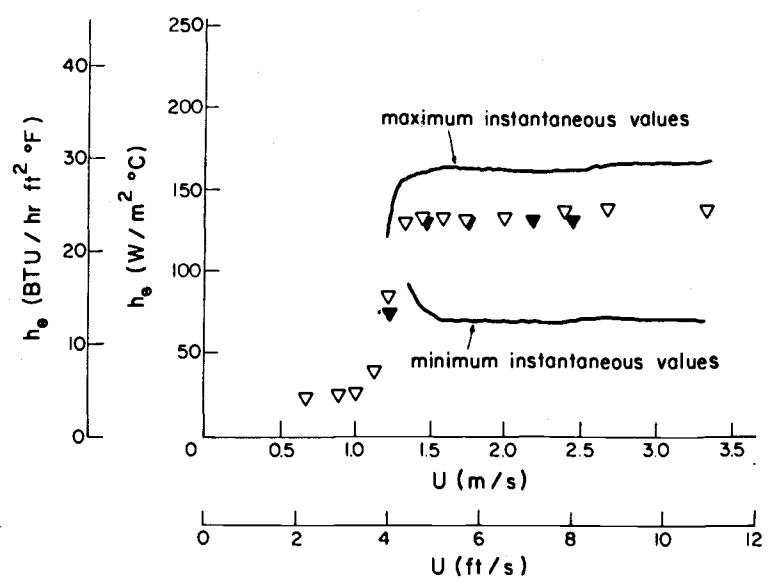
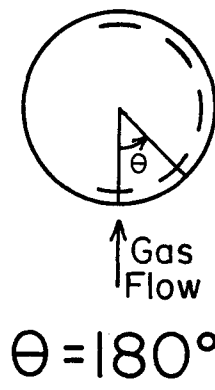
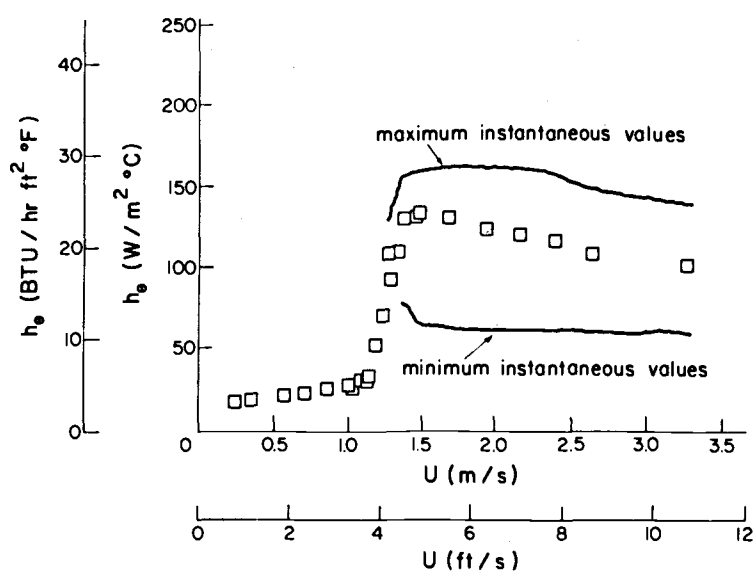


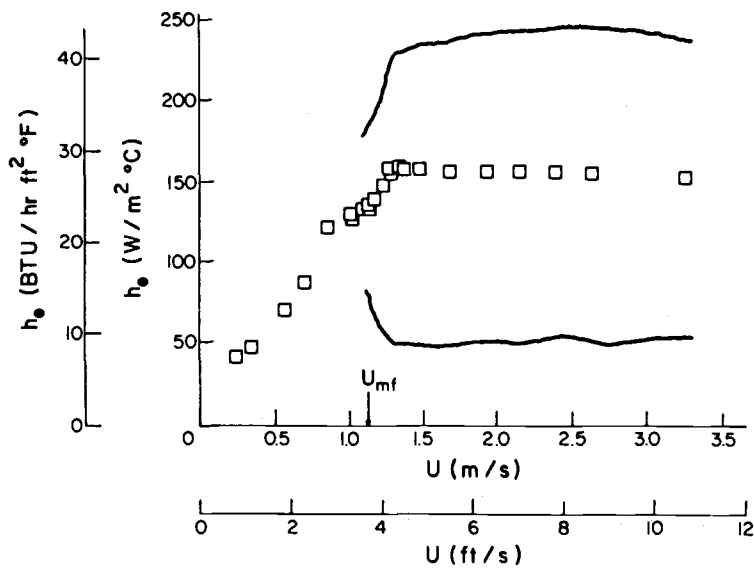
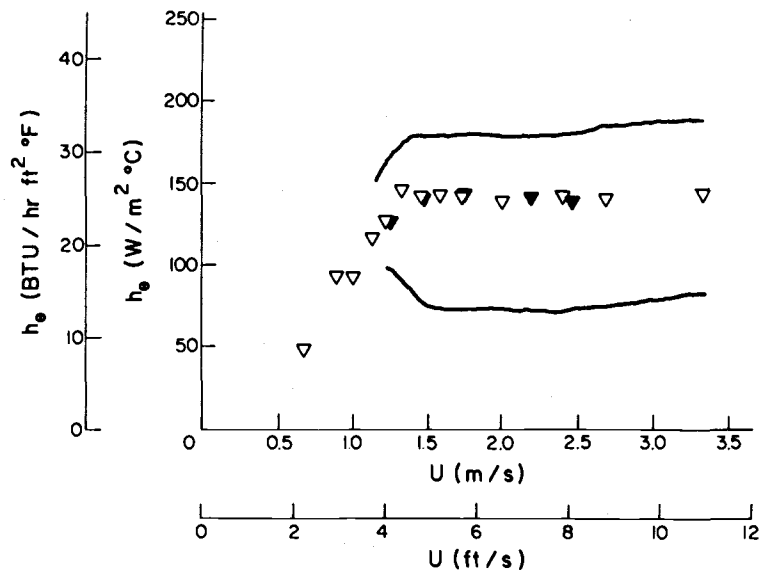
Figure 4.8. Time-averaged overall heat transfer coefficient as a function of superficial gas velocity, for $d_p = 1.3 \text{ mm}$.

SINGLE TUBE

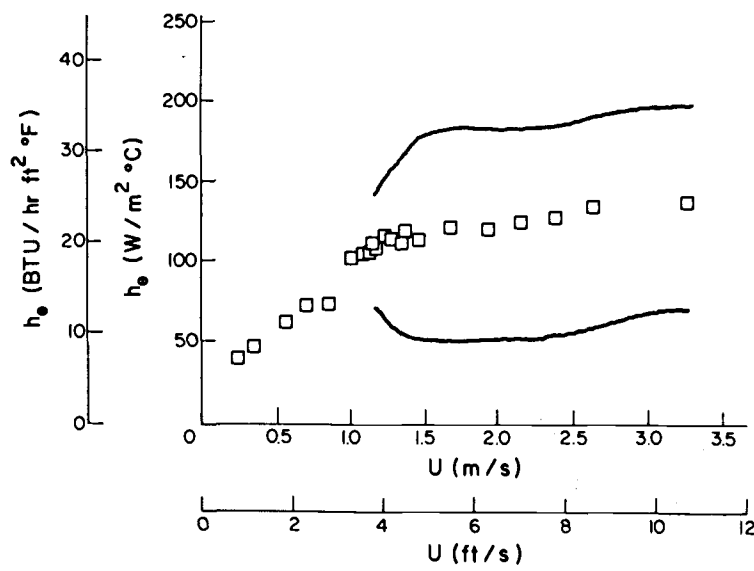
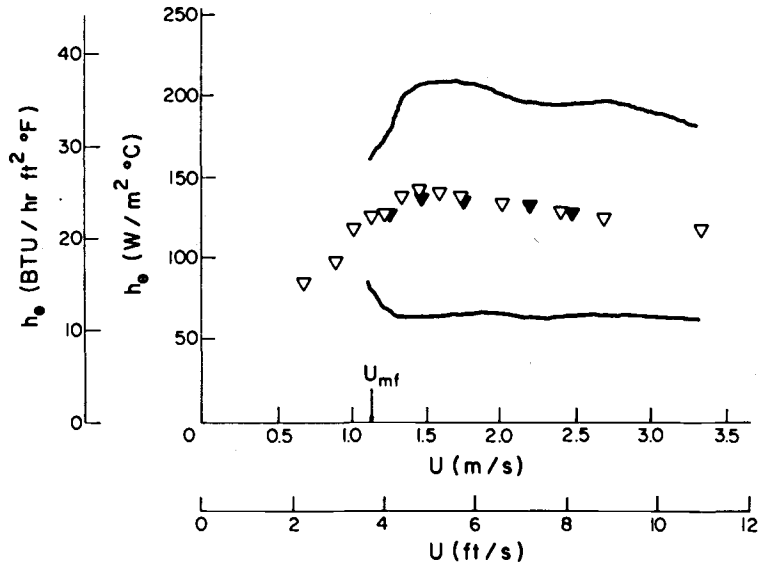
TUBE ARRAY



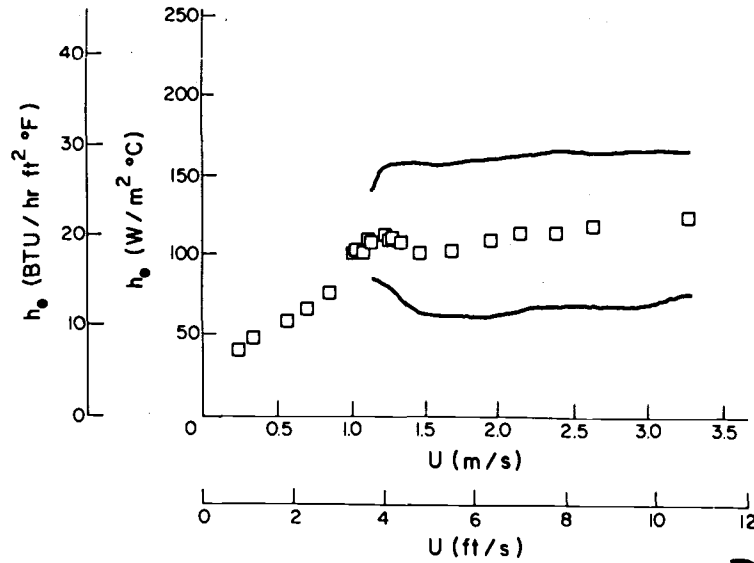
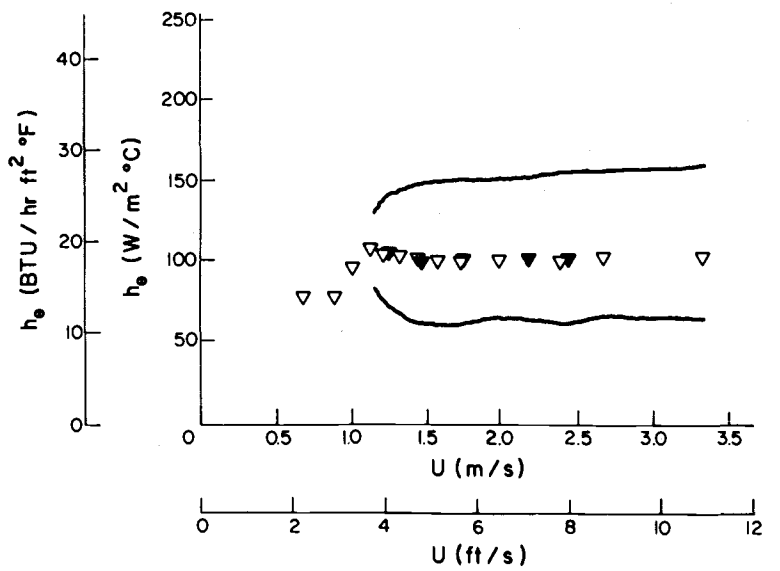
135°



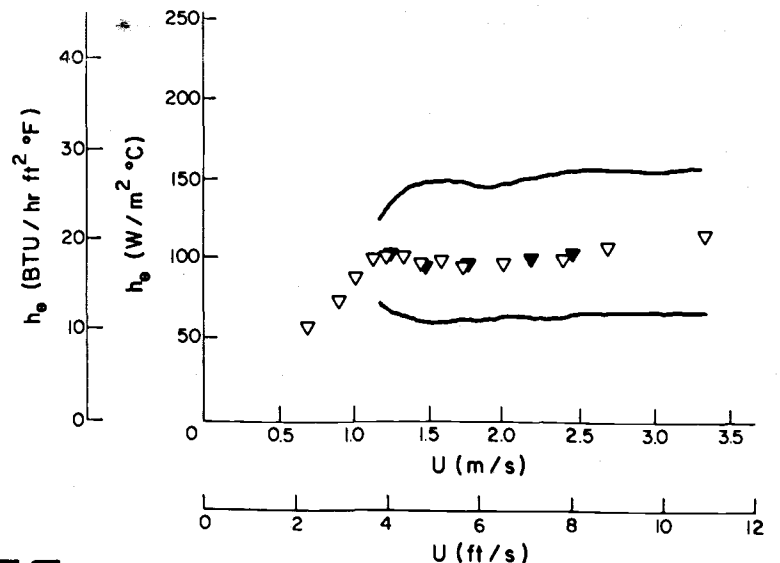
90°



45°



0°



DOLOMITE
 $d_p = 2.0 \text{ mm}$

SINGLE TUBE TUBE ARRAY

□ $H_o = 0.46 \text{ m}$ ▽
 $H_o = 0.71 \text{ m}$ ▼

Figure 4.9. Time-averaged local heat transfer coefficients as functions of superficial gas velocity, for $d_p = 2.0 \text{ mm}$ (lines indicate maximum and minimum instantaneous values, $h_{\theta i, \max}$ and $h_{\theta i, \min}$).

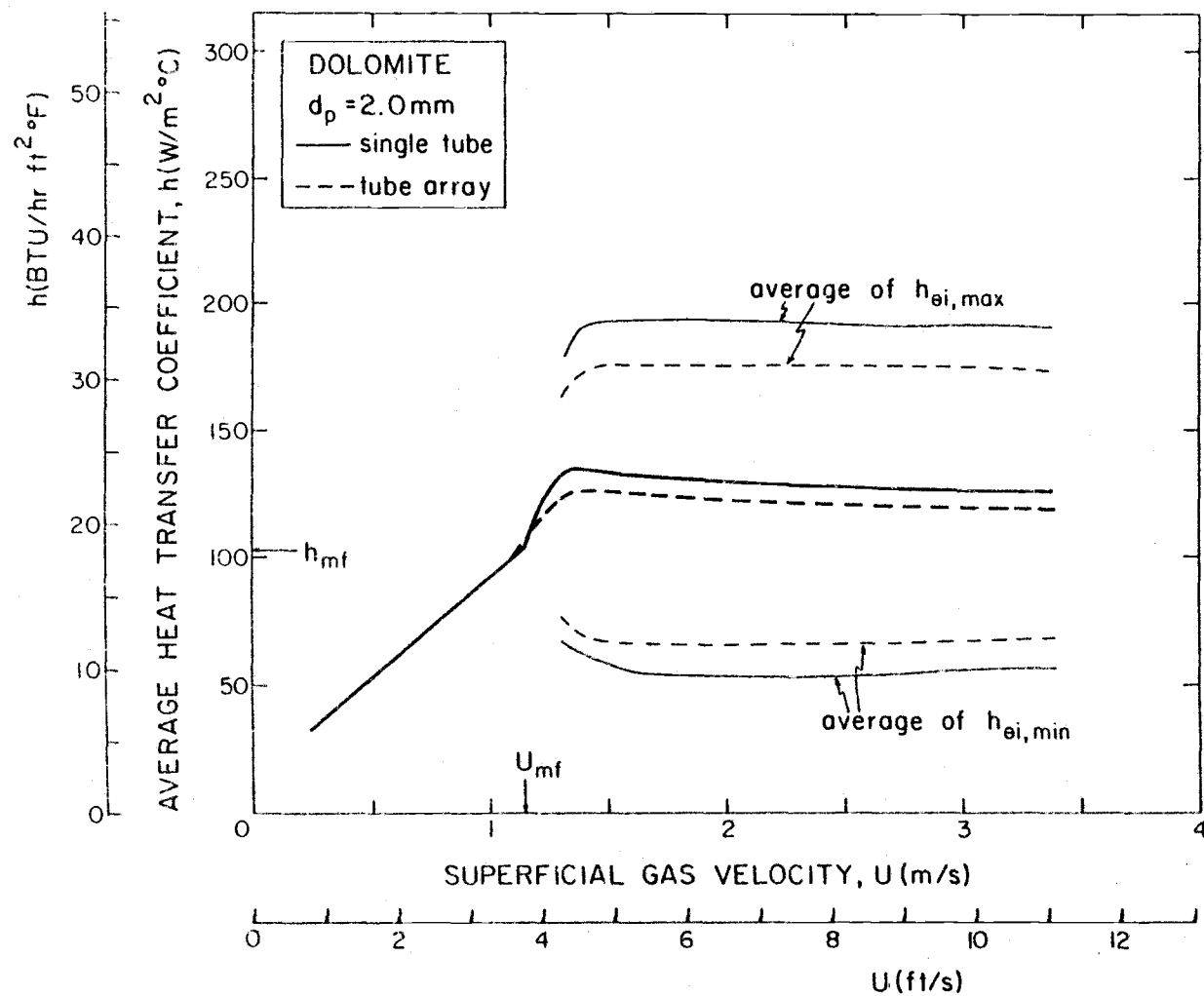
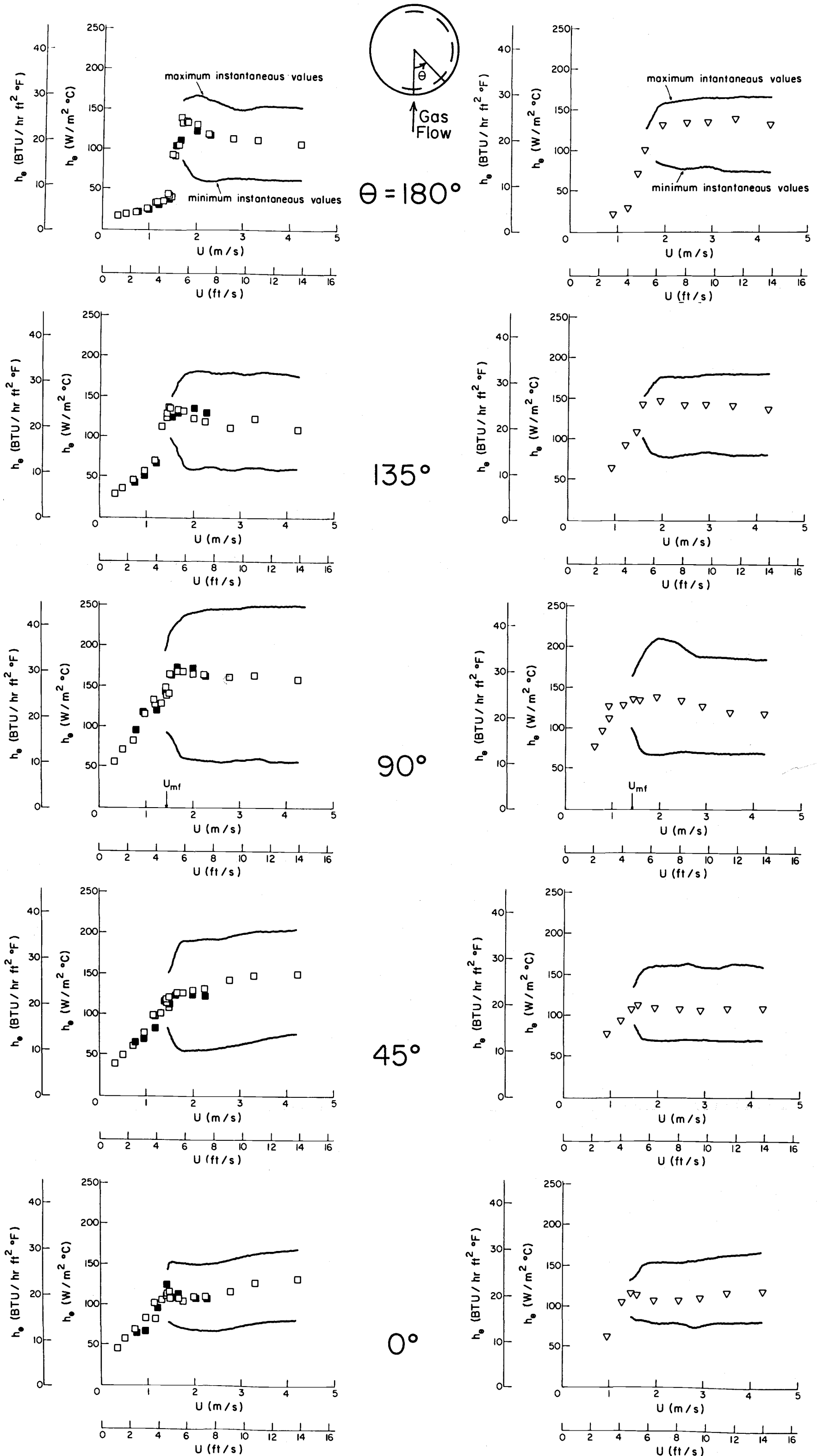


Figure 4. 10. Time-averaged overall heat transfer coefficient as a function of superficial gas velocity, for $d_p = 2.0 \text{ mm}$.

SINGLE TUBE

TUBE ARRAY



DOLOMITE
 $d_p = 2.85 \text{ mm}$

SINGLE TUBE TUBE ARRAY

□ $H_o = 0.46 \text{ m}$ ▽

■ $H_o = 0.71 \text{ m}$

Figure 4.11. Time-averaged local heat transfer coefficients as functions of superficial gas velocity, for $d_p = 2.85 \text{ mm}$ (lines indicate maximum and minimum instantaneous values, $h_{o,i,\max}$ and $h_{o,i,\min}$).

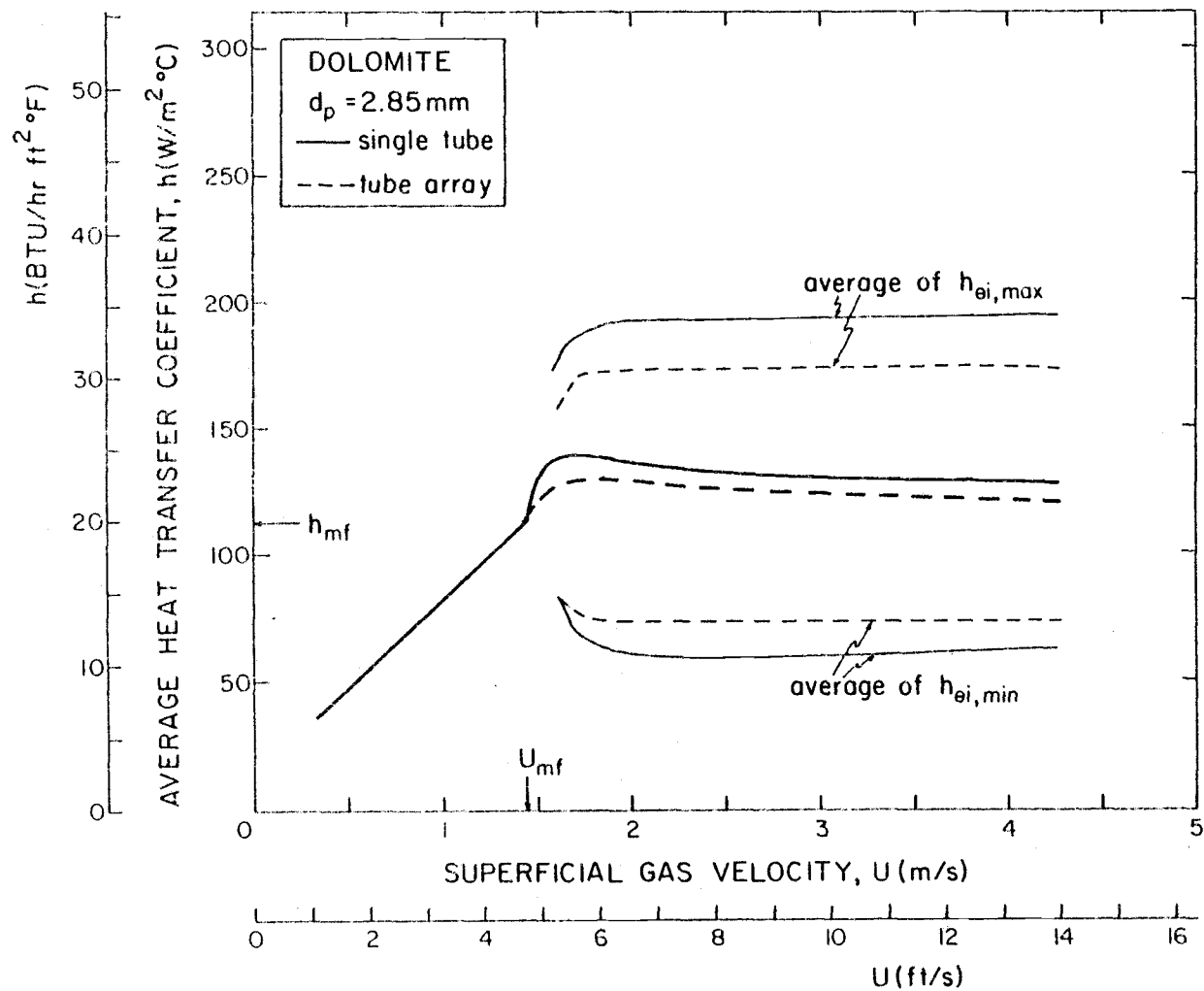
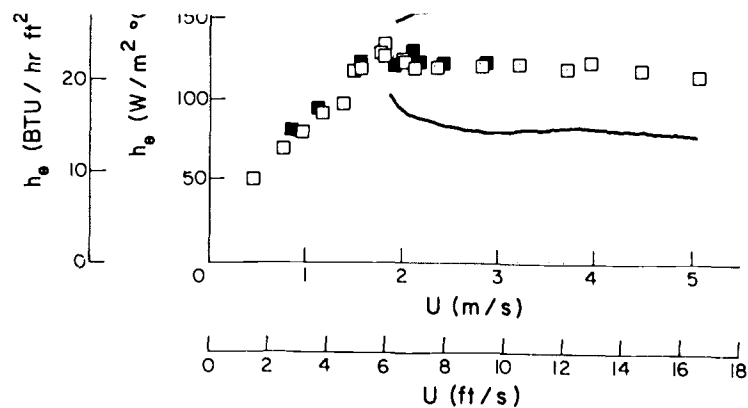
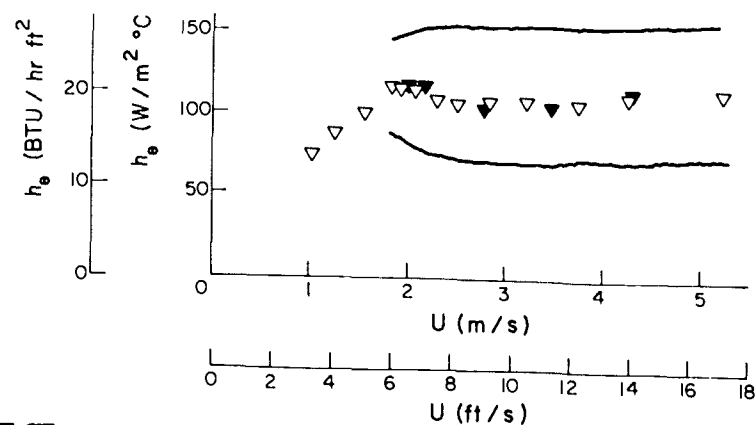


Figure 4. 12. Time-averaged overall heat transfer coefficient as a function of superficial gas velocity, for $d_p = 2.85 \text{ mm}$.



0°



DOLOMITE
 $d_p = 4.0 \text{ mm}$

SINGLE TUBE TUBE ARRAY

□ $H_o = 0.46m$ ▽
 ■ $H_o = 0.71m$ ▼

Figure 4. 13. Time-averaged local heat transfer coefficients as functions of superficial gas velocity, for $d_p = 4.0 \text{ mm}$ (lines indicate maximum and minimum instantaneous values, $h_{\theta i, \max}$ and $h_{\theta i, \min}$).

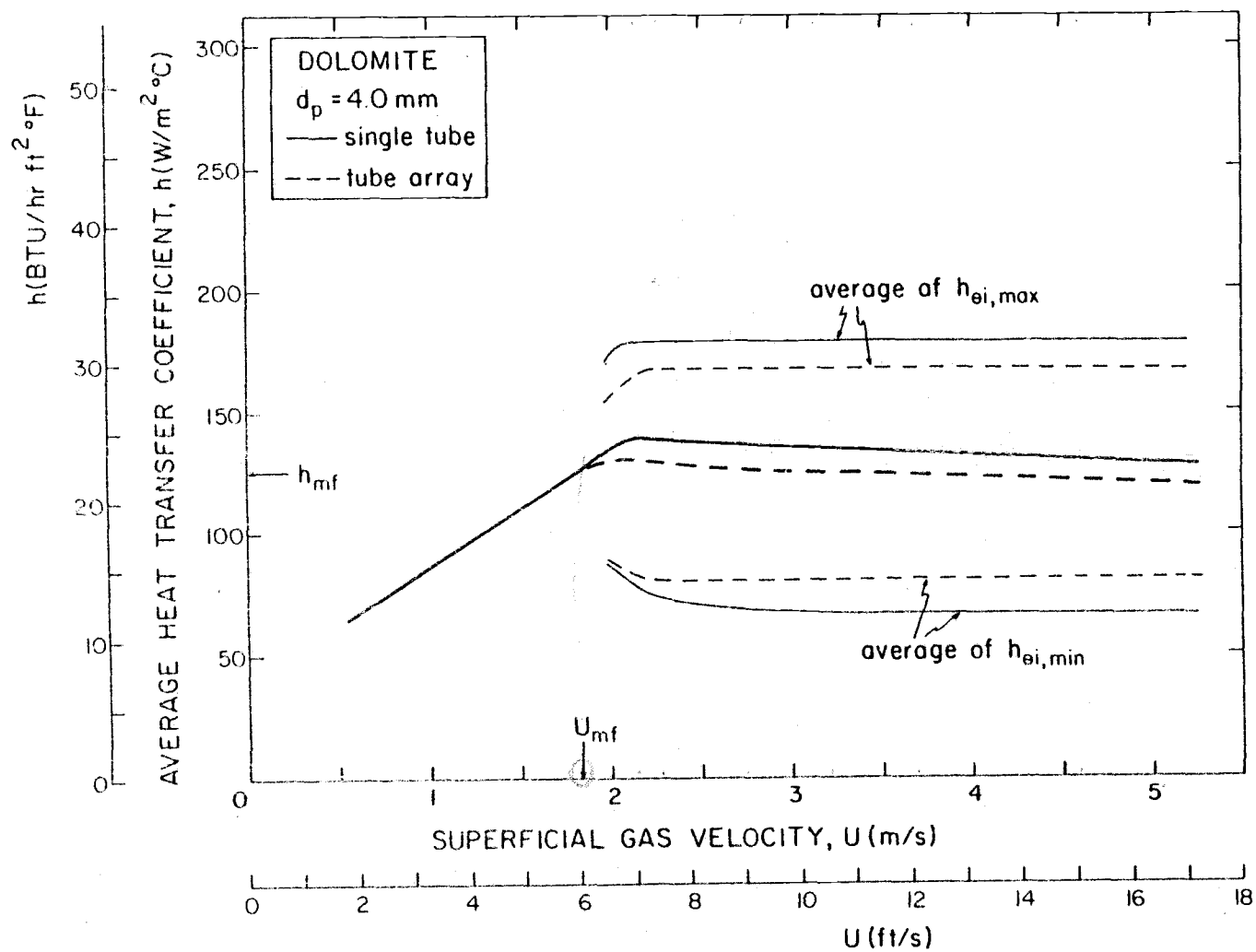
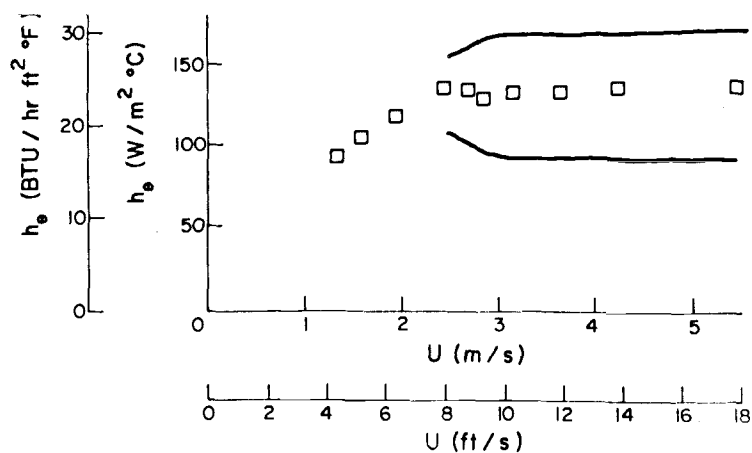
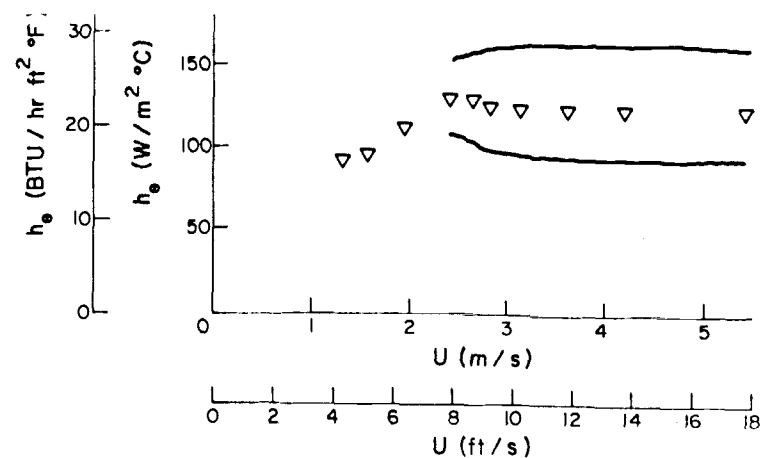


Figure 4. 14. Time-averaged overall heat transfer coefficient as a function of superficial gas velocity, for $d_p = 4.0$ mm.



0°



DOLOMITE

$d_p = 6.6 \text{ mm}$

SINGLE TUBE TUBE ARRAY

□ $H_o = 0.46 \text{ m}$ ▽

Figure 4. 15. Time-averaged local heat transfer coefficients as functions of superficial gas velocity, for $d_p = 6.6 \text{ mm}$ (lines indicate maximum and minimum instantaneous values, $h_{\theta i, \max}$ and $h_{\theta i, \min}$).

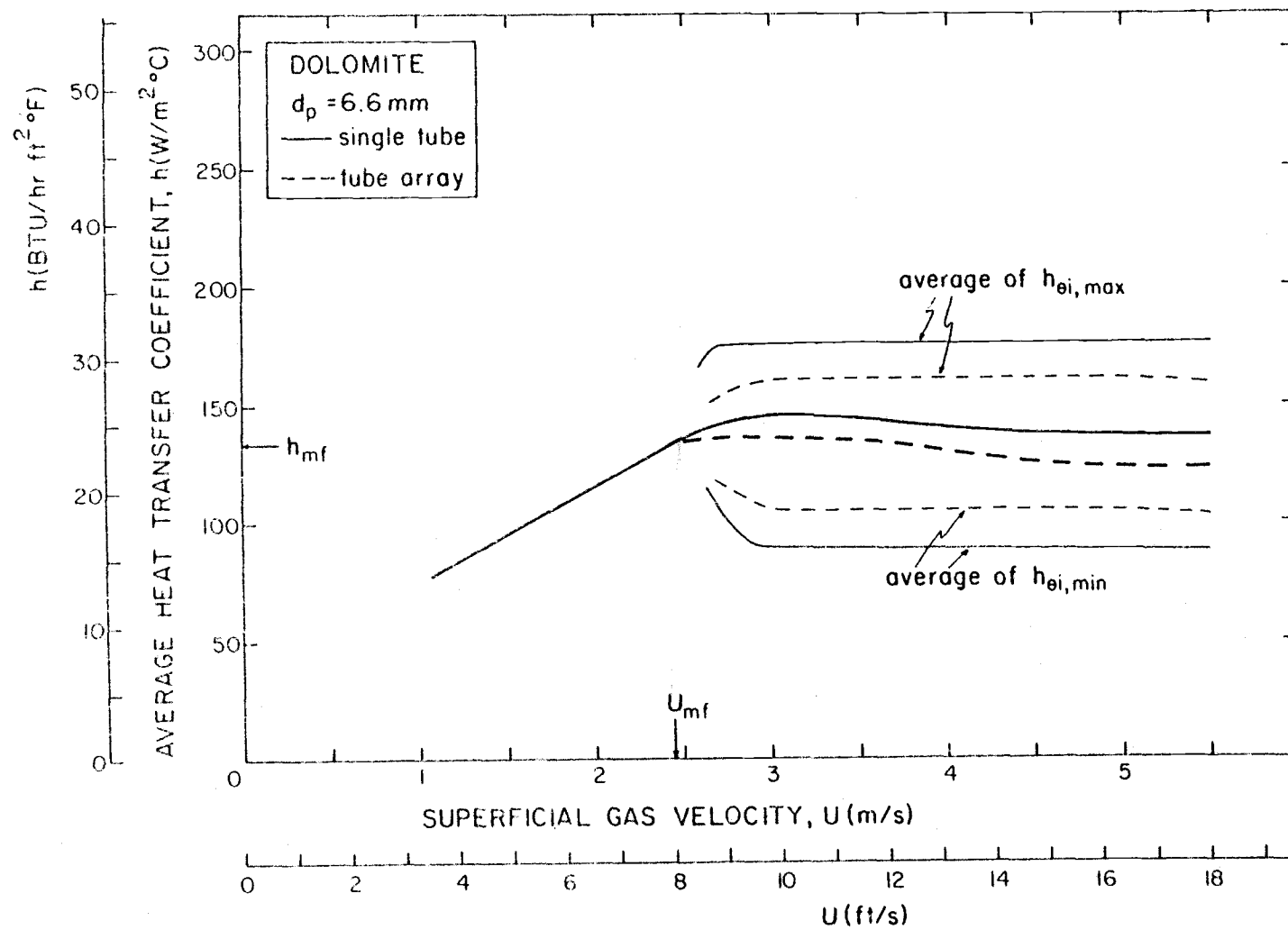


Figure 4. 16. Time-averaged overall heat transfer coefficient as a function of superficial gas velocity, for $d_p = 6.6 \text{ mm}$.

investigators interested in packed-bed heat transfer since local data of this sort are very scarce in literature.

Figures 4.3-4.16 establish that there is practically no influence of bed height on the heat transfer coefficient. This finding confirms similar observations made by McLaren and Williams [64] and Canada and McLaughlin [23] for only one or two particle sizes. It is significant from an economic standpoint since a relatively shallow bed may be used with substantial savings in blower operating costs, due to the lower bed pressure drop.

From a practical standpoint, our tube array and the single tube represent extremes corresponding to the minimum recommended and the maximum tube spacing, respectively. However, the difference in the heat transfer coefficients for these two cases is not very significant. Time-averaged local coefficients never differ by more than 20%, while the time-averaged overall coefficients are always within 12% of each other (the overall coefficient for the single tube being higher than the value for the bundle, at the same superficial velocity). This finding extends previous conclusions by Gelperin et al. [43], Lese and Kermode [59], and Bartel and Genetti [9], which applied to overall coefficients only and to particles significantly smaller than ours. It suggests that single-tube studies can be useful for predicting heat transfer to staggered bundles of tubes which are not spaced much closer than a pitch/diameter ratio of 2.¹

¹The differences between the two cases can be partially accounted for, at least qualitatively, by the increased gas velocity in the bed due to the presence of the array.

Instantaneous Coefficients

In general, the maximum and minimum instantaneous local coefficients tend to reach limiting values and level off at velocities not much in excess of U_{mf} . The same is then true for their respective averages calculated from equations (4.4) and (4.5). Figures 4.3-4.16 essentially show that the limiting values are attained as soon as there is sufficient movement and replacement of particles at the tube surface. The relatively constant values of $h_{\theta i, \max}$ and $h_{i, \max}$ suggest that the maximum heat transfer to (or from) the emulsion phase is independent of the superficial gas velocity.² The similar trend in values of $h_{\theta i, \min}$ and $h_{i, \min}$ suggests that heat transfer to the bubble phase is also independent of U . Once these limiting values are reached, the changes in the time-averaged coefficients with gas velocity are due only to changes in the fractions of time that each phase spends at the surface and the corresponding residence times.

The maximum and minimum instantaneous values are drastically affected by the particle diameter. Figure 4.17 illustrates the differences for the case in which particle size changes by an order of magnitude ($d_p = 0.37$ and 4.0 mm). Values shown were obtained at velocities where particle movement had reached a vigorous level (same excess gas velocity for both particle sizes, $U - U_{mf} = 0.6$ m/s). The amplitude of oscillations between minimum and maximum is much larger for a small particle than a coarser one. The use of finer particles could therefore cause a worrisome amount

²This finding seems to support the commonly used two-phase theory of fluidization [31, 82], according to which the gas velocity in the emulsion phase equals the interstitial gas velocity at minimum fluidization.

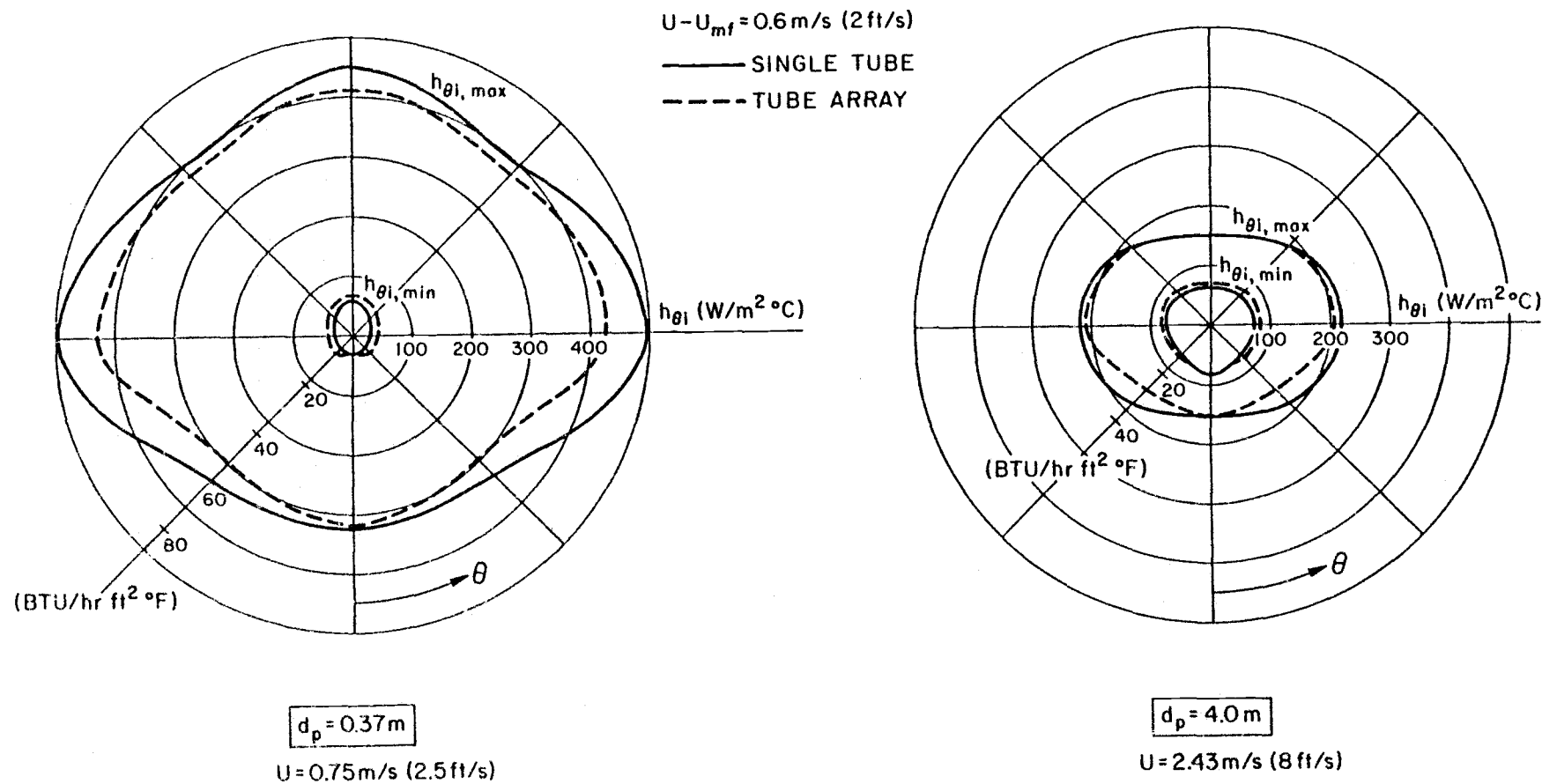


Figure 4. 17. Maximum and minimum instantaneous local heat transfer coefficients for $d_p = 0.37$ and 4.0 mm , at $U - U_{mf} = 0.6 \text{ m/s}$.

of thermal cycling in the tube material of actual fluid-bed combustors.³

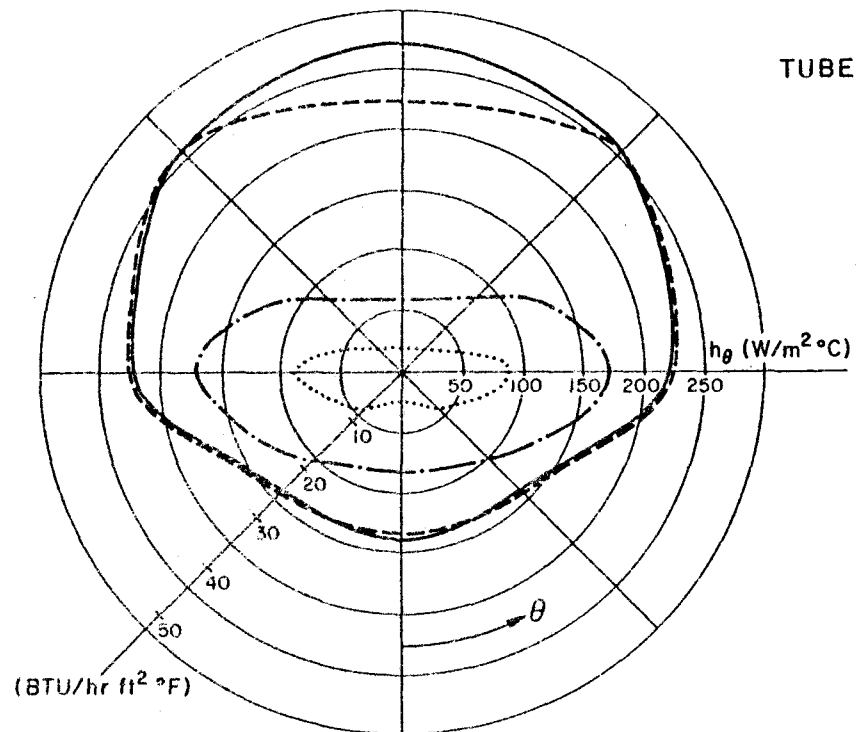
The presence of the tube bundle affects the instantaneous coefficients in such a way that the amplitude of oscillations is somewhat (but not drastically) reduced. This seems to be a direct result of the reduction in bubble size and the increase in the uniformity of bubbling, which are characteristic for the array. Thus, the use of a relatively well-packed array brings some advantage from the aspect of possible thermal cycling and fatigue in tubes.

It is important to note that the minimum instantaneous coefficient rises steadily with particle size. In fine particle beds, heat transfer coefficients essentially drop to zero when bubbles envelop the surface [66], and practically all models used to date [19] have neglected the contribution of bubbles to the heat exchange process. However, for intermediate and large particles, our data clearly indicate that the bubble contribution comprises a significant portion of the total coefficient and that the assumption of negligible heat transfer to (from) bubbles is incorrect.

Time-Averaged Local Coefficients

Figures 4.3, 4.5, 4.7, 4.9, 4.11, 4.13, and 4.15 indicate that the local coefficient at a particular angular position is influenced by particle size and gas velocity. Under certain conditions, there are dramatic differences between coefficients along the tube circumference. Figure 4.18 gives an illustration of these findings by comparing local coefficients for 0.37 and 4.0 mm particles, at U_{mf} and

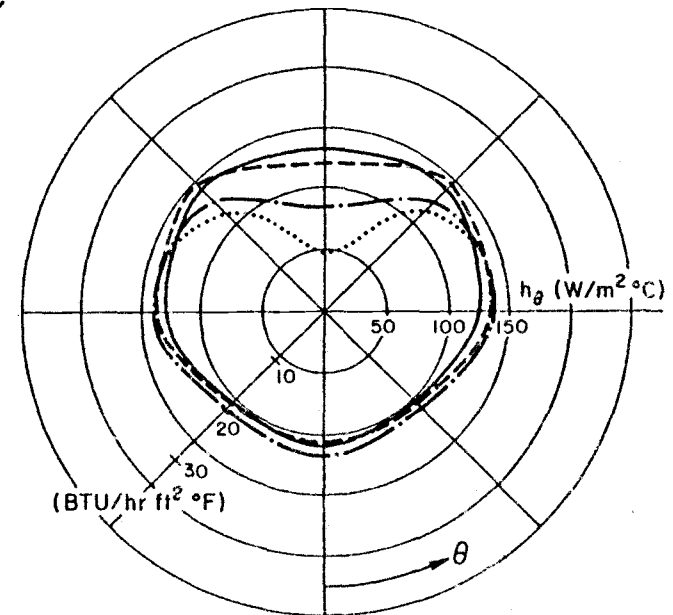
³On the other hand, finer particles do give higher time-averaged coefficients than larger ones (compare, for example, Figures 4.3 and 4.4 with 4.13 and 4.14).



$d_p = 0.37 \text{ mm}$

- $U/U_{mf} = 1.0$
- · — $U/U_{mf} = 1.1$
- $U/U_{mf} = 2.0$
- $U/U_{mf} = 5.0$

TUBE ARRAY



$d_p = 4.0 \text{ mm}$

- $U/U_{mf} = 1.0$
- · — $U/U_{mf} = 1.03$
- $U/U_{mf} = 1.5$
- $U/U_{mf} = 2.5$

Figure 4. 18. Time-averaged local heat transfer coefficients for $d_p = 0.37$ and 4.0 mm , at several values of U/U_{mf} .

low, intermediate, and high fluidizing velocities (similar comparisons can be made and trends followed for any two particle sizes by analyzing the above graphs).

In general, local coefficients are much more affected by velocity changes when small particles are fluidized. The change in the distribution of h_θ from U_{mf} to $2U_{mf}$ for the case of 0.37 mm particles is spectacular, while the corresponding change for $d_p = 4.0$ mm would pass as unnoticeable were it not for the variation at the 180° position.

The differences between individual coefficients around the tube circumference, at a given ratio of U/U_{mf} , are significant at lower flow rates. With an increase in the gas velocity the distribution tends to become relatively uniform, especially for large particles. Thus, higher velocities and larger particle diameters should be favored from the standpoint of thermal stresses in tubes.

Local coefficients at the top of the tube are obviously affected the most. This behavior is related to the formation of a stagnant cap of particles around the 180° position. The existence of this "lee stack" has been observed by Glass and Harrison [48] and Lese and Kermode [59] in fine-particle beds. We found the stack present at low velocities regardless of the particle size. However, when large particles were fluidized the stack became mobile at values of U/U_{mf} only slightly in excess of 1, while in the case of $d_p = 0.37$ mm it took a velocity equivalent to U/U_{mf} of 2 to "knock" the stack off with regularity. A large amount of corrosion noticed on top of actual fluid-bed combustor tubes at lower gas velocities [79] can be attributed to an immobile lee stack and its low heat transfer coefficient. The low coefficient causes local overheating and a consequent sulphur attack on the tube material.

The maximum local coefficient occurs at the sides of the tube when velocities are low, and at the top when the gas flow is increased (an indication that the lee stack is moving). Our distributions for h_θ for smaller particles (Figure 4.18) agree qualitatively with previous studies done in the fine-particle region [16, 42, 45], while the data on h_θ shown for the larger particles are, to our knowledge, the first of its kind.⁴

Further clues for explaining the differences in local heat transfer coefficients will come from the local capacitance data.

Time-Averaged Overall Coefficients

The significance of overall coefficients from a design standpoint has already been emphasized. A better insight into the data presented in Figures 4.4, 4.6, 4.8, 4.10, 4.12, 4.14, and 4.16 can be obtained by plotting all coefficients on the same graph, as is done in Figure 4.19. The results for both the single tube and the array are presented; however, for the sake of graphical clarity, the array data are plotted only for the region containing the maximum coefficient. Heat transfer coefficients at minimum fluidization, h_{mf} , are clearly indicated. We see that for the smallest particles the increase in the fluid-bed coefficient relative to h_{mf} is very pronounced, while in the case of the coarsest particles the corresponding rise is negligible. These changes are illustrated somewhat differently in Figures 4.20

⁴Cherrington et al. [28] did present some data for 1 mm limestone particles; however, the temperature of their heat transfer measuring element was quite different from the tube temperature, and a considerable error was thus introduced (see discussion in Section III.A). Their resulting overall coefficients are 100% higher than either ours or those measured by Canada et al. [23] for the corresponding particle size.

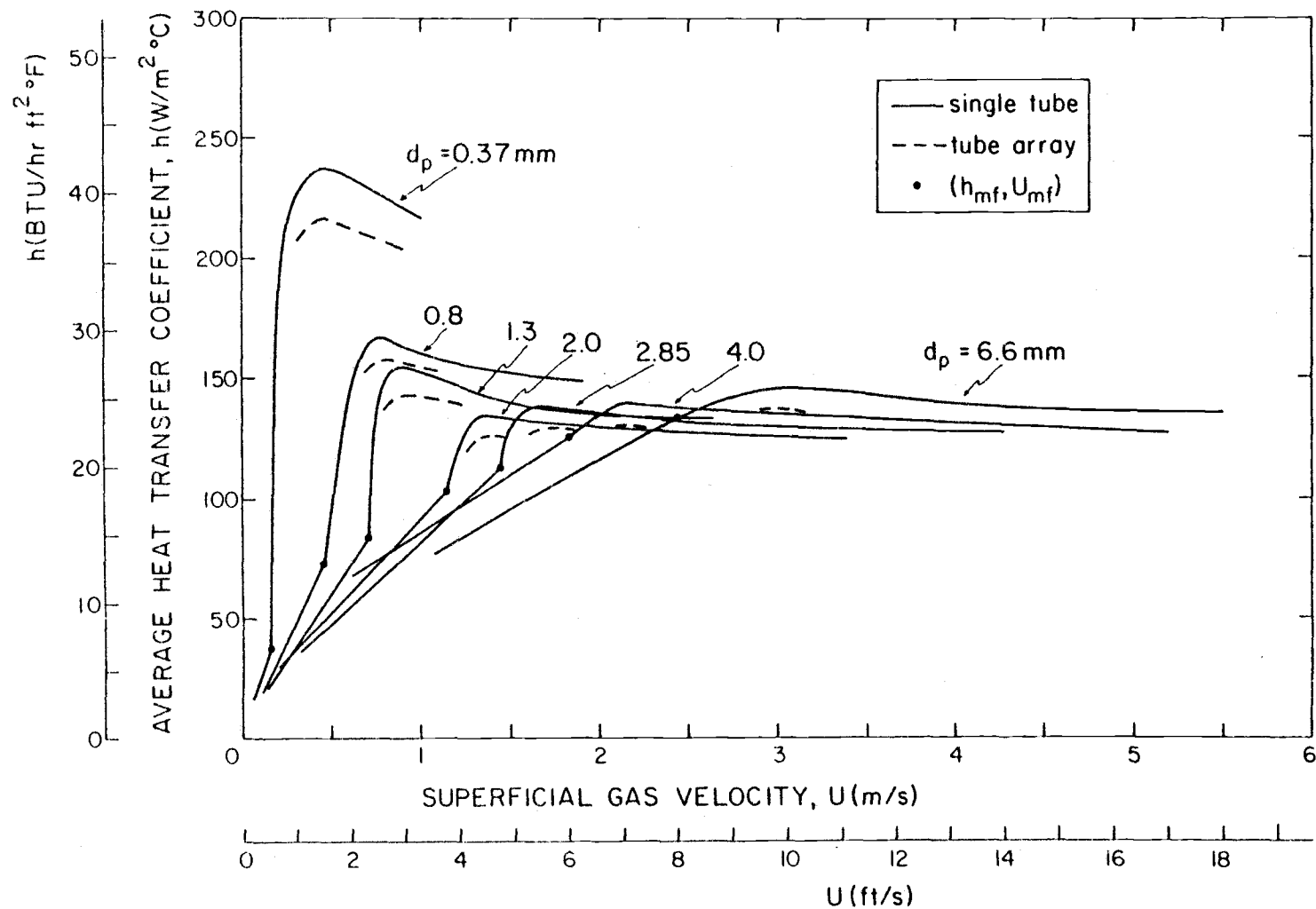


Figure 4.19. Time-averaged overall heat transfer coefficients for all particle sizes used, as functions of superficial gas velocity.

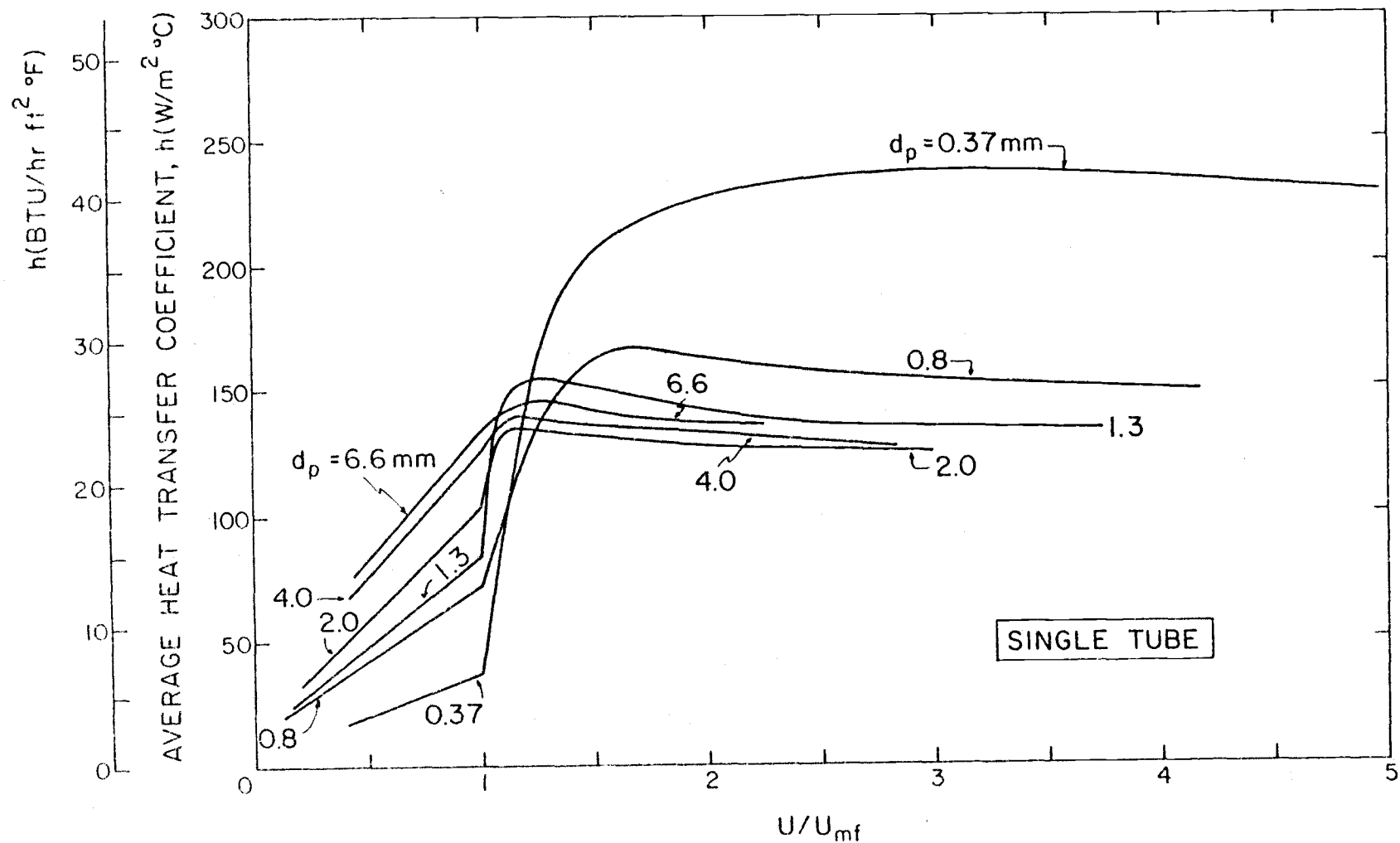


Figure 4.20. Time-averaged overall heat transfer coefficients for all particle sizes used, as functions of U/U_{mf} --single tube case.

(single tube) and 4.21 (array), where h is plotted as a function of U/U_{mf} . The maximum value of the ratio h/h_{mf} decreases from 6.33 (single tube) and 6.15 (array) for 0.37 mm particles to 1.09 and 1.03, respectively, for the 6.6 mm material. The shift is due to the increasing contribution of the gas convective mode in the heat transfer process and will be explained theoretically in subsequent chapters. Figure 4.22 shows the relationship between the maximum coefficient obtainable in the bed and particle size. The coefficient decreases with particle size for diameters smaller than 2 mm, but starts increasing again for larger particles. This resembles the trend observed for beds with an immersed vertical tube (Baskakov et al. [12], Denloye and Botterill [32]); however, our minimum in h_{max} occurs at a different value of d_p due to different tube orientation and operating conditions.

C. Results from Capacitance Measurements

Graphical Presentation

Data obtained from the capacitance probes are a source of information about the local and overall behavior of the emulsion and bubble phases around immersed tubes. This kind of information provides valuable aid in explaining heat transfer results.

Figure 4.23 shows typical voltage signals from two capacitance probes (at $\theta = 135^\circ$ and 45° positions) and illustrates the procedure for obtaining quantities of interest. The half-way level between the packed bed limit and the air limit is selected as the boundary for distinguishing between emulsion packets and bubbles. The individual emulsion and bubble residence times are counted over the full data-collecting period of 150 seconds. The average local

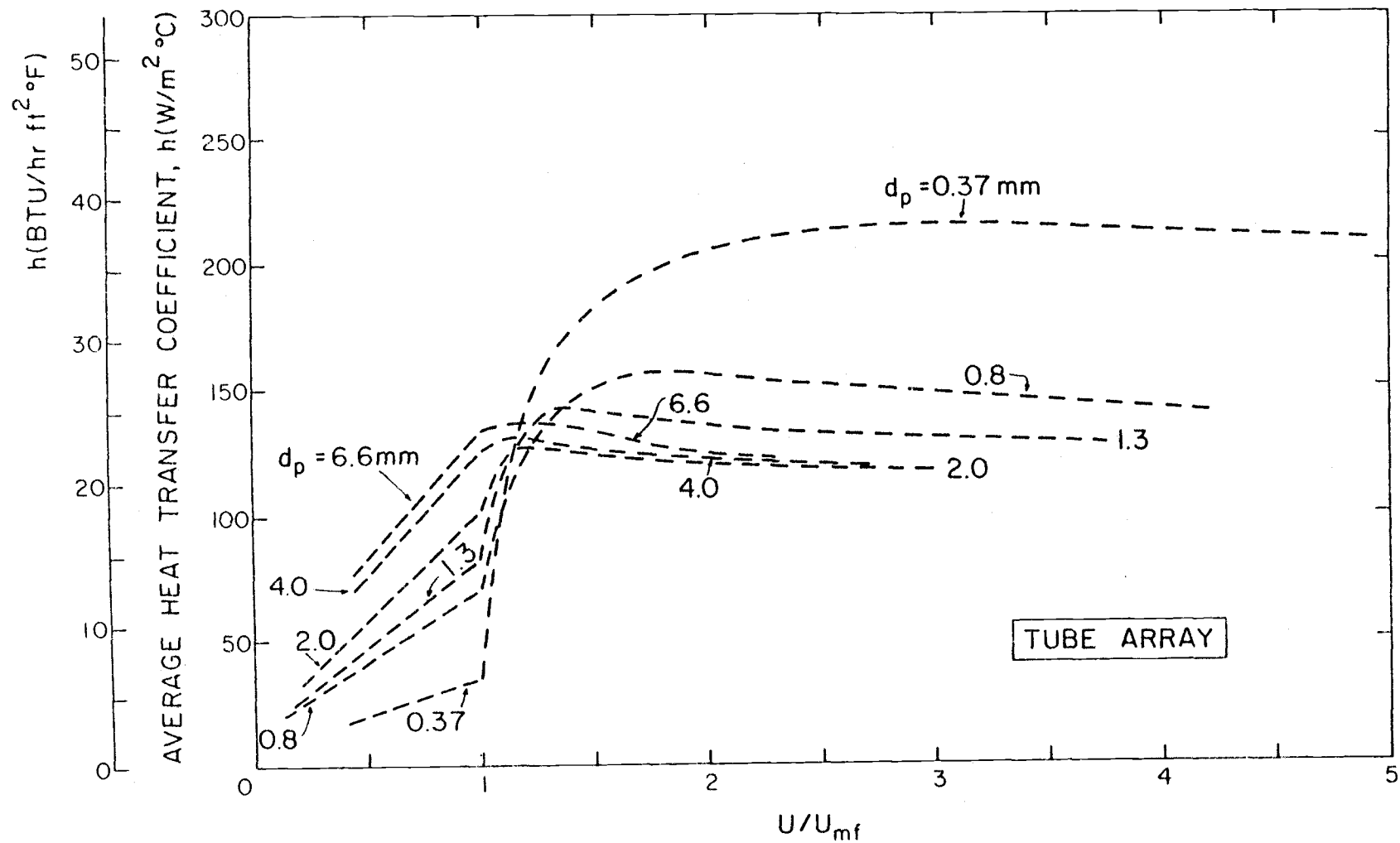


Figure 4.21. Time-averaged overall heat transfer coefficients for all particle sizes used, as functions of U/U_{mf} ---tube array case.

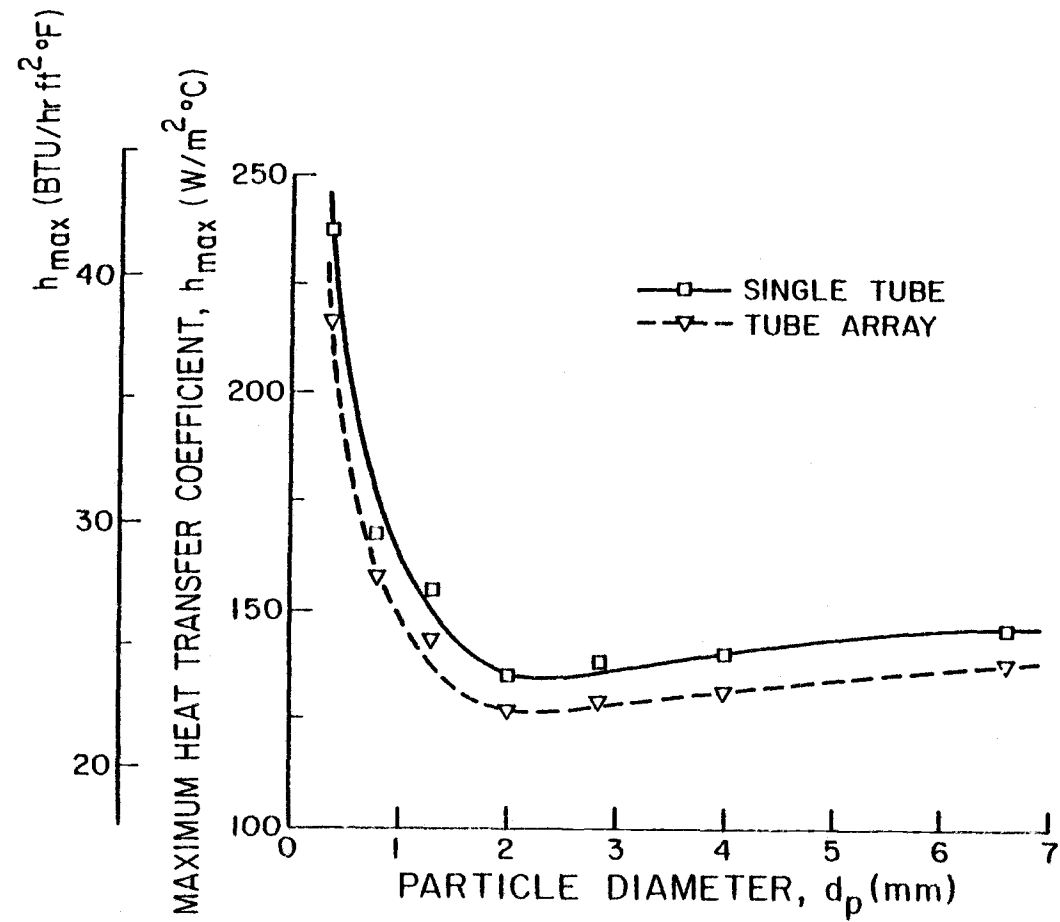
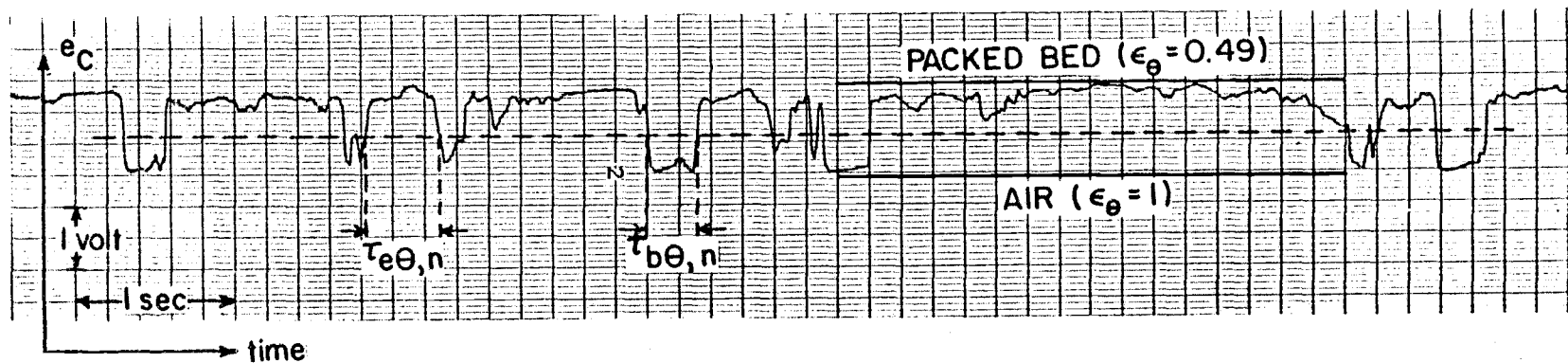
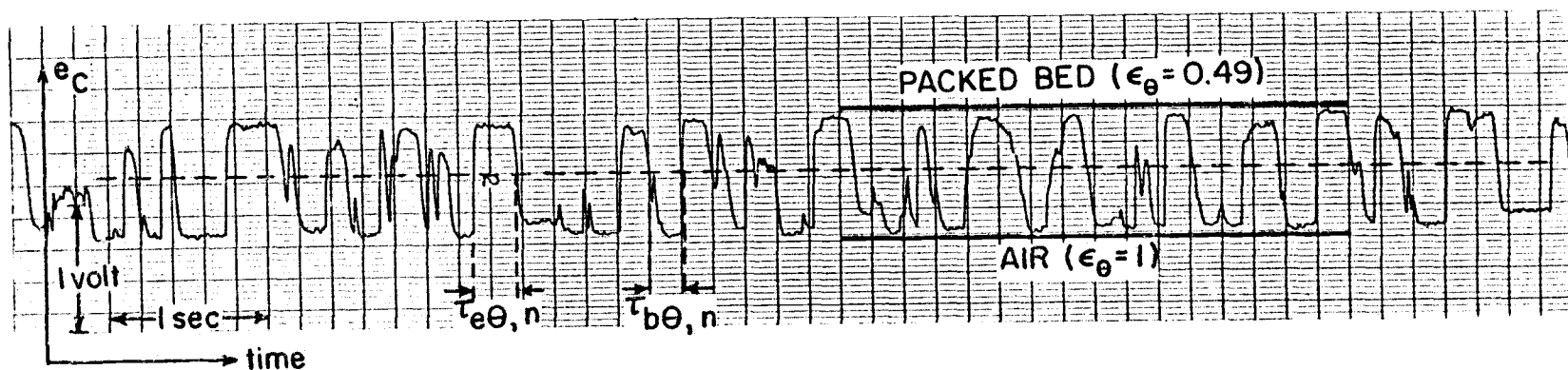


Figure 4.22. Maximum time-averaged overall heat transfer coefficient as a function of particle size.



$$d_p = 0.37 \text{ mm}, U = 0.4 \text{ m/s}, \theta = 135^\circ$$



$$d_p = 0.37 \text{ mm}, U = 0.4 \text{ m/s}, \theta = 45^\circ$$

Figure 4.23. Typical signals from capacitance probes, with local emulsion and bubble residence times indicated.

emulsion residence time is calculated from

$$\bar{\tau}_{e\theta} = \frac{1}{N} \sum_{n=1}^N \tau_{e\theta, n} \quad (4.6)$$

where N is the number of times that an emulsion packet contacts the probe. Similarly, the average local bubble residence time is

$$\bar{\tau}_{b\theta} = \frac{1}{N} \sum_{n=1}^N \tau_{b\theta, n} \quad (4.7)$$

(it should be noted that the method of estimating $\tau_{e\theta, n}$ and $\tau_{b\theta, n}$ could result in a slight overprediction of the average residence times).

The average values can now be used to calculate the fraction of time which the surface spends in contact with the emulsion:

$$(1-f_o)_\theta = \frac{\bar{\tau}_{e\theta}}{\bar{\tau}_{e\theta} + \bar{\tau}_{b\theta}} \quad (4.8)$$

The local frequency of replacement, usually referred to as the bubble frequency, is obtained from

$$n_\theta = \frac{(1-f_o)_\theta}{\bar{\tau}_{e\theta}} \quad (4.9)$$

Since the capacitance signal does not drift with time and since the response of the capacitance circuit (described in Section III. A and Appendix F) is approximately linear, the signals in Figure 4.23 can be used for the calculation of time-averaged local voidage. The value of ϵ_θ is obtained by linear interpolation between the packed bed and air limits.

As in the case of the heat transfer coefficients, local values for each of the described quantities can be used to calculate the

time-averaged value for the whole tube (see equation (4.3)). Thus, for example, the overall average emulsion residence time is

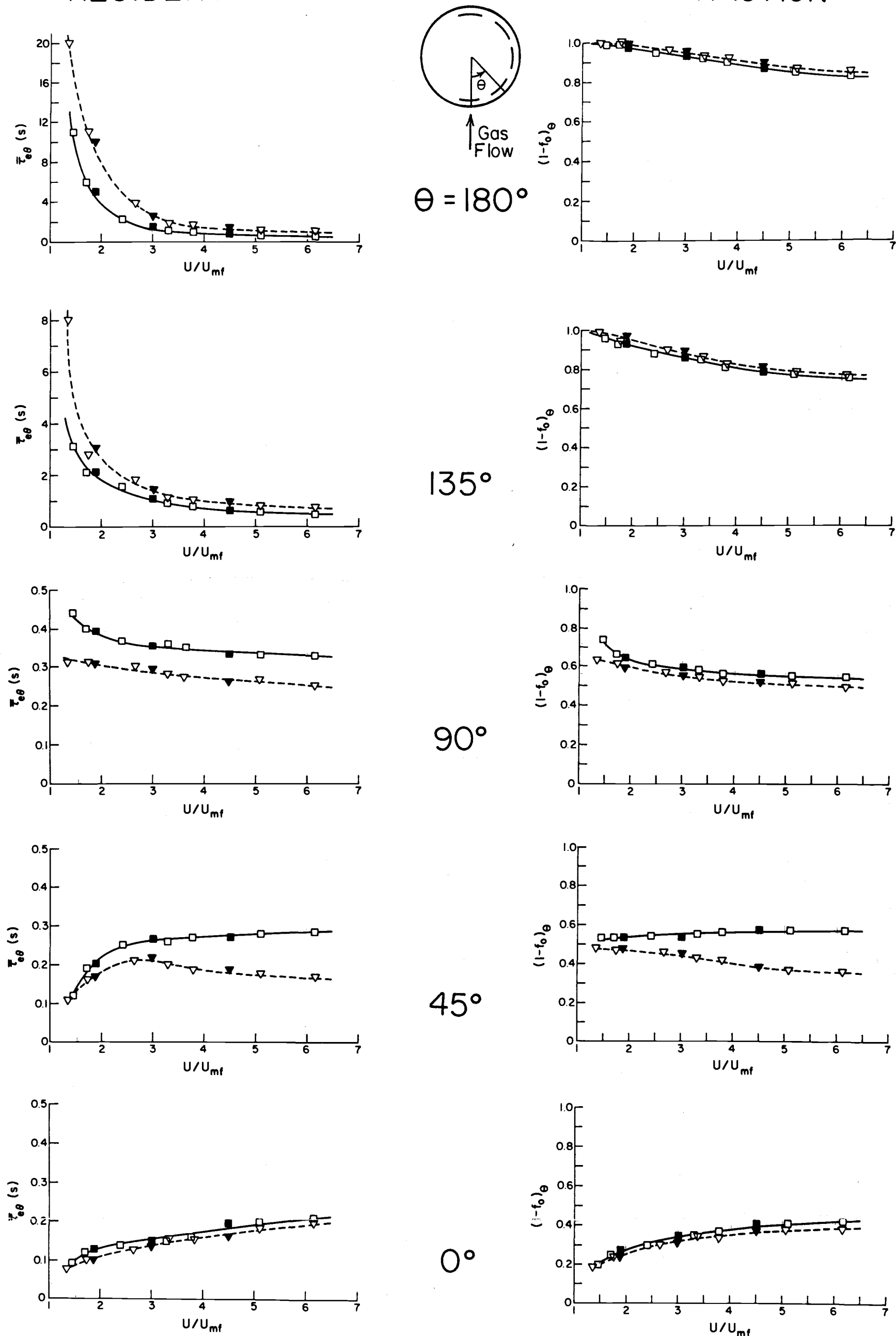
$$\bar{\tau}_e = \frac{\bar{\tau}_{e180^\circ} + 2\bar{\tau}_{e135^\circ} + 2\bar{\tau}_{e90^\circ} + 2\bar{\tau}_{e45^\circ} + \bar{\tau}_{e0^\circ}}{8} \quad (4.10)$$

For a particular location on the circumference of the instrumented cylinder, information about the quantities in question can be obtained from either or both of the capacitance probes and/or the nearest two pressure ports. The results which follow were obtained by averaging the data from both capacitance probes and were confirmed by calculations based on the pressure signals. In order to condense the graphical presentation of experimental results, we chose three particle sizes-- $d_p = 0.37, 1.3, \text{ and } 4.0 \text{ mm}$ --which are representative for the groups of smaller, intermediate, and larger diameters used in our study. Only results on emulsion residence times and contact fractions are presented since they represent quantities of particular interest for later theoretical treatment. The corresponding values of bubble residence times, contact fractions, and frequencies can be easily extracted from the graphs. Voidage results are not presented since they are only occasionally used in the text (specific values will be mentioned where necessary).

Figures 4.24, 4.25, and 4.26 present the average local emulsion residence times and local emulsion contact fractions for each of the representative particle sizes. Values for all five locations on the tube are shown as functions of the ratio U/U_{mf} . Full lines indicate single tube results, while broken lines connect the points obtained from array experiments. Figure 4.27 gives the overall average emulsion residence times for all three particle diameters. Similarly, Figure 4.28 shows the overall fraction of time which the tube spends in contact with the emulsion. From these figures, corresponding

AVERAGE EMULSION RESIDENCE TIME

EMULSION CONTACT FRACTION



SAND
 $d_p = 0.37 \text{ mm}$
 $U_{mf} = 0.15 \text{ m/s}$

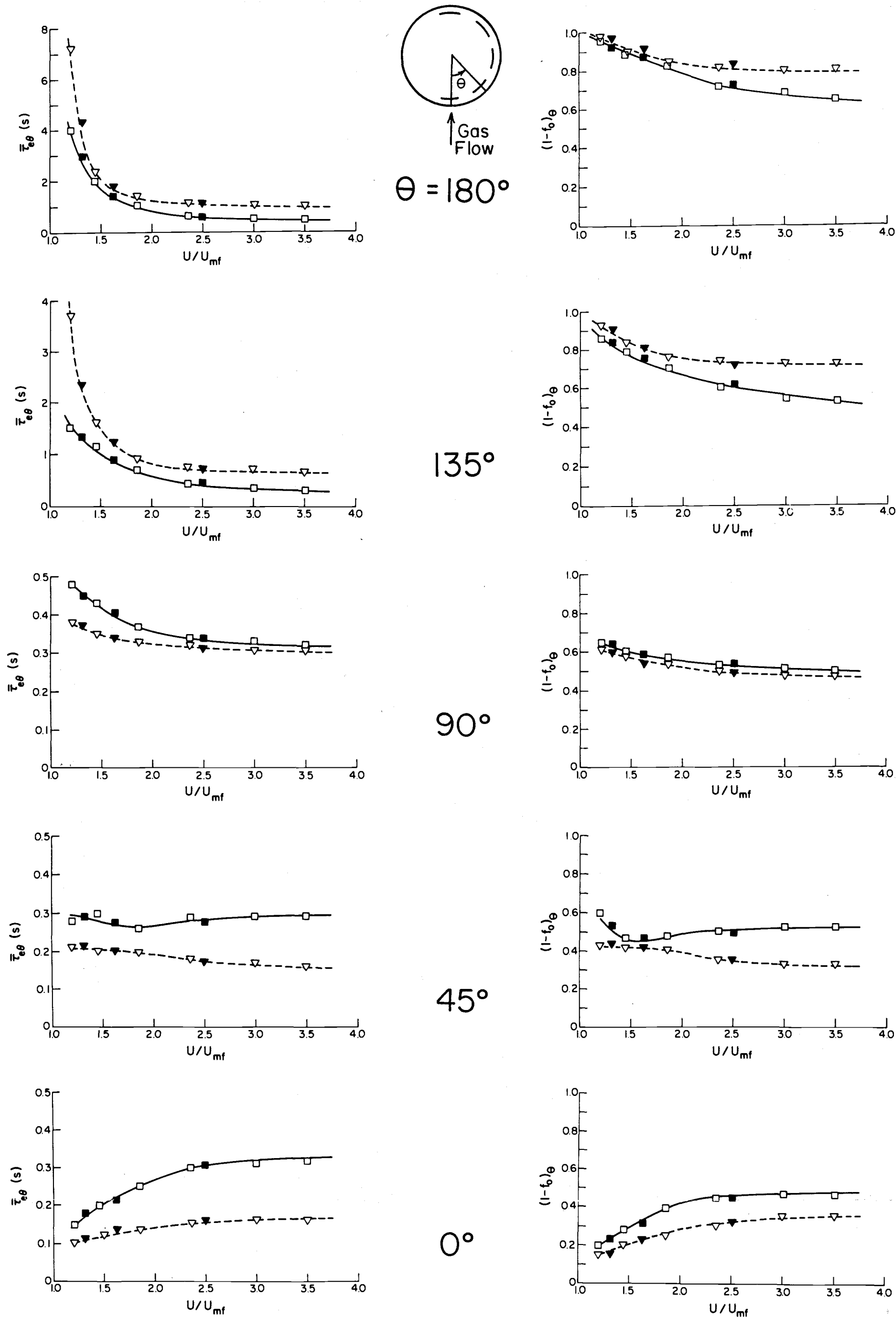
SINGLE TUBE TUBE ARRAY

—□— $H_0 = 0.46 \text{ m}$ --▽--
 —■— $H_0 = 0.71 \text{ m}$ --▼--

Figure 4.24. Average local emulsion residence times and local emulsion contact fractions as functions of U/U_{mf} , for $d_p = 0.37 \text{ mm}$.

AVERAGE EMULSION RESIDENCE TIME

EMULSION CONTACT FRACTION



SAND
 $d_p = 1.3 \text{ mm}$
 $U_{mf} = 0.70 \text{ m/s}$

SINGLE TUBE TUBE ARRAY

—□— $H_0 = 0.46 \text{ m}$ --▽--
—■— $H = 0.71 \text{ m}$ --▼--

Figure 4. 25. Average local emulsion residence times and local emulsion contact fractions as functions of U/U_{mf} , for $d_p = 1.3 \text{ mm}$.

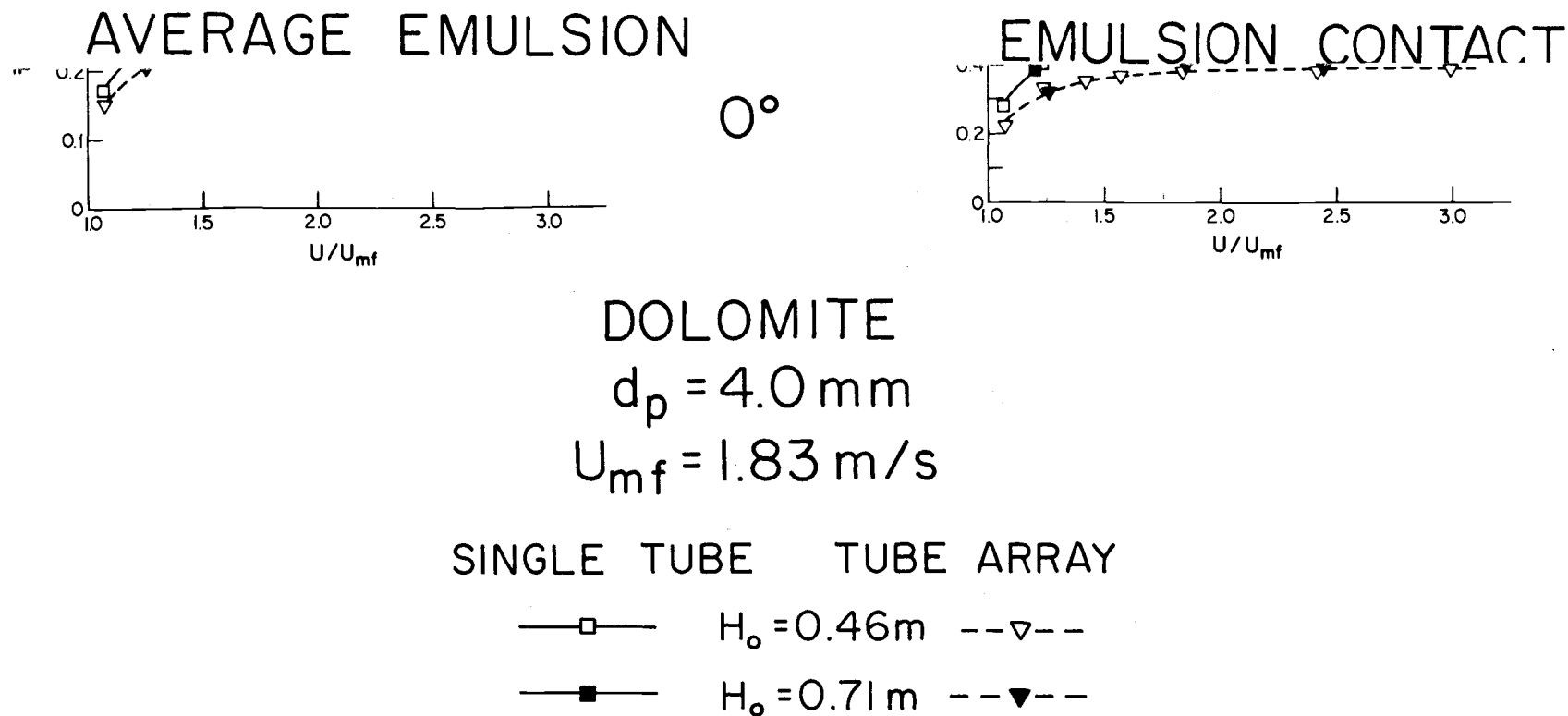


Figure 4.26. Average local emulsion residence times and local emulsion contact fractions as functions of U/U_{mf} , for $d_p = 4.0 \text{ mm}$.

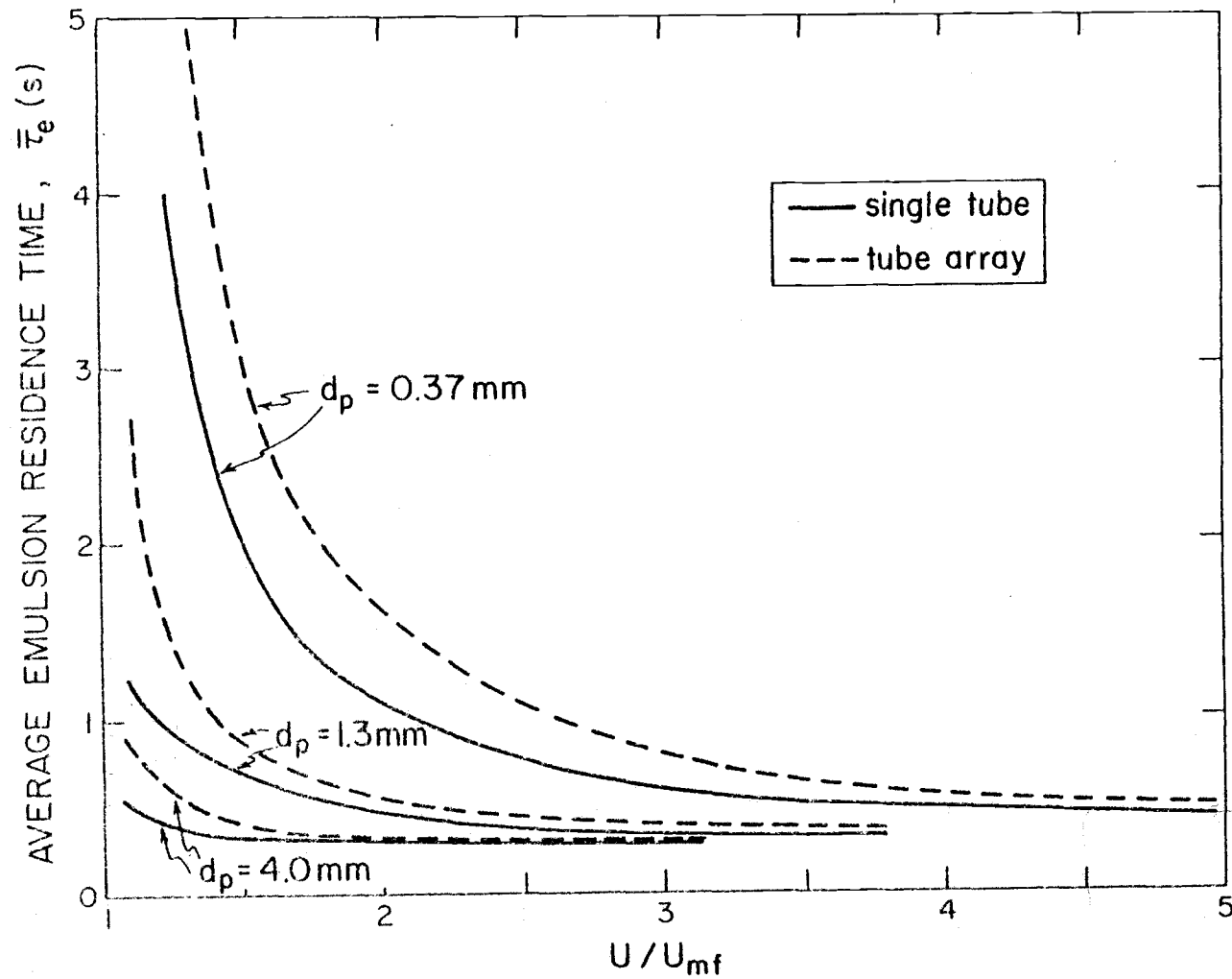


Figure 4.27. Overall average emulsion residence times for $d_p = 0.37$, 1.3 and 4.0 mm, as functions of U/U_{mf} .

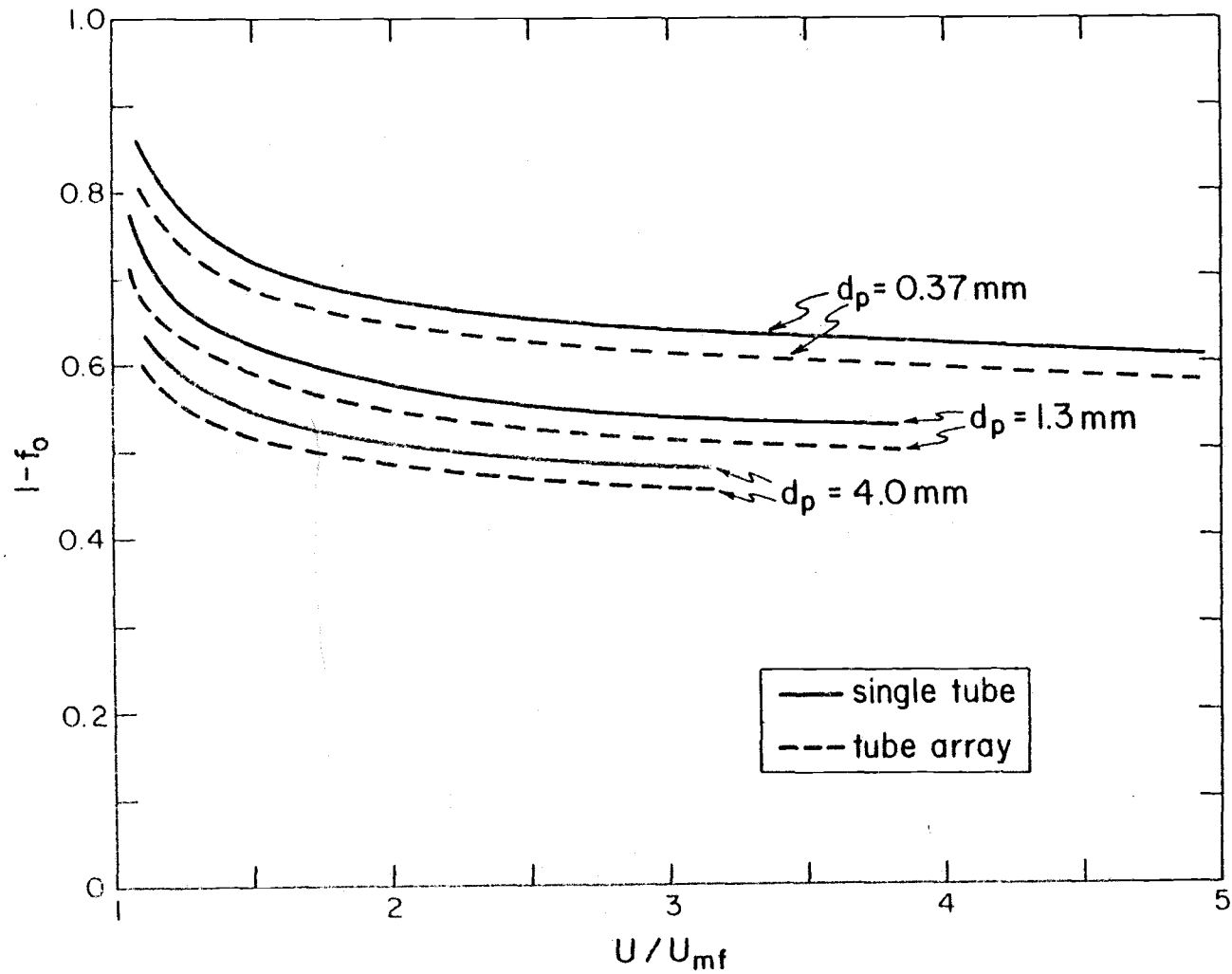


Figure 4.28. Overall emulsion contact fractions (fractions of time which tube spends in contact with emulsion) for $d_p = 0.37, 1.3$, and 4.0 mm, as functions of U/U_{mf} .

results for other particle sizes can be interpolated with ease. The information presented will be very valuable in the later modeling of heat transfer; however, as in Section B, comments and comparisons are called for at this stage.

General Comments

The data obtained from capacitance probes are closely tied to the heat transfer results presented in Section B. Emulsion residence times indicate the duration of the corresponding high instantaneous heat transfer coefficients, while the bubble residence times show how long the low instantaneous heat transfer lasts. Contact fractions give an indication of the respective contributions of the low and high instantaneous values to the time-averaged heat transfer coefficient. These data, together with the corresponding bubble frequencies, fully characterized the duty cycle of the heat transfer oscillations.

As in the case of heat transfer, there is no difference in the behavior of the emulsion or bubble phases for the two bed heights used.

When compared to the single tube case, the presence of the array seems to affect local behavior to a certain degree. At some angular positions this effect is pronounced; at other locations it is almost negligible. The effect on the average emulsion residence time for the whole tube (Figure 4.27) is noticeable only at low multiples of U_{mf} , while the difference in the overall emulsion contact fraction (Figure 4.28) between the two cases never exceeds 7%. Thus the results on the overall behavior confirm the heat transfer findings.

Local Behavior

Similarly to the procedure in the section on heat transfer, changes in local behavior with particle size and gas velocity (shown in Figures 4.24, 4.25, and 4.26) are best illustrated by an example, with the use of polar coordinates. Figure 4.29 shows the average local emulsion residence times for 0.37 and 4.0 mm particles, at three different multiples of U_{mf} . Figure 4.30 presents the corresponding values of local emulsion contact fractions.

As with the local heat transfer coefficients, $\bar{\tau}_{e\theta}$ and $(1-f_o)_\theta$ are more affected by velocity changes when small particles are fluidized. Increases in gas velocity tend to decrease the variations along the tube circumference. Emulsion behavior at the top of the tube is affected the most. At low velocities, the lee stack tends to spend a long time on the tube. The particles therefore get heated, which leads to a low local heat transfer coefficient.

It is interesting to compare the behavior of phases at the top and bottom of the tube. At the 180° position, the emulsion contact fraction is high and the residence time is long, indicating the presence of the lee stack. At this position, differences in behavior between small and large particles are most pronounced. For $d_p = 4.0$ mm the stack starts moving and spending less time on the tube at much lower multiples of U_{mf} . At the 0° position (lower stagnation point), the emulsion contact fraction is very low and the residence time short, indicating the presence of a void (air cushion). This cushion remains in one form or another even as velocity is increased, thus explaining the very slight changes in the corresponding heat transfer coefficients with particle size. At times, the air void also covers a portion of the 45° location. As velocity increases, particles seem to penetrate the cushion more and make contact with the heat transfer elements;

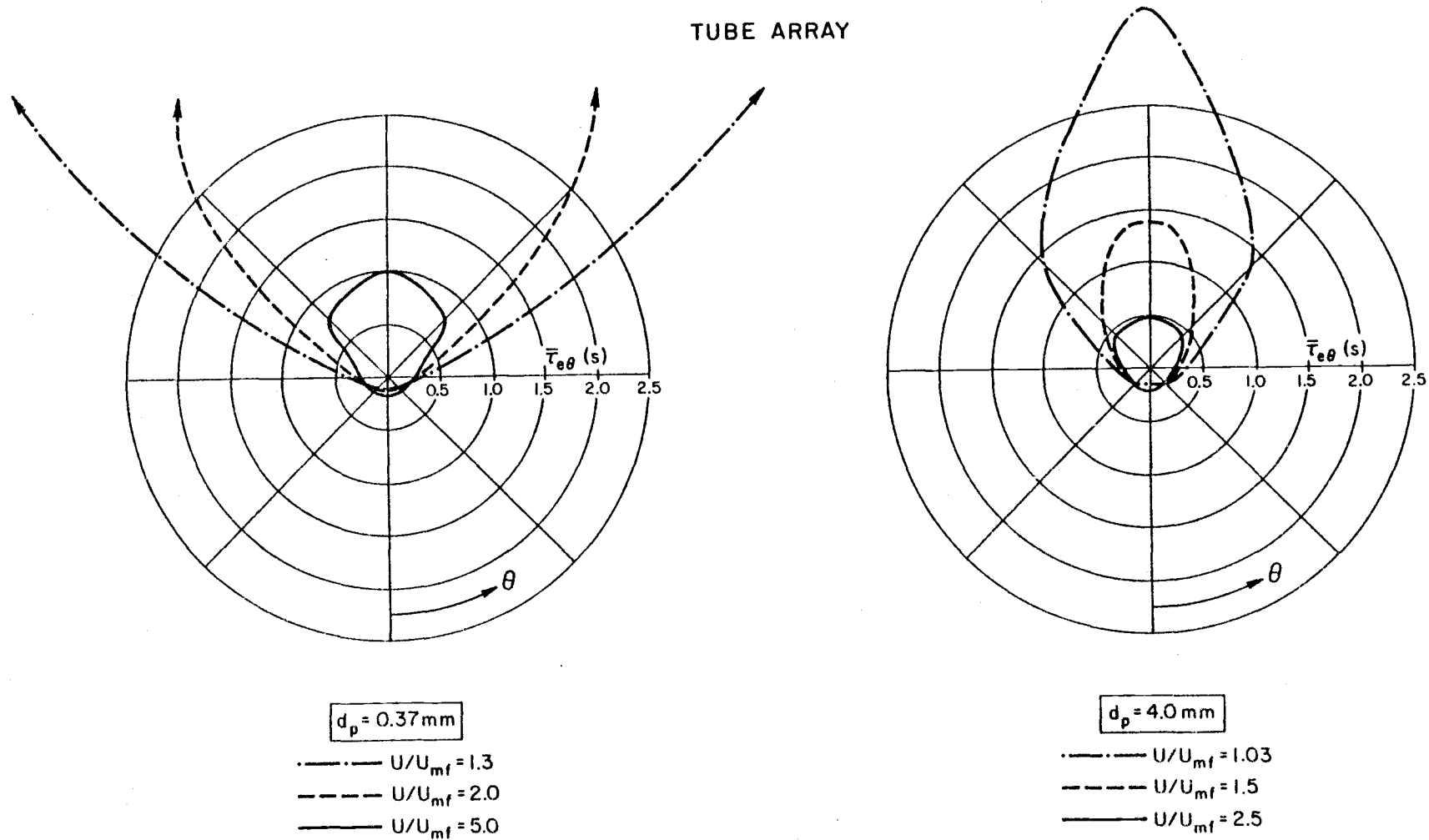
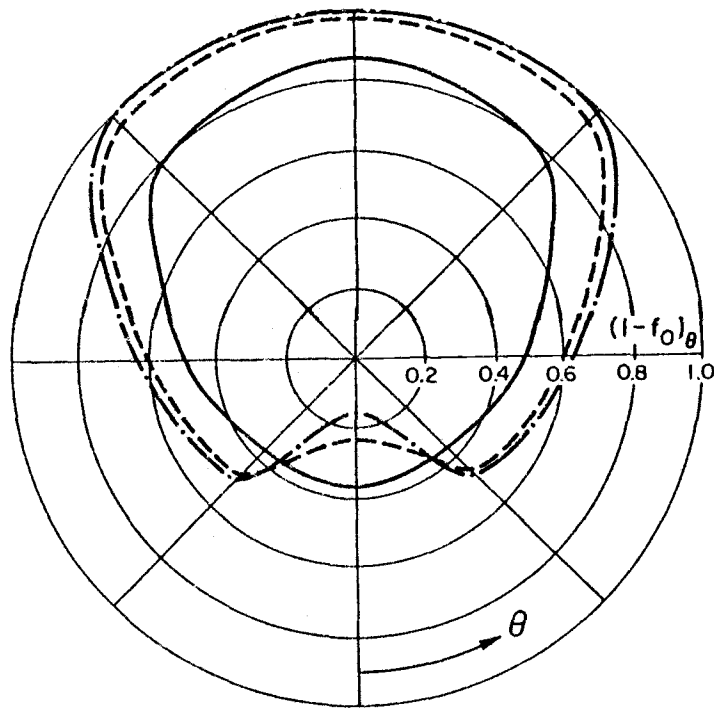


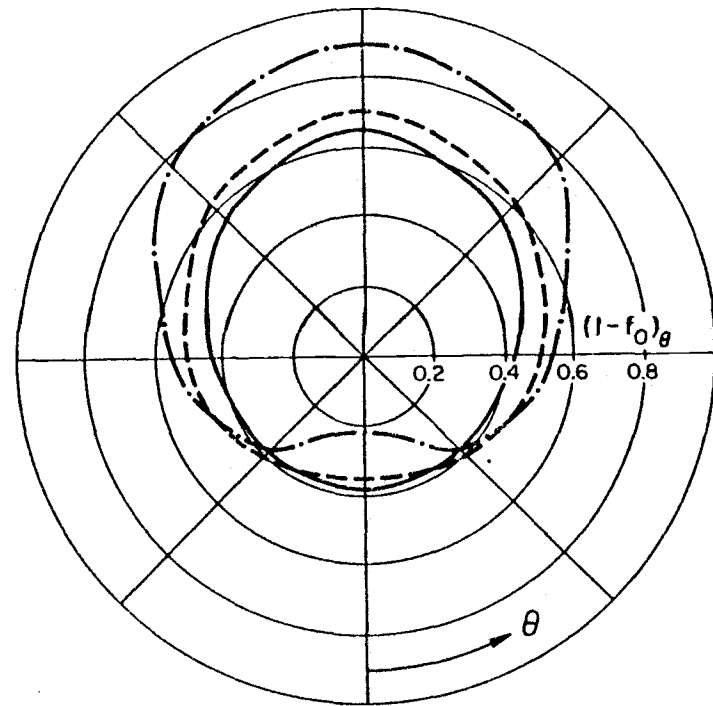
Figure 4. 29. Average local emulsion residence times for $d_p = 0.37$ and 4.0 mm , at several values of U/U_{mf} .

TUBE ARRAY



$d_p = 0.37 \text{ mm}$

— $U/U_{mf} = 1.3$
 - · - $U/U_{mf} = 2.0$
 - - - $U/U_{mf} = 5.0$



$d_p = 4.0 \text{ mm}$

— $U/U_{mf} = 1.03$
 - · - $U/U_{mf} = 1.5$
 - - - $U/U_{mf} = 2.5$

Figure 4.30. Local emulsion contact fractions for $d_p = 0.37$ and 4.0 mm , at several values of U/U_{mf} .

however, this contact is never in the form of dense packets, as indicated by the always relatively low $h_{\theta i, \max}$ at these locations. The local voidage, ϵ_{θ} , in the vicinity of the 0° position is in the range 0.93-0.83.

The local bubble frequency on the immersed tube surface can be calculated from the available data by using equation (4.9). It seems almost unaffected by particle size and, depending on the gas velocity, is in the range of 0-1.5 (180° position), 1.3-2.0 (90°), and 1.4-2.5 (45°). Bubble frequencies at similar heights in intermediate- and large-particle beds without internals have been reported as 0.9-2.0 [29].

Overall Behavior

The overall average emulsion residence times and contact fractions reflect the trends in the local values. Figure 4.27 indicates that, on the whole, finer particles spend more time at the tube surface than do coarser ones, with the differences becoming smaller as air velocity increases. Figure 4.28 shows that, for a particular particle size, the overall emulsion contact fraction--and therefore the voidage in the vicinity of the tube--does not change much after a relatively low value of U/U_{mf} is reached. As seen from Figure 4.30, when velocity is increased, $(1-f_o)_{180^{\circ}}$ goes down while $(1-f_o)_{0^{\circ}}$ goes up, thus offsetting each other and keeping $1-f_o$ practically unchanged. This is an interesting finding and will be elaborated in later development. At the moment, suffice it to say that it is this kind of information on the structural behavior in the vicinity of the tube that is necessary in explaining the accompanying heat transfer process.

D. Bed Expansion Results

All heat transfer models and correlations proposed to date use information on the overall bed expansion, in one form or another, to interpret changes in the heat transfer coefficient. We conducted a series of experiments, separate from the previous ones but under the same fluidizing conditions, to determine the bed expansion values which would correspond to the already presented heat transfer and local voidage data. The bed expansion ratio, H/H_0 , is obtained from pressure probe measurements as illustrated in Figure 4.31. From it, we obtain the volume fraction of bubbles in the bed, δ :

$$\delta = 1 - \frac{H_0}{H} \quad (4.11)$$

or the average bed voidage, ϵ :

$$\epsilon = 1 - \frac{H_0}{H} (1 - \epsilon_{mf}) \quad (4.12)$$

(see Kunii and Levenspiel [57]).

Figure 4.32 shows the average bed volume fraction for the emulsion phase, $1 - \delta$, as a function of U/U_{mf} for several of the particle sizes used. The individual data points, as well as a detailed analysis, are given by Jovanovic [54]. In short, there are very noticeable differences between data for the single tube and the array. The emulsion fraction levels off at 0.7-0.8 for high values of U/U_{mf} in the single tube case, while it rises steadily with gas velocity in the presence of the array.

Experimental data are compared with theoretical relations for beds of large and intermediate particles, which were recently developed by Bar-Cohen et al. [8]. The curve for stationary bubbles

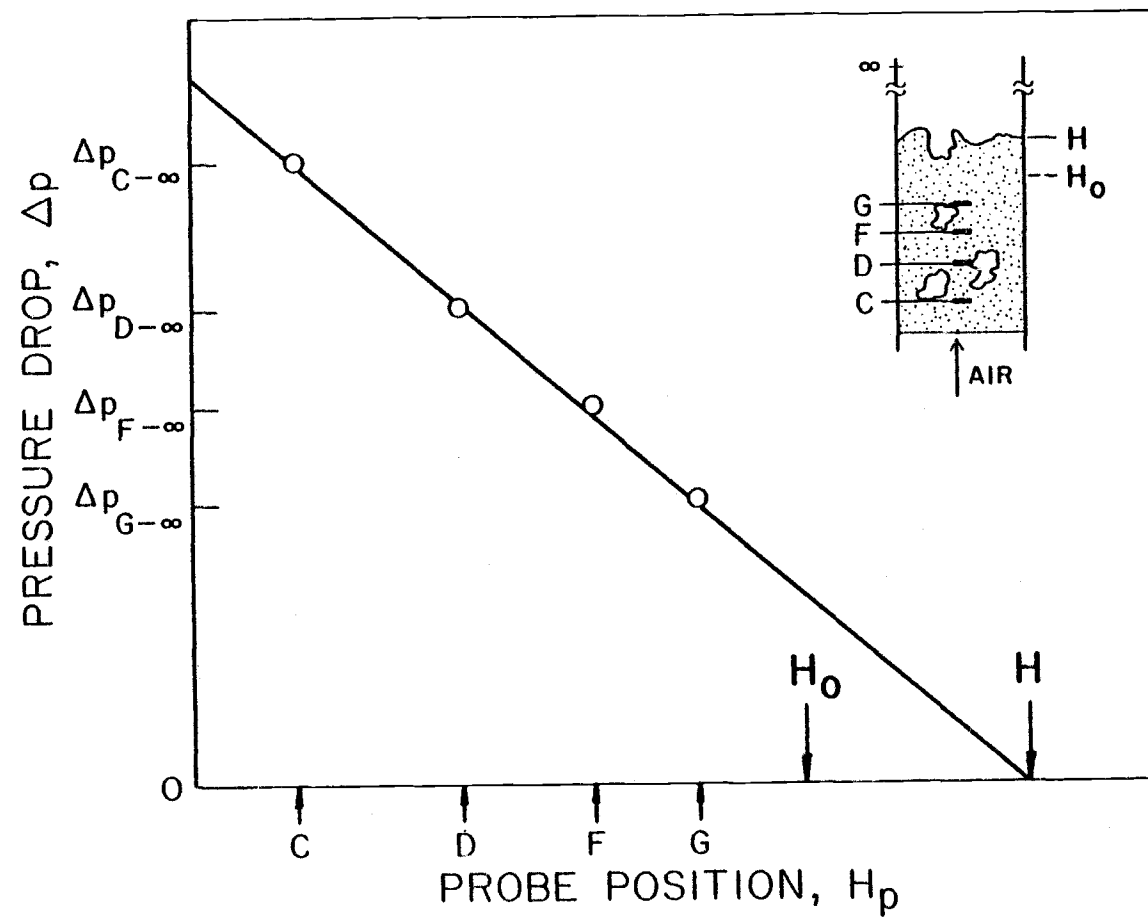


Figure 4.31. Calculation of bed expansion, H/H_0 , from pressure probe measurements.

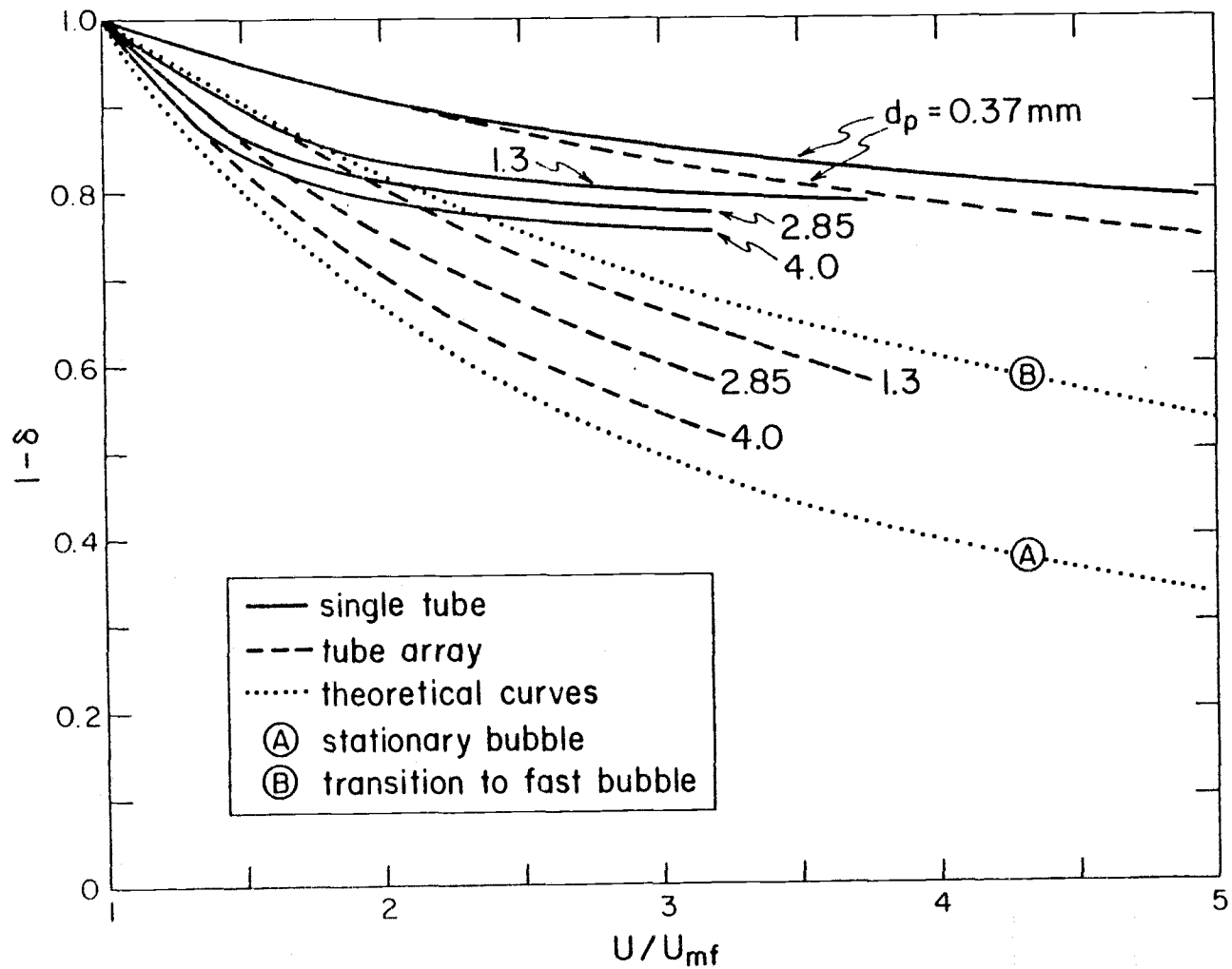


Figure 4.32. Average bed volume fraction for the emulsion phase, $1 - \delta$, as a function of U/U_{mf} .

(curve A)--an extreme for very large particles--is given by:

$$1 - \delta = \frac{2}{\frac{U}{U_{mf}} + 1} \quad (4.13)$$

while the transition curve between slow and fast bubbles (curve B)--roughly a boundary between large and fine particles--is represented by:

$$1 - \delta = \frac{2 + \frac{1}{\epsilon_{mf}}}{\frac{U}{U_{mf}} + 1 + \frac{1}{\epsilon_{mf}}} \quad (4.14)$$

with ϵ_{mf} taken as 0.43 for convenience. The only other data available for coarser-particle beds with immersed tubes--those of Canada et al. [25, 78] (obtained with special capacitance probes)--lie between curves A and B.

Although $1 - \delta$ is a space-averaged value and $1 - f_o$ represents a time-averaged quantity, to a first approximation the two are comparable. The important conclusion is that both theoretical predictions and experimental data point to the significant differences (in values as well as in trends) between the overall bed voidage (Figure 4.32) and the local voidage around a tube (Figure 4.28). Obviously, there is a discrepancy between the quantity used in heat transfer models and correlations and the actual quantity which is directly related to the heat exchange between the bed and immersed tubes.

V. HEAT TRANSFER NEAR MINIMUM FLUIDIZATION FOR LARGE PARTICLES: COMPARISON OF EXPERIMENTAL RESULTS WITH THE ADAMS ANALYTICAL MODEL

The following analysis will be devoted to a comparison of our data with a recently developed analytical model of heat transfer to a horizontal cylinder in beds of large particles. Only the single tube data obtained at gas velocities not significantly in excess of U_{mf} will be considered.

A. Regimes of Large-Particle Fluidization

Catipovic et al. [26] described regimes of fluidization for large particles ($d_p > 1 \text{ mm}$) and defined criteria for distinguishing between them in beds without tube arrays. For the case of our experiments with a single tube, Figure 5.1 illustrates these regimes and gives a qualitative map of their boundaries as a function of particle size and gas velocity.

At minimum fluidization the bed is essentially quiescent with only an occasional bubble generated at the side of the tube, as a result of the constriction in the vessel. With increasing gas flow rates, bubbles start forming regularly. As long as the velocity is not too much above U_{mf} , bubbles do not grow significantly in size and are called slow (they rise slower than the gas percolating through the emulsion). The rapidly growing bubble regime is reached at higher superficial velocities when the bubble grows as fast as it rises. If deep beds are used, rapidly growing bubbles turn into slugs. At very high velocities there is a transition to the turbulent regime in which large gas voids are absent.⁵

⁵ Fast bubbles are characteristic for fine particle beds and are not considered here.

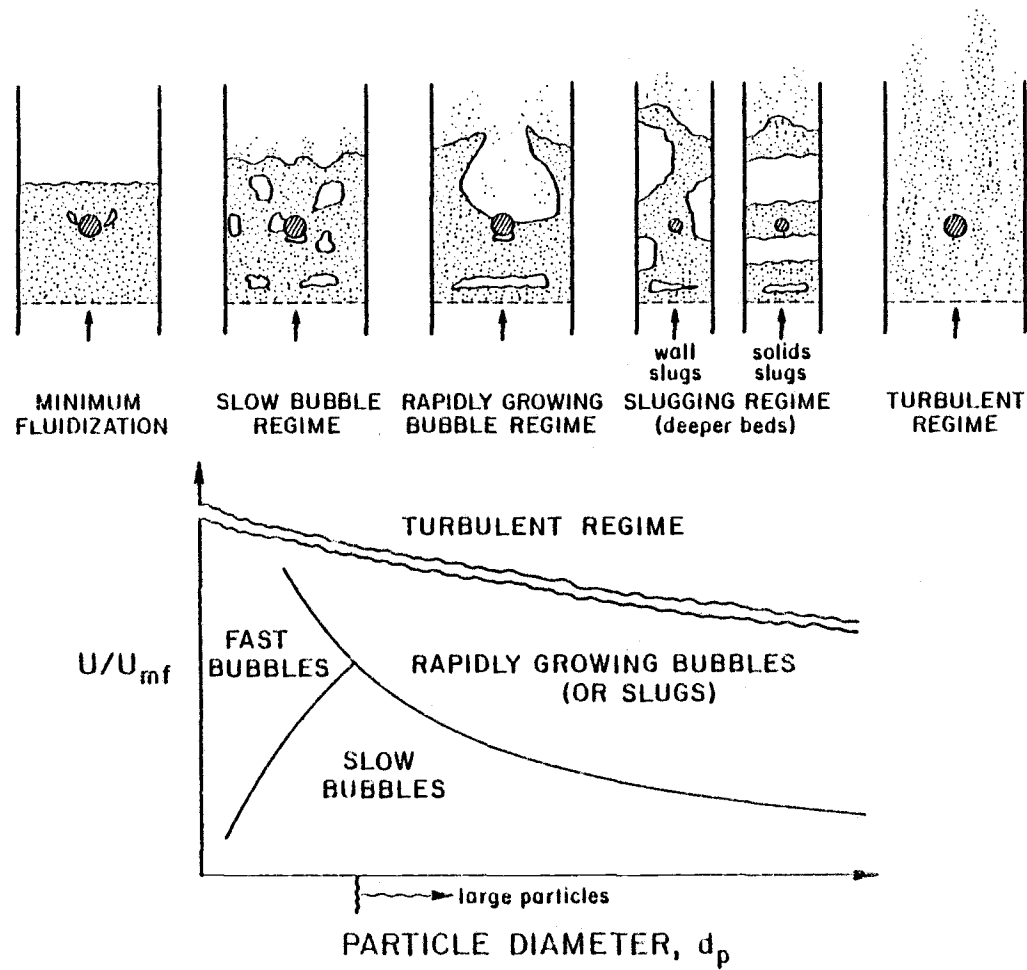


Figure 5. 1. Regimes of fluidization for large particles.

B. The Adams Analytical Model

Adams and Welty [1, 2] recently proposed a theory for coarse particles, according to which heat transfer by gas convection is the dominant mode of energy exchange between an immersed tube and the bed (this is a theory of the type first proposed by Levenspiel and Walton [60] in a rather simple form for bed-to-wall heat transfer). The suggested model represents the first attempt to analytically predict instantaneous and local heat transfer coefficients under certain fluidizing conditions. All the mathematical details, including a sophisticated computer program, have been worked out; however, the model needs to be verified experimentally.

One of the main assumptions of the model is that, due to their large thermal inertia, coarse particles remain essentially isothermal while in contact with the tube. Adams expected this assumption to be valid for particle diameters greater than 2-3 mm. Figure 5.2 shows the time required to convectively cool spherical dolomite or limestone spheres of different diameters, so that the temperature difference between the particle surface and the bed changes by 10% and 20% (curves are from references [1] and [2]). Also shown are some representative particle residence times--local as well as overall--obtained from our experiments. For most fluidizing velocities, it is safe to conclude that, if $d_p > 1 \text{ mm}$, the change in particle temperature during its contact with the surface can be neglected.

The model takes into account heat transfer resulting from gas flow within interstitial voids adjacent to the tube surface, as well as within bubbles contacting the tube. The interstitial contribution is obtained by an analysis of flow through channels of the type shown in Figure 5.3. The channel is bounded below by the tube wall and on the sides by imaginary surfaces which approximately define the domain of

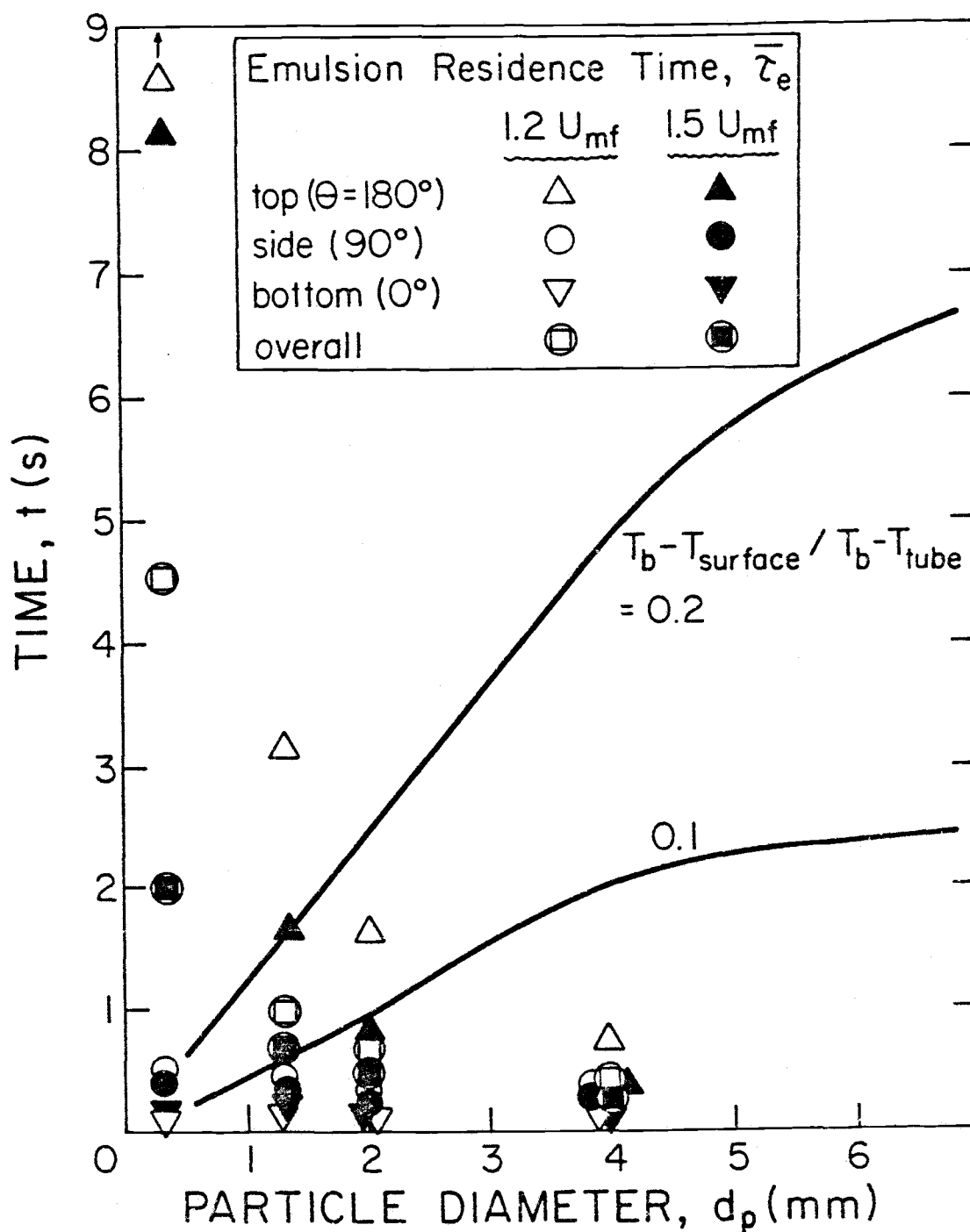


Figure 5.2. Transient cooling of a dolomite particle--theoretical curves [1, 2] are compared with our experimental data (residence times decrease further with increasing gas velocity).

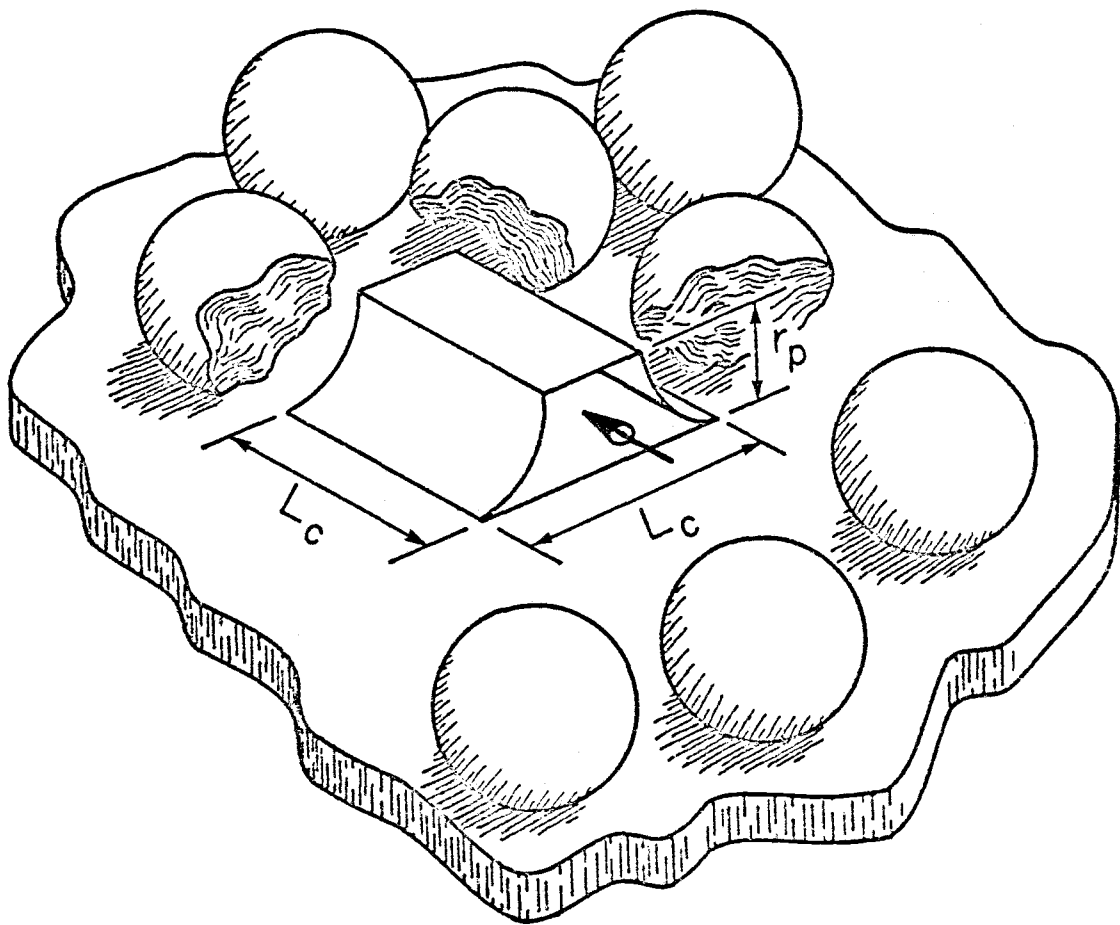


Figure 5.3. Interstitial channel.

circulating gas trapped between neighboring particles. The average spacing between particles, L_c , is determined from the local voidage at the tube surface. A two-dimensional boundary layer flow in the middle portion of the channel and a Stokes-like flow (negligible convection) in the cusped-corner region close to the particle contact point are separately considered. The effect of interstitial turbulence is incorporated. This channel flow model is used for both the loosely packed particles on the lower side of the tube, as well as the more densely packed lee stack. The convective heat transfer due to flow within a contacting bubble is obtained from a two-dimensional boundary layer analysis. The radiative heat transfer component for hot beds is also included.

A pressure field around the horizontal tube is assumed. From it and the local voidage distribution, the local interstitial velocity profile is determined. The interstitial gas velocity is then used in the boundary layer analysis to give values of local heat transfer coefficients. The computer program developed on the basis of the model can give instantaneous local coefficients, as well as the overall value, for a variety of cases involving either the emulsion phase only or the emulsion phase together with a bubble clinging to a certain portion of the tube. Time-averaged values for a given voidage distribution can also be obtained.

The Adams analysis is limited to a single immersed tube and to slow bubbles. Bubble size cannot greatly exceed the tube diameter (because of complications in analytical techniques). For our experimental conditions, with $H_o = 0.46$ m, slow bubbles are limited to a region indicated in Figure 5.4. Its boundaries were obtained from criteria suggested by Catipovic et al. [26] and recently validated experimentally by Jovanovic [54]. We see that the range of applicability of the Adams model is limited to relatively low values of

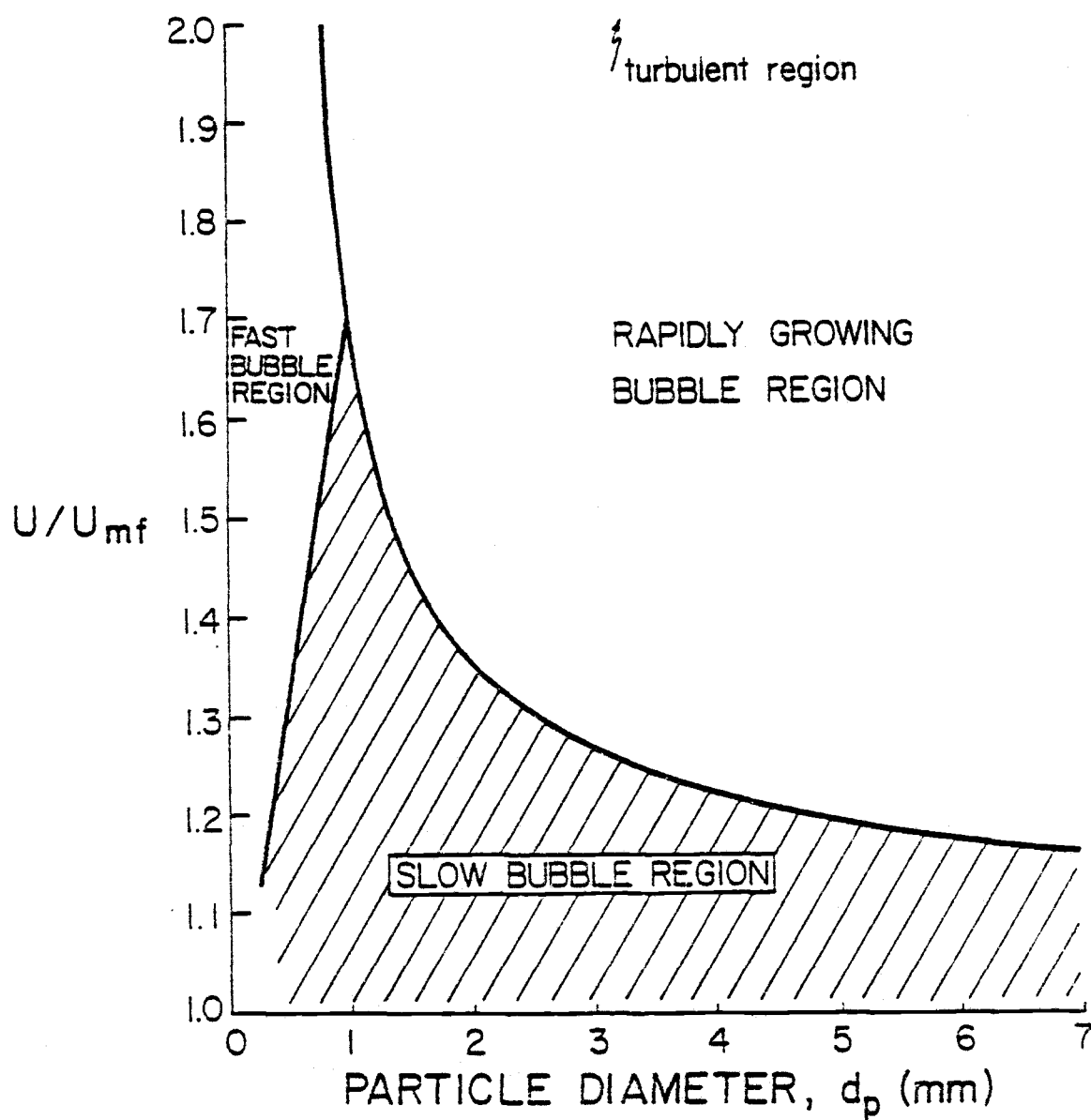


Figure 5.4. Boundaries of the slow bubble region--range of applicability of the Adams model--for dolomite particles, with $H_o = 0.46$ m.

U/U_{mf} , with the exact limiting value depending on the particle size. In our attempts to verify the analytical model, we shall use only the shallow bed data since the region of applicability is reduced further if a deeper bed is employed.⁶

If validated for the described fluidizing conditions, the model would be of considerable value because it can predict the effects of changing gas and particle physical properties, bed and tube temperatures, and tube diameter on bed-to-surface heat transfer.

C. Comparison of Time-Averaged Local Coefficients

In comparing experimental data with model predictions, we had to make sure that experimental conditions correspond to the situation modeled on the computer. For instance, we found that heat transfer coefficients at minimum fluidization should not be weighed against theoretical values because particle residence times, especially on the upper portion of the tube, are such that the assumption of isothermal particles is no longer valid. Therefore, we had to make certain that experimental results used in the comparison were obtained at velocities which guaranteed adequate particle replacement at the surface.

For the case where the emulsion phase covers the whole tube, we chose to compare analytical predictions with values obtained at velocities just slightly in excess of U_{mf} --so that only a few bubbles were generated. The voidage distribution used in the modeling reflected the actual voidage around the tube--there is a region of increased voidage in the vicinity of the lower stagnation point and a

⁶ When a deep bed is used, slugs may appear at values of U/U_{mf} which are below the indicated rapidly growing bubble boundary (see reference [26]).

stack of particles on top of the tube. The actual values used in the computer program, as well as the corresponding physical situation, are shown in Figure 5.5. The slightly increased voidage on the sides (as compared to ϵ_{mf}) reflects the fact that occasional bubbles pass by the cylinder and insure sufficient particle replacement. The voidage distribution shown essentially represents a time-averaged picture at a velocity slightly above minimum fluidization. Predicted values of the local heat transfer coefficients should therefore be compared with time-averaged experimental results.

The average voidage around the tube, resulting from the distribution shown in Figure 5.5, is 0.57. The gas velocity at which this voidage is measured experimentally depends on the particle size. The value of $\epsilon = 0.57$ corresponds approximately to a value of $1 - f_o = 0.73$. Table 5.1 shows the corresponding superficial velocities for the particles used, as well as some other quantities of interest (which will be used in later comparisons).

Table 5.1. Gas velocity at which the average voidage around the tube is 0.57 ($1 - f_o \approx 0.73$).

Particle diameter d_p (mm)	Superficial gas velocity U (m/s)	U/U_{mf}	Re_p
0.37	0.22	1.45	4.58
0.8	0.56	1.22	24.97
1.3	0.77	1.10	56.11
2.0	1.24	1.08	138.16
2.85	1.54	1.06	245.00
4.0	1.90	1.04	426.40
6.6	2.50	1.03	918.60

(Note: 1 m/s = 3.28 ft/s)

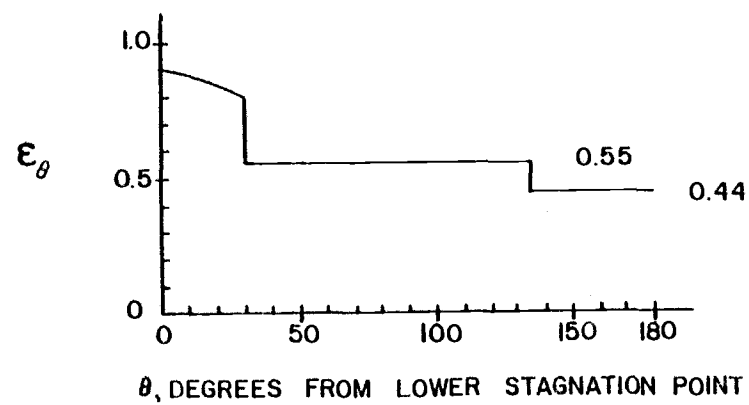
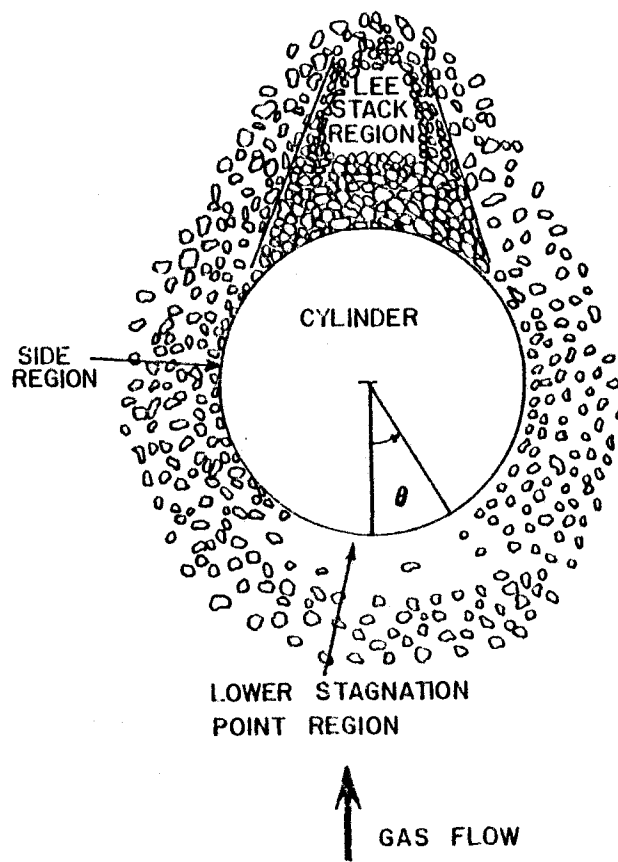


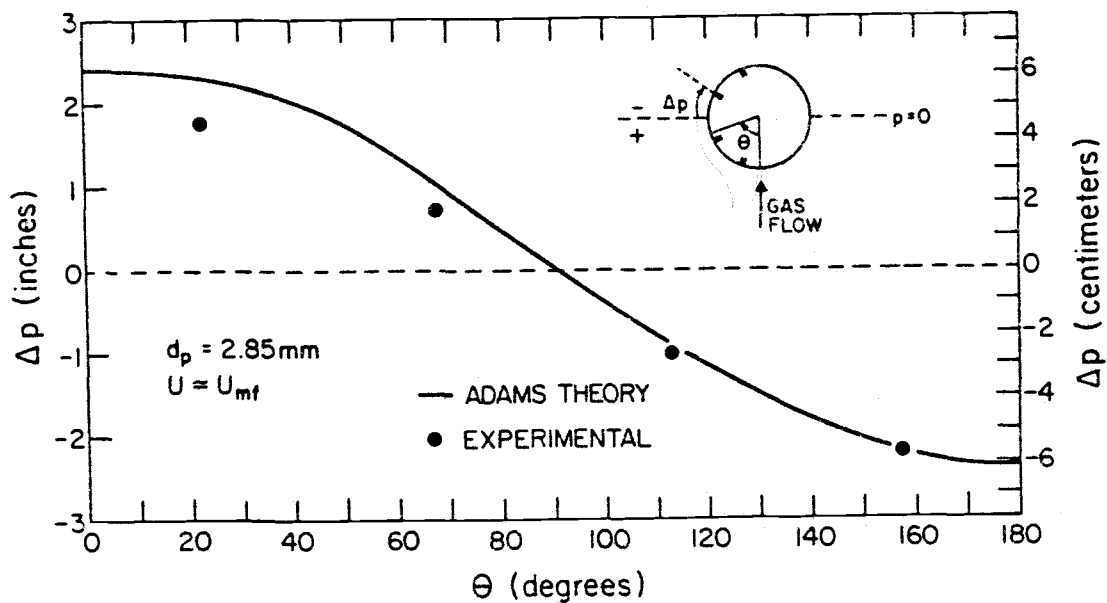
Figure 5.5. Voidage distribution at cylinder wall, used in the heat transfer modeling.

To validate the hydrodynamic portion of the analytical model, values of local pressure at the tube surface were calculated and compared with experimental data obtained using the pressure ports on the instrumented cylinder. The model assumes that, when the emulsion is contacting the tube, the local pressure distribution can be approximated by an equation closely resembling $\nabla^2 p = 0$ (Laplace's equation).⁷ Figure 5.6 shows the good agreement between predicted and experimental values of pressure variation along the cylinder circumference near U_{mf} , for particle diameters of 2.85 and 4.0 mm.

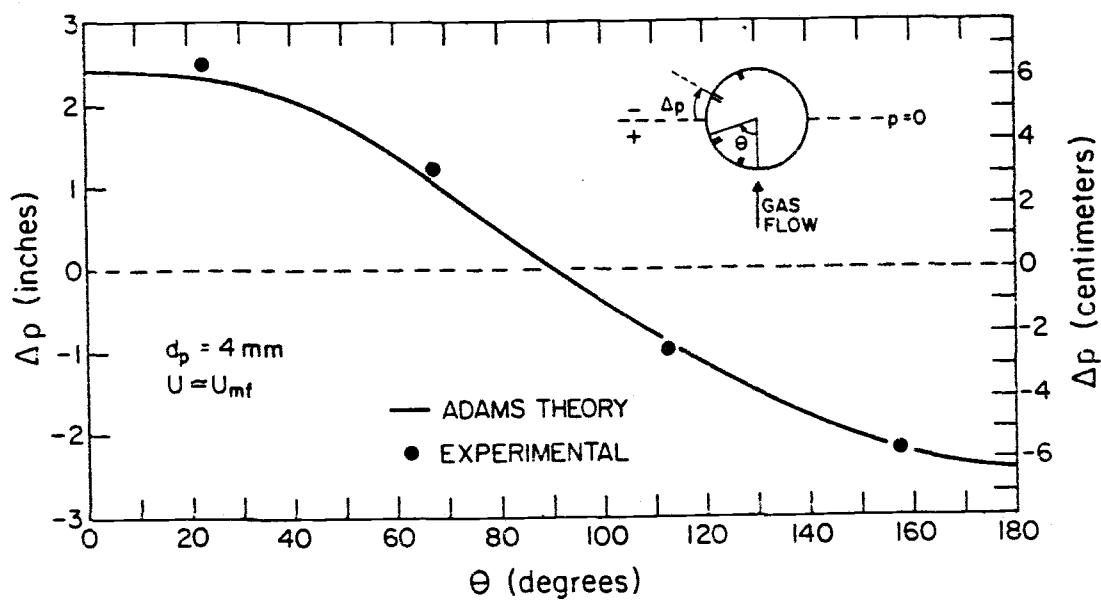
In the heat transfer comparisons which follow, the value of the interstitial turbulence intensity in the model was set at $u' = 0.2$, as suggested by experiments of Galloway and Sage [39] for large spherical particles. Figure 5.7 shows a typical comparison between theoretical and measured values of local heat transfer coefficients. The actual output of the Adams model computer program gives the local Nusselt number based on the cylinder diameter, $Nu_{D\theta}$, as a function of the angle measured from the lower stagnation point. From $Nu_{D\theta}$ values, local heat transfer coefficients for particular points on the tube circumference, h_θ , are obtained.

For a more meaningful comparison with measured values of h_θ , the theoretical coefficients should be averaged over the section of the cylinder which is covered by the platinum sensor (a sector of 30°). Figure 5.8 shows a detailed graphical summary of this type of comparison for particles used in our experiments. The graphs are

⁷The exact pressure calculation, as well as other procedures (interstitial velocity profile determination, heat transfer solution for the lower stagnation point region, assessment of the influence of interstitial turbulence, etc.) are described in detail in references [1] and [47].



(a)



(b)

Figure 5.6. Comparison between predicted and experimental values of pressure drop at cylinder surface, for (a) $d_p = 2.85 \text{ mm}$, and (b) $d_p = 4.0 \text{ mm}$ (Δp given in cm and inches of water column).

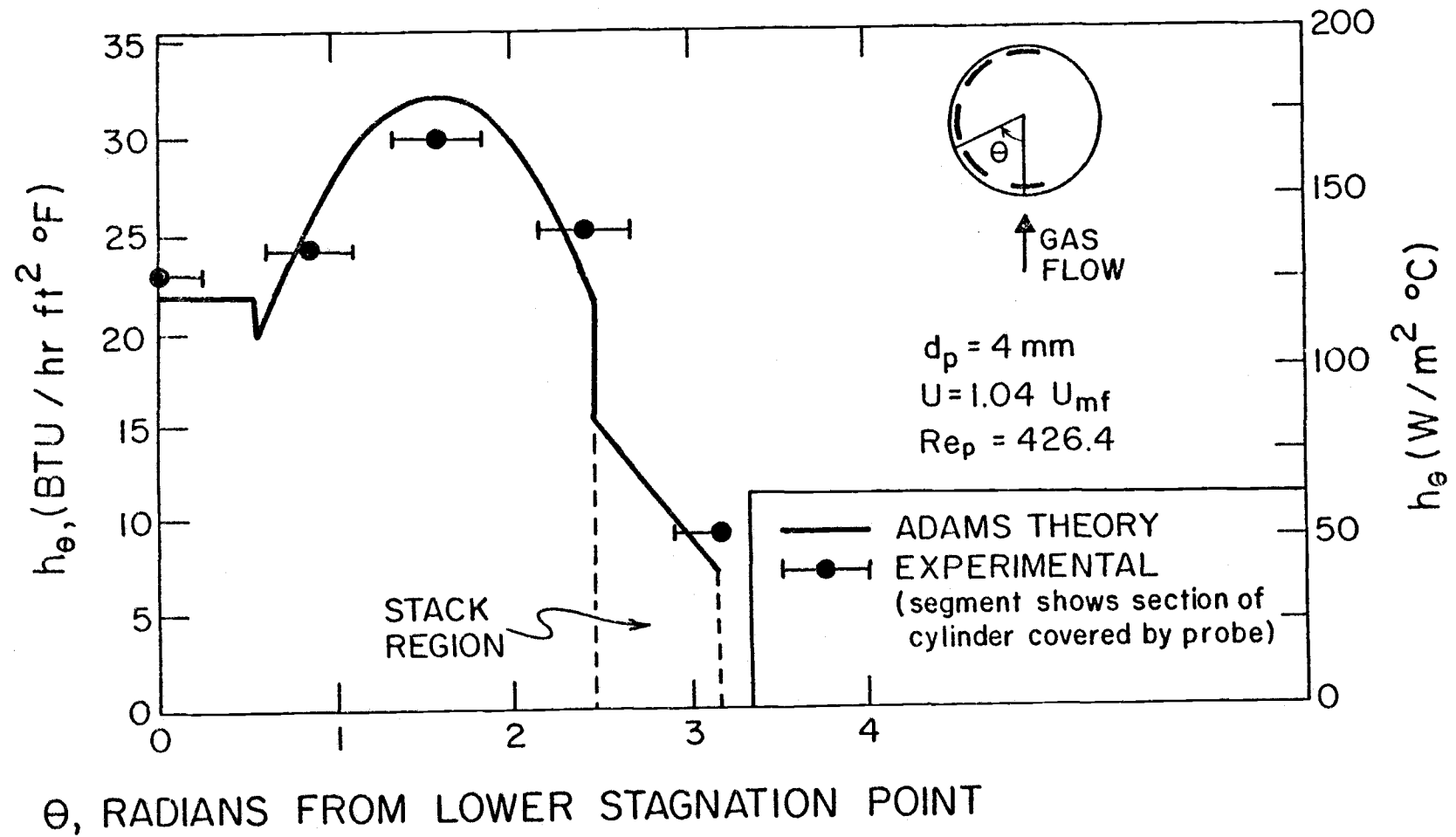


Figure 5.7. Comparison between theoretical and measured values of local heat transfer coefficients for $d_p = 4.0 \text{ mm}$.

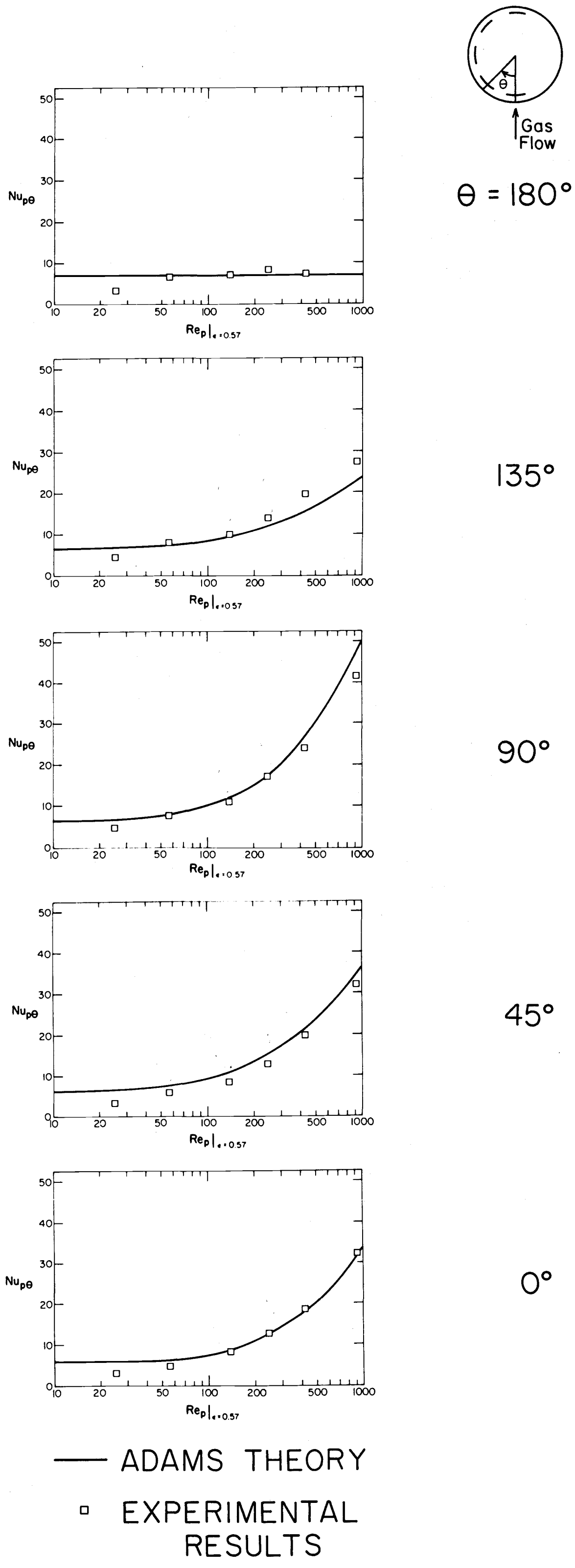


Figure 5.8. Comparison between theoretical and measured values of local Nusselt numbers, $Nu_{p\theta}$, for particles used in our study (see Table 5.1).

plotted in terms of dimensionless groups $Nu_{p\theta}$ and Re_p since such representation provides a convenient way of assessing the influence of physical properties on heat transfer behavior.

The agreement between experiment and theory is very satisfactory, both in values and trends, indicating the sound basis of the analytical model. Under our operating conditions, the lower limit of model's applicability seems to be around 1 mm ($Re_p \approx 40$); this significantly exceeds Adams' conservative estimate of 2-3 mm. As particle diameter decreases below 1 mm, the disagreement between predictions and data becomes significant, reaching 150-200% for 0.37 mm particles (not shown in Figure 5.8). The lower limit is obviously connected with the assumption of constant particle temperature. The thermal inertia of smaller particles is not sufficient enough to keep them isothermal while at the tube wall; therefore the actual heat transfer coefficient is well below the predicted. It must be noted that the actual limit of the model will depend on the physical properties of the gas and particles.

Actual and predicted local heat transfer coefficients shown in Figure 5.8 rarely differ by more than 15%. The somewhat larger differences at the 135° and 45° positions could be attributed to the problem of defining the exact boundaries of the stack on top and the air cushion at the bottom of the tube. As far as local coefficients go, our data are the only ones available for comparison at present.

The agreement is even more striking when the overall coefficients are considered.⁸ Figure 5.9 compares theory versus experiment for two cases, both with air as the fluidizing gas: a) our data using a 50.8 mm cylinder at atmospheric pressure, and b) data of

⁸The theoretical average for the whole tube is calculated by averaging the local point values over the circumference; the experimental average is obtained from equation (4.3).

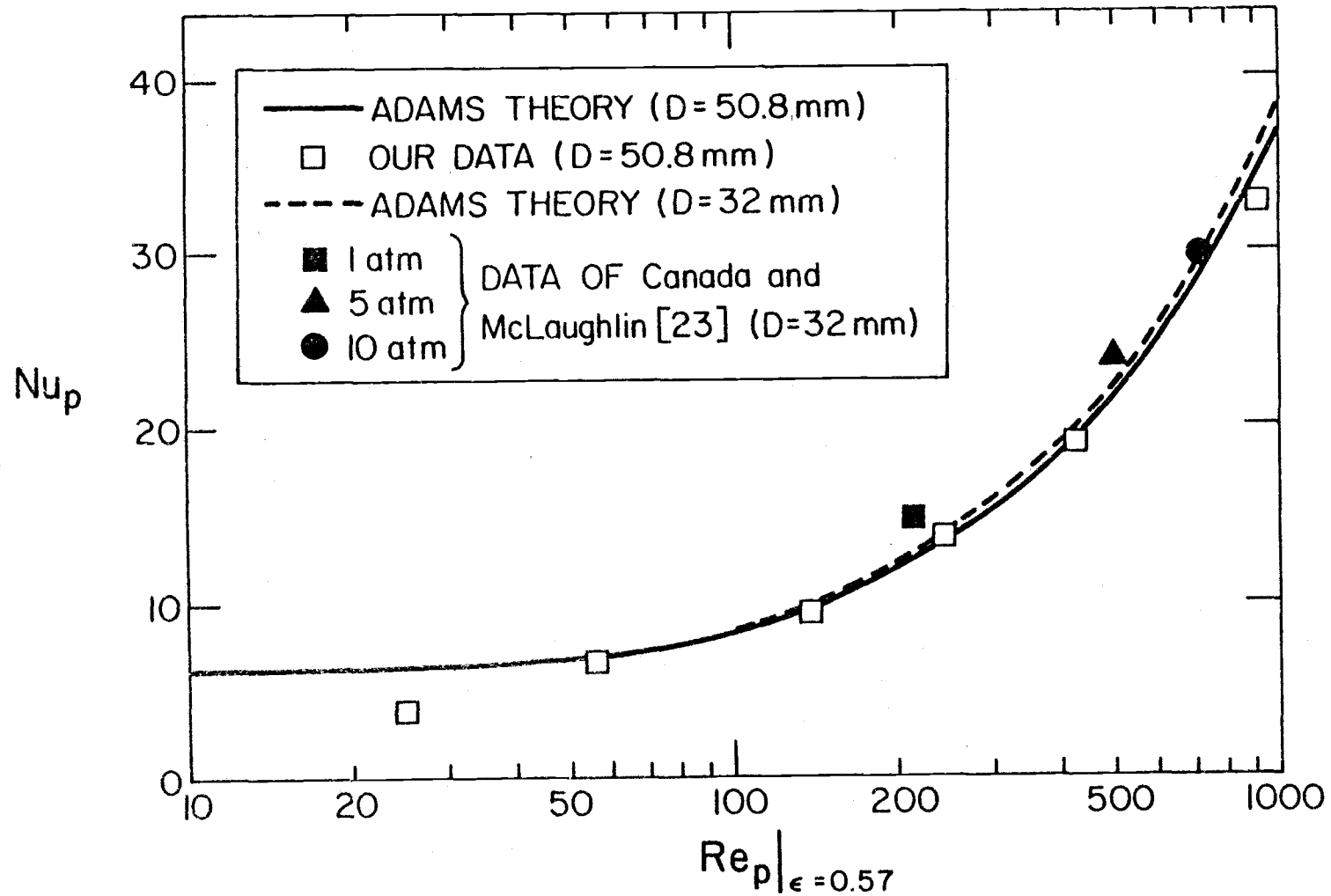


Figure 5.9. Comparison between theoretical and measured values of the overall Nusselt number, Nu_p , for particles used in our study and in reference [23].

Canada and McLaughlin [23] using a 32 mm cylinder in a bed of 2.6 mm glass particles at three different pressures (their heat transfer coefficients used for comparison were those obtained at $1.1 U_{mf}$). The model is successful in predicting the effect of gas properties (influenced by pressure) on heat transfer. It also correctly predicts the negligible influence of tube diameter.⁹

D. Comparison of Instantaneous Local Coefficients in the Presence of Bubbles

The Adams model can predict the distribution of instantaneous local heat transfer coefficients for practically any configuration of a single tube-size bubble clinging to the immersed cylinder. In order to obtain data for comparison with these predictions, we had to work at velocities slightly higher than in Section C so that relatively vigorous bubbling would be taking place. We also had to use an experimental setup somewhat different from the one described previously.

Plexiglass inserts were placed in the bed to reduce its thickness to 50 mm (2 in). In such a narrow bed, tube-size bubbles could be seen easily, thus facilitating the computer simulation of the situation in the bed. When in operation, this two-dimensional bed was back-lighted and filmed with a Nikon R-10 camera using a color film at 18 frames per second. For every frame registered on film, the corresponding heat transfer, voidage, and pressure signals were registered on the computer. These data gave instantaneous values of local heat

⁹For fine particles, Gelperin et al. [43, 45] suggest that heat transfer coefficients are independent of the tube diameter if it exceeds 20 mm. No such information has been reported for large particles.

transfer coefficients, voidage, and pressure drops which correspond to the picture on the film frame.

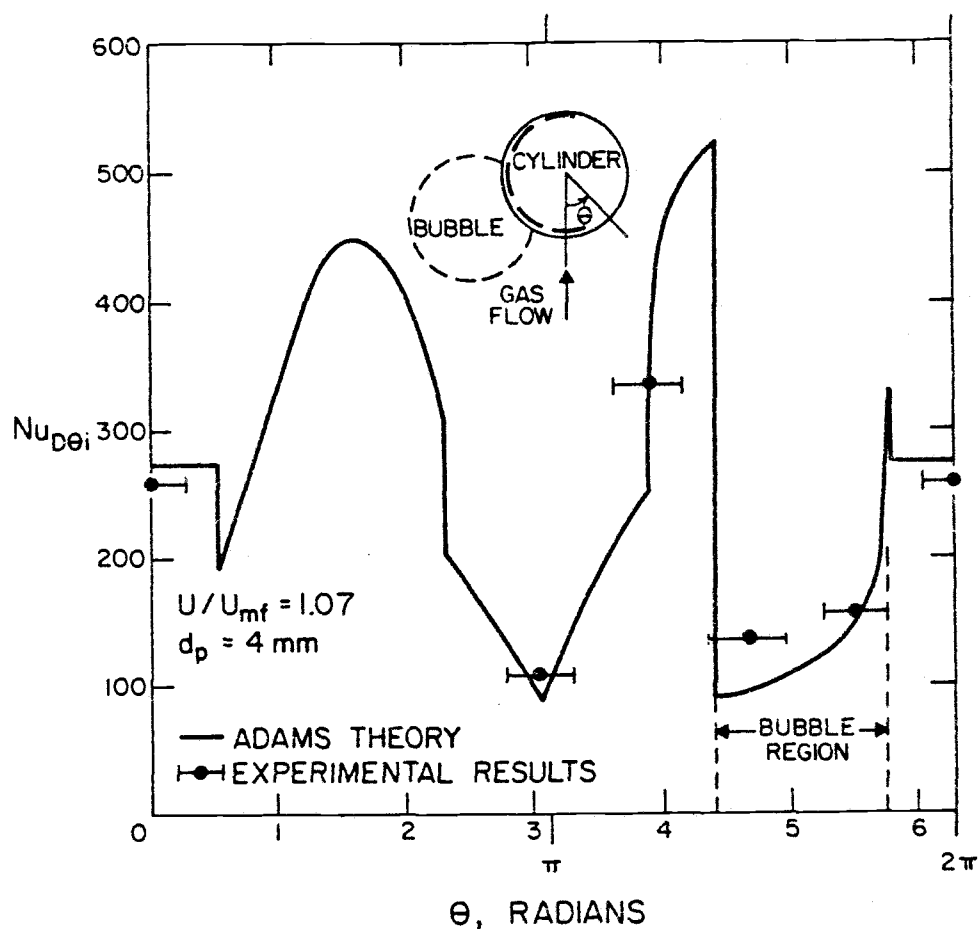
In addition to the narrow bed, data were collected in the wider bed as before. However, in this case bubble position had to be inferred from the capacitance and pressure readings around the cylinder perimeter. The resistance to particle motion in the two-dimensional bed caused the actual U_{mf} to rise, with the difference between this 2-D U_{mf} and the real U_{mf} becoming more significant as the particle diameter became larger. For example, there was no difference for 0.37 or 0.8 mm particles, but there was a significant deviation for 4.0 mm particles, with $U_{mf(2-D)} = 2.47 \text{ m/s}$ as compared to $U_{mf} = 1.83 \text{ m/s}$. However, with this discrepancy taken into account when simulating the situation in the narrow 2-D bed on the computer, the agreement between theoretical and experimental values was very satisfactory. The agreement for the case of the wider bed, where the above correction was not required, was just as good.

Several hundred movie frames were examined, and the corresponding predicted and experimental values were compared. In all of the computer simulations, the voidage distribution in the emulsion phase was as shown in Figure 5.5, with the exception that the voidage on the sides of the tube was taken as 0.5. Bubble phase was assigned a voidage of 1.0. As in the comparison of time-averaged values, the model gave good predictions for particle diameters of 1.3 mm and larger, with the agreement getting better as particle size increased. Predicted and measured values of instantaneous local heat transfer coefficients rarely differed by more than 15%, while the instantaneous average values for the whole circumference agreed to within 10%. Some illustrated examples are given in the figures which follow.

Figure 5.10 shows the actual output of the computer program (in terms of $Nu_{D\theta i}$), together with experimental values, for the bubble location indicated on the graph. The accompanying table compares theoretical values, averaged over the section of the tube covered by the corresponding platinum sensor, with experimental measurements. Figure 5.11 illustrates the good agreement between local heat transfer coefficients for the case of a bubble engulfing the bottom platinum sensor ($d_p = 4.0$ mm), while Figure 5.12 compares prediction vs. experiment for a bubble clinging to the side of the cylinder ($d_p = 2.85$ mm). As in Figure 5.10, the corresponding tables give numerical information on the agreement of sector-averaged values. Note that these comparisons were made for the narrow, two-dimensional bed. Figure 5.13, however, illustrates the agreement for the case where bubble position is inferred from capacitance and pressure readings in the wider bed ($d_p = 4.0$ mm).

The numerous cases with different bubble positions cannot all be presented. Suffice it to say that experimental data confirm the success of the Adams model in predicting the influence of bubble location on instantaneous local heat transfer coefficient distribution for particle diameters above 1 mm. The only larger percentage error between theory and experiment is for local coefficients on the side of the tube when a bubble is present there. This discrepancy can probably be attributed to the fact that the bubble is not particle-free as assumed in the model. Our movies and the signals from the capacitance probes (see Figures 3.6 and 3.7) indicate that particles occasionally "rain" through bubbles during bubble passage by the immersed tube (a phenomenon also brought to attention by Syromyatnikov et al. [64] for smaller particles).

It is interesting to note that for large particles the instantaneous local heat transfer coefficients for a given bubble configuration can,

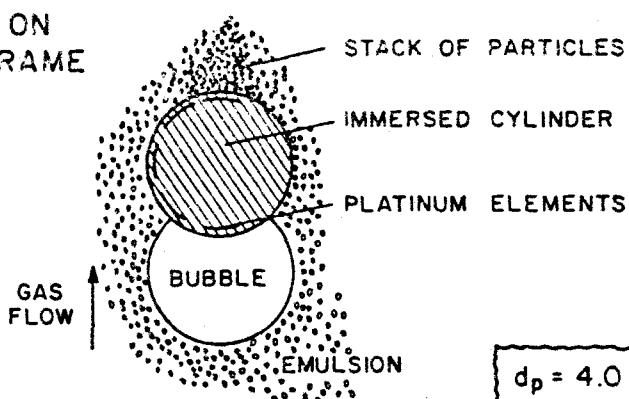


LOCATION		$Nu_{D\theta i}$	$Nu_{D\theta i}$	$Nu_{D\theta i}(\text{theory})/Nu_{D\theta i}(\text{experiment})$
θ		ADAMS MODEL	EXPERIMENTAL	
radians	degrees	(averaged over section of tube covered by probe)		
3.14	180	115	109	1.06
3.93	225	346	338	1.03
4.71	270	104	132	0.79
5.50	315	174	159	1.09
6.28	360	273	261	1.05
AVERAGE (for the whole tube)		220	203	1.08

To convert to h : $h = 0.56 Nu_D [W/m^2 \cdot ^\circ C] = 0.098 Nu_D [BTU/hr \text{ ft}^2 \cdot ^\circ F]$

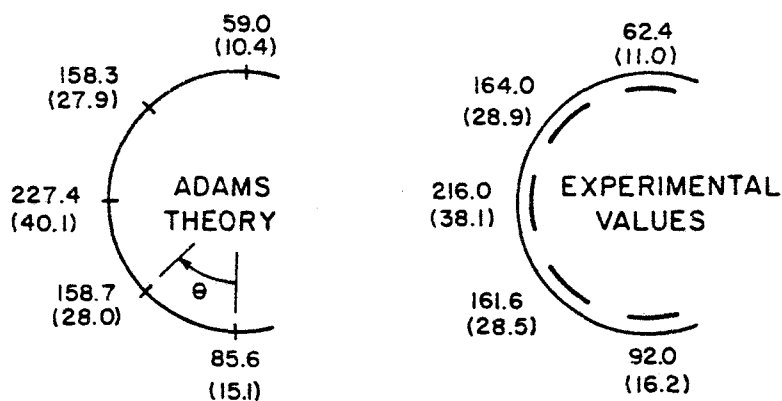
Figure 5.10. Comparison between theoretical and measured values of instantaneous local Nusselt numbers based on tube diameter, $Nu_{D\theta i}$, for bubble configuration shown ($d_p = 4.0 \text{ mm}$, narrow bed).

PICTURE ON
MOVIE FRAME



INSTANTANEOUS LOCAL VALUES

$h_{\theta i}$, $W/m^2 \cdot ^\circ C$ ($BTU/hr \cdot ft^2 \cdot ^\circ F$)

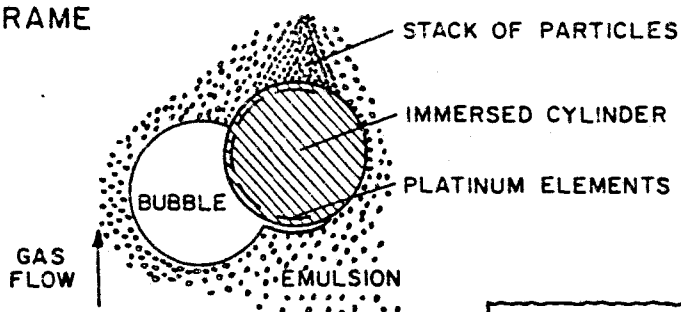


LOCATION θ degrees	$h_{\theta i}$ ADAMS MODEL (sector averaged) $W/m^2 \cdot ^\circ C$	$h_{\theta i}$ EXPERIMENTAL $W/m^2 \cdot ^\circ C$	$\frac{h_{\theta i}(\text{theory})}{h_{\theta i}(\text{experiment})}$
180	59.9	62.4	0.96
135	148.4	164.0	0.90
90	223.1	216.0	1.03
45	152.6	161.6	0.94
0	87.1	92.0	0.95
OVERALL	147.4	154.7	0.95

Note: $5.67 \text{ } W/m^2 \cdot ^\circ C = 1 \text{ } BTU/hr \cdot ft^2 \cdot ^\circ F$.

Figure 5. 11. Comparison between theoretical and measured values of instantaneous local heat transfer coefficients, $h_{\theta i}$, for bubble configuration shown ($d_p = 4.0 \text{ mm}$, narrow bed).

PICTURE ON
MOVIE FRAME

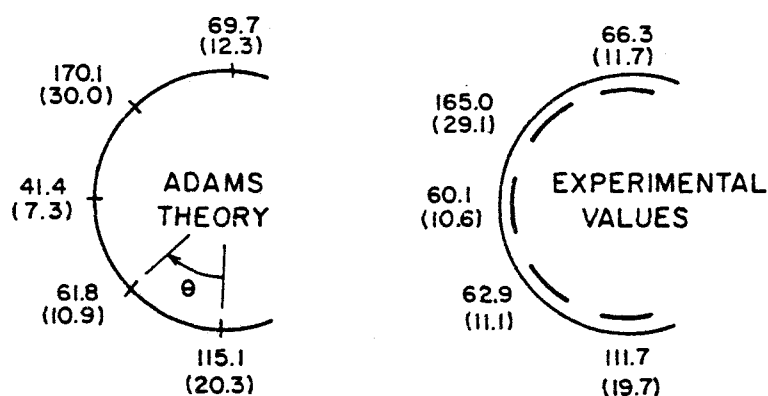


$$d_p = 2.85 \text{ mm}$$

$$U = 1.15 U_{mf}$$

INSTANTANEOUS LOCAL VALUES

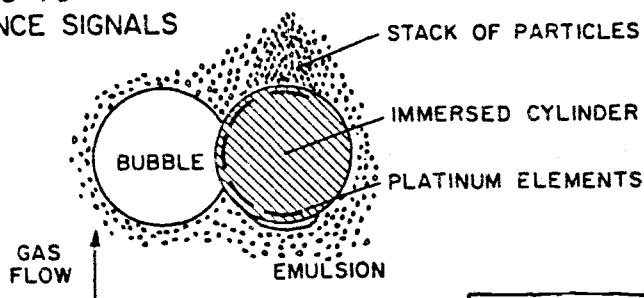
$h_{\theta i}$, $\text{W/m}^2\text{°C}$ ($\text{BTU/hr ft}^2\text{°F}$)



Note: $5.67 \text{ W/m}^2\text{°C} = 1 \text{ BTU/hr ft}^2\text{°F}$.

Figure 5.12. Comparison between theoretical and measured values of instantaneous local heat transfer coefficients, $h_{\theta i}$, for bubble configuration shown ($d_p = 2.85 \text{ mm}$, narrow bed).

BUBBLE POSITION
ACCORDING TO
CAPACITANCE SIGNALS

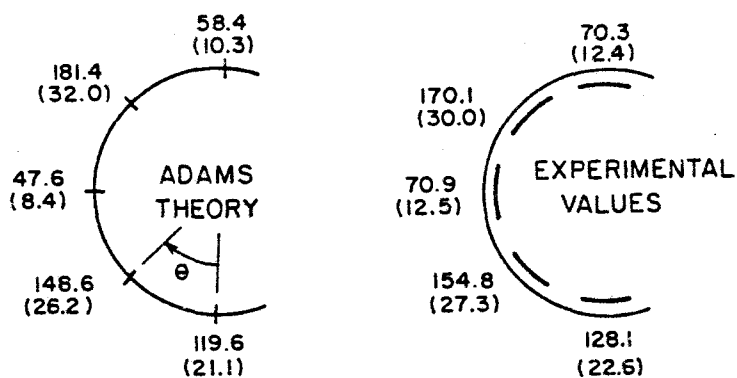


$$d_p = 4.0 \text{ mm}$$

$$U = 1.11 U_{mf}$$

INSTANTANEOUS LOCAL VALUES

$$h_{\theta i}, \text{ W/m}^2 \text{ } ^\circ\text{C} \text{ (BTU/hr ft}^2 \text{ } ^\circ\text{F)}$$



LOCATION θ degrees	$h_{\theta i}$ ADAMS MODEL (sector averaged) $\text{W/m}^2\text{ } ^\circ\text{C}$	$h_{\theta i}$ EXPERIMENTAL $\text{W/m}^2\text{ } ^\circ\text{C}$	$\frac{h_{\theta i}(\text{theory})}{h_{\theta i}(\text{experiment})}$
180	62.3	70.3	0.89
135	190.1	170.1	1.12
90	50.6	70.9	0.71
45	152.8	154.8	0.99
0	119.6	128.1	0.93
OVERALL	120.6	123.8	0.97

Note: $5.67 \text{ W/m}^2\text{ } ^\circ\text{C} = 1 \text{ BTU/hr ft}^2\text{ } ^\circ\text{F}$.

Figure 5.13. Comparison between theoretical and measured values of instantaneous local heat transfer coefficients, $h_{\theta i}$, for bubble configuration shown ($d_p = 4.0 \text{ mm}$, wider bed).

to a first approximation, be estimated from experimental values of $h_{\theta i, \max}$ and $h_{\theta i, \min}$ shown in Figures 4.7, 4.9, 4.11, 4.13, and 4.15. The high values are applicable for all positions covered by the emulsion, while the low values apply for parts of the tube immersed in a bubble.

E. Conclusions about the Adams Model

We consider the Adams model verified at lower temperatures. Experimental evidence proves the soundness of this analytical model derived from first principles. The accurate predictions of local instantaneous and time-averaged coefficients, with and without the presence of bubbles, give no reason to expect that the analysis for the gas convective heat transfer will be any less valid at high bed temperatures and pressures (the latter being of particular interest for dual-cycle utility applications). Validation of the thermal radiation portion of the model will require experimental work at high temperatures.

An apparent disadvantage of the model is that, strictly speaking, it is applicable only for a narrow range of U/U_{mf} ratios. However, it could prove to be useful for predictions in large-particle beds in general since coefficients slightly above U_{mf} appear to represent good first approximations for heat transfer at higher velocities (this certainly is the case for $d_p > 1 \text{ mm}$ at room temperature and atmospheric pressure--see Figures 4.7-4.16 and 4.19-4.20). Although the model treats only the single tube case, it could be applied relatively successfully to a tube bundle since our data in Chapter IV show a surprisingly small difference between the two.

VI. HEAT TRANSFER OVER A WIDE RANGE OF FLUIDIZING CONDITIONS: DEVELOPMENT OF A THEORETICAL MODEL

Chapter V dealt with heat transfer under rather specific fluidizing conditions. In the analysis which follows, we shall develop a general theoretical model applicable for a wide range of particle sizes (fine, intermediate and large particles) and fluidizing velocities (minimum fluidization, fast bubble region, slow bubble region, rapidly growing bubble region and slugging--see Figure 5.1 for illustration), as well as horizontal tube configurations (single tube, tube arrays). Our model assumes that the fluidized bed consists of the emulsion phase and the bubble phase. As such, it covers fluidizing conditions up to the high-velocity turbulent regime where the emulsion-bubble representation is no longer adequate.

We shall rely heavily on our experimental data for drawing conclusions about various components of the model. Although instantaneous and time-averaged local data will have an important role in the analysis, the primary aim of this chapter is the development of a reliable method for predicting the quantity of greatest importance for design--the time-averaged overall heat transfer coefficient.

A. Physical Model

In a bubbling or slugging fluidized bed, heat is transferred from (to) an immersed surface by packets of particles, by gas percolating between the particles of the packet and the surface, and by gas bubbles or slugs. The three heat fluxes occur in parallel, as shown in Figure 6.1. If the bed is operating at high temperatures, the radiative component has to be included as well. Gelperin and Ainshtein [42] proposed the most general equation for the effective heat transfer coefficient:

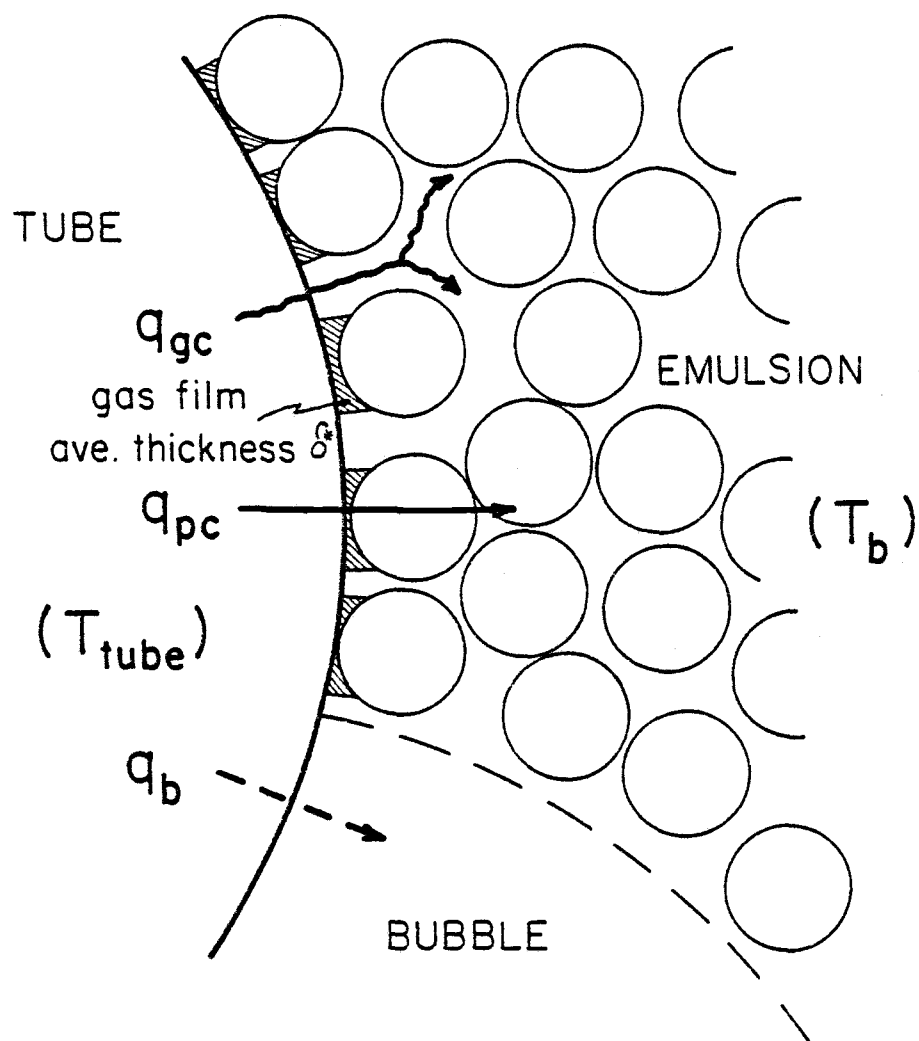


Figure 6.1. Model of heat transfer from an immersed tube to a fluidized bed.

$$h = (1-f_o)h_{pc} + (1-f_o)h_{gc} + f_o h_b + h_r \quad (6.1)$$

Although they were the first to make allowance for the quantity of heat transferred by gas convection and for the period when the exchange surface is shrouded by bubbles, the authors limited their analysis and experimental work to fine particles where only the particle convective mode was of importance. In such cases, heat is exchanged practically only by an unsteady-state transfer between the surface and emulsion packets. The packets rest on the surface for a short time, only to be swept away by bubble action and replaced by fresh emulsion from the bed. This constant particle and packet movement prompted the use of the adjective "particle convective".

In our application, we are interested in all modes of heat transfer except the radiative which becomes important at temperatures exceeding 600-700°C. Because of the physical picture on which it is based, the general equation applies for both the time-averaged overall coefficient and local coefficients:

$$h = (1-f_o)h_{pc} + (1-f_o)h_{gc} + f_o h_b \quad (6.2)$$

$$h_\theta = (1-f_o)h_{\theta pc} + (1-f_o)h_{\theta gc} + f_o h_{\theta b} \quad (6.3)$$

We shall use these equations throughout our analysis and focus on each of the terms.¹⁰

¹⁰In further development, whenever an equation is written for h , h_{pc} , h_{gc} , or h_b , it also applies for h_θ , $h_{\theta pc}$, $h_{\theta gc}$, or $h_{\theta b}$, respectively, with the corresponding local parameters inserted.

Particle Convective Component

Since the particle convective component makes up the packet theory of heat transfer, it has been dealt with in detail in fluid-bed literature. As a matter of fact, it is the only component to which considerable attention has been devoted. The surface-to-packet heat transfer is viewed in terms of two resistances in series: a) the contact resistance presented chiefly by the gas in the increased voidage close to the transfer surface, and b) the resistance within the emulsion packet phase (consisting of gas and solids). The problem of two thermal resistances in series has been solved for a variety of boundary conditions by Baskakov [10] and Gelperin et al. [42, 43], with a complete list of solutions for the instantaneous and time-averaged heat transfer coefficients given by Gelperin and Ainshtein [42] and Botterill [19]. For the case of greatest practical interest--that of the constant exchange surface temperature (in our case $T_{\text{tube}} = \text{const.}$)--a simplified solution for the time-averaged particle convective heat transfer coefficient can be used with negligible error in place of a complicated analytical expression:

$$h_{pc} = \frac{1}{R_c + R_e} \quad (6.4)$$

The effective value of the emulsion packet resistance, R_e , is derived from uniform surface renewal theory [95]:

$$R_e = 0.5 \sqrt{\frac{\pi \tau_e}{k_e \rho_e c_{ps}}} \quad (6.5)$$

The effective density of the emulsion packet may be taken as

$$\rho_e = \rho_s (1 - \varepsilon_{mf}) \quad (6.6)$$

The corresponding effective thermal conductivity can be estimated from relationships developed for thermal conductivity in packed beds (Yagi and Kunii [92, 93]) and may be written as

$$k_e = k_e^0 + 0.1 \rho_g c_{pg} d_p U_{mf} \quad (6.7)$$

where the stagnant bed conductivity, k_e^0 , can be calculated following the method of Kunii and Smith [58] or Baskakov [11]. Standard graphs for the calculation of k_e^0 as a function of k_s/k_g and ε_{mf} are given by Gelperin and Ainshtein [42] and Botterill [19].

The contact resistance was first introduced to modify the original packet theory of Mickley and Fairbanks [65], i. e., to account for the fact that, for very short emulsion packet residence times, the theory predicted extremely high values of the instantaneous heat transfer coefficient while experimental data showed a definite limit. This resistance is also instrumental in explaining the observed dependence of the heat transfer coefficient on particle size for fine-particle systems (h goes down as d_p increases). It has been handled in many ways: from introducing a zone of increased voidage adjacent to the surface (whose thickness was arbitrarily set at some fraction of the particle diameter), having a certain effective thermal conductivity (Baskakov [10, 11]), to using an artificial gas slab between the surface and the first layer of particles in order to fit experimental data (Gabor [38]). A good review of these mathematical exhibitions is given by Botterill [19]; in all versions, the resistance is independent of time to a first approximation.

However, the contact resistance can be treated more realistically by considering that, when particles are touching the surface,

conduction from surface to particle (or vice versa) takes place through the intervening gas layer which has an average thickness δ^* (see Figure 6.1). The thermal resistance is then

$$R_c = \frac{\delta^*}{k_g} = \frac{d_p/y}{k_g} \quad (6.8)$$

where δ^* is represented by a fraction of the particle diameter, d_p/y . This approach was recently used by Xavier and Davidson [91], who fitted their fine- and intermediate-particle data by adjusting the value of y (getting $y = 10$ for vertical and $y = 4$ for horizontal tubes), and Glicksman and Decker [49, 50, 84], who made an attempt to theoretically estimate y on the basis of surface roughness considerations. We shall use the same concept, except that the value of y will be determined directly from experiments.

Combining equations (6.4), (6.5), and (6.8), we obtain the following expression for the particle convective heat transfer coefficient:

$$h_{pc} = \frac{1}{\frac{d_p/y}{k_g} + 0.5 \sqrt{\frac{\pi \tau_e}{k_e \rho_e c_{ps}}}} \quad (6.9)$$

Gas Convective Component

Heat transfer by gas convection consists of the transfer through the boundary layer at the tube surface, as well as of the transfer caused by lateral mixing of the flowing gas. Since this mode of heat exchange is negligible in fine-particle beds (due to low gas velocities at which fluidization occurs), it has been dealt with only sparingly (Baskakov et al. [11, 12], Gabor [37], and Botterill et al. [20-22, 33]). Gas convective effects become very significant in large-particle beds

at any pressure and in intermediate-particle beds at elevated pressures.

For a quiescent fluidized bed, i. e., bed at minimum fluidization with no particle movement, $\bar{\tau}_e \rightarrow \infty$ ($R_e \rightarrow \infty$) and equations (6.4) and (6.9) indicate that $h_{pc} \rightarrow 0$. Since $1 - f_o = 1$ at U_{mf} , equation (6.2) gives

$$h_{mf} = h_{gc} \quad (6.10)$$

Due to the way in which equation (6.4) was obtained, equation (6.10) is an approximation. The question now arises as to how good an approximation it is.

The gas convective heat transfer component is difficult to measure directly. Baskakov and Suprun [13] used the analogy between convective heat and mass transfer to estimate it and obtain a correlation for the gas convective transfer from a vertical tube (mass transfer measurements can give the gas convective heat transfer component since there is no mass transfer equivalent of the particle convective mode). Gabor [37] developed a theoretical correlation for the gas convective heat transfer to (from) vertical immersed objects. Botterill and Denloye [20, 21] recently proposed a theoretical model of heat transfer to a quiescent bed containing a vertical cylinder. The same authors then followed with experimental data on quiescent bed heat transfer coefficients [21, 33]. The agreement between their results and all of the proposed correlations for the gas convective contribution is very satisfactory for intermediate and large particles and somewhat less adequate for fine particles (see detailed comparisons by Botterill and Denloye [20, 21, 33]). However, since the gas convective contribution in fine-particle fluidized beds happens to be negligible, we can conclude that equation (6.10) is a very good approximation. As such, it has been recently introduced in heat

transfer modeling by Denloye and Botterill [33] and Xavier and Davidson [91].

The logic behind equation (6.10) is simple. At U_{mf} , the bubble-induced particle convective component is absent, and h_{mf} consists practically only of the gas convective term. As gas velocity is increased, the two-phase theory tells us that the excess gas flows through the bed in the bubble phase. The flow in the emulsion phase should then remain essentially constant over a wide range of velocities. This view is very strongly supported by our experimental findings on the maximum instantaneous heat transfer coefficients--see Section IV.B and discussion on page 58, as well as further development in Section B of this chapter. Accordingly, the quiescent bed coefficient can be taken as a measure of the gas convective component, and equation (6.10) is then valid for a bubbling or a slugging bed operating at any superficial velocity.

The best illustration of how important the gas convective contribution becomes for larger particles is given by our results in Figures 4.19, 4.20, and 4.21. The quiescent bed coefficient, h_{mf} , makes up a spectacularly increasing portion of the total coefficient, h , with an increase in particle size.

Bubble Component

Heat transfer between a surface and a passing bubble or slug is the most neglected mode of energy exchange in fluidized beds. With the exception of a few short comments by Gelperin and Ainshtein [42] and Baskakov et al. [12], who suggest that for large particles the bubble component might be lumped into the gas convective component, this heat transfer mechanism has been totally ignored in published analyses. Based on our instantaneous measurements (see Section

IV. B and discussion on page 60), it is obvious that the bubble component has to be included in a heat transfer model for large particles. It could become very significant at elevated pressures. For a full grasp of the actual heat transfer occurrences in fluidized beds, as well as for a better prediction reliability, this component should be dealt with independently of the gas convective mode.

B. Clues from Experiment

Following the discussion in Section A, we can now express the time-averaged overall coefficient as:

$$h = \frac{1-f_o}{\frac{d_p/y}{k_g} + 0.5 \sqrt{\frac{\pi \tau_e}{k_e \rho_e c_{ps}}}} + (1-f_o)h_{mf} + f_o h_b \quad (6.11)$$

and the time-averaged local coefficients as:

$$h_\theta = \frac{(1-f_o)_\theta}{\frac{d_p/y_\theta}{k_g} + 0.5 \sqrt{\frac{\pi \tau_e}{k_e \rho_e c_{ps}}}} + (1-f_o)_\theta h_{\theta mf} + f_{o\theta} h_{\theta b} \quad (6.12)$$

Important clues about each term in these equations can be obtained from the numerous data collected in our study. Certain general conclusions can be drawn, and we hope that resulting correlations for the non-radiative portion of heat transfer will be valid for a wide variety of bubbling and slugging bed conditions, including high pressure and temperature.

Particle Convective Component

Information about the average gas layer thickness $\delta^* (= d_p / y)$, can be extracted from the maximum instantaneous heat transfer coefficient. According to Gelperin and Ainshtein [42] the instantaneous particle convective coefficient for the case of constant immersed surface temperature is:

$$h_{pci} = \frac{1}{R_c} \exp\left(\frac{R_{ei}}{R_c} \frac{1}{\sqrt{\pi}}\right)^2 \operatorname{erfc}\left(\frac{R_{ei}}{R_c} \frac{1}{\sqrt{\pi}}\right) \quad (6.13)$$

where R_{ei} , the instantaneous emulsion thermal resistance, is given by:

$$R_{ei} = \sqrt{\frac{\pi \tau_e}{k_e \rho_e c_{ps}}} \quad (6.14)$$

The maximum instantaneous coefficient occurs at the moment of initial contact between the emulsion packet and the heat transfer surface. At that instant τ_e is practically zero, which gives

$$h_{pci, \max} = \frac{1}{R_c} = \frac{k_g}{d_p / y} \quad (6.15)$$

When the emulsion phase covers the surface, $1 - f_o = 1$. According to our physical model, the instantaneous total coefficient then consists of the particle convective and the gas convective terms.

Therefore,

$$h_{i, \max} = h_{pci, \max} + h_{gci, \max} \quad (6.16)$$

However, since the gas convective term is always h_{mf} , we can

express the maximum instantaneous coefficient as

$$h_{i, \max} = \frac{k_g}{d_p/y} + h_{mf} \quad (6.17)$$

Analogously, for maximum instantaneous local coefficients, we have

$$h_{\theta i, \max} = \frac{k_g}{d_p/y_\theta} + h_{\theta mf} \quad (6.18)$$

To our knowledge, Baskakov et al. [12] are the only other investigators who used values of maximum instantaneous coefficients to acquire information about the contact resistance. However, they treated R_c in a different manner and worked with vertical cylinders in beds of fine particles only.

In Section IV. B we established that the maximum instantaneous local coefficients leveled off as soon as there was sufficient movement and replacement of particles at the tube surface. This occurred at velocities only slightly in excess of U_{mf} . Using these maximum values of $h_{\theta i}$ and the corresponding local values at minimum fluidization (see Figures 4.3, 4.5, 4.7, 4.9, 4.11, 4.13, and 4.15) in equation (6.18), we obtained information on the average gas layer thickness at various angular positions θ , shown in Table 6.1. Also presented in Table 6.1 are the values of y (and therefore δ^*) for the tube as a whole. These can be obtained from equation (6.17) using data for overall coefficients given in Figures 4.4, 4.6, 4.8, 4.10, 4.12, 4.14, and 4.16, or simply by averaging the values of y_θ according to the procedure described earlier--see equation (4.10).

The variations in the local and overall values of y (and δ^*) with particle size are small, and the mean values shown may be used with little error. The thickness of the gas layer is somewhat greater

Table 6.1. Information about the average thickness of the gas layer between the tube surface and particles (ST = single tube, TA = tube array).

		$\delta_{\theta}^* = \frac{d_p}{y_{\theta}}$					$\delta^* = \frac{d_p}{y}$
d_p (mm)	Tube configuration	Local values, y_{θ}					Overall value, y
		Angular position θ					
		180°	135°	90°	45°	0°	
0.37	ST	7	6	7	4.5	4	6
	TA	6	6	6	4	4.5	6.5
0.8	ST	7.5	6	6	4.5	4	5.5
	TA	7.5	5.5	5.5	4	3.5	5
1.3	ST	7	7.5	8	5	4	6.5
	TA	6.5	7	6.5	5	3.5	6
2.0	ST	9	6	7	5	4	6
	TA	9	6	6	4	3	5.5
2.85	ST	9	6	8.5	5.5	4	6.5
	TA	9	6	7	5	3.5	6
4.0	ST	9.5	7	8	6.5	4.5	7
	TA	10	7	8	6	4	7
6.6	ST	10.5	7	9	6.5	5	7.5
	TA	7	7	8	5.5	5	6.5
Range	ST	7-10.5	6-7.5	6-9	4.5-6.5	4.5	5.5-7.5
	TA	6-10	5.5-7	5.5-8	4-6	3-5	5-7
Mean value		8	7	7	5	4	6.0

at the 45° and 0° positions (bottom portion of the tube); this is consistent with the observations about the hydrodynamics in the lower region, as presented in Section IV. C.

As already pointed out, our main goal is the reliable prediction of the overall heat transfer coefficient, and we are therefore interested mostly in the average gas layer thickness for the tube as a whole (although local values will be discussed briefly on several later occasions). As seen in Table 6.1, a value of $\delta^* = d_p / 6.0$ characterizes the gas layer well, regardless of particle size or tube configuration. The contact resistance, therefore, increases linearly with particle diameter, thus imposing more severe limitations on heat transfer by conduction through the gas.

Going back to equations (6.17) and (6.18), we see that the maximum instantaneous values of heat transfer coefficients remain essentially unchanged with increasing gas velocity because both the contact resistance and the gas convective term are constant. If the gas convective contribution were to rise with U , as was assumed in a recent study by Glicksman and Decker [49, 50], the maximum instantaneous coefficients--local and overall--would rise accordingly.

The time-averaged overall particle convective coefficient can now be expressed as:

$$h_{pc} = \frac{1}{\frac{d_p}{6.0k_g} + 0.5 \sqrt{\frac{\pi \tau_e}{k_e \rho_e c_{ps}}}} \quad (6.19)$$

The knowledge of the gas layer thickness opens the door to the evaluation of the magnitudes of two series resistances comprising the particle convective component of heat transfer.

Using the overall average emulsion residence times, given in Figure 4.27, to evaluate the emulsion packet resistance, we obtained

the graph shown in Figure 6.2. With increasing particle diameter, the contact resistance constitutes a rapidly increasing portion of the total particle convective resistance. Practically regardless of the gas velocity, we can conclude that, under our operating conditions, the contact resistance can be used in place of the total resistance for particles greater than 1 mm. In other words, for diameters exceeding 1 mm, the particle convective component is independent of the emulsion behavior at the surface--emulsion residence time and bubble frequency do not affect the heat transfer process. We actually use this statement as a definition of large particles from the aspect of heat transfer behavior. Fine particles, on the other hand, are those for which the emulsion packet resistance is significantly greater than the contact resistance ($d_p < 0.2-0.3$ mm in our case). For the case of intermediate particles, the two resistances are comparable in magnitude.

The result that the emulsion packet resistance becomes negligible for large particles is tied to the fact that the particle remains essentially isothermal while in contact with the surface (see discussion in Section V.B, as well as Figure 5.2). The transient component of heat transfer then disappears from the picture.¹¹

¹¹ When smaller particles contact the hot heat transfer surface, several rows of particles are heated, and the emulsion packet is considered a continuum with effective thermal conductivity k_e . However, with increasing particle size, only one or a few rows are heated during the time of packet contact, and the effective thermal conductivity then starts approaching the thermal conductivity of solid, k_s . For a very large particle, which constitutes a packet by itself, $k_e = k_s$ and $\rho_e = \rho_s$. Care was taken of this in the calculation leading to Figure 6.2; however, the final outcome is rather insensitive to the value of k_e used-- $d_p = 1$ mm is the boundary of the large particle range.

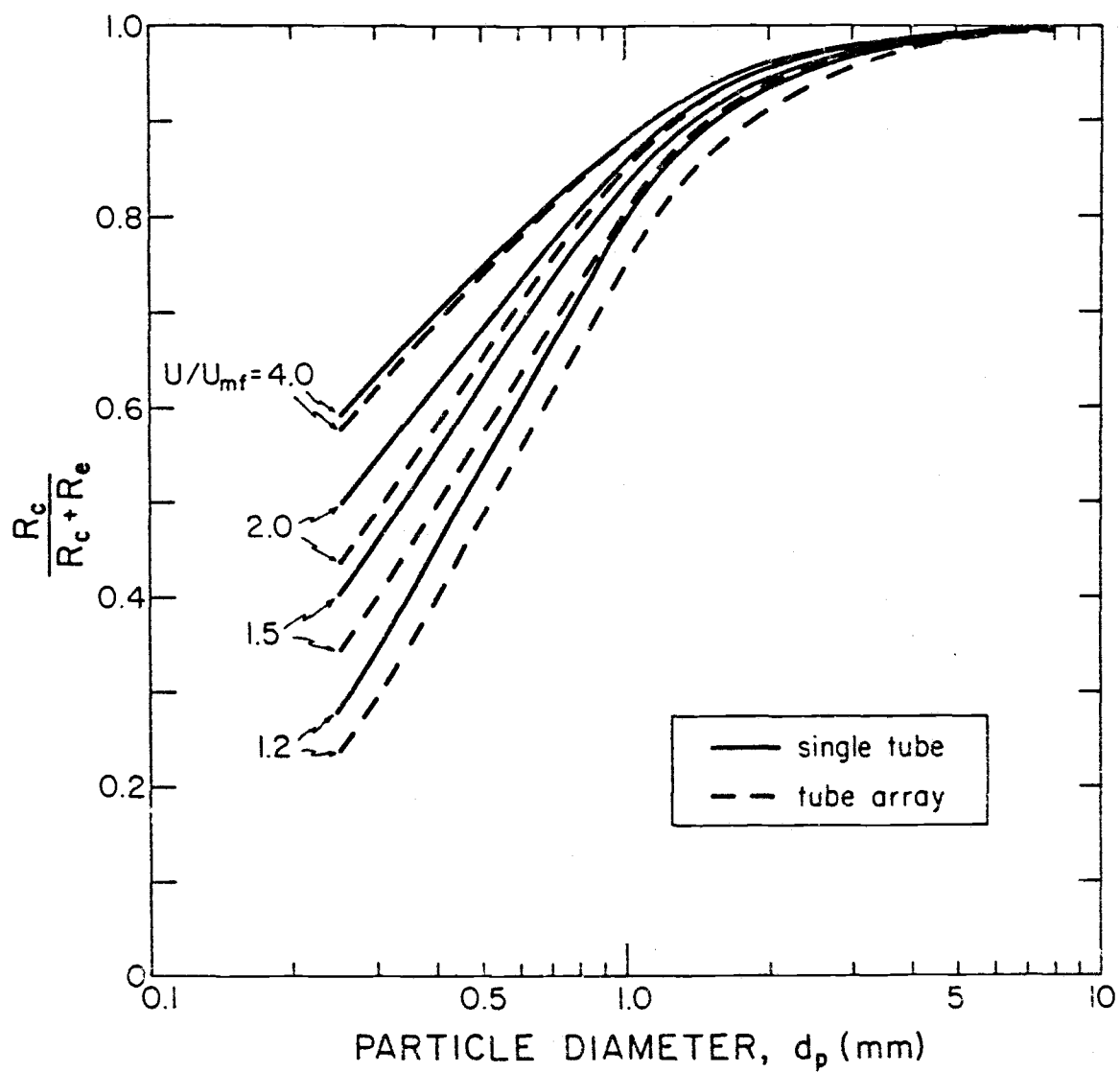


Figure 6.2. Fraction of total particle convective thermal resistance, $R_c + R_e$, due to the contact resistance, $R_c = d_p / 6.0k_g$, as a function of particle size, for our fluidizing conditions.

Figure 6.2 applies only to our experimental conditions. To obtain the lower boundary of the large particle region for the general case, we can proceed in two ways. A transient heating (or cooling) diagram of the type shown in Figure 5.2 can be constructed for any given case, and theoretical curves--obtained from transient conduction charts [1, 76]--can be compared with expected or measured emulsion residence times. If the particle residence time sufficiently exceeds the time necessary to change its surface temperature by 10 or 20%, the particle can be considered large. A more convenient method, using the particle thermal time constant, was recently proposed by Glicksman and Decker [49, 50]. We modified their approach in obtaining Figure 6.3 where τ_p is plotted as a function of d_p , with $\rho_s c_{ps} / k_g$ as a parameter (see Appendix G for details).

Two values of the parameter correspond to dolomite and quartz sand used in our experiments, while the third characterizes a hot fluidized bed operating at 1000°C (mean gas film temperature = 525°C). These are two extremes which may be encountered in practice (the value of the parameter is not affected significantly by pressure). The shaded region shows the range of particle residence times measured in our experiments; that is also the range to be expected in air-fluidized beds in general, on the basis of reported bubble frequencies [23, 25, 29, 40, 67, 97]. If $\tau_p \gg \bar{\tau}_e$, the particles are large--this is equivalent to stating that $R_c \gg R_e$ (or $R_e \approx 0$). If $\tau_p \ll \bar{\tau}_e$, we are dealing with fine particles ($R_e > R_c$), and h is a function of the residence time. Figure 6.3 shows that, in general, particles may be considered large if $d_p > 1$ mm and small if $d_p < 0.4$ mm. Intermediate particles are in between (in this case, $R_e \approx R_c$). We have been using this classification from the outset of our work.

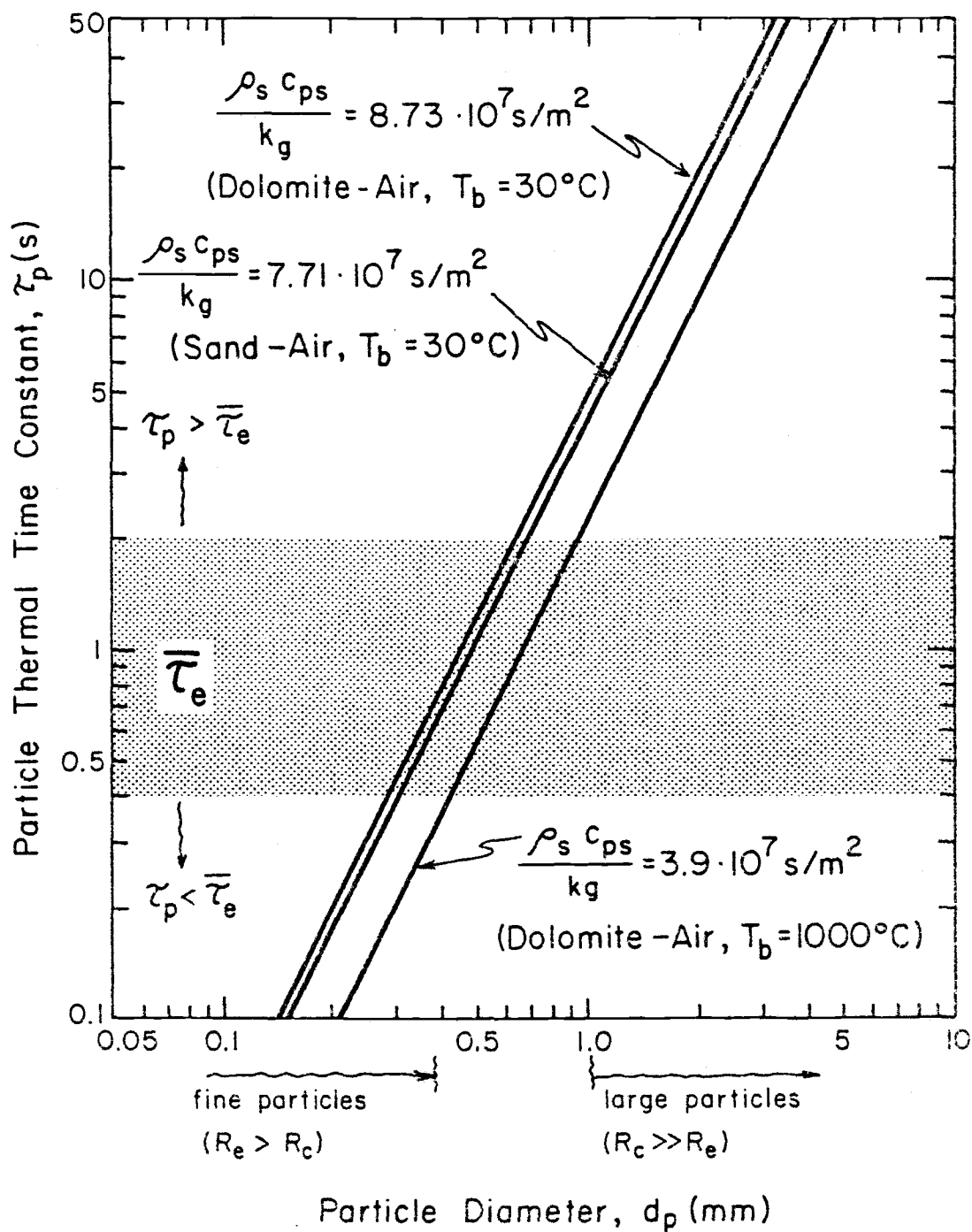


Figure 6.3. Particle thermal time constant as a function of particle size, and a comparison with emulsion (particle) residence times.

Gas Convective Component

Our experimental coefficients at minimum fluidization form a data base from which a correlation for the gas convective heat transfer coefficient can be developed. Unfortunately, additional h_{mf} data with which the correlation could be checked are practically impossible to find in literature. In all studies with horizontal tubes summarized in Table 2.1, the authors report only data for $U/U_{mf} > 1.1$. The single exception is a quiescent bed coefficient for $d_p = 0.885$ mm, reported by Xavier and Davidson [91].

As noted in Section A, quiescent bed coefficients for beds with vertical tubes have attracted the attention of several investigators. Correlations for h_{mf} are usually given in terms of the Archimedes number, Ar , which is a combination of the drag coefficient and the particle Reynolds number corresponding to the bed flow conditions. The heat transfer coefficient is thus related to the physical properties of the particles and to the thermal and physical properties of the gas. Table 6.2 lists d_p , Ar , and $Re_{p,mf}$ for what appear to be the only data on h_{mf} in beds with horizontal tubes. The corresponding quiescent bed Nusselt numbers are shown by points in Figure 6.4, where $Nu_{p,mf}$ is plotted as a function of Ar .

In order to obtain a correlation for h_{mf} , we examined the existing correlations for vertical tubes proposed by Baskakov and Suprun [13], Gabor [37], Baskakov et al. [12], and Botterill and Denloye [21, 33]. Intuitively, we would expect the quiescent bed coefficients for vertical and horizontal tubes to be rather similar. The differences in the fluid dynamic behavior between the two cases could, however, become quite significant when bubbling starts.

The correlation of Baskakov and Suprun [13],

Table 6.2. Information related to the gas convective component of heat transfer from (to) horizontal tubes.

Source	Material	d_p (mm)	Ar	U_{mf} (m/s)	$Re_{p, mf}$	Experimental		Baskakov-Suprun correlation	
						h_{mf} (W/m ² °C)	$Nu_{p, mf}$	h_{mf} (W/m ² °C)	$Nu_{p, mf}$
Our study	quartz sand	0.37	3.9×10^3	0.15	3.11	48.2	0.64	53.2	0.71
		0.8	3.93×10^4	0.46	20.59	73.2	2.11	70.9	2.05
		1.3	1.68×10^5	0.70	50.92	84.0	3.94	85.0	3.99
	dolomite	2.0	6.25×10^5	1.14	127.59	103.2	7.45	101.5	7.33
		2.85	1.81×10^6	1.44	229.65	113.4	11.7	116.2	11.96
		4.0	5.00×10^6	1.83	409.02	125.9	18.2	132.1	19.08
		6.6	2.25×10^7	2.44	901.16	133.8	31.9	158.0	37.6
Xavier and Davidson [91]	sand	0.885	5.5×10^4	0.47	23.28	82.0	2.62	75.1	2.40

(Note: 25.4 mm = 1 in; 1 m/s = 3.28 ft/s; 5.67 W/m²°C = 1 Btu/hr ft²°F)

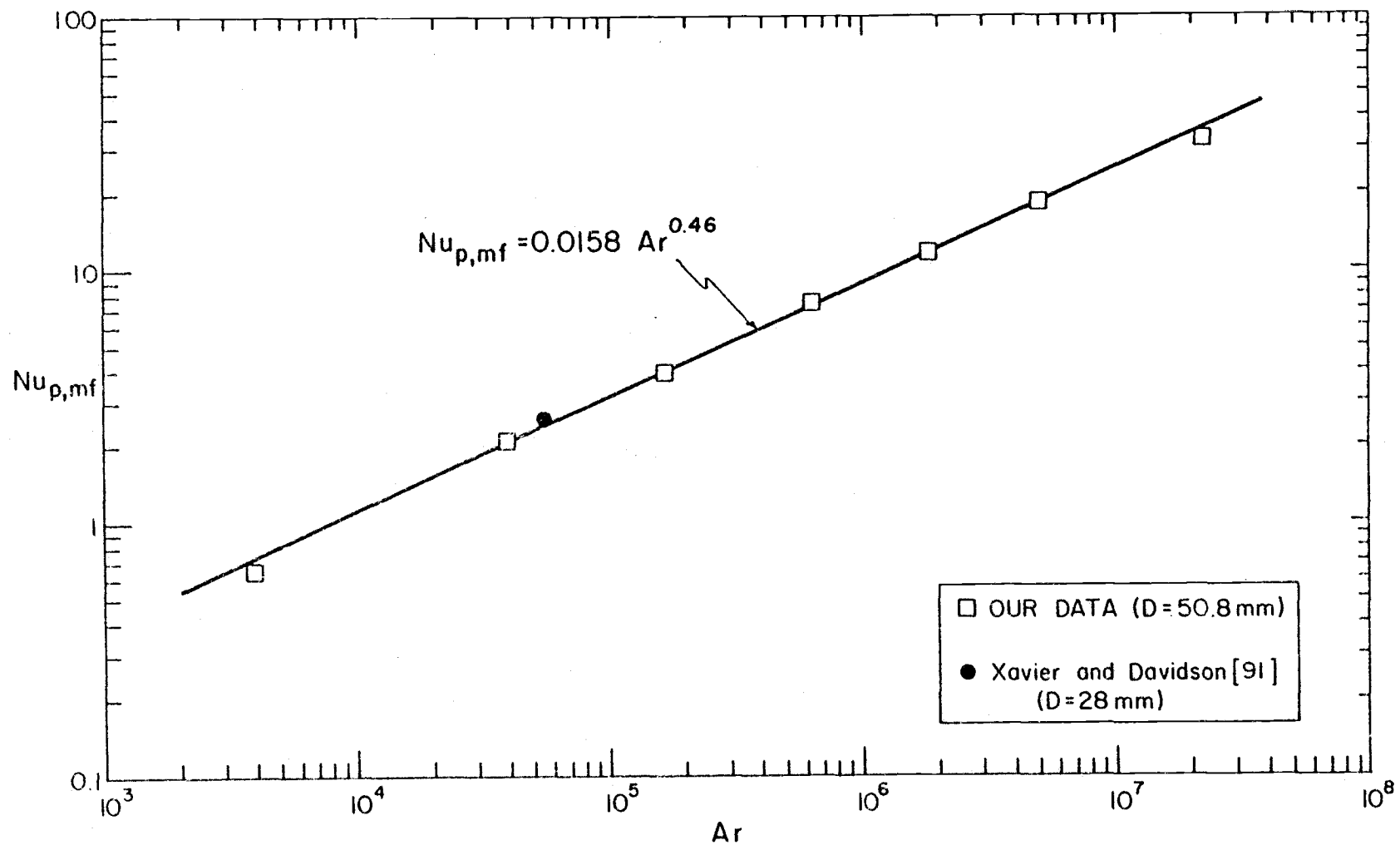


Figure 6.4. Gas convective Nusselt number as a function of Archimedes number in air-fluidized beds.

$$Nu_{p,mf} = 0.0175 Ar^{0.46} Pr^{0.33} \quad (6.20)$$

gives an excellent fit to the data given in Table 6.2 (other correlations were not as successful). For air -- $Pr = 0.73$ -- equation (6.20) becomes:

$$Nu_{p,mf} = 0.0158 Ar^{0.46} \quad (6.21)$$

Figure 6.4 shows the agreement between prediction and experiment. The Archimedes number is related to $Re_{p,mf}$ by the Wen and Yu correlation [89].

It appears, therefore, that equation (6.20) shows excellent promise for predicting the gas convective component in general. On the basis of our experiments and the apparent negligible influence of tube diameter (see discussion on page 102), the Baskakov-Suprun correlation should apply for single horizontal tubes and tube arrays with a pitch/diameter ratio ≥ 2 , when the tube diameter is greater than 20 mm.

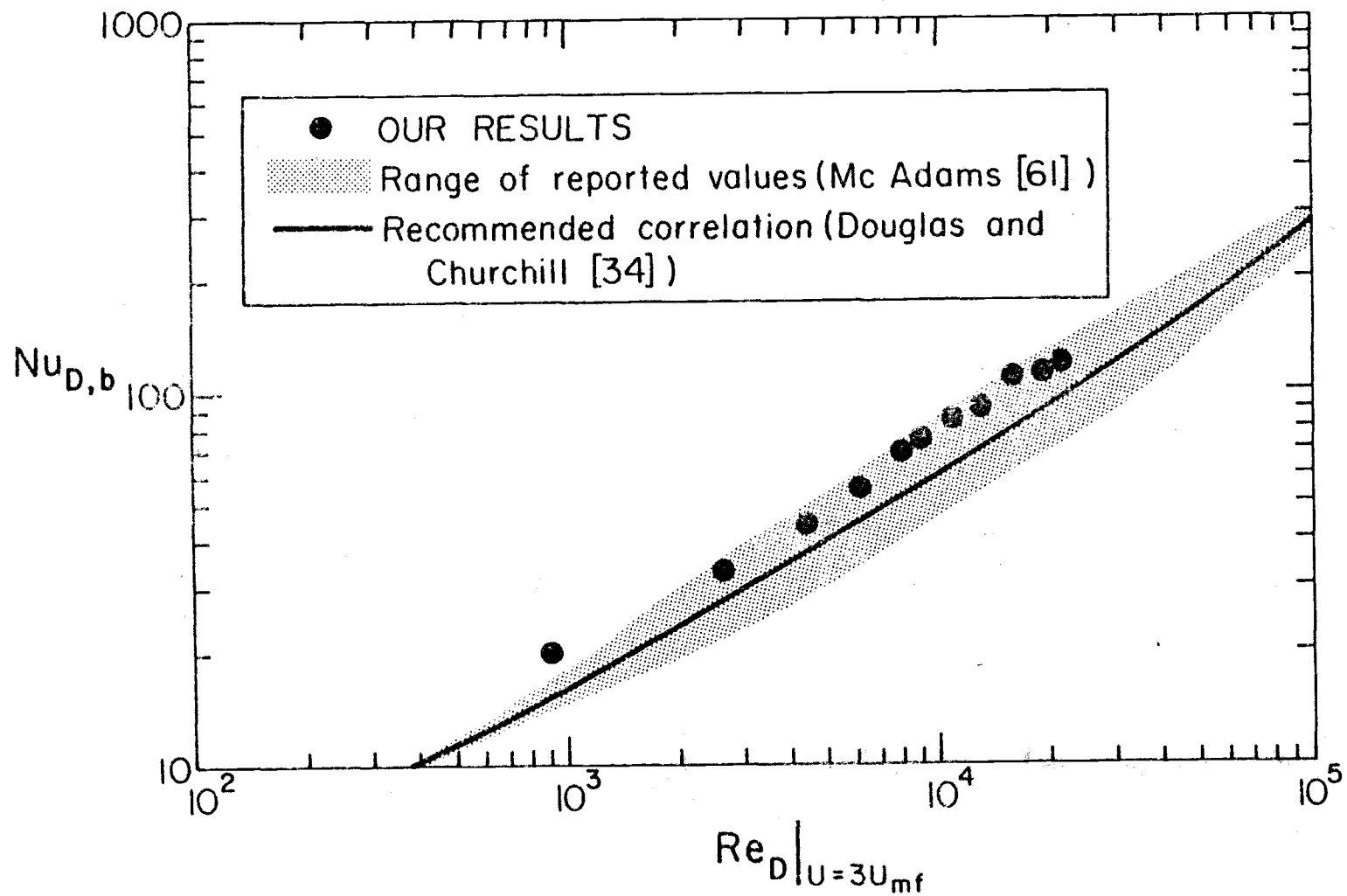
It is interesting to compare the predictions of $Nu_{p,mf}$ from Figure 6.4 with the values of Nu_p predicted by the Adams model (Figure 5.9). For particles greater than 2 mm ($Re_p > 127$ or $Ar > 6.25 \times 10^5$), the difference is less than 15%, which is to be expected when heat transfer behavior of large particles above U_{mf} is considered (see Figure 4.19 and discussion in Section IV.B). The added advantage of the Adams model is that it can give relatively good estimates of local coefficients at U_{mf} ; however, it does not apply for smaller particle diameters. The Baskakov-Suprun correlation successfully predicts the time-averaged overall quiescent bed coefficient for both large and intermediate particles.

Bubble Component

In Section V.D we showed that the Adams model was successful in predicting the local heat transfer coefficient to a bubble contacting the tube. The model assumes that the bubble is slow, i.e., the bubble throughflow is significantly higher than the bubble rise velocity, and that gas flows through the bubble with a velocity of $3 U_{mf}$ (a result of Davidson and Harrison's theoretical analysis [31]). We shall use this assumption in our model since it ought to apply in large- and intermediate-particle beds. From a heat transfer standpoint, it does not matter whether all of the gas is flowing through the bubble or whether some of it is recirculating through the cloud (see the discussion on slow and fast bubbles by Catipovic et al. [26]). In beds of fine particles, where bubbles are fast, the bubble component is negligible due to very low gas velocities.

In order to calculate the time-averaged overall coefficient to (from) a bubble or slug, h_b , we shall assume that, when a bubble covers the immersed tube, heat is transferred convectively to (from) the gas which flows around the tube at $3 U_{mf}$ ¹². The case of heat transfer in forced gas convection past a single horizontal cylinder has been treated extensively in literature [34, 56, 61, 88], and several correlations are available. Figure 6.5 shows the convective Nusselt number based on cylinder (tube) diameter, Nu_D , as a function of Re_D . Both the range of results reported by numerous investigators [61] and a correlating curve recommended by Douglas and Churchill [34] are presented. The points indicate the values of Nu_D obtained in forced convection experiments in our fluidization vessel. They lie

¹²As a result, h_b --which is also $h_{i,min}$ --will be independent of the superficial gas velocity. This is exactly what the experimental data in Section IV.B indicate.



in the upper portion of the shaded region, somewhat above the suggested curve (15-25%), which is most likely a result of the constriction in our vessel of limited width (see a more detailed discussion in Appendix D). When comparing prediction vs. experiment for the case of our fluid-bed heat transfer data, we shall use our values of $Nu_{D,b}$. However, in the general case, we suggest the use of the Douglas and Churchill correlation.

The values of the Reynolds number shown in Figure 6.5 are those which ought to be of importance in fluidized beds in general. For this range, Douglas and Churchill suggested the following equation (the symbols are changed to apply to our bubble heat transfer considerations):

$$Nu_{D,b} = 0.46(Re_D|_{3U_{mf}})^{0.5} + 0.00128(Re_D|_{3U_{mf}}) \quad (6.22)$$

Strictly speaking, equation (6.22) is applicable to air only. If a gas with a sufficiently different Prandtl number is used, $Nu_{D,b}$ should be multiplied by the factor $1.1 Pr^{0.33}$ [88].

Information on the Emulsion Contact Fraction

Our model requires the knowledge of the fraction of time which the tube spends in contact with the emulsion phase, $1 - f_o$. This quantity gives an indication of the time-averaged voidage in the vicinity of the tube. In Section IV.D we pointed out that there are very significant differences between this local voidage around the tube and the overall bed voidage which is usually used in heat transfer correlations. If the quantities $1 - f_o$ and $1 - \delta$ are compared, we see that the former is relatively insensitive to changes in the gas velocity above a certain low value of U/U_{mf} (Figure 4.28), while the latter

is a strong function of the superficial velocity, especially for the tube array case (Figure 4.32). This is a very important point since $1 - \delta$ is relatively easy to measure in a fluidized bed under practically any conditions (pressure measurements)--and is therefore used extensively in various analyses--while data on $1 - f_o$ are difficult to come by. However, only the information on local tube voidage is of significance for the heat transfer analysis because it reflects the corresponding fluid dynamic picture. The described differences attest to the importance of local measurements of the type performed in our study, and may be an explanation for the inadequacies of existing heat transfer correlations which will be discussed in Section VII. C.

In an attempt to obtain a general correlation for $1 - f_o$, we replotted the values shown in Figure 4.28 as a function of the excess gas velocity, $U - U_{mf}$, which is an indication of the bubble volume flow rate. Figure 6.6 presents the interesting result showing the emulsion contact fraction to be independent of particle size when plotted in this manner. For the single tube case, the equation

$$1 - f_o = 0.48 + \frac{0.065}{(U - U_{mf}) + 0.125} \quad (6.23)$$

gives the best fit through the data points. For the tube array case, the values of $1 - f_o$ are always about 7% lower:¹³

$$1 - f_o = 0.45 + \frac{0.061}{(U - U_{mf}) + 0.125} \quad (6.24)$$

¹³ As indicated in footnote 1 (page 57), the difference between the two cases could be accounted for by the increased gas velocity in the bed due to the presence of the array. However, this velocity correction is difficult to quantify.

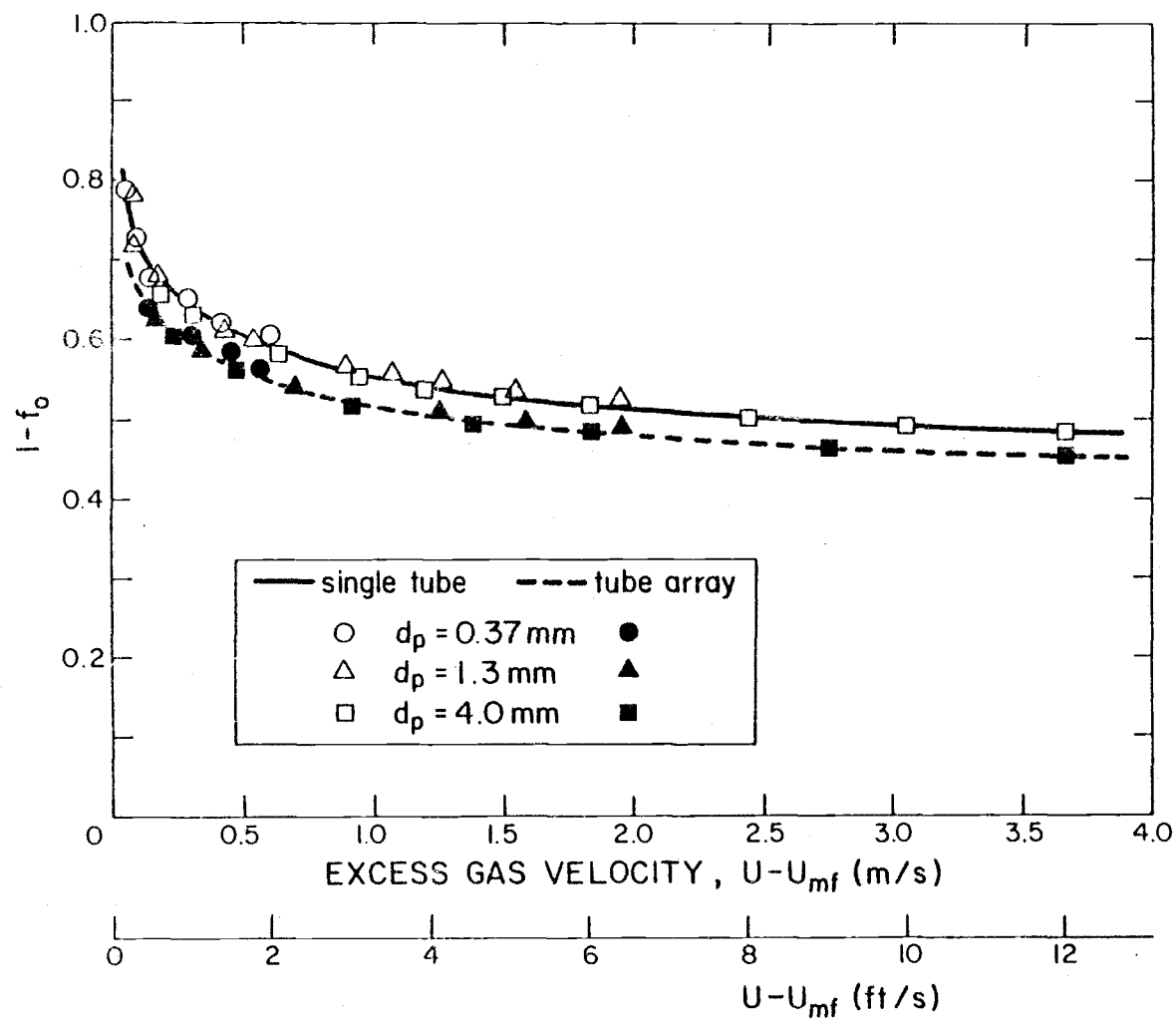


Figure 6.6. Overall emulsion contact fraction (fraction of time which tube spends in contact with emulsion) as a function of the excess gas velocity.

It should be noted once again that equations (6.23) and (6.24) (indeed, all the ideas developed in this chapter), are only valid up to the turbulent regime where the bubble-emulsion structure breaks up. The exact velocity at which the bed undergoes a transition to this regime is difficult to predict; the shift seems to occur at a lower multiple of U/U_{mf} for large particles than for smaller ones [26]. Bar-Cohen et al. [7] tentatively suggest that the turbulent regime is reached when $U = 0.5U_t$.

Although verified only in a cold bed at atmospheric pressure (in the size range $0.37 \text{ mm} < d_p < 6.6 \text{ mm}$), equations (6.23) and (6.24) can be considered a step in the right direction from the aspect of heat transfer modeling in beds containing horizontal tubes. Their generality remains to be tested.

C. Special Cases

Now that we have gained enough insight into the various components of the proposed model, we can examine equation (6.11) more carefully and see how it simplifies in special cases.

Fine Particles

For $d_p < 0.4 \text{ mm}$, the gas convective and bubble components are negligible ($h_{mf} \approx 0$ and $h_b \approx 0$), and equation (6.11) reduces to

$$h = \frac{1 - f_o}{\frac{d_p}{6.0k_g} + 0.5 \sqrt{\frac{\pi \tau_e}{k_e \rho_e c_{ps}}}} \quad (6.25)$$

The emulsion thermal resistance, R_e , comprises a major portion of the total resistance, and experimental information on emulsion residence times and/or bubble frequencies is necessary. Reliable a priori prediction of h is impossible without such data.

Fine-particle heat transfer to immersed surfaces has been reviewed extensively by Gelperin and Ainshtein [42] who showed that an equation similar to (6.25) is successful in predicting heat transfer coefficients to (from) a variety of objects placed in the bed. There is no reason to doubt that equation (6.25) will be successful for fine-particle beds with horizontal tubes in general.

Intermediate Particles

For particles with $0.4 \text{ mm} < d_p < 1 \text{ mm}$, h_{mf} and h_b still contribute noticeably less than the particle convective component; however, they should be included:

$$h = \frac{1-f_o}{\frac{d_p}{6.0k_g} + 0.5 \sqrt{\frac{\pi \bar{\tau}_e}{k_e \rho_e c_{ps}}}} + (1-f_o)h_{mf} + f_o h_b \quad (6.26)$$

The knowledge of emulsion residence times is again required. However, since R_c is of at least the same magnitude as R_e , $\bar{\tau}_e$ could possibly be estimated from the range indicated in Figure 6.3 without introducing a gross error in the heat transfer coefficient. Comparison of model predictions for intermediate particles with experimental results will be made in Chapter VII.

Large Particles

The case of large particles ($d_p > 1 \text{ mm}$) is of particular interest for coal combustion applications. Since $R_c \gg R_e$, the emulsion resistance drops out, and heat transfer coefficients can be accurately predicted without any knowledge of $\bar{\tau}_e$ and/or n . Gas convective and bubble contributions become very important. The heat transfer coefficient is expressed as:

$$h = (1-f_o) \frac{6.0k_g}{d_p} + (1-f_o)h_{mf} + f_o h_b \quad (6.27)$$

In terms of particle Nusselt numbers, equation (6.27) becomes

$$Nu_p = (1-f_o)6.0 + (1-f_o)Nu_{p,mf} + f_o Nu_{p,b} \quad (6.28)$$

Since the correlation for the bubble contribution is given in terms of $Nu_{D,b}$, we can also write

$$Nu_p = (1-f_o)6.0 + (1-f_o)Nu_{p,mf} + f_o \frac{d_p}{D} Nu_{D,b} \quad (6.29)$$

All terms in equation (6.29) can be calculated directly from equations (6.20), (6.22), and (6.23) or (6.24), or obtained graphically from Figures 6.4, 6.5, and 6.6. Strictly considering, equations (6.27) and (6.29) are valid only when $U > 1.2 U_{mf}$ -- R_e is assumed to be zero, but it could still contribute to h for $U/U_{mf} < 1.2$ (see Figure 6.2). Chapter VII will analyze the agreement between predictions based on these equations and experimental data.

D. Significance of the Model

If verified by experiments over a wide range of fluidizing conditions, the proposed model could have far-reaching significance. In addition to predicting the time-averaged overall coefficient, it can predict the maximum instantaneous value--see equation (6.17):

$$h_{i, \max} = \frac{6.0k_g}{d_p} + h_{mf} \quad (6.30)$$

as well as the minimum instantaneous value:

$$h_{i, \min} = h_b \quad (6.31)$$

A complete picture of the heat transfer process could thus be obtained, with information available on several important design factors.

As mentioned earlier, the entire analysis of this chapter applies to local coefficients as well as overall coefficients--see equation (6.12). However, in such a case it is difficult to quantify all of the components of the model. While the values of y_θ may be obtained from Table 6.1, and the values of $h_{\theta mf}$ for large particles may be estimated roughly from the Adams model (Figure 5.9), it would be a practically impossible task to reliably quantify $(1-f_o)_\theta$, $h_{\theta mf}$, and $h_{\theta b}$ in the general case. We shall therefore limit ourselves to the overall coefficients, with only a short qualitative discussion on local data being given in the next chapter.

VII. COMPARISON BETWEEN MODEL PREDICTIONS AND EXPERIMENTAL RESULTS

The theoretical model developed in Chapter VI will now be tested with our data, as well as with data of other investigators for intermediate and large particles. The amount of desired heat transfer information available in literature is rather limited.

A. Our Results

Intermediate Particles

Figure 7.1 shows the agreement between our results for 0.37 mm and 0.8 mm particles--with both the single tube and the tube array cases considered--and the corresponding predictions of the proposed model. Predicted values were calculated using equation (6.26), with the individual terms obtained from equations (6.21), (6.23) or (6.24), and Figure 6.5. Average emulsion residence times were taken from Figure 4.27.¹⁴

Model predictions for the time-averaged overall coefficient generally lie within less than 6% of the experimental data. The model correctly predicts the occurrence of a maximum in h .

¹⁴Strictly considered, the average emulsion residence time which goes into equation (6.26) should be the root-square average--see the development of the original packet theory by Mickley et al. [66]. This average is statistically weighed in favor of longer residence times and has been used in some theoretical analyses of fine-particle heat transfer [70,77]. However, since our method of estimating the emulsion residence times tends to slightly overpredict $\bar{\tau}_e$ (see Section IV.C), we consider our arithmetic average to be a good approximation of the root-square average.

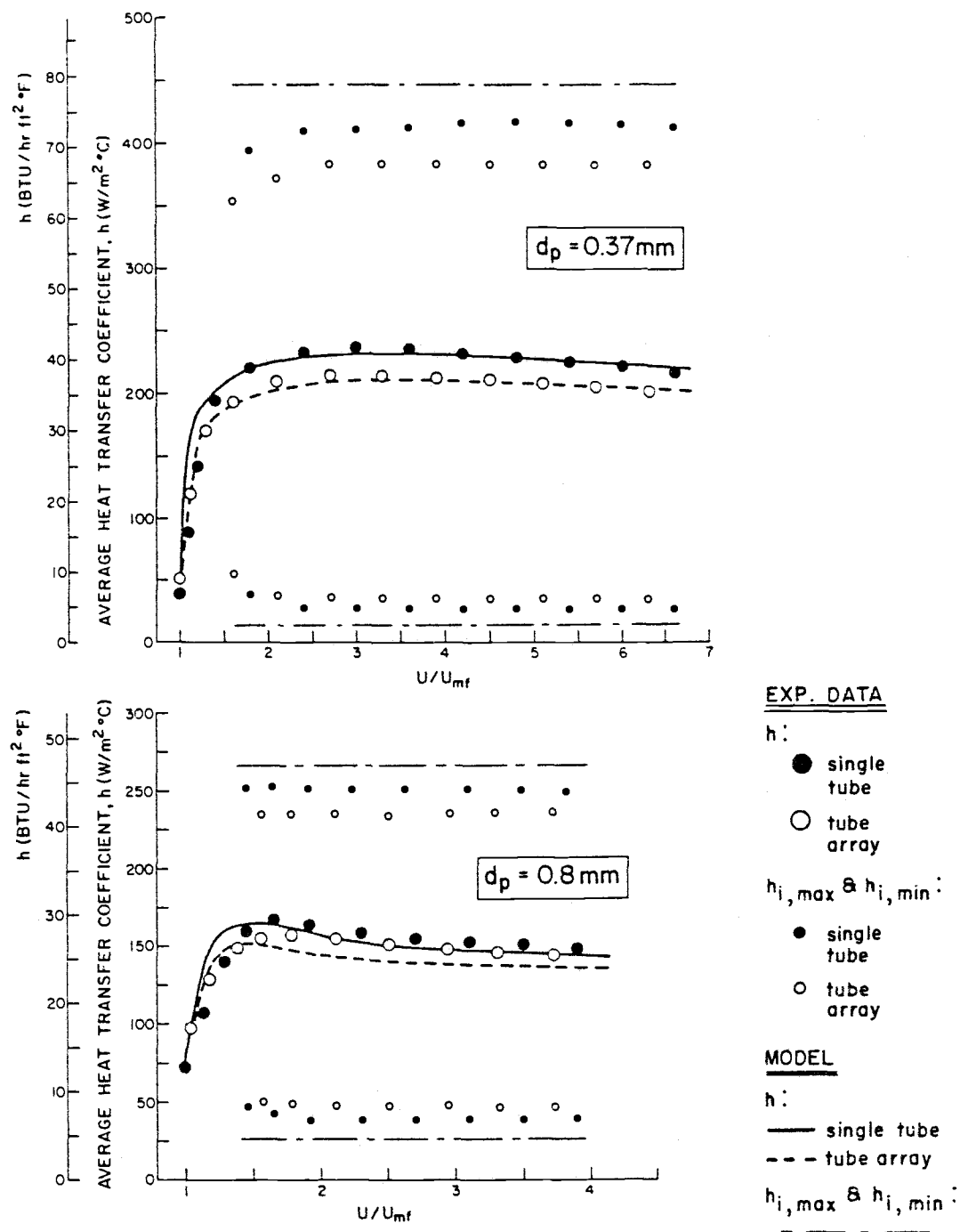


Figure 7.1. Comparison of model predictions with our experimental results for intermediate particles.

The maximum and minimum instantaneous coefficients are also successfully predicted (from equations (6.30) and (6.31)). The value of $h_{i, \max}$ occurs at the moment of initial contact between the tube surface and an emulsion packet (once the contact is established, the instantaneous coefficient starts decreasing). The model prediction of $h_{i, \max}$ is within 5-12% of the measured value, depending on whether the single tube or the tube array is under consideration. The minimum instantaneous value, $h_{i, \min}$, occurs when a bubble engulfs the tube. It is underpredicted by the model, but the discrepancy can easily be explained. As mentioned in Section V.D, there are indications that bubbles are not particle-free as assumed--particles seem to "rain" through them, probably accounting for the increased $h_{i, \min}$.

We were successful in predicting the values of h because of the available data on emulsion residence times. If this information is not available, a rough estimate of h can still be made. Namely, for intermediate particles R_e is in the range $(0.3-1)R_c$ (see Figure 6.2), and the heat transfer coefficient is not as sensitive to an error in $\bar{\tau}_e$ as in the case of fine particles (where $R_e > R_c$). The residence time could be estimated from the general range shown in Figure 6.3. If we assume $\bar{\tau}_e = 1$ s for the whole range of fluidizing velocities, we would overpredict h at low multiples of U/U_{mf} (by 35% for $d_p = 0.37$ mm and by 12% for $d_p = 0.8$ mm, when $U/U_{mf} = 1.2$) and underpredict it at higher velocities (by 13% for $d_p = 0.37$ mm and by 7% for $d_p = 0.8$ mm, when $U/U_{mf} > 4$).

Large Particles

Figure 7.2 displays the agreement between our results and model predictions for particles larger than 1 mm. Again, both the

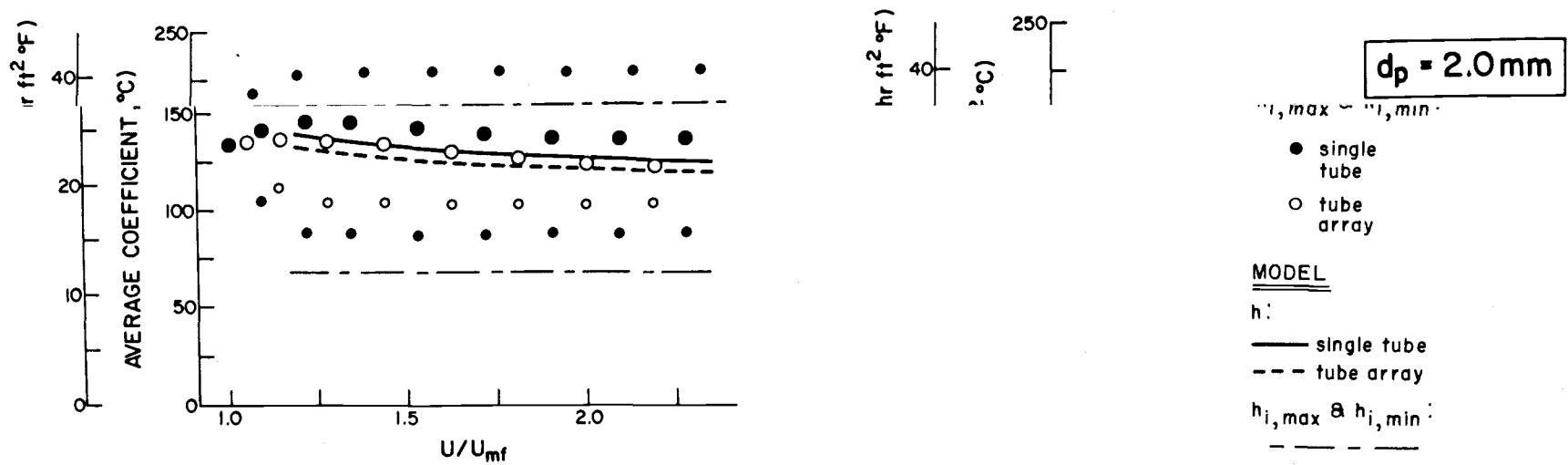


Figure 7.2. Comparison of model predictions with our experimental results for large particles.

single tube and the array cases are shown. Values of h are predicted from equation (6.29), which is used in conjunction with equations (6.21), (6.23) or (6.24), and Figure 6.5.

Our model underpredicts the time-averaged overall coefficients by less than 10%. As pointed out in Section VI. C, in the case of large particles the model is valid when $U > 1.2 U_{mf}$. As a result, it does not predict that there should be a maximum in h (which generally occurs at a velocity slightly below $1.2 U_{mf}$, if $d_p > 1 \text{ mm}$). The prediction at $1.2 U_{mf}$ is, in fact, the maximum predicted value.

The maximum instantaneous values are predicted to within less than 8% of the actual data. These coefficients occur not only at the moment of first contact between the heat transfer surface and the emulsion phase, but practically throughout their interaction. This behavior is a direct result of the disappearance of the unsteady-state conduction mode of heat transfer.

The minimum instantaneous coefficients are underpredicted by as much as 30%, and this discrepancy is the cause of the slight underprediction in the time-averaged overall coefficients. In addition to the phenomenon of particles raining throughout the bubbles (as explained for intermediate particles), an additional explanation for the discrepancy is possible in the case of coarser solids. Namely, for $d_p > 1 \text{ mm}$, the transition to the rapidly growing bubble regime occurs at low multiples of U/U_{mf} -- see Figure 5.4. The large, exploding bubbles characteristic for this region can promote short-circuiting of the gas, causing the bubble throughflow to reach values in excess of $3 U_{mf}$. This topic is discussed by McGrath and Streatfield [63], Geldart [41], Cranfield and Gliddon [30], and McGaw [62], with values as high as $5 U_{mf}$ being suggested. The experimental values of h_p for the tube array lie above the corresponding

values for the single tube; this difference is explained in footnote 13 (page 134).

General Comments about Time-Averaged Overall Coefficients

The good agreement between theoretical predictions and experimental data is an indication that all components of the heat transfer process were properly accounted for by the model. For further illustration, we shall compare model prediction vs. experiment for each of the three contributions to the maximum time-averaged overall coefficient, h_{\max} . Table 7.1 lists the values of U/U_{mf} at which h_{\max} occurs, for both the single tube and the tube array. The actual values of h_{\max} as a function of d_p are given in Figure 4.22. Figure 7.3 shows the excellent agreement of predictions for the particle convective, gas convective, and bubble contributions with the corresponding experimental values, as a function of particle size. The graph is constructed for the single tube case, but corresponding percentages for the array are very similar.

Table 7.1. Value of U/U_{mf} corresponding to the maximum time-averaged overall coefficient.

d_p (mm)	U/U_{mf}	
	Single tube	Tube array
0.37	3.12	3.12
0.8	1.65	1.75
1.3	1.16	1.35
2.0	1.16	1.18
2.85	1.15	1.20
4.0	1.16	1.16
6.6	1.25	1.20

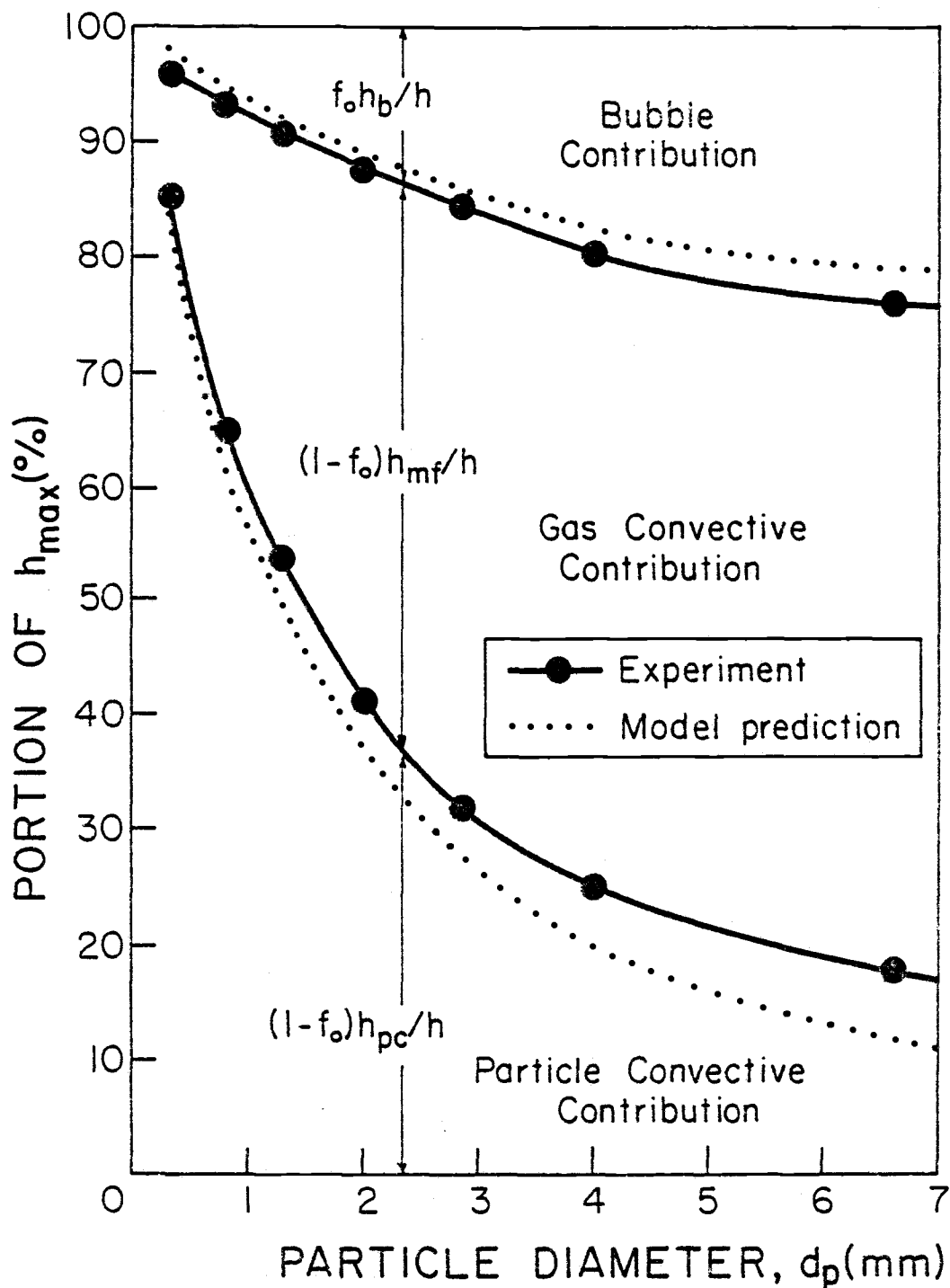


Figure 7.3. Comparison between model predictions and experimental results for each of the three contributions to the maximum time-averaged overall coefficient.

Figure 7.3 provides good insight into the effect of particle size on the heat transfer coefficient and explains some of the results discussed in Chapter IV. The large rise from h_{mf} to h_{max} in beds of smaller particles (see Figures 4.19-4.21) is due to the fact that the particle convective component, which is absent at minimum fluidization, constitutes a major portion of h when fluidization gets well under way. In large-particle beds, the corresponding rise is small because the gas convective component, which represents the quiescent bed coefficient, contributes very significantly to the overall coefficient. The role of h_{pc} decreases noticeably with increasing particle size.

The bubble contribution should not be neglected in large-particle beds since it can amount to 20% of the total transfer. However, for $d_p < 0.4$ mm, both h_b and h_{mf} contributions can be neglected, as was done in equation (6.25).

The trend in values of h_{max} with a change in particle size, shown in Figure 4.22, is easily explained by our model. When $d_p < 2$ mm, the particle convective coefficient represents the dominant component; its actual value decreases with an increase in d_p . When $d_p > 2$ mm, the gas convective coefficient takes over; its value rises with particle size.

Figures 7.1 and 7.2 indicate that the model is successful in predicting the very gradual decrease in h after h_{max} is reached. The main reason for this important finding is the use of information on the voidage in the immediate vicinity of the tube. Had we used the average voidage data for the bed as a whole, the predicted values of h would have decreased significantly with an increase in gas velocity.

Comments about Local Coefficients

In Chapter VI we stated that the proposed model is perfectly applicable for calculating local heat transfer coefficients. Indeed, if our local data on y_θ , $\bar{\tau}_{e\theta}$, $h_{\theta mf}$, $h_{\theta b}$, and $(1-f_o)_\theta$ are used in equation (6.12), the predicted values fall within 10-15% of the local heat transfer results. However, it appears practically impossible to obtain general correlations for the above-mentioned local quantities. We shall therefore not dwell on this matter, but we will illustrate the ability of equation (6.12) to explain the interesting local behavior described in Chapter IV.

Figure 4.18 shows that the local coefficient at the 180° position increases spectacularly with U/U_{mf} for small particles, while it is almost unaffected by gas velocity for large d_p . The corresponding changes in the average emulsion residence times and the emulsion contact fractions are illustrated in Figures 4.29 and 4.30, respectively. For both $d_p = 0.37$ mm and $d_p = 4.0$ mm, $\bar{\tau}_{e180^\circ}$ changes substantially with U/U_{mf} , while $(1-f_o)_{180^\circ}$ is not particularly affected. What, then, causes the difference in the heat transfer behavior between the two cases?

For small particles, h_{180° is a strong function of $\bar{\tau}_{e180^\circ}$ --see equation (6.25)--and a sharp decrease in the average emulsion residence time causes a very noticeable increase in h_{180° . For particles larger than 1 mm, h_{180° is practically independent of $\bar{\tau}_e$ --see equation (6.27)--and drastic changes in emulsion residence times are not reflected in the local heat transfer behavior.

B. Results of Other Investigators

In order to test the applicability of our model under fluidizing conditions different from those used in the current study, theoretical predictions will be compared with data of other investigators. Most of the previous work in beds with horizontal tubes has dealt with fine particles; of the studies listed in Figure 2.1, only the data of Xavier and Davidson [91] and Canada et al. [23, 78] can be used for a meaningful comparison with our model.

Results of Xavier and Davidson

Xavier and Davidson [91] fluidized sand particles ($d_p = 0.385$ and 0.885 mm) in a 0.305 m square bed, with 28 mm diameter cylinders immersed on a 76 mm triangular pitch. Only the central cylinder, located 0.4 m above the distributor, was heated and used for heat transfer measurements. Their experimental conditions were therefore somewhat similar to ours for intermediate particles.

The agreement between the authors' results and our tube array data for 0.37 mm and 0.8 mm particles is remarkable, with differences below 5% . Our proposed model is therefore in good agreement with this study.

Xavier and Davidson correlated their data using the equation

$$h = h'_{pc} + h_{gc} \quad (7.1)$$

with $h_{gc} = h_{mf}$ and h'_{pc} having a form very similar to our particle convective contribution, $(1-f_o)h_{pc}$. They fitted their results by trying different values of y and found that a gas layer thickness of $d_p/4$ gave the best agreement. Their study is of interest

because information on $\bar{\tau}_e$ and $1 - f_o$ was obtained from observations of maximum bed height, which enabled the determination of bubble velocity (see reference [91] for details). This method offers an alternative to our local capacitance and/or pressure measurements.

Results of Canada, McLaughlin and Staub

Canada et al. [23, 78] used a 0.305 m square vessel to fluidize glass particles with $d_p = 0.65$ and 2.6 mm. They worked with 32 mm diameter tubes arranged in a triangular array having a pitch/diameter ratio in the range 2.5-3. Several tubes in the bundle were instrumented for measurement of time-averaged overall coefficients. Considerable attention was devoted to studying heat transfer in the turbulent regime; however, other regimes were also covered.

Canada and McLaughlin [23] worked with air at atmospheric pressure; some of these results are further elaborated by Staub and Canada [78]. Canada and McLaughlin also obtained heat transfer coefficients with air at 5 and 10 atmospheres. In addition, in special General Electric Company reports [24], the authors present a limited number of data with Freon-12 as the fluidizing gas (for $d_p = 2.6$ mm).

The reported data at atmospheric conditions seem to agree well with our results and consequently with our model (glass properties of relevance to intermediate- and large-particle heat transfer--primarily density--are quite similar to those of sand and dolomite). Coefficients for 0.65 mm particles fall between our values for $d_p = 0.37$ and 0.8 mm, while data for 2.6 mm glass spheres are within 10-15% of our results for $d_p = 2.0$ and 2.85 mm. Our attention, however, will be devoted to the authors' experiments at high pressure and with Freon-12 because they provide a reliable

basis for testing our model under significantly different conditions.

Figure 7.4 presents the comparison between experimental results of reference [23] for 2.6 mm glass particles and model predictions for h_i with air at 5 and 10 atm. The range of reported values includes coefficients measured at several positions in a 10-row array. Predictions differ by 10-15% from the results, with the model again underpredicting h_i probably due to the underprediction of h_b .¹⁵ Our predictions of $h_{i,max}$ and $h_{i,min}$ are also shown; however corresponding experimental values could not be measured (to our knowledge, the instantaneous data obtained in our study are the only results of their kind for intermediate and large particles). At values of U/U_{mf} in excess of 3.5, the authors report a transition to the turbulent region. There is no accompanying noticeable shift in the heat transfer coefficient; however, our model does not represent a realistic picture for this regime in which the bubble-emulsion structure breaks down.

The proposed model correctly predicts a significant increase in heat transfer with a rise in operating pressure (and an accompanying proportional rise in air density). Figure 7.5 illustrates how the model explains this behavior, with U taken as $1.2 U_{mf}$. Practically all of the increase in h_i is due to the increase in the gas convective contribution, $(1-f_o)h_{mf}$. The quiescent bed coefficient rises substantially with pressure because of the increased air mass flow rate--the model predicts a three-fold increase in h_{mf} in going from 1 to 10 atm.

¹⁵ In obtaining predictions for heat transfer coefficients, we averaged the values of $1 - f_o$ from equations (6.23) and (6.24), the reason being that the wide-spaced array used by Canada et al. lies between our single tube and tube array cases. Otherwise, the procedure for calculating h_i was the same as in Section A.

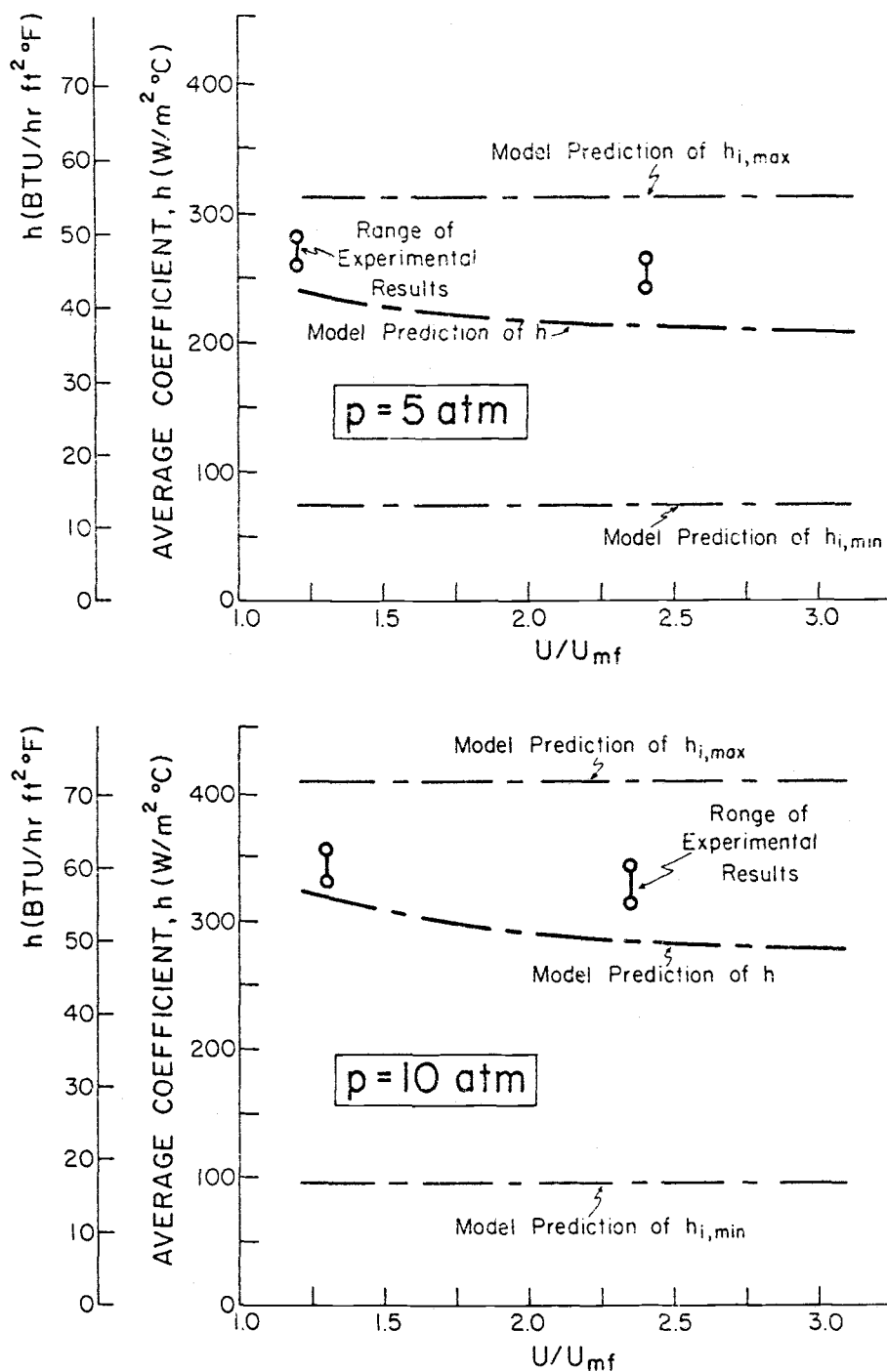


Figure 7.4. Comparison between experimental results reported by Canada and McLaughlin [23] and predictions of our model, for 2.6 mm glass particles at air pressures of 5 and 10 atm.

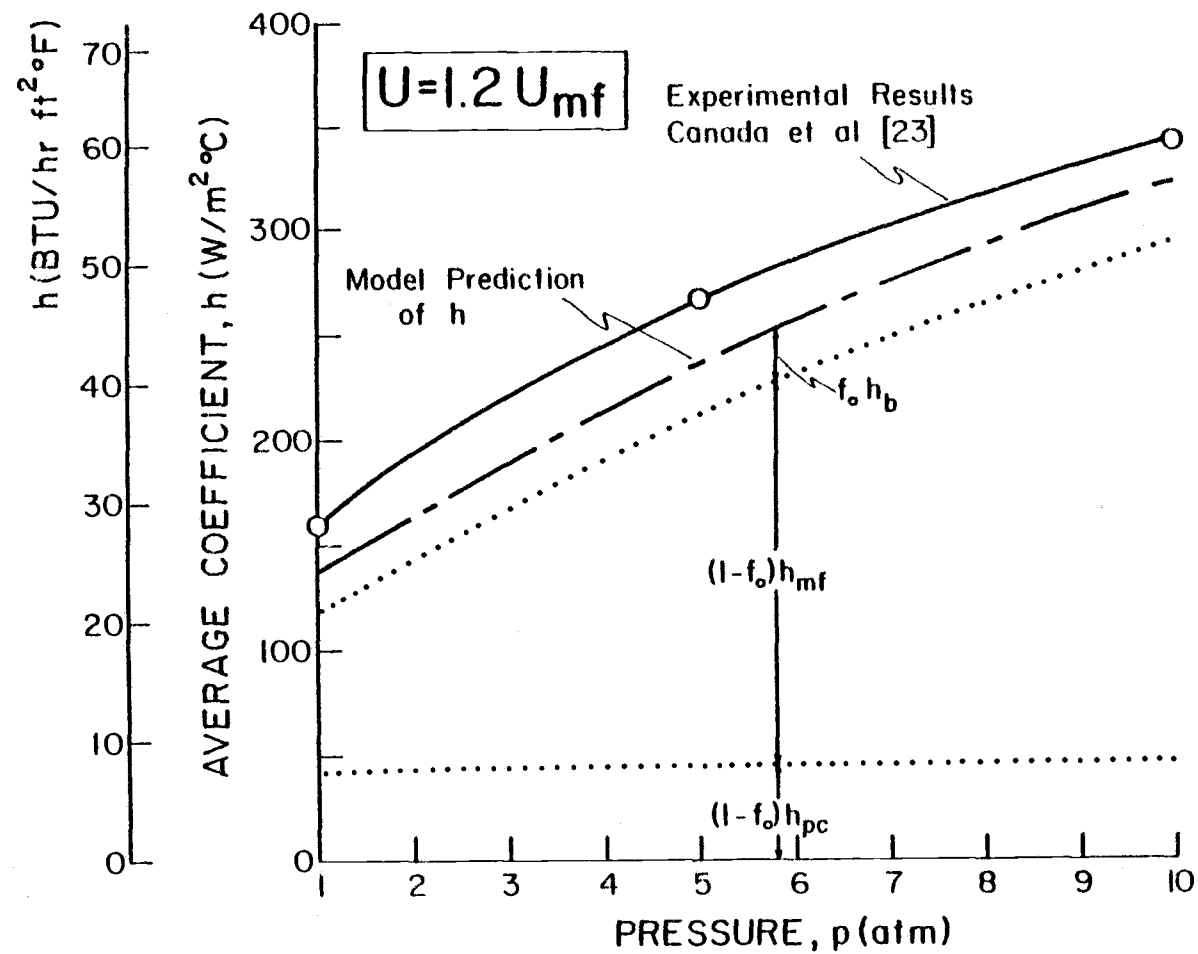


Figure 7.5. Comparison between experimental results, showing the dependence of heat transfer coefficient on pressure, and corresponding model predictions ($d_p = 2.6 \text{ mm}$, $U = 1.2 U_{mf}$).

Heat transfer data with Freon-12 as the fluidizing gas are particularly interesting because several physical properties of Freon differ significantly from those of atmospheric air. For example, under the operating conditions described by Canada et al. [24], $\rho_{Fr} = (5-10)\rho_{air}$, $c_{pFr} = 0.65 c_{pair}$, $k_{Fr} = 0.43 k_{air}$, and $\mu_{Fr} = 0.63 \mu_{air}$.¹⁶ Figure 7.6 displays the very satisfactory agreement between experimental data of reference [24] and predictions of our model, for $d_p = 2.6$ mm and Freon-12 at 1.2 and 2.3 atm. Predicted values of h were calculated by combining equation (6.29) with equations (6.20), (6.22), and (6.23)/(6.24) (see footnote 15 on p. 151).

C. Comparison of Existing Heat Transfer Correlations with Experimental Results

The inadequacy of several existing correlations for heat transfer to (from) horizontal tubes was briefly touched upon in Sections II.B, IV.D, and VI.B. Their unreliability has been discussed by Andeen and Glicksman[4], Chen[27], and Tung et al. [84]. We shall not, therefore, concentrate too much on this matter; a summary and two illustrative examples should suffice.

Table 7.2 lists four correlations for the time-averaged overall coefficient and their authors. To our knowledge, these are the only correlations available in literature. The first three were essentially developed for fine-particle beds and are, as such, applicable only for

¹⁶The value of μ_{Fr} used by authors of reference [24] is incorrect. In our calculations, we used the viscosity obtained from a recent comprehensive survey of physical properties of the Freon family of fluorocarbons, given by F. Aerstin and G. Street in the book "Applied Chemical Process Design," p. 220-223, Plenum Press, New York, 1978.

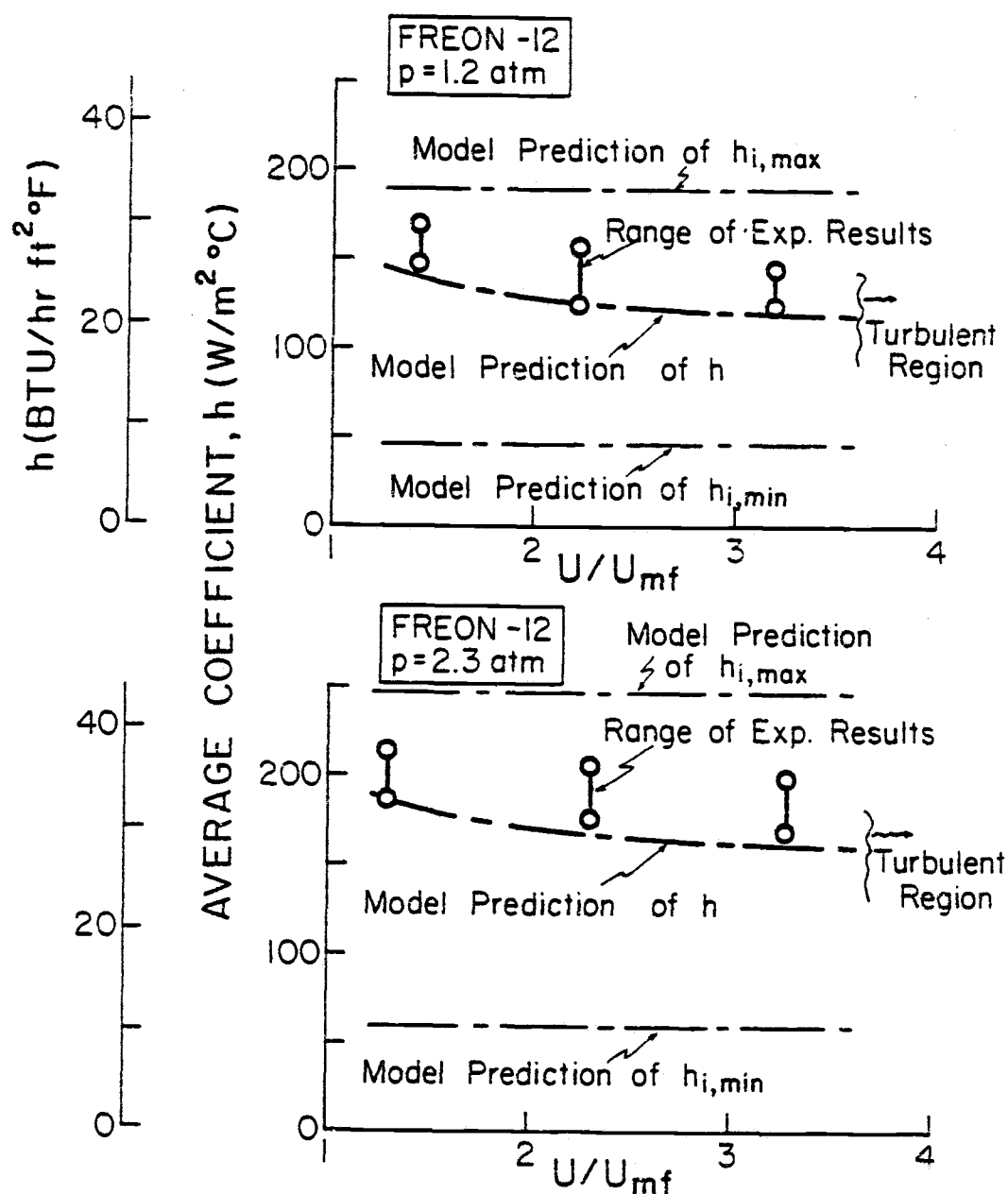


Figure 7.6. Agreement between experimental results reported by Canada et al. [24] and predictions of our model, for 2.6 mm glass particles and Freon-12 at 1.2 and 2.3 atm.

Table 7.2. Summary of existing correlations for heat transfer to horizontal tubes in fluidized beds.

Author	Correlation
Vreedenberg [86]	$Nu_D = \frac{hD}{k_g} = 420 \left(\frac{c_{ps} \mu_g}{k_g} \right)^{0.3} \left[\left(\frac{U_d \rho_s}{\mu_g} \right) \left(\frac{\mu_g^2}{d_p^3 \rho_s^2} \right) \right]^{0.3}$
Andeen and Glicksman [4] ("Modified Vreedenberg Correlation")	$Nu_D = \frac{hD}{k_g} = 900(1-\epsilon)Pr^{0.3} \left[\left(\frac{U_d \rho_s}{\mu_g} \right) \left(\frac{\mu_g^2}{d_p^3 \rho_s^2} \right) \right]^{0.326}$
Gelperin et al. [46]	$Nu_p = \frac{hd_p}{k_g} = 0.815Pr^{0.33} \frac{6(1-\epsilon)}{\epsilon} \left[\frac{Re_p}{6(1-\epsilon)} \right]^{0.32}$
Glicksman and Decker [49, 50, 84]	$Nu_p = \frac{hd_p}{k_g} = (1-\delta)(9.42 + 0.042Re_p Pr)$

a narrow range of particle sizes and fluidizing velocities. When extrapolated to coarser particles, they give predictions which may differ significantly from experimental results. The correlation of Glicksman and Decker [49, 50, 84] was developed specifically with particles larger than 1 mm in mind. However, as already discussed, our experimental data show that it is based on incorrect assumptions.

Vreedenberg's correlation [86] does not include the effect of changing voidage, and is, in general, moderately successful only for fine-particle beds at low velocities (when the voidage is low). The Modified Vreedenberg correlation [4] was developed to account for changes in bed voidage, but falls short of successful predictions under many fluidizing conditions of practical interest [84]. The correlation of Gelperin et al. [46] is not reliable in assessing the influence of particle size on h [4]. The model of Glicksman and Decker assumes that $1 - f_o = 1 - \delta$ and that h_{gc} increases proportionally with U . Since both of these assumptions are wrong (see discussions in Sections IV.D, VI.A, and VI.B), possible correct predictions from this correlation can only be a result of accidental cancellation of errors.

The unreliability of these correlations is best illustrated when predictions based on them are compared to some of our experimental data. Note that the correlations of Andeen and Glicksman and Gelperin et al. use values of the average bed voidage, ϵ , while the correlation of Glicksman and Decker takes into account changes in $1 - \delta$. Information needed for calculating predicted values of h can be obtained from Figure 4.32, where $1 - \delta$ is plotted as a function of U/U_{mf} . Average bed voidage can be obtained from $1 - \delta$ by combining equations (4.11) and (4.12):

$$\epsilon = 1 - (1 - \epsilon_{mf})(1 - \delta) \quad (7.2)$$

We shall use our tube array data since that is the case of actual practical interest.

Figures 7.7 and 7.8 illustrate the (dis)agreement between predicted values and experimental results for 1.3 mm and 4.0 mm particles, respectively. In general, Vreedenberg's correlation and its modified version underpredict h , while the correlations of Gelperin et al. and Glicksman and Decker give values which are too high. One can never be particularly certain when any of these correlations might come close to actual values of the heat transfer coefficient. As illustrated, each correlation may deviate from experimental h by more than 100%. The discrepancies may become even larger at higher operating pressures (particularly for the first three correlations listed in Table 7.2). To add to the confusion, not only are the values of h predicted wrongly, but trends with changing d_p and U are sometimes completely misrepresented.

D. Conclusions about the Proposed Model

Our proposed theoretical model is successful in predicting the time-averaged overall heat transfer coefficient for a variety of fluidizing conditions involving intermediate and large particles. It has withstood the test of our experimental results, as well as of results reported by other investigators who employed vessels of different size and tube arrays of different geometries. The model correctly predicts the influence of particle size, superficial velocity, and physical properties of the fluidizing gas on heat transfer behavior. In addition, it is capable of reliably predicting the three components of heat transfer, which results in correct estimates of maximum and minimum instantaneous coefficients. The proposed theory and related

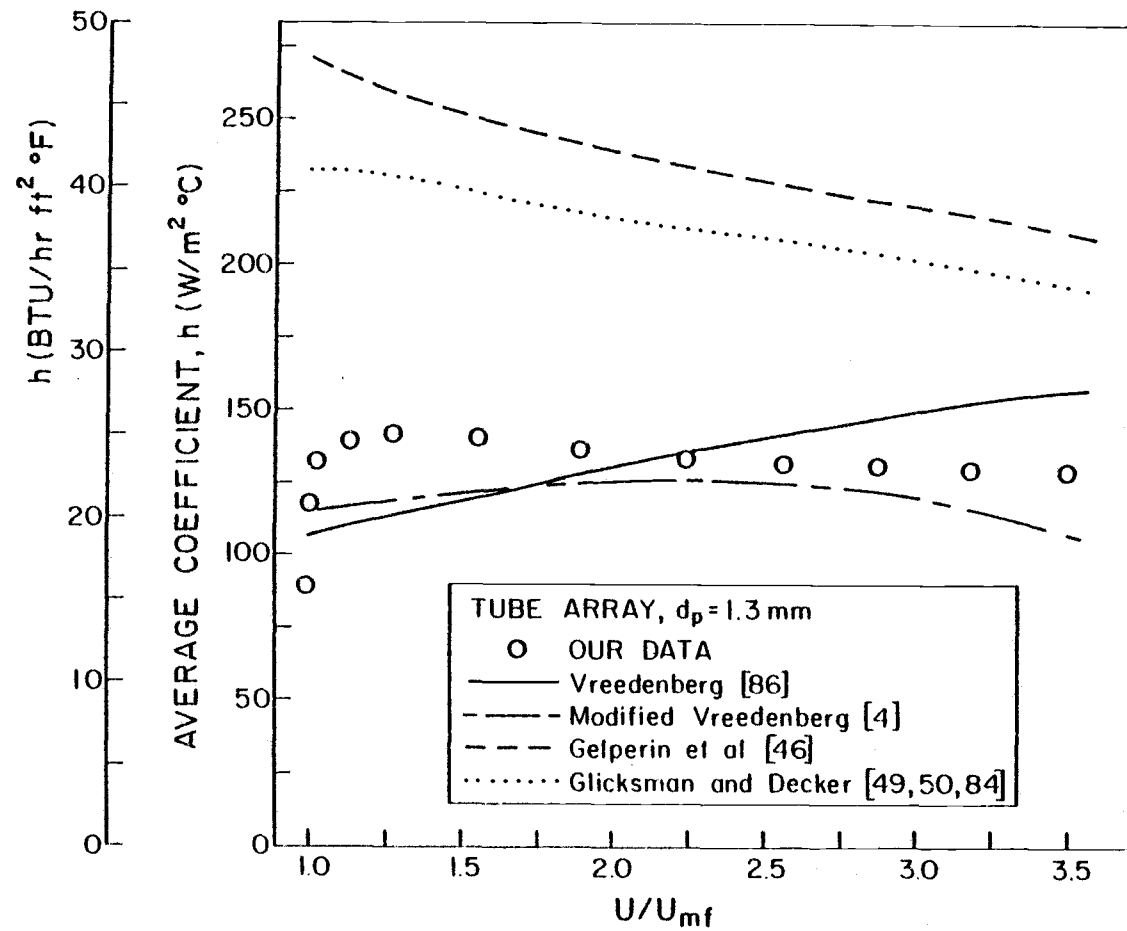


Figure 7.7. Comparison between our experimental results and predictions based on four existing correlations for horizontal tubes ($d_p = 1.3$ mm).

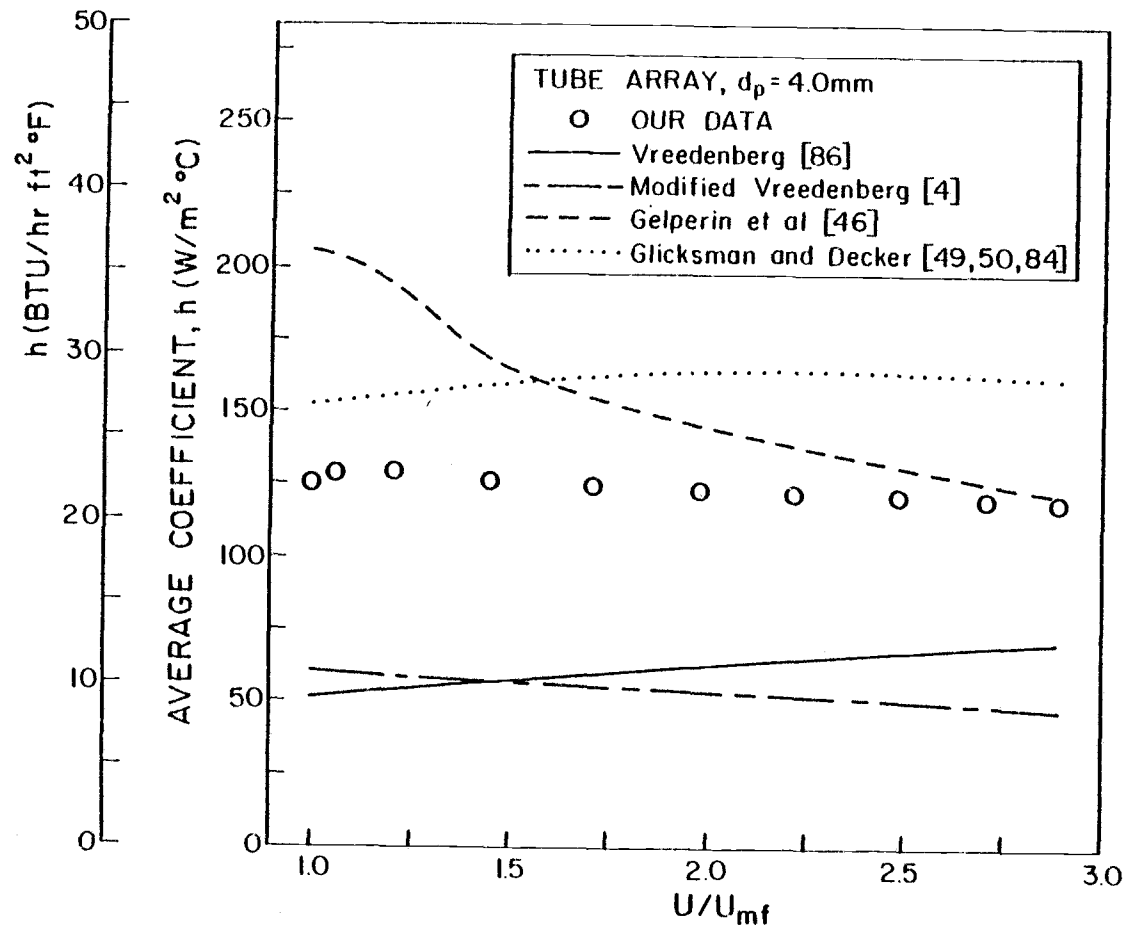


Figure 7. 8. Comparison between our experimental results and predictions based on four existing correlations for horizontal tubes ($d_p = 4.0\text{ mm}$).

equations show that a mechanistic model based on the actual physical picture of the heat transfer process has very definite advantages over the often inadequate and unreliable correlations based on a purely empirical approach.

We have reason to feel confident that the model will give good predictions for the conductive and convective modes under any operating conditions. Heat transfer in high-temperature beds is of particular interest for fluidized-bed combustion of coal and other materials. Here, radiative heat transfer enters the picture. This research area has barely been touched upon, with only a very limited number of overall heat transfer data being reported [53, 64, 90] and with just two studies attempting to address the problem from a more fundamental viewpoint [12, 15]. Only when the radiative component can be reliably predicted and separated from conduction and convection, will the confirmation of our model at high temperatures be possible.

VIII. SUMMARY AND CONCLUSIONS

Heat exchange between a fluidized bed and immersed horizontal tubes attracts considerable attention because of the increasing significance of new processes for fluid-bed combustion of coal and other materials. We carried out a detailed experimental and theoretical study with the purpose of filling the gap which exists in heat transfer involving intermediate and large particles ($d_p > 0.4$ mm).

Chapter I gives an introduction to the subject, while Chapter II reviews the shortcomings of previous studies.

Chapter III describes the experimental equipment which we developed in order to obtain data of particular importance for a thorough analysis of the heat transfer process. We give a detailed description of an instrumented cylinder which makes possible simultaneous measurements of instantaneous, as well as time-averaged, local heat transfer coefficients, voidage and surface pressure variations at several positions around the circumference of an immersed tube.

Chapter IV presents a large body of experimental data which we obtained for a wide range of particle sizes ($d_p = 0.37$ - 6.6 mm) and gas velocities ($U = 0.1$ - 5.6 m/s), in a cold bed (0.48 m \times 0.13 m cross section) with atmospheric air as the fluidizing gas. Two types of runs were made--with a single immersed tube and with a closely spaced staggered tube array (pitch/diameter ratio = 2). Results suggest the following conclusions:

- a) Differences in heat transfer coefficients for the single tube and the tube array are not very significant.
- b) Bed height has practically no effect on heat transfer to the instrumented tube.

- c) Maximum and minimum instantaneous coefficients in a bubbling bed--measured when the tube is covered by emulsion and bubbles, respectively--are not influenced by the superficial gas velocity. Instantaneous heat transfer oscillations are much more pronounced for finer particles; their amplitude is surprisingly small for large particle diameters.
- d) Local coefficients are influenced by particle size and superficial velocity. Coefficients at the top of the tube are affected the most and are related to the behavior of the "lee stack" of particles.
- e) Information obtained from voidage and pressure measurements around the tube provides valuable clues in explaining heat transfer results.
- f) There are very significant differences between the local voidage around the tube and the overall bed voidage.

In Chapter V, we compare experimental results for large particles with the Adams analytical model, which was recently developed for fluidized beds near minimum fluidization. Our experimental work fully verifies the model which gives accurate predictions of local instantaneous and time-averaged heat transfer coefficients, with and without the presence of bubbles.

In Chapter VI, we propose a theoretical model applicable over a wide range of fluidizing conditions in bubbling and slugging beds. The model assumes that energy exchange between a tube and a cold bed takes place by three parallel paths--heat is transferred by packets of particles, by gas percolating between particles and the tube surface, and by bubbles or slugs. Clues from experiment are used to develop general correlations for the particle convective, gas convective, and bubble heat transfer coefficients (equations 6.19, 6.20 and 6.22, respectively), as well as for the local voidage around a

horizontal tube (equation 6.23 or 6.24). A theoretical analysis shows that, from a heat transfer viewpoint, particles can be classified as fine ($d_p < 0.4$ mm), intermediate (0.4 mm $< d_p < 1$ mm), and large ($d_p > 1$ mm). For each of these cases, we present equations which predict the time-averaged coefficient for the tube as a whole (equations 6.25-6.29). We also give equations for the maximum and minimum instantaneous values of the heat transfer coefficient (equations 6.30 and 6.31).

Chapter VII compares predictions based on the proposed model with our experimental results, as well as with results of other investigators for intermediate and large particles. We show the model to be reliable over a wide range of conditions, including operation with air at elevated pressure and Freon-12. We feel confident that the proposed theory and related equations will give good predictions for the conductive and convective modes of heat transfer under any fluidizing conditions.

BIBLIOGRAPHY

1. Adams, R. L., "An Analytical Model of Heat Transfer to a Horizontal Cylinder Immersed in a Gas Fluidized Bed," Ph. D. Thesis, Oregon State University, Corvallis, Ore., 1977.
2. Adams, R. L., and J. R. Welty, "A Gas Convection Model of Heat Transfer in Large Particle Fluidized Beds," *AIChE J.*, 25, in press (1979).
3. Andeen, B. R., and L. R. Glicksman, "The Fluidized Bed Dry Cooling Tower," in *Cooling Towers*, Vol. 2, *A Chem. Eng. Progr. Technical Manual*, AIChE, New York, 1975.
4. Andeen, B. R., and L. R. Glicksman, "Heat Transfer to Horizontal Tubes in Shallow Fluidized Beds," ASME Paper No. 76-HT-67, ASME-AIChE Heat Transfer Conference, St. Louis, Mo. (1976).
5. Angevine, P. A., "Fluid Bed Technology for Waste Disposal and Resource Recovery," Paper No. 55b, AIChE 83rd National Meeting, Houston, Tx. (1977).
6. Baeyens, J., and D. Geldart, "Fluidized Bed Incineration-A Design Approach for Complete Combustion of Hydrocarbons," in *Fluidization - Proceedings of the Second Engineering Foundation Conference (2-6 April 1978)*, ed. by J. F. Davidson and D. L. Keairns, p. 264, Cambridge University Press, Cambridge, U.K., 1978.
7. Bar-Cohen, A., L. Glicksman, and R. Hughes, "Fluid Dynamic Modelling of Fluidized Bed Combustors," in *Proceedings of the Fifth International Conference on Fluidized Bed Combustion (12-14 December 1977)*, Vol. III, p. 458, MITRE Corp., McLean, Va., 1978.
8. Bar-Cohen, A., L. R. Glicksman, and R. W. Hughes, "Theoretical Relations for Void Fraction in Aggregatively Fluidized Beds," *Int. J. Multiphase Flow*, 5, in press (1979).
9. Bartel, W. J., and W. E. Genetti, "Heat Transfer from a Horizontal Bundle of Bare and Finned Tubes in an Air Fluidized Bed," *AIChE Symp. Ser.*, 69 (128), 85 (1973).

10. Baskakov, A. P., "The Mechanism of Heat Transfer between a Fluidized Bed and a Surface," *Int. Chem. Eng.*, 4, 320 (1964).
11. Baskakov, A. P., High Speed Non-Oxidizing Heating and Heat Treatment of Metals in a Fluidized Bed (in Russian), Metallurgia, Moscow, U.S.S.R., 1968.
12. Baskakov, A. P., B. V. Berg, O. K. Vitt, N. F. Filippovsky, V. A. Kirakosyan, J. M. Goldobin, and V. K. Maskaev, "Heat Transfer to Objects Immersed in Fluidized Beds," *Powder Technol.*, 8, 273 (1973).
13. Baskakov, A. P., and V. M. Suprun, "Determination of the Convective Component of the Heat Transfer Coefficient to a Gas in a Fluidized Bed," *Int. Chem. Eng.*, 12, 324 (1972).
14. Baskakov, A. P., O. K. Vitt, V. A. Kirakosyan, V. K. Maskaev, and N. F. Filippovsky, "Investigation of Heat Transfer Coefficient Pulsations and of Mechanism of Heat Transfer from a Surface Immersed into a Fluidized Bed," in *La Fluidisation et Ses Applications - Congres International (1-5 October 1973)*, Vol. I, Cepadues, Toulouse, France, 1973.
15. Basu, P., "Bed-to-Wall Heat Transfer in a Fluidized Bed Coal Combustor," *AIChE Symp. Ser.*, 74 (176), 187 (1978).
16. Berg, B. V., and A. P. Baskakov, "Investigation of Local Heat Transfer between a Fixed Horizontal Cylinder and a Fluidized Bed," *Int. Chem. Eng.*, 14, 440 (1974).
17. Bernis, A., F. Vergnes, P. Le Goff, and J. P. Mihe, "Une Sonde à Film Chaud pour Mesure Locale et Instantée du Coefficient de Transfert de Chaleur dans un Lit Fluidisé Gaz-Solide," *Powder Technol.*, 17, 229 (1977).
18. Bernis, A., F. Vergnes, and P. Le Goff, "Influence du Passage d'une Bulle sur le Coefficient Instantané de Transfert de Chaleur à une Paroi Immersée dans un Lit Fluidisé," *Powder Technol.*, 18, 267 (1977).
19. Botterill, J. S. M., *Fluid-Bed Heat Transfer*, Academic Press, London, 1975.

20. Botterill, J.S.M., and A.O.O. Denloye, "A Theoretical Model of Heat Transfer to a Packed or Quiescent Fluidized Bed," Chem. Eng. Sci., 33, 509 (1977).
21. Botterill, J.S.M., and A.O.O. Denloye, "Gas Convective Heat Transfer to Packed and Fluidized Beds," AIChE Symp. Ser., 74 (176), 194 (1978).
22. Botterill, J.S.M., and M. Desai, "Limiting Factors in Gas-Fluidized Bed Heat Transfer," Powder Technol., 6, 231 (1972).
23. Canada, G.S., and H.M. McLaughlin, "Large Particle Fluidization and Heat Transfer at High Pressures," AIChE Symp. Ser., 74 (176), 27 (1978).
24. Canada, G.S., M.H. McLaughlin, and F.W. Staub, Two-Phase Flow and Heat Transfer in Fluidized Beds, Eighth and Ninth Quarterly Reports, prepared for the Electric Power Research Institute (Contract RP 525-1), SRD-77-110 and SRD-77-150, General Electric Corporate Research and Development, Schenectady, N. Y., 1977.
25. Canada, G.S., M.H. McLaughlin, and F.W. Staub, "Flow Regimes and Void Fraction Distribution in Gas Fluidization of Large Particles in Beds without Tube Banks," AIChE Symp. Ser., 74 (176), 14 (1978).
26. Catipovic, N.M., G.N. Jovanovic, and T.J. Fitzgerald, "Regimes of Fluidization for Large Particles," AIChE J., 24, 543 (1978).
27. Chen, J.C., "Heat Transfer to Tubes in Fluidized Beds," ASME Paper No. 76-HT-75, ASME-AIChE Heat Transfer Conference, St. Louis, Mo. (1976).
28. Cherrington, D.C., L.P. Golan, and F.G. Hammitt, "Industrial Application of Fluidized Bed Combustion-Single Tube Heat Transfer Studies," in Proceedings of the Fifth International Conference on Fluidized Bed Combustion (12-14 December 1977), Vol. III, p. 184, MITRE Corp., McLean, Va., 1978.
29. Cranfield, R.R., and Geldart, D., "Large Particle Fluidization," Chem. Eng. Sci., 29, 935 (1974).

30. Cranfield, R.R. and B.J. Gliddon, "Adsorption in Shallow Fluidized Beds of Large Particles," *Instn. Chem. Engrs. Symp. Ser.*, 38, H4 (1976).
31. Davidson, J.F., and D. Harrison, *Fluidised Particles*, Cambridge University Press, Cambridge, U.K., 1963.
32. Dean, J.A. (Editor), *Lange's Handbook of Chemistry*, 11th Ed. McGraw-Hill, New York, 1973.
33. Denloye, A.O.O., and J.S.M. Botterill, "Bed to Surface Heat Transfer in a Fluidized Bed of Large Particles," *Powder Technol.*, 19, 197 (1978).
34. Douglas, W.J.M., and S.W. Churchill, "Recorrelation of Data for Convective Heat Transfer between Gases and Single Cylinders with Large Temperature Differences," *Chem. Eng. Progr. Symp. Ser.*, 52 (18), 23 (1956).
35. Feller, W., *An Introduction to Probability Theory and Its Applications*, 2nd Ed., Vol. I, Wiley, 1957.
36. Foltz, G.E., and R.B. Mesler, "The Measurement of Surface Temperatures with Platinum Films During Nucleate Boiling of Water," *AIChE J.*, 16, 44 (1970).
37. Gabor, J.D., "Heat Transfer to Particle Beds with Gas Flows Less than or Equal to that Required for Incipient Fluidization," *Chem. Eng. Sci.*, 25, 979 (1970).
38. Gabor, J.D., "Wall-to-Bed Heat Transfer in Packed and Fluidized Beds," *Chem. Eng. Progr. Symp. Ser.*, 66 (105), 76 (1970).
39. Galloway, T.R., and B.H. Sage, "A Model of the Mechanism of Transport in Packed, Distended, and Fluidized Beds," *Chem. Eng. Sci.*, 25, 495 (1970).
40. Geldart, D., "The Size and Frequency of Bubbles in Two- and Three-dimensional Gas-Fluidised Beds," *Powder Technol.*, 4, 41 (1970/71).
41. Geldart, D., "The Effect of Particle Size Distribution on the Behavior of Gas Fluidized Beds," *Powder Technol.*, 6, 201 (1972).

42. Gelperin, N.I., and V.G. Ainshtein, "Heat Transfer in Fluidized Beds," in Fluidization, ed. by J.F. Davidson and D. Harrison, p. 471, Academic Press, London, 1971.
43. Gelperin, N.I., V.G. Ainshtein, and L. A. Korotyanskaya, "Heat Transfer between a Fluidized Bed and Staggered Bundles of Horizontal Tubes," *Int. Chem. Eng.*, 9, 137 (1969).
44. Gelperin, N.I., V.G. Ainshtein, and L. A. Korotyanskaya, "Heat Transfer between a Fluidized Bed and Tube Bundles with Various Tube Arrangements" (in Russian), *Zh. Vses. Khim. Obshchest.*, 14 (1), 120 (1969).
45. Gelperin, N.I., V.G. Ainshtein, L. A. Korotyanskaya, and J. P. Perevozchikova (in Russian), *Teor. Osnovy Khim. Tekhnol.*, 2 (3), 428 (1968).
46. Gelperin, N.I., V. Y. Kruglikov, and V. G. Ainshtein, "Heat Transfer between a Fluidized Bed and the Surface of a Single Tube in Longitudinal and Transverse Gas Flow" (in Russian), *Khim. Prom.*, 6, 358 (1958).
47. George, A., N. Catipovic, and J. Welty, "An Analytical Study of Heat Transfer to a Horizontal Cylinder in a Large Particle Fluidized Bed," ASME-AIChE 18th National Heat Transfer Conference, San Diego, Ca. (1979).
48. Glass, D.H., and D. Harrison, "Flow Patterns Near a Solid Obstacle in a Fluidized Bed," *Chem. Eng. Sci.*, 19, 1001 (1964).
49. Glicksman, L.R., and N. Decker, "Heat Transfer Component Model," in Modeling of Fluidized Bed Combustion of Coal, Quarterly Technical Progress Report (No. 7), prepared for the U.S. Department of Energy (Contract E(49-18)-2295), MIT-2295-1-7, p. 94, Massachusetts Institute of Technology Energy Laboratory, Cambridge, Mass., May 1978.
50. Glicksman, L.R., and N. Decker, "Heat Transfer in Fluidized Beds with Large Particles," paper submitted to *Chem. Eng. Sci.*, January 1979 (personal communication).

51. Glicksman, L., R. Peloux, N. Decker, and T. Shen, "Thermal Stresses and Fatigue of Heat Transfer Tubes Immersed in a Fluidized Bed Combustor," in Proceedings of the Fifth International Conference on Fluidized Bed Combustion (12-14 December 1977), Vol. III, p. 700, MITRE Corp., McLean, Va., 1978.
52. Hodgkinson, N., and G.G. Thurlow, "Combustion of Low-Grade Material in Fluidized Beds," AIChE Symp. Ser., 73 (161), 108 (1977).
53. Howe, W.C., and C. Aulisio, "Control Variables in Fluidized Bed Steam Generation," Chem. Eng. Progr., 73 (7), 69 (1977).
54. Jovanovic, G., "Gas Flow in Fluidized Beds of Large Particles: Experiment and Theory," Ph.D. Thesis, Oregon State University, Corvallis, Ore., 1979.
55. Kilkis, B., F.M. DeGeyter, and J.J. Ginoux, "Hydrodynamics of a Two-Dimensional Fluidized Bed in the Vicinity of a Cylinder with Horizontal Axis," in La Fluidisation et Ses Applications - Congres International (1-5 October 1973), Vol. I, Cepadues, Toulouse, France, 1973.
56. Knudsen, J.G., and D.L. Katz, Fluid Dynamics and Heat Transfer, McGraw-Hill, New York, 1958.
57. Kunii, D., and O. Levenspiel, Fluidization Engineering, Wiley, New York, 1969.
58. Kunii, D., and J.M. Smith, "Heat Transfer Characteristics of Porous Rocks," AIChE J., 6, 71 (1960).
59. Lese, H.K., and R.I. Kermode, "Heat Transfer from a Horizontal Tube to a Fluidized Bed in the Presence of Unheated Tubes," Can. J. Chem. Eng., 50, 44 (1972).
60. Levenspiel, O., and J.S. Walton, "Bed-Wall Heat Transfer in Fluidized Systems," Chem. Eng. Progr. Symp. Ser., 50 (9), 1 (1954).
61. McAdams, W.H., Heat Transmission, 3rd Ed., McGraw-Hill, New York, 1954.

62. McGaw, D.R., "The Development of a Mechanism for Gas-Particle Heat Transfer in Shallow Fluidized Beds of Large Particles," *Chem. Eng. Sci.*, 32, 11 (1977).
63. McGrath, L., and R.E. Streatfield, "Bubbling in Shallow Gas-Fluidized Beds of Large Particles," *Trans. Instn. Chem. Engrs.*, 49, T70 (1971).
64. McLaren, J., and D.F. Williams, "Combustor Efficiency, Sulphur Retention and Heat Transfer in Pilot-Plant Fluidized Bed Combustors," *J. Inst. Fuel*, 42, 303 (1968).
65. Mickley, H.S., and D.F. Fairbanks, "Mechanism of Heat Transfer to Fluidized Beds," *AIChE J.*, 1, 374 (1955).
66. Mickley, H.S., D.F. Fairbanks, and R.D. Hawthorn, "The Relation between the Transfer Coefficient and Thermal Fluctuations in Fluidized-Bed Heat Transfer," *Chem. Eng. Progr. Symp. Ser.*, 57 (32), 51 (1961).
67. Miller, G., V. Zakkay, and G. Kiviat, "The Effects of Finned Tubing on Fluidized Bed Performance," in *Proceedings of the Fifth International Conference on Fluidized Bed Combustion* (12-14 December 1977), Vol. III, p. 156, MITRE Corp., McLean, Va., 1978.
68. Noack, R., "Lokaler Wärmeübergang an Horizontalen Rohren in Wirbelschichten," *Chemie. Ing. Techn.*, 42, 371 (1970).
69. Oberhettinger, F., and L. Badii, *Tables of Laplace Transforms*, Springer-Verlag, New York, 1973.
70. Özkaynak, T.F., and J.C. Chen, "Average Residence Times of Emulsion and Void Phases at the Surface of Heat Transfer Tubes in Fluidized Beds," *AIChE Symp. Ser.*, 74 (174), 334 (1978).
71. Perry, R.H., and C.H. Chilton (Editors), *Chemical Engineers' Handbook*, 5th Ed., McGraw-Hill, New York, 1973.
72. Petrie, J.C., W.A. Freeby, and J.A. Buckham, "In-Bed Heat Exchangers," *Chem. Eng. Progr.*, 64 (7), 45 (1968).
73. *Proceedings of the Fourth International Conference on Fluidized Bed Combustion* (9-11 December 1975), MITRE Corp., McLean, Va., 1976.

74. Proceedings of the Fifth International Conference on Fluidized Bed Combustion (12-14 December 1977), Volumes I-III, MITRE Corp., McLean, Va., 1978.
75. Samson, T., "Heat Transfer to Objects in Fluidized Beds," in *La Fluidisation et Ses Applications - Congres International* (1-5 October 1973), Vol. I, Cepadues, Toulouse, France, 1973.
76. Schneider, P.J., *Temperature Response Charts*, Wiley, New York, 1963.
77. Selzer, V.W., and W.J. Thomson, "Fluidized-Bed Heat Transfer --the Packet Theory Revisited," *AIChE Symp. Ser.*, 73 (161), 29 (1977).
78. Staub, F.W., and G.S. Canada, "Effect of Tube Bank and Gas Density on Flow Behavior and Heat Transfer in Fluidized Beds," in *Fluidization - Proceedings of the Second Engineering Foundation Conference* (2-6 April 1978), ed. by J.F. Davidson and D.L. Keairns, p. 339, Cambridge University Press, Cambridge, U.K., 1978.
79. Stringer, J., "High Temperature Corrosion of Metals and Alloys in Fluidized Bed Combustion Systems," in *Proceedings of the Fifth International Conference on Fluidized Bed Combustion* (12-14 December 1977), Vol. III, p. 682, MITRE Corp., McLean, Va., 1978.
80. Strom, S.S., T.E. Dowdy, W.C. Lapple, J.B. Kitto, T.P. Stanoch, R.H. Boll, and W.L. Sage, *Preliminary Evaluation of Atmospheric Pressure Fluidized Bed Combustion Applied to Electric Utility Large Steam Generators*, EPRI Report No. RP 412-1, Electric Power Research Institute, Palo Alto, Calif., February 1977.
81. Syromyatnikov, N.I., V.M. Kulikov, and V.N. Korolev, "Structural and Hydrodynamic Conditions of Fuel Combustion in a Low-Temperature Fluidized Bed," *J. Inst. Fuel*, 50, 169 (1977).
82. Toomey, R.D., and H.F. Johnstone, "Gaseous Fluidization of Solid Particles," *Chem. Eng. Progr.*, 48 (5), 220 (1952).
83. Tuma, J.J., *Handbook of Physical Calculations*, McGraw-Hill, New York, 1976.

84. Tung, S.E., J. Goldman, and J.F. Louis, "FBC-Modelling and Data Base, " in Proceedings of the Fifth International Conference on Fluidized Bed Combustion (12-14 December 1977), Vol. III, p. 406, MITRE Corp., McLean, Va., 1978.
85. Tuot, J., and R. Clift, "Heat Transfer around Single Bubbles in a Two-Dimensional Fluidized Bed, " AIChE Symp. Ser., 69 (128), 78 (1973).
86. Vreedenberg, H. A., "Heat Transfer between a Fluidized Bed and a Horizontal Tube, " Chem. Eng. Sci., 9, 52 (1958).
87. Weast, R. C. (Editor), CRC Handbook of Chemistry and Physics, 57th Ed., CRC Press, Cleveland, Ohio, 1976.
88. Welty, J.R., C.E. Wicks, and R.E. Wilson, Fundamentals of Momentum, Heat, and Mass Transfer, 2nd Ed., Wiley, New York 1976.
89. Wen, C.Y., and Y.H. Yu, "A Generalized Method for Predicting the Minimum Fluidization Velocity, " AIChE J., 12, 610 (1966).
90. Wright, S.J., R. Hickman, and H.C. Ketley, "Heat Transfer in Fluidized Beds of Wide Size Spectrum at Elevated Temperatures," Brit. Chem. Eng., 15, 1551 (1970).
91. Xavier, A.M., and J.F. Davidson, "Heat Transfer to Surfaces Immersed in Fluidized Beds, Particularly Tube Arrays, " in Fluidization - Proceedings of the Second Engineering Foundation Conference (2-6 April 1978), ed. by J.F. Davidson and D.L. Keairns, p. 333, Cambridge University Press, Cambridge, U.K., 1978.
92. Yagi, S., and D. Kunii, "Studies on Effective Thermal Conductivities in Packed Beds, " AIChE J., 3, 373 (1957).
93. Yagi, S., and D. Kunii, "Studies on Heat Transfer Near Wall Surface in Packed Beds, " AIChE J., 6, 97 (1960).
94. Yerushalmi, J., N.T. Cankurt, D. Geldart, and B. Liss, "Flow Regimes in Vertical Gas-Solid Contact Systems, " AIChE Symp. Ser., 74 (176), 1 (1978).

95. Yoshida, K., D. Kunii, and O. Levenspiel, "Heat Transfer Mechanisms between Wall Surface and Fluidized Bed," *Int. J. Heat Mass Transfer*, 12, 529 (1969).
96. Young, D. T., "Fluidized Combustion of Beds of Large, Dense Particles in Reprocessing HTGR Fuel," Paper No. 80c, AIChE 70th Annual Meeting, New York (1977).
97. Zakkay, V., and G. Miller, "Advanced Heat Exchanger Configuration for Coal-Fired Fluidized Beds," Paper No. 28a, AIChE 71st Annual Meeting, Miami Beach, Fla. (1978).

APPENDICES

APPENDIX A

Temperature Control Circuit for the Heat
Transfer Measuring Elements

Figure A.1 shows a simple block diagram of the heat transfer element temperature control circuit. A voltage e_0 is applied across a platinum heater and a series 0.50Ω resistor. The voltage drop across the 0.50Ω resistor is e_1 , and it is proportional to the current through the heater. The voltage difference $e_0 - e_1$ is the drop across the heater; therefore the product $(e_0 - e_1)e_1$ is proportional to the power dissipated by the heater (and hence the heat transfer coefficient). In addition, the ratio $(e_0 - e_1)/e_1$ is proportional to the resistance of the heater. This ratio is calculated by divider 1 and occurs at the output, where it is subtracted from the set point.

The signal entering the lower part of the block diagram (divider 2) is the offset between the desired temperature and the actual heater temperature (ΔT). Thus, the output of divider 2 is proportional to $\Delta T/e_1$. However, the output of divider 2 is also e_1 . (This can be seen by noting that e_1 is the input to a high gain amplifier. Figure A.1 shows that the signal going to the negative input of the high gain amplifier is e_1 , with the difference between positive and negative inputs being multiplied by the gain of the amplifier to produce a voltage e_0 . Since e_0 is not enormously large, the difference between voltages at the positive and negative inputs to the amplifier must be approximately zero; hence the input to the positive terminal of the amplifier must be very nearly e_1).

It follows, therefore, that $(\text{const.})\Delta T/e_1 = e_1$, or $e_1^2 = (\text{const.})\Delta T$. Since e_1 is proportional to the current through the heater, and because the resistance of the heater is approximately constant, we conclude that e_1^2 is proportional to the power dissipated by the heater. Thus, the voltage applied to the heating element

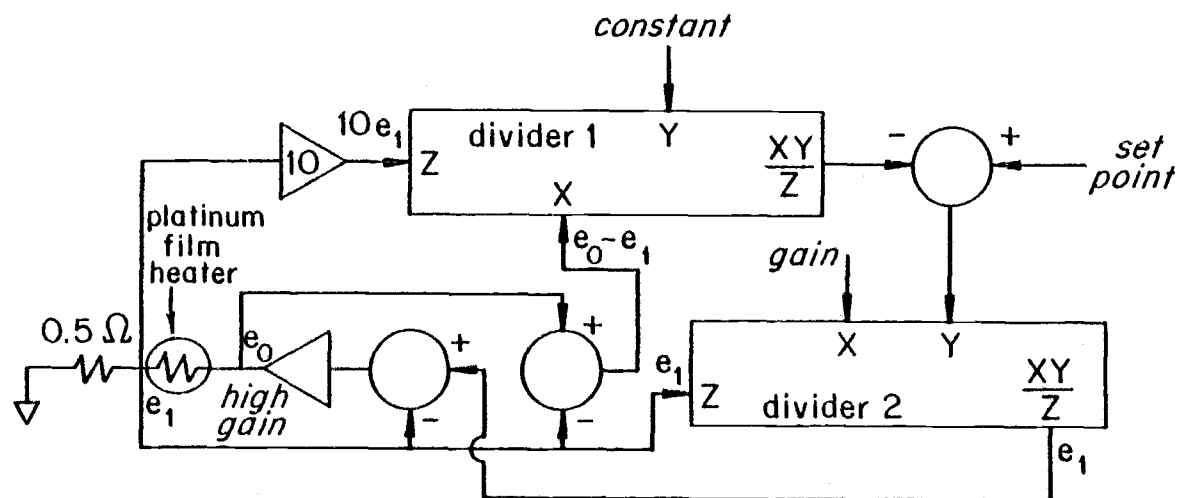


Figure A.1. Block diagram of a heating element temperature control circuit.

is such that the power is proportional to the offset in temperature. Since the temperature of the platinum probe is linearly related to the power input, the overall system is (approximately) linear. As a result, its stability does not depend on the operating temperature. A single dominant time constant is involved, and it is possible to use a large feedback loop gain with a correspondingly small offset in temperature (less than 1°C).

The detailed circuit for the temperature controller is shown in Figure A.2. The circuit on the bottom half of the page is parallel in its structure to the block diagram shown in Figure A.1. The circuit on the top half of the page is effectively a mirror image of the bottom one. The overall layout of the printed circuit card used in the course of our experiments corresponds closely to the layout of the circuit diagram.

[illegible]

178

APPENDIX B

Mathematical Model for the Heat Transfer
Measuring Elements

The power response of the heat transfer measuring element to a change in the heat transfer coefficient can be estimated theoretically from a mathematical model for the temperature distribution throughout the element. The borosilicate piece can be considered as a uniform semi-infinite solid in the direction normal to the surface, with heat generation in the platinum film covering the glass. The physical picture and the variables involved are shown in Figure B.1(a) (for convenience, symbols P_t and h_t are used in place of the usual $P(t)$ and $h(t)$). The specific boundary condition for the problem, stemming from the action of the control circuit, is that the heat generation is proportional to the difference between the temperature of the surface and the desired set point temperature (see Appendix A). The temperature distribution is mathematically given by

$$\frac{\partial T}{\partial t} = \frac{k_1}{\rho_1 c_{p1}} \frac{\partial^2 T}{\partial z^2} \quad (\text{B. 1})$$

with the initial condition

$$T = T_{\text{set}} \quad \text{at} \quad t = 0 \quad (\text{B. 2})$$

and boundary conditions

$$T \rightarrow T_{\text{set}} \quad \text{at} \quad z \rightarrow \infty \quad (\text{B. 3})$$

$$P_t = K(T_{\text{set}} - T) = h_t(T - T_b) - k_1 \frac{\partial T}{\partial z} \quad \text{at} \quad z = 0 \quad (\text{B. 4})$$

(Note: equation (B. 4) applies per unit area).

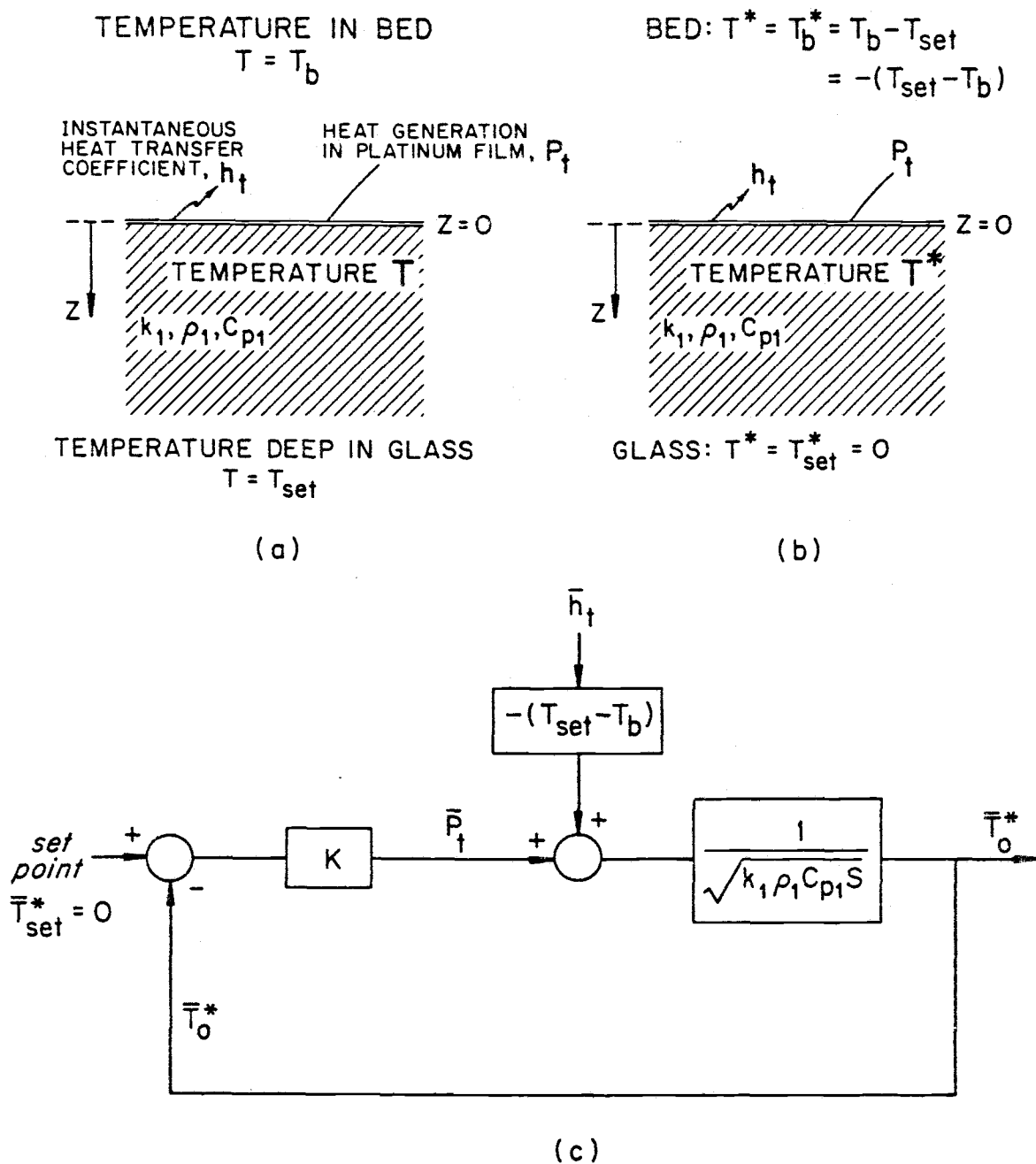


Figure B.1. (a) Sketch of variables involved; (b) sketch of deviation variables involved; (c) block diagram representation of the system.

Introducing the deviation variable $T^* = T - T_{\text{set}}$, we obtain (see Figure B.1(b))

$$\frac{\partial T^*}{\partial t} = \frac{k_1}{\rho_1 c_{p1}} \frac{\partial^2 T^*}{\partial z^2} \quad (\text{B.5})$$

with

$$T^* = 0 \quad \text{at} \quad t = 0 \quad (\text{B.6})$$

$$T^* \rightarrow 0 \quad \text{at} \quad z \rightarrow \infty \quad (\text{B.7})$$

$$P_t = -KT^* = h_t(T^* + T_{\text{set}} - T_b) - k_1 \frac{\partial T^*}{\partial z} \quad \text{at} \quad z = 0 \quad (\text{B.8})$$

We are operating under conditions where $T^*(=T-T_{\text{set}}) \ll T_{\text{set}} - T_b$. The temperature difference $T_{\text{set}} - T_b$ is at least 50°C in all our experiments, while the control circuit does not allow $T - T_{\text{set}}$ to exceed 1°C . Equation (B.8) therefore becomes

$$P_t = -KT^* = h_t(T_{\text{set}} - T_b) - k_1 \frac{\partial T^*}{\partial z} \quad \text{at} \quad z = 0 \quad (\text{B.8a})$$

The same simplification can be made by assuming that $K \gg h_t$ (it will be seen later from numerical values that this inequality is satisfied).

Taking Laplace transforms in Equation (B.5), with $\alpha_1 = k_1/\rho_1 c_{p1}$, and using equations (B.6) and (B.7), we obtain

$$\bar{T}^*(s, z) = C_1(s) e^{-\sqrt{s/\alpha_1} z} \quad (\text{B.9})$$

while the same operation on equation (B.8a) gives

$$\bar{P}_t(s) = -K\bar{T}^*(s, 0) = \bar{h}_t(s)(T_{\text{set}} - T_b) - k_1 \frac{\partial \bar{T}^*(s, 0)}{\partial z} \quad (\text{B.10})$$

Using $\bar{T}^* = \bar{T}^*(s, z)$, $\bar{T}_o^* = \bar{T}^*(s, 0)$, $\bar{P}_t = \bar{P}_t(s)$, and $\bar{h}_t = \bar{h}_t(s)$ for convenience, we proceed by differentiating (B. 9),

$$\frac{\partial \bar{T}^*}{\partial z} = -\sqrt{\frac{s}{\alpha}} \bar{T}^* \quad (\text{B. 11})$$

and substituting for the derivative in (B. 10) to obtain

$$\bar{T}_o^* + \frac{\bar{h}_t}{K} (T_{\text{set}} - T_b) = -\frac{k_1}{K} \sqrt{\frac{s}{\alpha}} \bar{T}_o^* \quad (\text{B. 12})$$

Simplification of (B. 12) gives

$$\frac{\bar{T}_o^*}{\bar{h}_t} = -\frac{T_{\text{set}} - T_b}{K(1 + \frac{k_1}{K} \sqrt{\frac{s}{\alpha}})} \quad (\text{B. 13})$$

Noting that $-K\bar{T}_o^* = \bar{P}_t$, we obtain the relationship between the power dissipation and the heat transfer coefficient:

$$\frac{\bar{P}_t}{\bar{h}_t} = \frac{T_{\text{set}} - T_b}{1 + \frac{\sqrt{k_1 \rho_1 c_{p1}}}{K^2} \sqrt{s}} \quad (\text{B. 14})$$

which is shown in a block diagram form in Figure B. 1(c).

Taking the inverse Laplace transform of equation (B. 14) for a unit step change in the surface heat transfer coefficient [69] gives the equation

$$P(t) = (T_{\text{set}} - T_b) \left(1 - e^{-\frac{K^2}{k_1 \rho_1 c_{p1}} t} \operatorname{erfc} \frac{K}{\sqrt{k_1 \rho_1 c_{p1}}} \sqrt{t} \right) \quad (\text{B. 15})$$

which is the power response of the heat transfer measuring element to a step change in $h(t)$. We can see that the time constant of our system is

$$\tau_s = \frac{k_1 \rho_1 c_{pl}}{K^2} \quad (\text{B. 16})$$

For the physical properties of borosilicate glass [71, 87]

($k_1 = 0.87 \text{ W/m}^\circ\text{C}$, $\rho_1 = 2230 \text{ kg/m}^3$, $c_{pl} = 753 \text{ J/kg}^\circ\text{C}$) and the effective controller gain used in our work

($K = 10^4 \text{ BTU/hr ft}^2^\circ\text{F} = 5.67 \times 10^4 \text{ W/m}^2^\circ\text{C}$), the time constant is $\tau_s = 0.45 \text{ ms}$. The response time (i.e., time necessary to reach 98% of the final power value) is $t_r = 4\tau_s = 1.80 \text{ ms}$. This is in excellent agreement with the actual response times of the platinum elements, which were measured on an oscilloscope in the range 2.0-2.5 ms.

Final note: in actual experiments the temperature of the copper cylinder was held slightly below T_{set} for stability reasons. This allowed a small "zero level" power to be dissipated even when $h_t = 0$ (i.e., instead of $P_t = -KT^*$, we had $P_t - P_o = -KT^*$). Further details are given in Appendix C.

APPENDIX C

Calibrating Procedure for Determining the Temperatures
of the Platinum Heating Elements

When the copper cylinder was held at a temperature exactly equal to that of the platinum element, the stability of the control circuit, primarily its response to a drop in the heat transfer coefficient, was adversely affected. However, if the temperature of the instrumented cylinder was lowered just slightly, the circuit responded as designed. In the course of our experiments, the temperatures of the different platinum films ranged from 93 to 96°C, while the copper rod was always kept at 91°C.

Even when there was no heat transferred between the platinum film and the bed, a certain amount of power was dissipated because of conduction to the surrounding epoxy resin and copper. The amount of heat conducted and the exact temperature of the platinum heater were determined in the following manner. Under normal fluidizing conditions, the power dissipated by the film heater could be divided into two parts:

$$P_{t, \text{total}} = P_t + P_o = h_t A (T_{\text{Pt}} - T_b) + C_{\text{cond}} (T_{\text{Pt}} - T_{\text{Cu}}) \quad (\text{C. 1})$$

When there was no heat exchanged with the bed, $h_t = 0$, all of the power was dissipated by conduction:

$$P_o = C_{\text{cond}} (T_{\text{Pt}} - T_{\text{Cu}}) \quad (\text{C. 2})$$

The exact conduction constant and the platinum temperature were calculated by measuring the "zero level" power at different temperatures of the copper cylinder. The platinum film was covered with an insulating foam to obtain a zero heat transfer coefficient, and

measurements were performed after steady state had been reached. The following numerical example from one of the calibrations illustrates the procedure:

$$\text{at } T_{Cu} = 60^{\circ}\text{C}, P_o = 0.91 \text{ W}$$

$$\text{at } T_{Cu} = 75^{\circ}\text{C}, P_o = 0.52 \text{ W}$$

Using equation (C. 2) for each case,

$$0.91 = C_{cond}(T_{Pt} - 60)$$

$$0.52 = C_{cond}(T_{Pt} - 75)$$

and solving simultaneously, we obtain

$$T_{Pt} = 95^{\circ}\text{C}$$

$$C_{cond} = 0.026 \text{ W}/^{\circ}\text{C}$$

The conduction constants for the five probes were all in the range 0.022-0.026 W/ $^{\circ}\text{C}$. Periodic checks revealed that the individual C_{cond} remained at their original values throughout our study; this meant that the properties of the epoxy resin were not affected by the temperatures used.

With the platinum film temperature and the conduction constant known, equation (C. 1) is used to calculate the exact power dissipated to the fluidized bed, P_t or $P(t)$. $P_{t, total}$ is obtained from the instantaneous voltage and current readings (measured by the control circuit):

$$P_{t, total} = e(t)i(t) \quad (\text{C. 3})$$

Then,

$$P(t) = e(t)i(t) - C_{cond}(T_{Pt} - T_{Cu}) \quad (\text{C. 4})$$

This value of the power is used in equation (3. 1) to give the instantaneous heat transfer coefficient.

APPENDIX D

Comparison of Measured and Predicted Heat Transfer
Coefficients in Air FlowNatural Convection

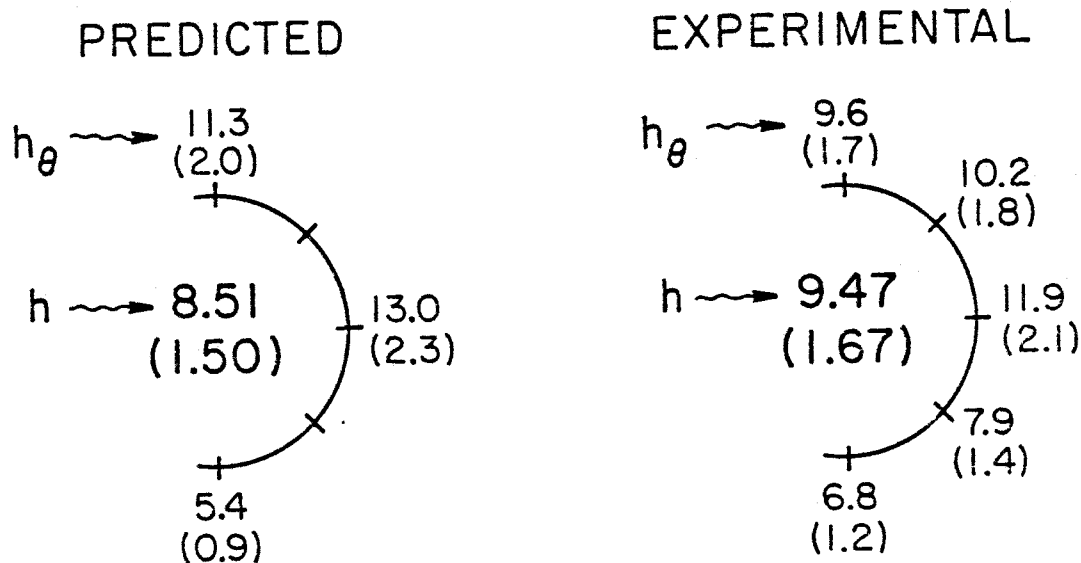
The accuracy of the instrumented cylinder in the low heat transfer coefficient range was tested by measuring the natural convection heat transfer from its surface. The cylinder was placed horizontally in a stagnant air atmosphere, and local and overall coefficients were measured at several surface temperatures.

The agreement with predicted values for the overall tube coefficient reported in literature [61, 88] was very good, usually to within 10-12%. Figure D.1(a) shows a typical example with $T_{Cu} \approx T_{Pt} = 102^{\circ}\text{C}$ and $T_{air} = 30^{\circ}\text{C}$ ($Gr_D Pr = 557,000$). The experimental overall coefficient is obtained from local values according to equation (4.3). There is a lack of predictions for local heat transfer data in literature; our experimental values are therefore compared only with approximate values obtained from correlations for vertical and horizontal heated plates [61, 88].

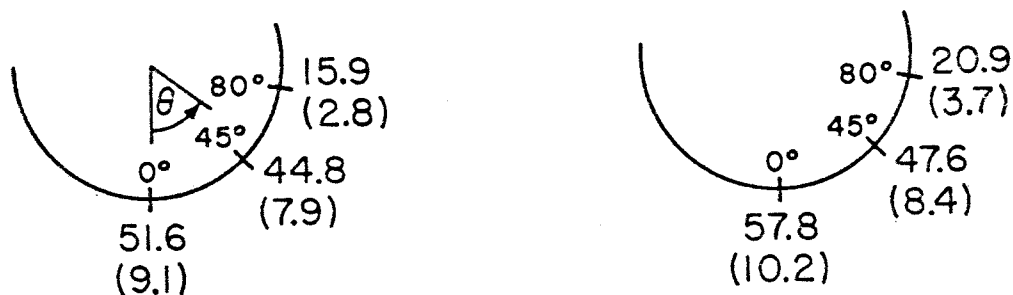
Forced Convection

The literature data and correlations for local coefficients are rather limited, especially in the Reynolds number range obtainable in our apparatus. Knudsen and Katz [56] give a correlation for predicting local coefficients on a horizontal cylinder up to $\theta = 80^{\circ}$. Experimental values measured when the instrumented cylinder was placed in our fluidization vessel and exposed to air flow were compared with these predictions, and the results were satisfactory. Figure D.1(b)

LOCAL AND OVERALL HEAT TRANSFER COEFFICIENTS $W/m^2 \cdot ^\circ C$ ($BTU/hr \cdot ft^2 \cdot ^\circ F$)



(a) NATURAL CONVECTION, $Gr_D Pr = 557,000$



(b) FORCED CONVECTION, $Re_D = 7200$

Figure D.1. Comparison between predicted and experimental heat transfer coefficients in air flow: (a) natural convection, $Gr_D Pr = 557,000$; (b) forced convection, $Re_D = 7200$.

shows a typical example with $Re_D = 7,200$ ($T_{Cu} \approx T_{Pt} = 93^\circ\text{C}$; $T_{air} = 30^\circ\text{C}$). The only worrisome discrepancy occurs at the $\theta = 80^\circ$ position, but that is to be expected because of the flow constriction in our vessel of limited width.

Predictions for the overall tube coefficients in forced convection can be found in most standard heat transfer texts. Figure 6.5 shows the agreement of our experimental values with a large body of results from previous investigations, as well as with a recommended correlating curve. Our values lie somewhat above the suggested curve, in the upper portion of the shaded region indicating the range of reported results. This, again, is probably due to the constriction in our vessel.

APPENDIX E

Error Analysis of Heat Transfer Measurement

The instantaneous heat transfer coefficient is calculated from equation (3.1):

$$h(t) = \frac{P(t)}{A(T_{Pt} - T_b)} \quad (E.1)$$

with the instantaneous power dissipation given by

$$P(t) = e(t)i(t) \quad (E.2)$$

From Appendix A we have

$$e(t) = e_0 - e_1 \quad (E.3)$$

and

$$i(t) = \frac{e_1}{R_o} \quad (E.4)$$

where R_o is the 0.5Ω resistor shown in Figure A.1. Therefore,

$$h_t = h(t) = \frac{(e_0 - e_1)e_1}{R_o A(T_{Pt} - T_b)} \quad (E.5)$$

Taking the logarithm of both sides of equation (E.5),

$$\ln h_t = \ln(e_0 - e_1) + \ln e_1 - \ln R_o - \ln A - \ln(T_{Pt} - T_b) \quad (E.6)$$

and differentiating

$$d \ln h_t = d \ln(e_0 - e_1) + d \ln e_1 - d \ln R_o - d \ln A - d \ln(T_{Pt} - T_b) \quad (E.7)$$

we obtain (approximately)

$$\frac{\Delta h}{h} = \frac{\Delta(e_0 - e_1)}{e_0 - e_1} + \frac{\Delta e_1}{e_1} - \frac{\Delta R_o}{R_o} - \frac{\Delta A}{A} - \frac{\Delta(T_{Pt} - T_b)}{T_{Pt} - T_b} \quad (E.8)$$

Squaring equation (E.8), we have

$$\begin{aligned} \left(\frac{\Delta h}{h}\right)^2 = & \left[\frac{\Delta(e_0 - e_1)}{e_0 - e_1}\right]^2 + \left(\frac{\Delta e_1}{e_1}\right)^2 + \left(\frac{\Delta R_o}{R_o}\right)^2 + \left(\frac{\Delta A}{A}\right)^2 \\ & + \left[\frac{\Delta(T_{Pt} - T_b)}{T_{Pt} - T_b}\right]^2 + \text{cross terms} \end{aligned} \quad (E.9)$$

Taking the time average of equation (E.9) and noting that for independent or uncorrelated errors the average of the cross terms approaches zero (see, for example, Feller [35]), we obtain the mean square relative error:

$$\overline{\left(\frac{\Delta h}{h}\right)^2} = \overline{\left[\frac{\Delta(e_0 - e_1)}{e_0 - e_1}\right]^2} + \overline{\left(\frac{\Delta e_1}{e_1}\right)^2} + \overline{\left(\frac{\Delta R_o}{R_o}\right)^2} + \overline{\left(\frac{\Delta A}{A}\right)^2} + \overline{\left[\frac{\Delta(T_{Pt} - T_b)}{T_{Pt} - T_b}\right]^2} \quad (E.10)$$

The relative error in the heat transfer coefficient is then

$$RE_h = \sqrt{\overline{\left[\frac{\Delta(e_0 - e_1)}{e_0 - e_1}\right]^2} + \overline{\left(\frac{\Delta e_1}{e_1}\right)^2} + \overline{\left(\frac{\Delta R_o}{R_o}\right)^2} + \overline{\left(\frac{\Delta A}{A}\right)^2} + \overline{\left[\frac{\Delta(T_{Pt} - T_b)}{T_{Pt} - T_b}\right]^2}} \quad (E.11)$$

In a typical case, the following quantities were measured and/or estimated from instrument specifications:

$$\left. \begin{aligned} e_0 - e_1 &= 2.0 \text{ V} \\ \Delta(e_0 - e_1) &= 0.01 \text{ V} \end{aligned} \right\} \frac{\Delta(e_0 - e_1)}{(e_0 - e_1)} = 0.005$$

$$\begin{array}{lcl}
 \left. \begin{array}{l} e_1 = 0.7 \text{ V} \\ \Delta e_1 = 0.005 \text{ V} \end{array} \right\} & \frac{\Delta e_1}{e_1} = 0.007 \\
 \\
 \left. \begin{array}{l} T_{\text{Pt}} - T_b = 55^\circ\text{C} \\ \Delta(T_{\text{Pt}} - T_b) = 0.5^\circ\text{C} \end{array} \right\} & \frac{\Delta(T_{\text{Pt}} - T_b)}{T_{\text{Pt}} - T_b} = 0.009 \\
 \\
 \left. \begin{array}{l} R_o = 0.5 \Omega \\ \Delta R_o = 0.01 \Omega \end{array} \right\} & \frac{\Delta R_o}{R_o} = 0.02
 \end{array}$$

The area of the platinum heater is 1.02 cm^2 . However, some of the power is also transferred to the bed through the epoxy surrounding the glass piece (see Figure 3.4). Accounting for the conductivity of the epoxy resin, we have taken the heat transfer area, A , to be 1.20 cm^2 . The error in this calculation is estimated at 6%, i. e., $\Delta A/A = 0.06$.

Going back to equation (E.11), we now have

$$RE_h = \sqrt{(0.005)^2 + (0.007)^2 + (0.02)^2 + (0.06)^2 + (0.009)^2} \quad (\text{E.12})$$

or finally,

$$RE_h = 0.064 \quad (\text{E.13})$$

The relative error in our measurements is therefore 6.4%. The 95% confidence interval is approximately twice the relative error; thus the h values can be expected to be in error by less than 13%.

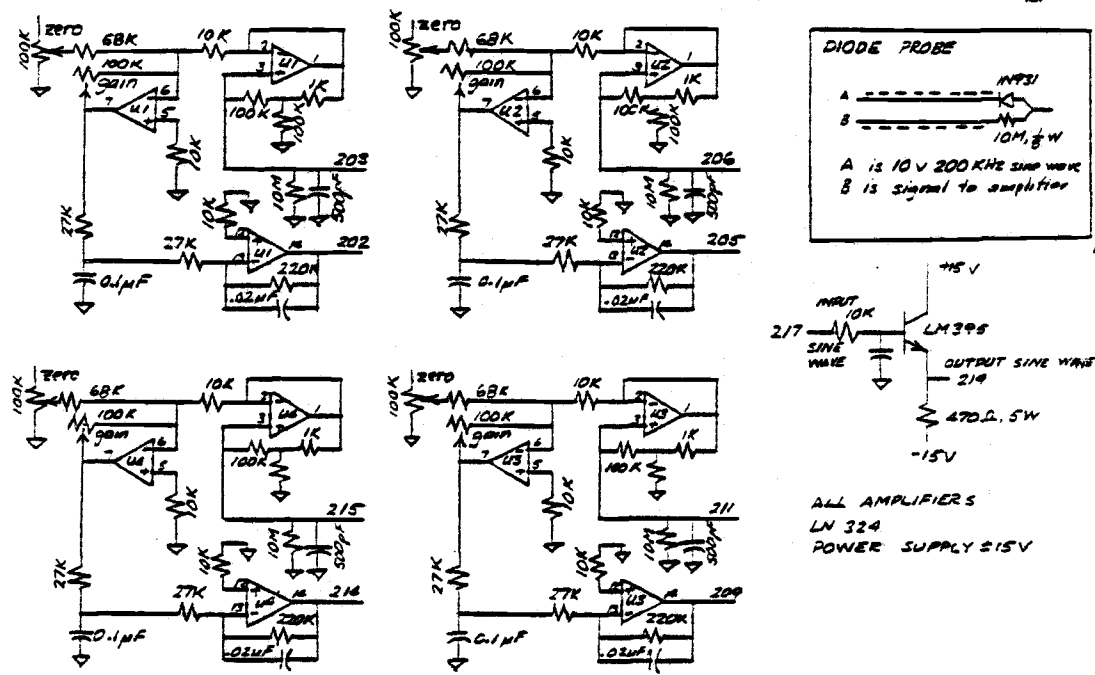
APPENDIX F

Capacitance Element Circuitry

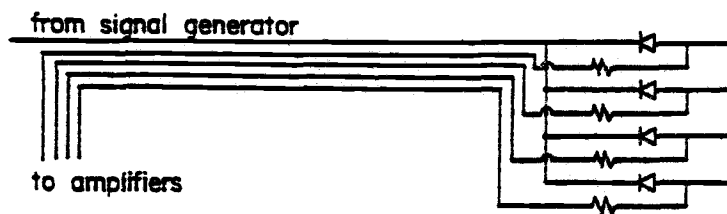
Voidage detector amplifiers are used with capacitance elements to obtain local voidage data in the vicinity of these probes. Figure F. 1(a) is a schematic diagram of a voidage detector amplifier circuit card. The circuits are used for bubble detection and for measuring time-averaged absolute voidages.

The multiple probes are connected in the vicinity of the instrumented cylinder in the manner shown in Figure F. 1(b). This arrangement reduces the capacitive loading on the signal generator and makes it possible to use a lead as long as 20 feet. If individual leads were used for each probe, then either shorter leads or a more powerful output amplifier would be needed to deliver a 200 KHz signal.

CAPACITANCE CIRCUITRY (ADJUSTABLE ZERO & GAIN) FOR DIODE TYPE PROBES SEP 21, 1977
TJF



(a)



(b)

Figure F.1. (a) Voidage detector amplifier card circuitry;
(b) connection of multiple capacitance elements.

APPENDIX G

Particle Thermal Time Constant as a Function of Particle Size

Following the procedure of Glicksman and Decker [49, 50], the low value of the Biot modulus for standard fluidized particles (sand, dolomite) in heated air indicates that the temperature gradients through the particle can be neglected. The time constant, τ_p , is then:

$$\tau_p = \frac{V_p \rho_s c_{ps}}{A_p h} \quad (G.1)$$

For spheres with heat transfer from one side,

$$\frac{V_p}{A_p} = \frac{d_p}{3} \quad (G.2)$$

Assuming that the primary mechanism for heat transfer between the particle and the tube surface is the conduction across the particle/tube gap, the heat transfer coefficient can be approximated by

$$h \approx \frac{k_g}{\delta^*} \quad (G.3)$$

where δ^* is some fraction of d_p . Taking the average gas thickness obtained from our experiments, equation (G.3) becomes

$$h \approx \frac{6.0 k_g}{d_p} \quad (G.4)$$

Combination of equation (G.1) with (G.3) and (G.4) gives

$$\tau_p = \frac{1}{18} \frac{\rho_s c_{ps}}{k_g} d_p^2 \quad (G.5)$$

When τ_p is plotted as a function of d_p on a log-log scale, a straight line with a slope of $\rho_s c_{ps} / 18 k_g$ is obtained.